

Optical variability of counterparts of ROSAT X-ray sources near the North Ecliptic Pole

von
Diplom-Physiker Carsten Simon
aus Berlin

von der Fakultät II – Mathematik und Naturwissenschaften –
der Technischen Universität Berlin
zur Erlangung des akademischen Grades

Doktor der Naturwissenschaften
– Dr. rer. nat. –

genehmigte Dissertation

Promotionsausschuß:

Vorsitzender: Prof. Dr. rer. nat. Gebhard von Oppen

Berichter: Prof. Dr. rer. nat. Klaus Beuermann

Berichter: Prof. Dr. rer. nat. Erwin Sedlmayr

Tag der wissenschaftlichen Aussprache: 18.1.2005

Berlin 2005
D83

Zusammenfassung

Carsten Simon:

Variabilität der optischen Gegenstücke von ROSAT Röntgenquellen am Nordekliptikalen Pol

Bei den optischen Gegenstücken von Röntgenquellen handelt es sich häufig um die Kerne von aktiven Galaxien (AGN, active galactic nuclei). Viele dieser Objekte sind optisch variabel, und da die Zeitskalen und Art der Variabilität wichtige Hinweise auf die physikalische Natur und Struktur dieser Objekte geben kann, ist die Suche nach variablen AGN ein lohnendes Unterfangen.

Um eine solche Suche nach variablen AGN und anderen Objekten durchzuführen, wurde eine Stichprobe von 167 Röntgenquellen aus der Region rund um den nordekliptikalen Pol (NEP) aus den Quellenkatalogen der ROSAT-Himmelsdurchmusterung ausgesucht.

Gleichzeitig mit der ROSAT-Himmeldurchmusterung aufgenommene optische Beobachtungen standen aus einem gemeinsamen Projekt mit dem Karl-Schwarzschildt-Observatorium Tautenburg zur Verfügung. Insgesamt wurden 89 Schmidtplatten aus einem Gebiet von 35 Quadratgrad um den NEP und mit einer zeitlichen Überdeckung von 30 Monaten analysiert.

Diese Schmidtplatten wurden mit dem PDS1010 Mikrodensitometer der Technischen Universität Berlin digitalisiert. Um die gewonnenen Daten zu verarbeiten, wurden verschiedene photometrische Methoden getestet und bezüglich der erreichbaren Genauigkeiten und nutzbaren Helligkeitsbereiche verglichen.

Die Daten wurden mit der ausgewählten Methode, einer Kombination von Vermessung der Schwärzungsprofile und Integration von Schwärzungswerten mit variablen Integrationsradien, reduziert. Hilfsdaten wie das "Seeing" der Schmidtplatten und Ausdehnung der Objekte werden dabei berücksichtigt.

Zur Analyse der Variabilität der Objekte wurde auf dem Vergleich von kleinen Feldern beruhende differentielle Photometrie angewendet. Um darüber hinaus auch echte photometrische Helligkeiten zu bestimmen, wurden die Messungen in ein gemeinsames photometrisches System überführt und dieses System mittels photometrischer Standardsterne kalibriert. Sonderfälle wie besonders helle Sterne und durch Nachbarsterne gestörten Objekte wurden ebenfalls diskutiert.

Die photometrische Genauigkeit (Standardabweichung) der differentiellen Photometrie beträgt 0.03 mag bei Objekten mit einer Helligkeit von 18 mag, 0.1 mag bei 20 mag Helligkeit.

Unter Benutzung publizierter Daten und eigener Beobachtungen wurden die optischen Gegenstücke zu den Röntgenquellen auf aus den Schmidtplatten gewonnenen Suchkarten identifiziert. Das Resultat sind photometrische Helligkeiten, Angaben zur Variabilität und optische Lichtkurven für alle Objekte.

Unsere Stichprobe enthält 79 AGN, von denen 37 mit Sicherheit und 10 möglicherweise variabel sind. Die Lichtkurven der variablen oder evtl. variablen Objekte, Suchkarten und Identifikationen für alle Objekte aus unserer Stichprobe sind in dieser Arbeit enthalten. Einige interessante Objekte werden detaillierter besprochen.

Abstract

Carsten Simon:

Optical variability of counterparts of ROSAT X-ray sources near the North Ecliptic Pole

Optical counterparts of X-ray selected sources to a large part consist of active galactic nuclei (AGN). A large proportion of these counterparts turns out to be optically variable, and because the timescales and manner of this variability can give important clues regarding the physical nature and structure of the counterparts, searching for variable AGN is a worthwhile undertaking.

In order to perform such an optical variability survey, a subset of 167 X-ray sources in an area around the NEP was selected in this work from the X-ray catalogues derived from the ROSAT all-sky survey (RASS).

Contemporaneous optical observations were available from a collaboration with the Karl-Schwarzschildt observatory (KSO) Tautenburg. A total of 89 plates were analyzed, covering an area of 35 degrees square around the NEP and spanning a timebase of 30 month.

The Schmidt plates were scanned with the PDS1010 Microdensitometer of the Technical University Berlin. To process these data, several methods to derive photometric data were implemented and compared regarding attainable precision and dynamic range.

The entire set of plate data were reduced with the method of choice, a combination of profile fitting and variable-aperture density integration which also incorporates constraints from plate seeing and object extension data.

For variability analysis, a highly precise method for differential photometry based on the comparison of small fields was implemented. To derive meaningful data beyond pure differential photometry, i.e. true photometric magnitudes, the measurements were also transformed into a mean common photometric system after the differential photometry and were calibrated using photometric standard stars. Special cases like bright stars and stars closely blended were also discussed.

The attained photometric precision (standard deviation) of the differential photometry is about 0.03 mag for 18 mag objects, 0.1 mag for 20 mag objects.

Using mostly published data and some own observations, the optical counterparts for the selected X-ray sources were identified on finding charts derived from the Schmidt plate observations, yielding photometric magnitudes, variability data and optical lightcurves for the X-ray counterparts.

As a result, we have identified 79 AGN within our sample, of which 37 show definite and 10 show probable variability. The optical lightcurves for all counterparts with confirmed or possible variability are published in this work. Identification data and finding charts for all variable and non-variable objects are also published. Several of the more interesting objects are discussed in some more detail.

Contents

Zusammenfassung	i
Abstract	iii
1 Introduction	1
1.1 Active galactic nuclei	1
1.2 X-ray observations of AGN	3
1.3 Variability in AGN	3
1.4 X-ray vs. Optical variability in X-ray sources	5
1.5 Aims	6
2 The X-ray data	9
2.1 The ROSAT satellite	9
2.2 The ROSAT all-sky survey	13
2.3 Assembly of the complete X-ray source list	16
2.4 Source selection for the variability survey	18
3 The optical data	23
3.1 The need for wide-field observations	23
3.2 Observed sky area	23
3.3 Origin of the optical data	24
4 Preparing the data for processing	29
4.1 Digitizing the optical data	29
4.1.1 Scanning aperture and stepsize	29
4.1.2 Scanning small fields	30
4.1.3 Practical considerations	31
4.1.4 Measurement imperfections	31
4.2 Handling of plate faults and visual disturbances	32
4.3 General properties and imperfections of photographic plates	33
4.3.1 Characteristic curve	33
4.3.2 Plate background	35
4.4 Astrometric properties of the Tautenburg Schmidt plates	37
4.4.1 Coordinate transformations	37
4.4.2 Astrometric standard stars	39
4.4.3 Discussion of astrometric results	39
5 Basic photometric methods	43
5.1 Integration of intensities	43
5.2 Density integration with fixed aperture	44
5.3 Density integration with variable aperture depending on source brightness	44
5.4 Radial profile determination	47
5.5 Profile parameter fitting	49
5.6 Profile fitting including saturation effects	50

5.7	Measured vs. calculated magnitude index, D–Intercept	52
5.8	Density integration with profile-dependent aperture	52
5.9	Discussion of the different integration methods	55
5.10	Calibration of magnitude indices	55
6	Advanced topics - analysis of sets of fields	59
6.1	Plate stacking	59
6.2	Seeing effects and determination of plate seeing	60
6.3	Extended Objects	60
6.4	Constrained fits for object parameter determination	61
6.5	Determination of plate sensitivity	62
7	Variability analysis	69
7.1	Matching small fields	69
7.2	Reduction of all plates and all fields into a common system	72
7.3	Bright stars	79
7.4	Evaluating the effects of near neighbours	81
7.5	Discussion of the results of the photometry	82
7.5.1	Photometric precision	82
7.5.2	Photometric errors for bright stars	85
7.5.3	Properties of the Tautenburg Schmidt plates	85
7.5.4	Comparison with similar studies	87
8	The NEP X-ray sources – identifications, variability and physical properties	93
8.1	Identification of X-ray counterparts	93
8.2	Identification contents of the NEP X-ray sample	94
8.3	Variability of optical counterparts	94
8.4	Comparison with similar studies from the literature	99
8.5	Discussion of individual objects	101
9	Outlook	113
9.1	Further improvements in photometry and variability analysis	113
9.2	Physical parameters of the extragalactic NEP X-ray sources	113
9.3	Using time-resolved X-ray data	114
9.4	A closer look at interesting objects	114
	Appendix	116
A	Bibliography	117
B	Acknowledgements	127
C	Plate data of used Schmidt plates	129
D	X-ray data for all sources	133
E	Optical data and identifications for all sources	141

F	Time-resolved photometric data	149
G	Finding charts	185
H	Curriculum Vitae	271

List of Figures

1	The ROSAT satellite	10
2	ROSAT X-ray telescope schematic	11
3	ROSAT PSPC assembly	12
4	RASS image of the SEP	14
5	RASS exposure map	15
6	X-ray completeness of the NEP variability survey	19
7	The Tautenburg Schmidt telescope	25
8	Distribution of the X-ray sources in the NEP area	26
9	Time coverage of the optical and X-ray data	27
10	Spread of characteristic curves of several plates	34
11	Photographical density for extended and pointlike sources	35
12	Large-scale plate background variations	36
13	Histogram of astrometric positional accuracy	40
14	Image data for star B=12.0 mag	45
15	Image data for star B=14.6 mag	46
16	Image data for star B=18.8 mag	46
17	Image data for star B=20.5 mag	47
18	Image data of extended source	48
19	Schematic: determination of the radial profiles	49
20	Gaussian fit for faint and bright stars	51
21	Density intercept for bright source	53
22	Density intercept for faint source	54
23	Photometric calibration of two standard sequences	57
24	Hierarchy of plates - scan fields - objects	63
25	Single scan, stacked image and DSSII-Image of one sample field	64
26	Seeing plots for good seeing and bad seeing	65
27	Plate seeing and extended objects	65
28	Example of Object extension plot	66
29	Distribution of the optical extensions of objects	67
30	Transformation of raw magnitudes to a mean common system	72
31	Residua and standard deviation vs. instrumental magnitude	73
32	Mean standard deviation vs. instrumental magnitude	74
33	Variability scatterplot for field 1RXS J180251.3+660540	75
34	Variability scatterplot for field 1RXS J182320.1+641924	76
35	Variability scatterplot for field 1RXS J180328.4+673806	77
36	Variability scatterplot for field 1RXS J180413.4+675412	77
37	Variability scatterplot for bright objects	80
38	Apparent variability by disturbances from near neighbours	82
39	Mean photometric precision	84
40	Distribution of seeing values of the Tautenburg plate sample	86
41	Distribution of plate sensitivity of the Tautenburg plate sample	86
42	Comparison of photographic and CCD lightcurve for KAZ 102	90
43	Magnitude distribution of X-ray counterparts	95
44	Redshift distribution of X-ray counterparts	95

45	Source extension of X-ray counterparts	96
46	Source variability of X-ray counterparts	98
47	Lightcurve of 1RXS J180216.3+641546 / G227-22	105
48	Lightcurve of 1RXS J182157.4+642051 / 1E 1821+64.3	105
49	Lightcurve of 1RXS J175505.8+651951 / IPC17549.6521	106
50	Lightcurve of 1RXS J180026.2+635719	106
51	Lightcurve of IY Dra	107
52	Lightcurve of 1RXS J180849.9+663431	107
53	Lightcurve of 1RXS J180328.4+673806 / Kaz 102	108
54	Lightcurve of 1RXS J181829.0+674127 / HS 1818+6740	108
55	Lightcurve of 1RXS J175813.2+674319	109
56	Lightcurve of 1RXS J180413.4+675412 / EX Dra	109
57	Lightcurve of 1RXS J174700.3+683626 / Kaz 163	110
58	Finding charts layout	185

List of Tables

1	List of all used Tautenburg Schmidt plates	129
2	X-ray data of all sources	134
3	Optical data and available identifications of all sources	142

1 Introduction

1.1 Active galactic nuclei

AGN (active galactic nuclei), especially in their most violent and powerful form of QSOs (termed quasi-stellar objects for historical reasons), are the most luminous objects known to man, and because of this, they are also among the oldest and most distant objects that have been observed in physical form. The study of old and distant QSOs reveals a glimpse back into the beginning of the universe; also, on its way to the observer, their light travels through all intervening space, occasionally probing interesting objects on the way. Because of this, QSO and AGN receive much attention in current astrophysical research.

In the widely accepted "unified" model of AGN, a supermassive black hole with a surrounding accretion disk forms the center of the AGN, with a BLR (broad line region) and NLR (narrow line region) surrounding this center. The black hole and accretion disk are situated in or close to the center of a surrounding "host" galaxy. The BLR, located next to and around the accretion disk, is a region of relatively high temperature and electron density, with a large velocity range due to rotational and turbulent motion, with relatively small amounts of matter and a linear size and volume which is small compared to the scale of the galaxy; the BLR is the source of the broad, permitted emission lines or of the broad component of permitted emission lines, mostly from Hydrogen, Helium, Carbon, and Magnesium. In contrast, going further outwards, the NLR is a much calmer region with lower internal velocities, temperatures and electron densities, reaching well out into the surrounding galaxy, much further than the BLR, and containing much more mass; the NLR is the source of permitted and forbidden emission lines, e.g. of Hydrogen and Oxygen. Orders of magnitude for the most important physical parameters (temperature, electron density, radius and mass of involved matter, taken from Osterbrock 1993) are $T \approx 10^4$ K, $N_e \approx 10^{9.5} \text{ cm}^{-3}$, $r \approx 3 \cdot 10^{-2}$ pc, $M \approx 10M_\odot$ for the BLR and $T \approx 10^4$ K, $N_e \approx 10^4 \text{ cm}^{-3}$, $r \approx 10^2$ pc, $M \approx 10^6M_\odot$ for the NLR. The BLR and NLR are not filled homogeneously, but rather clumped and with filaments, where filling factors for BLR and NLR can be determined from model calculations and are of the order of 10^{-1} (BLR) and 10^{-3} (NLR).

Besides the emission lines, a thermal continuum from the accretion disk and non-thermal continuum from reprocessing of radiation contributes to the total emission, with strength and power-law indices which are not only depending on the individual object but also subject to variability for each single object.

Also, the emission of a relativistic plasma jet, supposedly aligned with the spin axis of the central black hole, is seen in many AGN.

Depending on physical and observational parameters like

- mass and accretion rate of the black hole,
- composition and density of the surrounding plasma, gaseous matter and dust
- size and brightness of the galaxy surrounding the black hole and

- alignment of the spin axis of the black hole and the accretion disk to the line of sight
- source distance to the observer

a wide variety of observational classes of objects can result, the most important being

QSO which are the most luminous form of AGN, where the division between QSO and the (lower-luminosity) Seyfert galaxies is drawn by definition and somewhat arbitrarily at an absolute magnitude of $M_B = -23$ mag. QSOs are detectable up to very high redshifts of (currently) almost $z = 7$. Both because of the high luminosity of the AGN and the large distance of most QSOs, the surrounding host galaxy is invisible in almost all QSOs.

Seyfert1-Galaxies which are – except for the by definition lower luminosity and consequently smaller average distance – similar to QSO, with broad permitted and narrow forbidden emission lines. In high-resolution optical observations of weaker and nearer Seyfert1-galaxies, the underlying host galaxy is visible.

Seyfert2-Galaxies with narrow permitted and forbidden lines, i.e. a weak or obscured BLR, and on the average weaker, more reddened and with a higher dust content than Seyfert1's. In some nearby Seyfert2-galaxies, the NLR can be resolved by high-resolution optical observations.

intermediate classes of Seyfert-Galaxies There is no sharp division between Seyfert1 and Seyfert2-galaxies; rather, Seyfert galaxies form a continuum with regard to the relative strength of the permitted and forbidden emission lines, and intermediate types Seyfert 1.5 (with strong broad and narrow components of permitted lines), 1.8 (with strong narrow and weak broad components of the permitted lines $H\alpha$ and $H\beta$) and 1.9 (with a weak broad component visible in $H\alpha$ only) have been defined.

Liners (low-ionisation nuclear emissionline regions, Heckman 1980) are a continuation of Seyfert2-galaxies to even lower luminosities and ionisation levels, where narrow emission lines, photoionised by a weak non-thermal continuum, are only weakly detected. Indeed, the phenomenon extends right to the limit of present-day detectability, and it seems likely that even weaker objects still exist, undetectable for the currently available observation techniques. Evidence of Liner activity is even found in nearby galaxies like M31, and the proportion of galaxies with Liner activities is an unsolved problem but may be quite high. Given the fact that an accreting AGN may use up all its fuel, there is even the possibility of dormant i.e. temporarily inactive AGN.

BL-Lac objects seem to form a completely different class of objects observationally, their main characteristic being a total or almost total absence of *any* (emission and absorption) lines, and a non-thermal continuum. Also, radio emission, polarisation of the emitted radiation and fast and strong variability are common in BL Lac. However, the most probable explanation

is that BL Lac are AGN seen under special viewing conditions, i.e. that the line of sight is aligned with the direction of the AGN jet, and we are seeing synchrotron radiation together with the effects of relativistic beaming.

For comprehensive reviews see e.g. Osterbrock (1993) or Antonucci (1993).

1.2 X-ray observations of AGN

Although AGN were originally discovered in the radio domain, X-ray emission is a common and prominent property of all AGN, and X-ray studies are an important tool for finding new AGN and for new insights into the physical mechanisms that are at work within AGN.

The first X-ray observations of AGN go back to the 1960s, starting with short-term rocket and balloon observations; because of the longer and uninterrupted observations possible with satellites, X-ray observation satellites soon became the most important tool for astrophysical X-ray observations. X-ray surveys, X-ray imaging, observations of spectra and studies of variability were first pioneered, then in widespread use by a long line of observational X-ray satellites, the most important being UHURU (1970), HEAO-2 (Einstein Observatory, 1978), EXOSAT (1983), GINGA (1987) and ROSAT; recent and still active observatories include XMM-Newton and CHANDRA, and the observational progress by larger and better instruments seems unbroken.

X-ray observations of AGN are of particular importance mainly because of the following reasons:

- X-ray emission is an extremely common property in AGN. Indeed, given the "unified" AGN model, X-ray emission should occur in **all** AGN because of the presence of the hot accretion disk, and non-detection of X-ray emission should only occur due to observational constraints like X-ray obscuration of the emitting region or insufficient detection sensitivity for faint or high-redshift objects.
- X-ray emissions come at least partially from the innermost part of the AGN's central engine, where other observational methods cannot penetrate. Because of that, variability of the X-ray emission is generally more rapid than at any other frequency bands.
- X-ray observations complement observations in other spectral bands with regard to the analysis of the ongoing physical processes.

For a comprehensive review see e.g. Mushotzky et al. (1993).

1.3 Variability in AGN

Variability is a common phenomenon in AGN; depending on the observed timebase and temporal resolutions, spectral band and observational precision, some, most or almost all observed AGN show a certain degree of variability. For a comprehensive review of X-ray and optical variability in AGN see e.g. Mushotzky et al. (1993) and Ulrich et al. (1997).

Taking advantage of this widespread occurrence of variability, we can use it as a tool to improve our knowledge of single well-observed sources, test the physical models of AGN and even to find new AGN.

- It is possible to study the variability of known AGN by (preferably simultaneous) observations on different timebases, timescales and in different spectral bands and model the physical nature and the geometrical and physical parameters (e.g. object classification, size and alignment of emission regions, accretion rates) of an object. In other words, we use variability as a tool for an intensive study of a single object.

It is mostly well-known bright AGN that tend to be observed in that way; some examples are 3C273, NGC 4151 and NGC 5548 (see e.g. Ulrich et al. 1997 for observations and literature concerning those objects), KAZ 102 (Treves et al. 1995) or Boller et al. 2003.

- Statistical studies of the variability properties of a set of objects can be used to determine statistics of the physical parameters of a set of objects, on a lesser degree of precision when compared to the previous point.

Examples of this kind of studies are Grupe et al. (2001), Koo and Kron (1982), Koo et al. (1986), Hook et al. (1994), Hawkins and Veron (1993), Cristiani et al. (1990) and also to a small extent this work.

- Because variability is a common property in AGN, it can be used as a selection criterium to find AGN in surveys. Since AGN are not the only objects known to show variability, other properties (e.g. proper motion and spectral or color properties) should be used as well to allow for a more effective discrimination between AGN and galactic objects. See Hawkins (1986) and Treves et al. (1989).

The combined use of variability and proper motion as a survey criterium (see e.g. Majewski et al. 1991, Scholz et al. 1997 or Brunzendorf and Meusinger 2001) seems to be very successful if a sufficient time base, photometric depth and photometric precision of the survey is attained. It is also subject to selection effects totally different from those that plague other AGN search techniques like surveys based on X-ray-emission or radio emission of the AGN or on color criteria and is, therefore, at least, a good complement to those other techniques. Indeed, the method seems to be remarkably free from selection effects; see e.g. Brunzendorf and Meusinger (2002) for a discussion of the attainable completeness.

For all three approaches, a thorough understanding of the physical processes within AGN and the effects leading to variability is necessary. For studies on sets of objects, a knowledge of the statistical probability of variability and the concerned timescales is as well required.

To allow further studies of these properties in a set of objects in a limited, well-studied sky area, selected according to rather strict criteria, we have undertaken a comprehensive survey of the optical variability of a set of X-ray selected AGN

at the north ecliptic pole, with a timespan of the optical observations of 30 month. The area of the north ecliptic pole (abbreviated NEP from now on) was an obvious target for such an undertaking because of the ROSAT all-sky survey observation characteristics (see Chapter 2.2 for a more in-depth discussion) and the availability of a wealth of additional data (see Chapter 3.2), in particular the "ROSAT north ecliptic pole survey" (see e.g. Henry et al. 2001, Gioia et al. 2003).

AGN are not the only variable objects found in this kind of survey. X-ray emitting stars also show optical variability to a certain extent. We have identified those stars where possible; however, they are not our main topics of interest, and we mainly list their measured properties regarding variability without going into too much details.

1.4 X-ray vs. Optical variability in X-ray sources

The classes of objects that are found in a X-ray selected sample are well-known from previous large-scale identification projects like e.g. the Einstein Observatory medium sensitivity survey (Maccacaro et al. 1982, Stocke et al. 1983, Gioia et al. 1984) and the Einstein Observatory extended medium sensitivity survey (Gioia et al. 1990, Stocke et al. 1991) as well as from more recent works like the ROSAT north ecliptic pole survey (Henry et al. 2001, Mullis 2001) and other projects (e.g. Zickgraf et al. 1997, Appenzeller et al. 1998). Possible X-ray counterparts are

AGN including QSOs, Seyfert galaxies and BL Lac objects,

galactic objects i.e. normal stars, dwarf stars, cataclysmic variables, X-ray binaries and planetary nebulae,

galaxy clusters,

normal galaxies, including cooling flow galaxies.

The exact composition of a sample depends on the observed area, mainly on galactic latitude which influences the ratio of extragalactic vs. galactic objects, and on the spectral response of the X-ray telescope, which influences the relative numbers of X-ray-hard and -soft sources in a certain sample, e.g. with a certain flux limit. Some examples are given in Chapters 8.2 (for this work) and 8.4 (for some well-studied standard samples from literature).

To give some crude idea of the typical identification contents of an X-ray selected sample, note that about half of the counterparts are AGN, one quarter are stars, and one eighth is made up of clusters of galaxies, with the remaining sources belonging to diverse classes like CVs, PNs, normal galaxies etc.

Regarding variability of those objects, there are classes where X-ray or optical variability is not to be expected on observable timescales, like galaxy clusters or normal (cooling flow) galaxies. There are objects like (non-binary) stars where variability is possible; some classes of objects like QSOs and Seyfert galaxies where variability is very common; and there are objects like cataclysmic variables and X-ray binaries where variability is the rule.

The expected timescales of variability depend on spectral band (X-ray or optical) and object class. For AGN, optical short-term variability of the continuum on

timescales as low as a few hours has been observed, whereas there is no upper limit to the timescale of long-term variability. Most data on optical variability comes from a few well-observed and well-sampled objects, mostly from multi-wavelength campaigns of NGC 4151, NGC 5548 and 3C273. Observed timescales of optical variability in these objects range from a few hours to years; for examples see Ulrich et al. (1997). In the X-ray domain, timescales are still shorter, and the most extreme objects (e.g. NGC 6814, Mushotzky et al. 1993) can show significant changes in less than 100 seconds.

The manner of observed variability is rich and very diverse, with chaotic and irregular changes dominating. Strengths and timescales depend on luminosity and class of the observed objects – with low-luminosity objects showing more rapid changes –, whereas the percentage of variable objects depends also on the time-base and precision of the observations – longer observational timebases and more precise observations tend to find more variable objects. Some recent examples from literature are cited in Chapter 7.5.4.

When discussing and analysing variability of different components of the compound AGN spectrum (X-ray and optical), it is important to separate the emission processes (continuum, broad line region, narrow line region); continuum and broad line variability is the rule, while narrow line variability is generally not observed because of the much larger size of the NLR and corresponding greater timescales for changes, which are not (yet) observable. Vice versa, the timescales of variability of spectral components tell us the size of the emitting region, and this analysis forms an important contribution to AGN models.

1.5 Aims

There are three main aims to the work presented here.

- We present a method for photographic photometry on Schmidt plates. This method is elaborated in Chapters 4 and 5. Although most of the topics and techniques presented are quite old and well-known, we have tried to introduce some new ideas to reach a higher level of precision (see e.g. Chapter 6.4).
- This photographic photometry is extended and applied to entire sets of plates (Chapters 6 and 7). Using the resulting set of photometric data, a technique for differential photometry and variability analysis is developed which allows high photometric precision for small fields to be reached.

Although these methods are applied only to photographic photometry in this work, it is important to note that they can be applied to *any* kind of time-series of photometric data and thus would permit a higher precision to be reached also for CCD-based observations.

- These photometric techniques are applied to an X-ray selected set of objects near the NEP (see Chapters 2 and 3 for the definition and selection of the sample and Chapter 8 for a discussion of the results). This includes

a discussion of all X-ray sources (Appendix D, E, F, G and Chapter 8.5) with identifications, finding charts and lightcurves where applicable.

From these data, statistical results for the frequency and timescales of optical variability in AGN can be calculated.

2 The X-ray data

The main aim of this work is a study of the optical long-term variability of X-ray selected sources near the NEP. This chapter is intended to introduce the instruments and means by which the X-ray data were produced and explain the source selection process.

2.1 The ROSAT satellite

ROSAT, short for "Röntgensatellit", was built, launched and operated as an international collaboration led by the German MPE (Max-Planck-Institut für extraterrestrische Physik). After a proposal made by the MPE in 1975, initial project studies started as early as 1977. The satellite was originally due to be launched in 1987 with an US space shuttle; after the "Challenger" accident, the mission was shifted for launch with a Delta expendable carrier in 1990.

The main mission objectives of ROSAT were to conduct an extensive, all-sky survey of the X-ray sky with an unprecedented sensitivity and positional accuracy and to perform pointed observations of X-ray sources afterwards, in a guest-observer mode. The main scientific instrument was the ROSAT X-ray telescope with a carousel sensor assembly containing two position-sensitive proportional counters and the high-resolution imager. The second scientific instrument was the wide-field camera, piggybacked to the XRT.

A short summary of the ROSAT scientific instruments (from Briel et al. 1997):

XRT – X-ray telescope The ROSAT XRT is a grazing-incidence, Wolter type I mirror telescope with four nested paraboloid/hyperboloid mirror shell pairs. Focal length is 2.4 m, the aperture of the outer (largest) shell is 83.5 cm; the on-axis geometric collecting area is 1141 cm², with the effective area depending on photon energy and off-axis angle. The field-of-view of the telescope, when used with the PSPC (see below), is 2 degrees in diameter; the angular resolution depends mainly on the off-axis angle, with a blur radius of a point source of 3 arcsec on-axis, and up to 3 arcmin at the border of the field-of-view.

PSPC – position-sensitive proportional counter The PSPC is a multiwire proportional chamber.

The XRT+PSPC-assembly is sensitive for X-ray photons with energies of 0.1 – 2.4 keV. The effective area as a function of energy is determined by the combination of the reflectivity of the X-ray telescope and the quantum efficiency of the detector/entrance window assembly. The shape of this sensitivity function is very non-linear, with local peaks near 0.28 and 1 keV and separated by very low sensitivity from 0.28 to about 0.4 keV, making the transformation from countrates to spectral fluxes non-trivial and also dependent on the energy distribution of the source.

The PSPC spatial resolution is about 25 arcsec in the center field of the telescope and slightly energy-dependent, while for higher off-axis values the

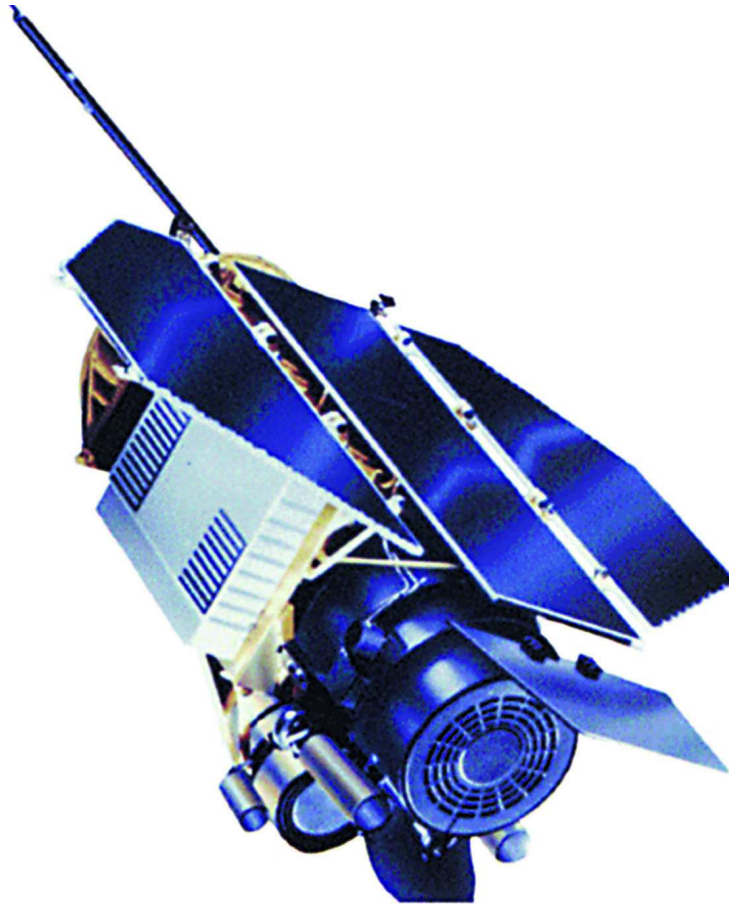


Figure 1: The ROSAT satellite, artist's impression. The entrance window of the XRT (X-ray telescope) is located at the lower right (large opening covered by a circular mesh). The smaller circular opening to the left is the entrance window of the XUV-sensitive WFC (wide-field camera). Between the XRT and the WFC, two star sensors can be seen. The whole assembly is covered by a large solar panel (upper right) which provides electrical energy and also shields the telescopes and satellite body from solar thermal radiation. The entire satellite is about 4m in length and has a total weight of about 2.4 tons. (Picture courtesy of MPE)

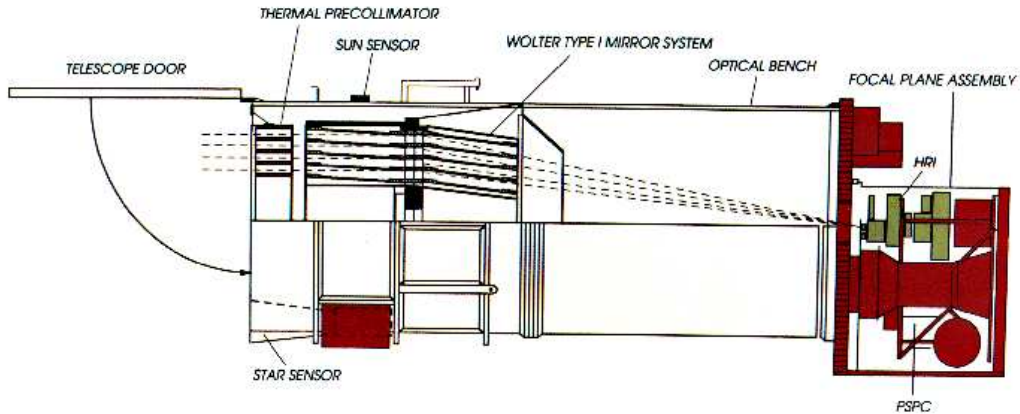


Figure 2: The ROSAT XRT (X-ray telescope) consists of a nested Wolter-telescope with grazing-incidence optics, with the detector assembly (PSPC and HRI) positioned at right at the telescope’s focus. (Picture courtesy of MPE)

(energy-independent) increased blur radius of the telescope dominates. The spectral resolution is about 27% FWHM at 1.5 keV but varies with photon energy. A pulse-height analyser allows a determination of the photon energy E (in keV) with a FWHM ΔE of

$$\frac{\Delta E}{E} \approx 0.43 \sqrt{\frac{E}{0.93}}$$

Because the PSPC is a gas-filled detector operating in a vacuum environment, the entrance window of the detector is stabilized against the pressure difference by a three-stage mechanical support structure (a rib structure and two wire meshes with different wire thickness and spacing). This support structure causes a certain amount of shielding which makes observations with a stationary detector unfeasible because sources located behind the support structures are blocked or at least weakened; this is no concern during the all-sky survey because of the scanning movement but requires a small ”wobble” movement during pointed observations. The presence of the support structure is important to us because it introduces subtle variability effects into the X-ray data which cannot be eliminated wholly, making interpretation of X-ray variability a challenging task (Fuhrmeister and Schmitt 2003).

HRI – high-resolution imager The HRI is a position-sensitive microchannel plate with a better spatial resolution than the PSPC (4 arcsec on-axis) but with a smaller field-of-view (38 arcmin diameter) and practically no spectral resolution. The HRI was not used during the ROSAT all-sky survey, and no HRI data are used in this work.

WFC – wide field camera ROSAT’s second, smaller scientific instrument, the



Figure 3: The ROSAT PSPC (position sensitive proportional counter) assembly, with the entrance window and filter wheel at the top. (Picture courtesy of MPE)

WFC, consists of three nested Wolter mirror shells, with a focal length of about 0.5 m, a maximum aperture of about 50 cm, and a detector assembly consisting of a curved microchannel plate and a filter wheel. The WFC is sensitive in the XUV band, for photon energies 0.05 – 0.21 keV. Because the WFC is coaligned with the XRT it also participated in the ROSAT all-sky survey; however, because of the smaller sensitivity of the WFC, combined with the strong galactic absorption at XUV wavelength, source detections and fluxes are usually available only for galactic sources and for the brightest of our sources, and the WFC is of no concern to this work.

ROSAT was launched into earth orbit on June 1st, 1990. After an initial bring-up phase where spacecraft performance and instrument performance and calibrations were checked (PVC i.e. performance, verification, calibration phase), observations for the ROSAT all-sky survey (RASS) were performed mainly between July 30th, 1990, and January 25th, 1991.

After the completion of the RASS, several years of pointed observation followed, yielding a wealth of scientific data that is still being used today. After exhaustion of all but a small remnant of the PSPC gas supply in 1994, the ROSAT XRT continued to be used with the HRI as the main detector. The satellite was finally switched off in 1999, exceeding its nominal lifetime of 18 month by more than a factor of five.

Although ROSAT did not perform the first X-ray all-sky survey, it has increased the number of objects known from all-sky surveys by more than two orders of magnitude. More recent observatories, most notably *ASCA*, *BeppoSAX*,

Chandra/AXAF and *XMM-Newton*, have again increased spatial and spectral resolution and collecting area for pointed observations, and introduced CCD sensors into X-ray astronomy; however, with the failure of the german ABRIXAS mission, the RASS will be *the* definitive X-ray survey mission for some years to come, with the next possible successor (ROSITA, "Roentgen Survey with an Imaging Telescope Array") planned for launch after 2007.

2.2 The ROSAT all-sky survey

As described above, the ROSAT all-sky survey was one of the main science objectives of the ROSAT mission.

During a period of roughly half a year, the satellite scanned the celestial sphere in great circles during each of its 96-min orbits. Each great circle would always contain the poles of the ecliptic and scan a strip of sky 2 degrees across; the plane of the great circles rotated by 1/365 of a full circle per day, so that the entire sky was covered by the scans in a 6-month's period.

That way, the ecliptical poles were exposed during half a year for about 30 seconds every 96 minutes, yielding a total exposure of up to 40 ksec; while in the ecliptical plane, where the 2-degree wide survey strips take 2 days to drift across a source, the integrated exposure decreases to about 400 sec. This scanning law makes the ecliptical poles an ideal area for long-term X-ray variability studies because of the deep exposure and the long visibility of sources. See Fig. 4 for an impression of the deeper coverage at the ecliptical poles.

In practice, the ideal scanning law described above does not quite hold:

- The PSPC detector has to be switched off when the satellite is exposed to intense charged particle radiation, e.g. during solar flares or during passage through the south-atlantic anomaly (SAA) or the earth's radiation belts. Roughly one quarter of the theoretically possible observation time is lost for this reason. Because the passage through the SAA primarily influences southern sky areas, southern sky areas and in particular the south ecliptic pole have a systematically less deep coverage than the northern areas.
- Because of a severe spacecraft malfunction, the last week of the survey in January 1991 data was lost, and the missing sky areas were scanned in February and August 1991. A small amount of data for the RASS was also taken as part of the PVC phase in June 1990 before the start of the proper RASS scanning. Lastly, some sky fields that still had no or less-than-desirable coverage were observed in pointing mode in february 1997 ("RASS repair"; ROSAT news No. 52, MPE 1997).
- Changes in the scanning law made due to time constraints shortly before completion of the sky survey also make the exposure map somewhat heterogeneous.

The resulting exposure map from all survey data is shown in Fig. 5.

From the attitude data of the satellite and the calibration data of the science instruments, position, timing and energy of the individual detected X-ray photons

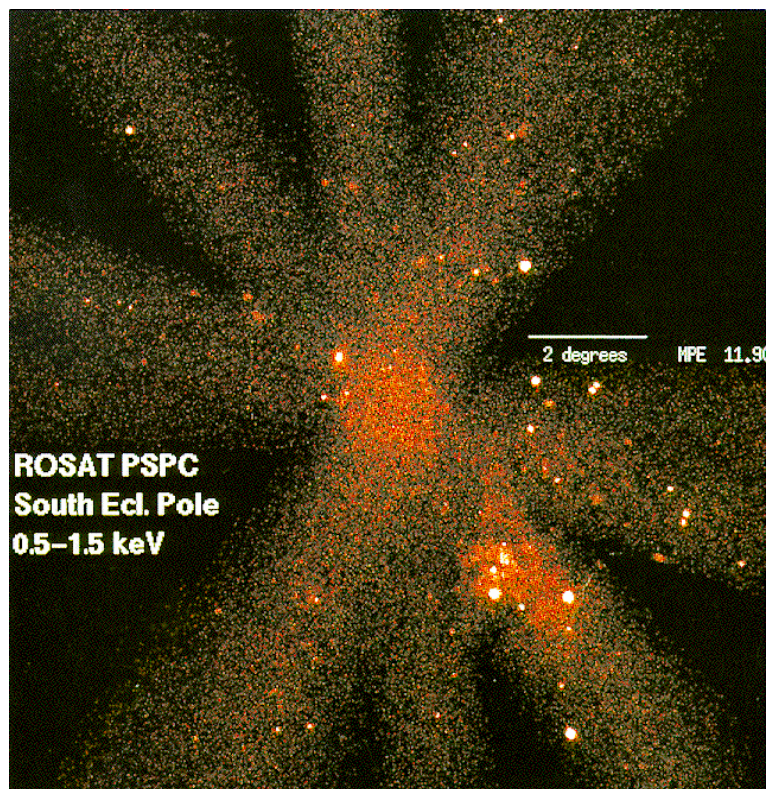


Figure 4: Partial RASS image of the SEP. Please note how the survey scan strips overlap at the position of the ecliptical pole to form a much deeper image. (Picture courtesy of MPE)

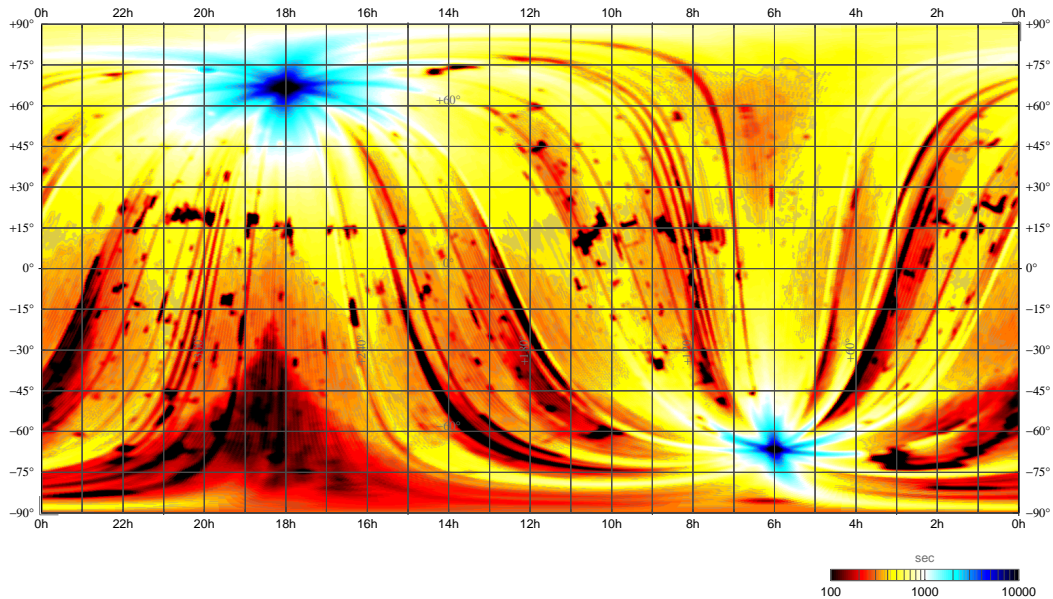


Figure 5: Exposure map of the ROSAT all-sky survey, in equatorial coordinates. The two dark areas mark the ecliptical poles where the exposure times is longest. (Picture courtesy of MPE)

were collected. The subsequent source detection and screening process as well as the properties of the resulting data set is described in detail in Voges et al. (1999).

From the resulting list of X-ray sources, a subset of sources, the RASS BSC (bright source catalog) was selected according to the following selection criteria:

- object countrates ≥ 0.05 cts/sec
- detection likelihood (see Voges et al. 1999) ≥ 15
- number of photons ≥ 15

In addition, all resulting sources had to pass a visual screening where sources with doubtful values for some of the derived parameters were flagged.

The resulting dataset, i.e. the RASS BSC, contains 18.811 sources with source positions and positional errors, source and background countrates, exposure time and dates of observations, hardness ratios, detection likelihoods, extension, reliability and screening data and many other supporting data.

For an extension of the RASS BSC to fainter fluxes (RASS FSC i.e. faint source catalog; Voges et al. 2000), the above-mentioned constraints were relaxed as follows:

- no constraint for object countrates
- detection likelihood ≥ 7
- number of photons ≥ 6

No visual screening was performed for these sources.

The resulting dataset, i.e. the RASS FSC, contains an additional 105.924 sources.

2.3 Assembly of the complete X-ray source list

In this chapter, the somewhat heterogenous X-ray sample that was used as a base for the optical identification and for the selection of sources for the variability analysis is described.

The production of a scientific catalog like the RASS BSC or FSC is a very time-consuming task. While the data on which both catalogs are based was taken mainly in 1990, the final version of the RASS BSC became available to the scientific community in June 1996; the RASS FSC became publicly available in May 2000. During this time, data analysis was ongoing, and improvements to the data reduction and calibration pipeline were continuously being made.

At the time when the Tautenburg Schmidt plates became available, it was not desirable to wait for the final source detection procedure to be finished for the NEP region, so preliminary data had to be utilized. Below is a list of the different sources of X-ray data that were used:

SASS data While ROSAT was collecting data for the RASS, the resulting X-ray photon data were gathered in strips of two days observation time each. These sky strips were then each analysed using the SASS (standard analysis software system) data reduction software package developed specifically for the analysis of ROSAT data.

This approach allows for a very quick analysis, but there are a number of shortcomings, especially for sources located close to the ecliptical pole.

- For sources located close to the border of a strip, source data are unreliable because only a part of the source's photons are contained.
- At the time of the SASS data reduction, early in the ROSAT project, there were still errors in the aspect solution of the satellite, leading to systematical errors in the position of X-ray sources.
- For sources near the ecliptical poles, where the strips overlap to a great extent, the source detection process in each strip uses only a fraction of the available photons, so the sensitivity of the source detection process is much decreased.
- For the same reason, sources near the ecliptical poles are usually detected several times, a source of confusion during the identification of the optical counterparts.

Despite these drawbacks, the SASS data was invaluable for setting up the first target list, for a preliminary identification of X-ray counterparts and for the subsequent placement of the small scan fields within our Schmidt plates. The preliminary, SASS-based target list was later superseded by the results from the RASS BSC and RASS FSC. Despite the preliminary nature of the

SASS results, no X-ray sources were missed with respect to the final source catalogs (RASS BSC and FSC). The number of spurious sources that were taken from the preliminary lists but are missing in the final source lists is very low (6 sources in the complete source list, of which 5 were scanned on the Schmidt plates).

RASS BSC and FSC After the completion of the RASS, the resulting X-ray strip data were co-added by a shift-and-add technique using X-ray sources with known positions. The resulting photon maps take full advantage of the deeper exposure at the ecliptical poles and have been used to generate the RASS BSC and FSC (see Chapter 2.2) by a sophisticated background determination and source detection process described in Voges et al. (1999).

About 87% of the X-ray sources (146 out of 167) have RASS detections; for about 75% of the sources the RASS is the sole X-ray data source, the difference being sources that do have RASS detections but where data from deep pointings (e.g. NEP deep survey, see below) is also available.

Regarding completeness, our source list is complete down to fluxes of 0.05 cts/sec, the limit of the RASS BSC, and almost complete, excluding only 4 faint extended sources down to 0.015 cts/sec. Regarding the total content of the RASS FSC down to its somewhat fuzzy sensitivity limit, our target list is far from complete, nor was it ever intended to be, containing only 146 out of 760 sources (RASS BSC+FSC) in the area covered by the Schmidt plates.

NEP deep survey The NEP deep survey (Bower et al. 1996) takes advantage of two very deep pointed observations with an added exposure time of 79.1 ksec, aimed exactly at the NEP, yet again doubling the exposure of the RASS at the point where its exposure time is largest.

For the NEP deep survey, the central 15.5 arcmin radius of the field of view of these pointed observations were analyzed. 20 X-ray sources have been detected; many (9 out of 20) of the sources are also found in the RASS BSC+FSC. With the help of optical follow-up observations 18 of the 20 sources have been identified. All but one object (RXJ 1759.0+6624, a QSO at $z=1.74$, the weakest X-ray source of the NEP deep survey) are contained in our source list.

Catalogs of ROSAT pointed observations from PSPC and HRI All ROSAT pointed observations have been routinely processed by the ROSAT consortium using SASS and visually checked afterwards; the resulting source lists have been compiled into the "ROSAT Source Catalog of Pointed Observations with the Position Sensitive Proportional Counter" (2RXP) and the "ROSAT Source Catalog of Pointed Observations with the High Resolution Imager" (1RXH), containing (2RXP/1RXH) 100,048/56,401 sources and covering 17.3%/1.94% of the sky. These catalogs have been checked for X-ray sources that had been contained within the preliminary target lists but are not contained within the RASS source catalogs (BSC and FSC).

It must be pointed out that our target list is in no way complete regarding the pointed observations; the coverage of pointed observation in the NEP area is very patchy, and the source catalogs with this patchy sky coverage have not been analysed down to any flux or countrate level; rather, the catalogs of pointed observations were used as an auxilliary source of information to help identify sources already included in our preliminary target lists.

That way, 20 sources have been found in the "ROSAT Source Catalog of Pointed Observations with the Position Sensitive Proportional Counter" (2RXP) only, i.e. are not contained within the RASS BSC or FSC data.

From the entire set of 167 sources, 17 sources were also detected in HRI images and are contained in the "ROSAT Source Catalog of Pointed Observations with the High Resolution Imager" (1RXH). No source was detected in the 1RXH catalog only.

Preliminary MPE data Preliminary RASS and identification data, namely

- SASS source lists from RASS strip data and preliminary source correlations and identifications for those sources (Hasinger 1991, Thomas 1991)
- preliminary source source lists from the RASS merged NEP cap (Böhringer 1992)
- preliminary source lists from the RASS BSC and FSC data (Voges 1996)

were kindly provided by several MPE and ESO scientists and were used to set up the preliminary target lists. Although these data were very valuable to set up the scan lists, the X-ray data were later superseded by the final data (RASS BSC+FSC, NEP deep survey, catalogs of ROSAT pointed observations).

The resulting completeness histogram of our RASS-detected X-ray sources when compared to the RASS FSC is shown in Fig. 6. Because of the low number of affected sources, no comparable analysis was done for the sources detected in pointed observations only.

2.4 Source selection for the variability survey

From the source list described in Chapter 2.3, a subsample was selected for scanning and subsequent variability analysis.

Because of the processing constraints described in Chapter 4.1.2, it was necessary to limit the number of scanned fields on the Schmidt plates as far as possible. Sources where optical variability could be excluded without any reasonable doubt or where no sensible results of the optical photometry could be expected were excluded from the target list for variability analysis (and were consequently not scanned on the Schmidt plates). Much care was taken to handle the "deletion" criteria rather strictly so as not to introduce observational bias into our results.

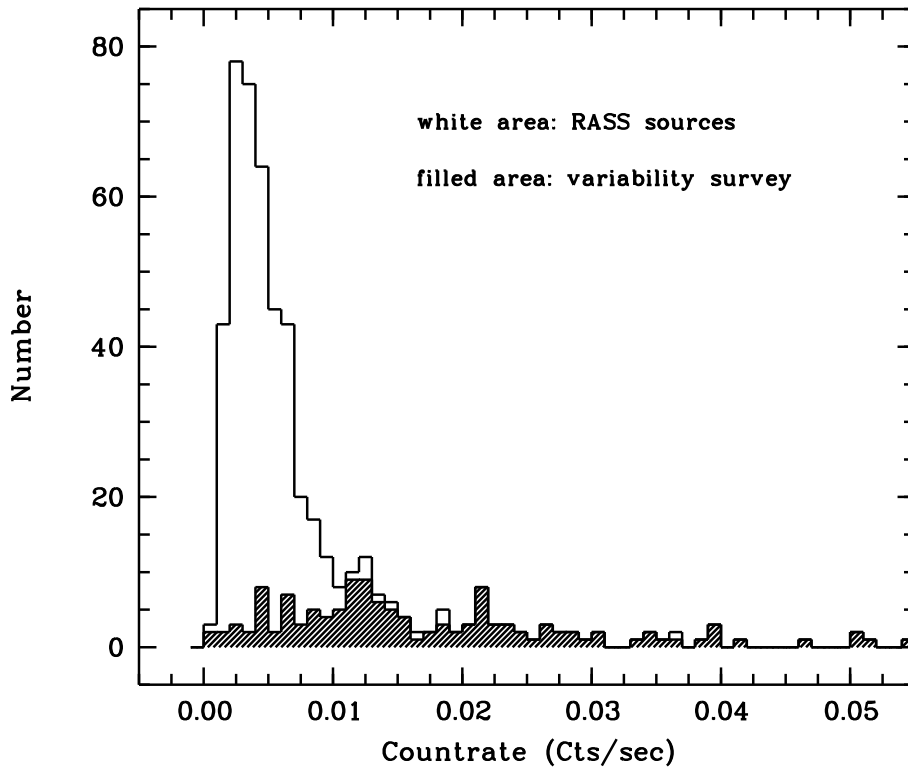


Figure 6: X-ray completeness histogram of the NEP variability survey as a function of Countrate. Please note that the variability survey is complete for sources brighter than the bright cutoff of the histogram (0.05 cts/sec) which corresponds to the sensitivity limit of the RASS BSC and includes almost all X-ray point sources down to 0.01 cts/sec, excluding mainly faint *extended* sources which are not of much interest in a variability survey anyway.

The following criteria were checked for the decision whether an X-ray counterpart was to be included in the variability survey:

Position The X-ray source must be located within the sky area covered by the Schmidt plates. Taking plate center and plate size into account, the (quick and dirty) necessary condition is that

- $17^{\text{h}} 26^{\text{m}} \leq \text{right ascension} \leq 18^{\text{h}} 33^{\text{m}}$
- $63^{\circ} 27' \leq \text{declination} \leq 69^{\circ} 37'$

There are sources that fulfill these constraints but were nevertheless never scanned. This was partly due to the fact that the constraint used above is not exact and partly because the sources might be located on areas obscured by the photometric wedge that was always exposed onto the plate. These sources were deleted from our primary source list and do not enter the identification statistics and variability survey.

Optical and X-ray brightness of counterpart Sources whose counterparts were bright stars (brighter than ≈ 12 mag) were not included in the variability survey because reliable photometry was not possible for these sources. Sources for which no optical counterpart was visible on the stacked plates are too weak to allow photometry on the single plates; these sources were deleted from the scan target list, except if they were located on the center plate (plate area "C"). This was done for the faint hope that flares would be found for those weak objects, which is more promising on the center plates because of the more frequent coverage of these sources. However, no such flare event was recorded.

Known or suspected physical nature of counterpart Sources like planetary nebulae where optical variability of the counterpart could be excluded beyond reasonable doubt or sources like galaxy clusters where no single counterpart fit for sensible photometry and variability analysis could be defined were excluded from the scan list. On the other hand, sources where variability of the optical counterpart was a distinct possibility (e.g. confirmed AGN) were included in the scan list even for very faint objects which would otherwise be excluded because of the expected inferior quality of the photometric results.

distance from NEP Although the distance from the NEP was no primary selection parameter for the decision of inclusion or exclusion of an X-ray counterpart in the scan list, it influences the selection because of the higher number of plates available for sources which are located within the overlap region of the plate areas, close to the NEP.

Although the combination of different selection criteria could introduce observational biases into our sample, much care was taken to minimize those effects by deleting only objects where no variability could reasonably be expected or no meaningful photometry could be performed. There is a slight remaining preference for

faint known AGN over objects of the same magnitude range but with unknown physical nature. However, this concerns fewer than 10 sources from a total of 167.

3 The optical data

3.1 The need for wide-field observations

In a *contemporaneous* X-ray / optical survey, the optical observations must be done during the X-ray (i.e. ROSAT) observations. However, the majority of the ROSAT X-ray sources were expected to be new, formerly unknown sources. Combined with the processing time-lag of the ROSAT survey data, this makes any dedicated small-field CCD photometry impossible, where precise coordinates would be required at the start of the campaign. Therefore the accompanying optical observations had to be done using wide-field instruments, which, at the time of the ROSAT survey, meant Schmidt telescopes; for most observations, this is still valid even today, after more than 10 years.

3.2 Observed sky area

Because of their special position on the celestial sphere, the poles of the ecliptic often receive very deep exposures by whole-sky scanning satellites. With the ROSAT X-ray survey scanning characteristics as given in Chapter 2.2, it is natural to perform an X-ray variability survey at the north or south ecliptical pole. Several other properties of the ecliptical poles also made them an ideal choice for an optical survey:

- large angular distance to moon (and planets);
- no bright stars in the near vicinity;
- location far from the galactic plane, i.e. low galactic star density and a large expected ratio of extragalactic to galactic X-ray counterparts.

Including both ecliptical poles in a survey would double the potential sample size. However, it would also imply that the optical observation time must be doubled, in contrast to the X-ray survey observations which are done anyway. In addition, the practical difficulties are numerous: Both ecliptical poles cannot be observed with the same telescope, and for the southern hemisphere, the UK Schmidt telescope (Siding springs, Australia) was not available for this project. Even if two comparable telescopes at the northern and southern hemisphere had been available, subtle biases between the northern and southern optical samples would be hard to exclude. Because of this, choosing just one ecliptical pole as a survey area was preferred.

Furthermore, because the Large Magellanic Cloud (LMC) is only 3 degrees away from the south ecliptical pole, the star density there is much higher, making identifications much more difficult and costly in terms of telescope-time and also diminishing the ratio of distant extragalactic X-ray counterparts. The higher galactic column density at the SEP and the deeper RASS exposure at the NEP (because of ROSAT observing constraints) also makes the north ecliptical pole a more sensible target.

Also useful is the wealth of infrared, optical and radio data data already existing for the NEP region (IRAS deep survey: Hacking and Houck 1987; Optical

multi-colour survey: Gaidos et al. 1993; Infrared: Kümmel and Wagner 2000; 38 MHz: Lacy et al. 1992; 1.4 GHz: White and Becker 1992; 1.5 GHz: Kollgaard et al. 1994; 11cm: Loiseau et al. 1988; 4.85 GHz: Becker et al. 1991).

The existence of an extensive observation and identification programme, the ROSAT north ecliptic pole survey (Mullis 2002, Mullis 2001, Henry et al. 1995, Voges et al. 2001, Henry et al. 2001, Gioia et al. 2003) also made the availability of additional data for our sources very likely.

Last not least the NEP is visible all year from Tautenburg, Germany, where observation time for an extensive optical survey was available. All these facts point to the north ecliptic pole as a natural choice for a multi-frequency, long-term study of extragalactic sources.

3.3 Origin of the optical data

The optical data were taken at Tautenburg (Germany) with the 2m-Telescope of the Thüringer Landessternwarte (formerly Karl-Schwarzschildt-Observatory). This is a multi-purpose instrument, switchable between Schmidt-, Cassegrain- and Coude-Configuration. In its Schmidt configuration, the telescope has a free aperture of 1.34m (largest in the world) and a focal length of 4m. The resulting plate scale is 51.4 arcsec/mm (or: 19.4 $\mu\text{m}/\text{arcsec}$), each Schmidt plate covers an unvignetted field of 3.2 x 3.2 degrees square. Because no field-flattener is employed, the focal plane of the telescope is slightly curved, and the plates are bent within the plate-holder accordingly.

The plate emulsion used was ZU 21, a non-hypered, blue-sensitive emulsion from ORWO Wolfen, with properties similar to the well-known Kodak 103a-O emulsion. In combination with the used Schott GG13 filter, the emulsion passband closely matches the Johnson-B band. For a description of the emulsion properties see Brunzendorf and Meusinger (1999), Hoegner and Ziener (1978) and Ziener (1971).

To allow a characterization of the photographic properties of each plate, a photometric wedge was exposed onto all plates. During exposure within the telescope, a small area near the plate border was kept unexposed, covered by a stop. Immediately after exposure this area was exposed through a wedge filter with known characteristics and with an exposure time identical to the sky exposure time, to avoid any differences in long-time exposure sensitivity decrease (i.e. Schwarzschildt-effect).

To cover a larger survey area, five different plate centers were used for the exposures, where one field was centered straight at the NEP (sky area "C", centered at 18^h, 66° 34^m), and the other four fields (areas "I" to "IV") were shifted slightly in right ascension and declination, containing the NEP within one corner. This way the sky coverage of the optical survey was extended to 35 square degrees.

Altogether a total of 189 plates, starting from January 1990 to September 1992, were taken into consideration for this work. Because of this large number, it was decided to use only the best plates for variability analysis. A rough visual plate grading, taking into account the seeing and sky brightness during plate exposure, is performed routinely at Tautenburg, and this data was used to select a subset of



Figure 7: The 2m-Schmidt telescope of the Thüringer Landessternwarte Tautenburg, within its dome. All the optical data used within this work was taken with this telescope. (Picture courtesy of KSO Tautenburg)

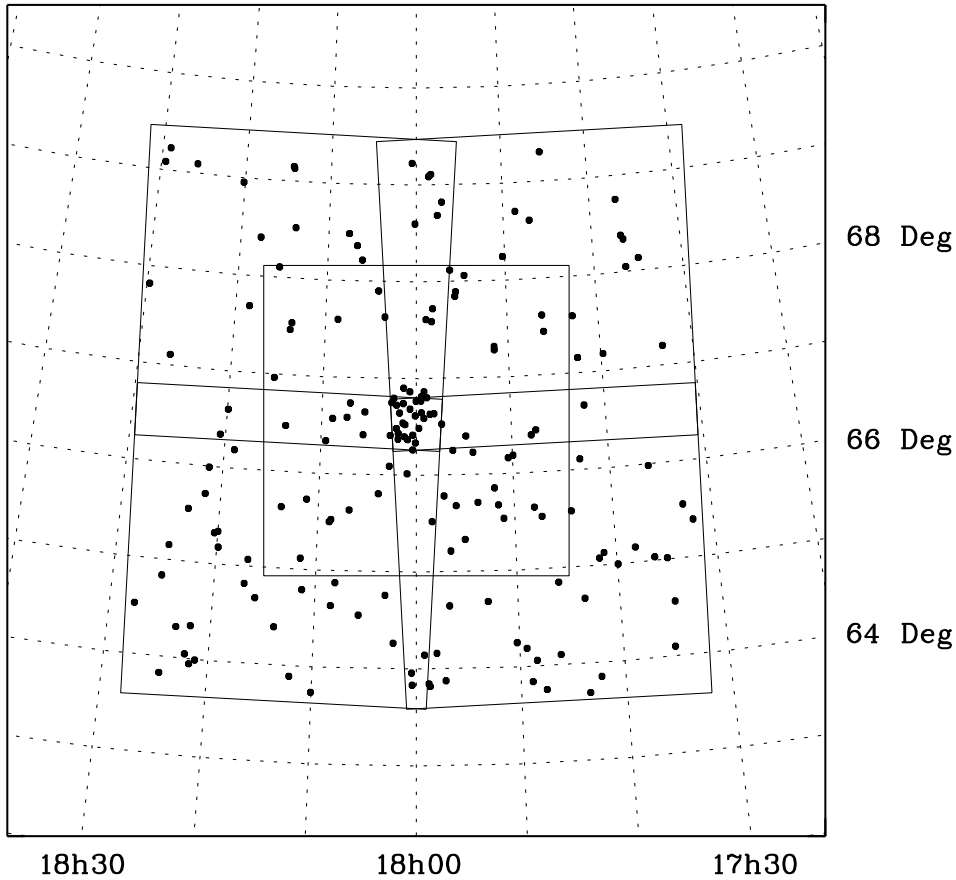


Figure 8: Distribution of the X-ray sources in the NEP area. The placement of the 5 plate areas is also outlined. The areas and plate centers are area "C" (center $18^{\text{h}} 00^{\text{m}} 00^{\text{s}}$, $+66^{\circ} 34'$, exactly on the NEP), area "I" (center $18^{\text{h}} 13^{\text{m}} 30^{\text{s}}$, $+67^{\circ} 54'$), area "II" (center $18^{\text{h}} 13^{\text{m}} 30^{\text{s}}$, $+65^{\circ} 14'$), area "III" (center $17^{\text{h}} 46^{\text{m}} 30^{\text{s}}$, $+67^{\circ} 54'$), area "IV" (center $17^{\text{h}} 46^{\text{m}} 30^{\text{s}}$, $+65^{\circ} 14'$).

all plates.

A total of 89 plates, 17 from the center field and 72 from the off-center fields, taken from February 1990 to August 1992 and thereby covering a timespan from 6 month before to 18 month after the ROSAT all-sky survey, were analyzed. For a listing of plates, plate centers and exposure times see Tab. 1. The distribution of the seeing values and plate limits as derived by the analysis in Chapters 6.2 and 6.5 is depicted in Fig. 40 and 41.

Because of the outstanding position of the NEP already mentioned in Chapter 3.2, it was decided to include the NEP in a set of sky areas used for long-term studies at Tautenburg, and exposures were obtained even after the end of the ROSAT NEP project, until August 1996; the regular usage of photographic plates at Tautenburg was ended in January 1998 with the switchover to CCD observations.

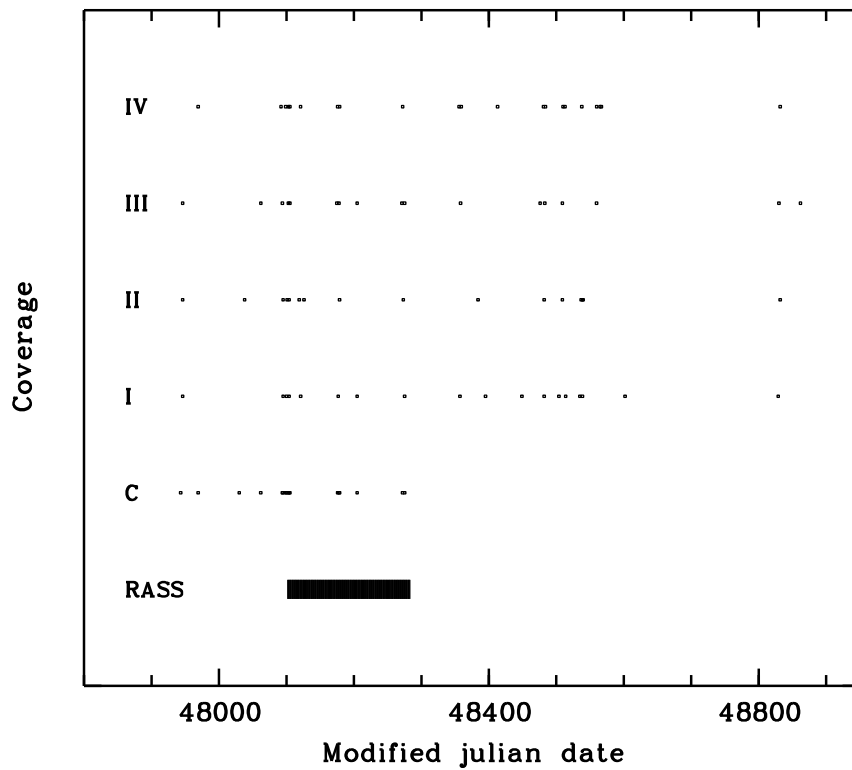


Figure 9: Time coverage of the optical and X-ray data. Shown is the coverage of the main portion of the RASS – excluding PVC and late observations – and the processed Schmidt plates (Center area and areas I – IV); not shown are the times of pointed ROSAT observations which are also available for some sources

4 Preparing the data for processing

To allow a photometric processing of the plates, they must first be made available for computer-based image analysis. The first processing step thus is digitization of all plates.

4.1 Digitizing the optical data

The Schmidt plates were digitized at the TU Berlin, using a Perkin-Elmer PDS 1010 Microdensitometer. This device allows photographic plates or films up to 25 x 25 cm² to be scanned. A spatial positioning precision of 1 μm is achieved using servo mechanisms and etched glass position encoders. The scanning speed can be varied from virtually zero up to 40 mm/sec.

The optical scanning assembly consists of a double microscope assembly where one microscope is used to focus the light of a power-regulated halogen bulb onto the plate. According to the local blackening of the photographic emulsion (the density of the plate) a certain amount of light is transmitted through the second microscope and an aperture assembly onto a photomultiplier which is used to measure the local photographic density of the plate. The effective size of the scanning light spot is determined by choosing aperture size and the focal length of the scanning microscope objective i.e. the enlargement of the microscope assembly.

The photomultiplier of the microdensitometer basically measures the light passing through the photographic plate, i.e. the plate transmission T . However, for a description of the photometric plate properties the plate density D is more natural and useful, where $D = -\log T$. The logarithmic scale allows a precise description of weak objects and of plate properties at the plate background level without sacrificing range.

For digitizing the analog signal representing the light intensity and directly calculating the logarithm of the intensity to obtain plate density values, a fast digital logarithmic converter (MDS 3.2, acquired from the Astronomical Institute Münster) is used. This device does not possess the disadvantages of the combination logarithmic amplifier / analog-to-digital-converter normally used, where a strong density-dependent delay is introduced into the logarithmic signal, necessitating very slow scanning speeds if plates with high contrasts or high densities are to be measured.

4.1.1 Scanning aperture and stepsize

The choice of the aperture is influenced by several boundary conditions:

- The set of possible apertures is determined by existing hardware i.e. by aperture stops and microscope enlargements
- The scanning aperture must be small enough to resolve the smallest details on the plate containing information. According to the sampling theorem, this means that the scanning aperture must be no larger than half the size of the smallest picture detail on the plate. If the plate seeing was n arcsec

during exposure, the scanning aperture for that plate must be at most $n/2*$ (scale factor) μm .

- Although a scanning aperture as derived from the sampling theorem is sufficient to represent the image contents of a plate completely, photometric precision is improved by using still smaller scanning apertures. This is because although all photometric analysis of plates is later done in the density space, the microscope/photomultiplier assembly of the microdensitometer measures intensities. If there is a strong density gradient within the scanning aperture, the mean measured density within one pixel will be $D_m = \log \bar{I} \neq \bar{D}$. This error can be decreased by decreasing the scanning aperture.
- A smaller scanning aperture means more digitized data points for the same plate area, resulting in increased storage requirements and processing time.

To enable a smooth and uniform processing of all plates and to avoid systematic effects in the photometric analysis, scanning aperture and stepsize cannot be adapted to the individual plate but must rather be kept constant across the entire set of plates. Therefore these parameters must be adapted to the plates with the best seeing.

The best Tautenburg Schmidt plates have a seeing values of 1.9 arcsec, which corresponds to a seeing disc diameter of about 40 μm FWHM. The maximum permissible scanning aperture and stepsize is therefore 20 μm . Because of the advantages of a higher resolution mentioned above, a slight oversampling of the data was chosen, and scanning aperture and stepsize were fixed to 10 μm for all plate scans for this work.

Although those activities are not connected with the work described here, it is maybe worth mentioning that plate scanning at the Tautenburg observatory itself, using the TPS ("Tautenburg plate scanner") CCD plate scanner developed and operated there, is done with exactly the same scanning aperture of 10 μm (Meusinger 2002).

4.1.2 Scanning small fields

Because of hardware limitations (scanning speed and data storage), it is not possible to scan entire plates. Scanning the entire plate area (ca. 230 x 230 mm) takes several days per plate with the maximum scanning speed of the PDS 1010 Microdensitometer, even with the fast logarithmic converter. Furthermore, the generated data volume would by far have exceeded what was manageable with the available means of data storage (1/2 inch magnetic tapes) of the microdensitometer when the plates were scanned, in 1992/1993. Last not least, because the X-ray counterparts are relatively scarce on the photographic plates, we are simply not interested in the information in most of the area of the photographic plates.

It is therefore better to scan only the area we are interested in. Small fields (4.8 x 4.8 mm², corresponding to 4.1 x 4.1 arcmin²) were scanned around the positions of the X-ray counterparts and photometric reference fields. Still smaller fields (1x1 mm²) around astrometric reference stars chosen from an astrometric catalogue were also scanned to enable an astrometric calibration of the plates.

4.1.3 Practical considerations

The entire microdensitometer is placed within a darkened room under a dust cover to avoid light disturbance and dust contamination during measurements. A small fan provides forced ventilation through a filter to avoid diffusion of dust into the dust cover during measurements and cooling for the entire microdensitometer. The whole set-up of the microdensitometer including electronics and data storage was part of the work done for this thesis.

To prepare for a measurement, the photographic plate was aligned and fixed onto the plate holder with spring holders and adhesive tape. Focus and slit alignment of both microdensitometer microscopes were checked, and the photomultiplier voltage was adjusted to adapt to different plate background densities. After a two-hour interval to allow the whole apparatus to reach thermal equilibrium, all settings were checked and readjusted if necessary.

The actual measurement starts with the scanning of the plate wedge and astrometric reference fields. Afterwards the fields around the X-ray counterparts and photometric reference fields are scanned. Including a tape change necessary because of the limited data storage space, this takes 15 to 20 hours. Afterwards, three astrometric reference fields and the plate wedge are rescanned to check for changes in plate alignment or photometric adjustment (see Chapter 4.1.4).

All scanning was done using a control program provided by the PDS manufacturer Perkin-Elmer, called "scansalot". The digitized data were stored on 1/2 inch magnetic tapes by the PDS control system and were transferred for further processing to a DEC VaxStation 3100 running the ESO scientific image processing program MIDAS.

4.1.4 Measurement imperfections

During digitization of the photographic plates, various problems might arise which would compromise precision or reliability of the plate data.

Reliability of the measured plate coordinates: Although the plates are fixed with adhesive tape to the plate holder and the whole measurement assembly is always given ample time to reach thermal equilibrium, slippage of the photographic plate against the plate holder cannot be totally excluded. Also, the position encoders of the plate scanners measure relative positions only, and electronic glitches might result in loss of the positional reference frame i.e. faulty coordinates.

To verify the reliability of the coordinates over the entire measurement, the whole set of astrometric reference stars necessary for definition of the plate coordinate system is scanned *before* the photometric (i.e. target) fields, and three of the astrometric reference stars, chosen such that they are distributed well over the entire plate, are rescanned *afterwards*. The positions of these stars before and after measurement of the target fields are then compared, and deviations are flagged.

Reliability of the measured densities: The photodensitometer assembly within the PDS1010 does not measure "true" densities (which would imply simultaneously measuring the light intensity before and after passage of the photographic plate) but instead uses just one photomultiplier to measure the light intensity after passage through the plate and relies on a constant intensity of the light source.

This assumption might fail for several reasons:

- Although certain measures (like a stabilized power supply for the halogen bulb) have been taken to ensure a constant intensity, the brightness of the halogen bulb might change during the measurement, especially when it is coming near the end of its lifetime.
- The precision of the measurement depends on a precise alignment of the measurement assembly, which includes the necessity to adjust the slit assembly. If this adjustment changes during the measurement, e.g. for thermal reasons (and again, the measurement assembly is given ample time to reach thermal equilibrium before the measurement starts), precision of the density measurement will be impaired

To verify the reliability of the measured densities, the photometric wedge which is located on all plates was scanned before and after the measurement of the target fields. The wedge images was then compared (i.e. subtracted, filtered and the result visually inspected) to ensure that no change had taken place during the measurement.

4.2 Handling of plate faults and visual disturbances

The occurrence of local disturbances like plate scratches, dust specks, satellite trails and emulsion faults (holes, density gradients) is inevitable in a survey encompassing close to a hundred plates. To avoid negative impacts on photometric precision, all (more than 5100) scanned fields were visually inspected. Depending on the severity of the fault, two countermeasures were taken:

- For sources where enough of an object's image remains undisturbed, a mask image was created where all disturbed pixels were flagged. During processing of the plate data, these pixels were then omitted.

There were 771 images, of a total of over 5100 scanned fields, where such a mask image was used.

- Sources where too small a part of the image remained undisturbed to allow a reliable profile calculation were deleted from the plate matching process by creating an entry in a "processing exception list" used by the plate matching routines.

There were 38 entries where this was the case, again from a total of over 5100 scanned fields.

4.3 General properties and imperfections of photographic plates

Photographic plates have been used in astronomy for more than a hundred years. Although modern detectors like CCDs are far superior in terms of sensitivity and dynamic range, the large area of photographic plates still makes them the instrument of choice when large areas must be observed, like in sky surveys (this is about to change with large-area or even whole-sky multicolour CCD sky surveys like the Sloan Digital Sky Survey). However, for data analysis and photometry using photographic plates (e.g. Schmidt plates) it is extremely important to be aware of the shortcomings and nonlinearities of the photographic emulsion when used as a detector.

4.3.1 Characteristic curve

A photographic plate exposed to light responds (after development and fixing) with a blackening of the emulsion. If we consider the photographic emulsion as a radiation detector, we must relate the light intensity I , integrated over the exposure time, to the density D of the plate. This density D is measured by illuminating the photographic plate with an intensity I_0 and measuring the intensity I_m after passage through the photographic emulsion. The density is then calculated as $D = -\log(I_m/I_0)$. A density of zero means an ideally clear plate where no light is lost during passage, a totally black plate would have an infinite density.

The response function $D(I)$ of the photographic plate is called the "characteristic curve" of an emulsion. It is of fundamental importance for the analysis of photographic data. The principal regions are:

- plate background: A minimum density of the plate because of limited transparency of glass carrier and emulsion;
- linear regime: where the relation between D and $\log I$ is approximately linear; the steepness of the characteristic curve is a measure for the contrast of the emulsion;
- saturation regime: A maximum density of the plate which can not be exceeded

and transition regions in between.

High-precision photometric data analysis of photographic plates is only possible within the (approximately) linear region of the characteristic curve. This means that photometric precision suffers for weak objects where the density at the core of the point spread function (PSF) of a star does not reach the linear regime as well as for objects above a certain brightness where the central part of the PSF of a star is saturated; the photometric errors for these objects are very hard to calculate.

A common way to improve photometric precision for weak objects is to use a "preflash", i.e. a weak uniform additional lightsource calculated to move the weakest sky objects into the linear part of the characteristic curve. This, however, only makes sense for observations with negligible sky background (otherwise the sky background does what the preflash would be intended for) and was not done

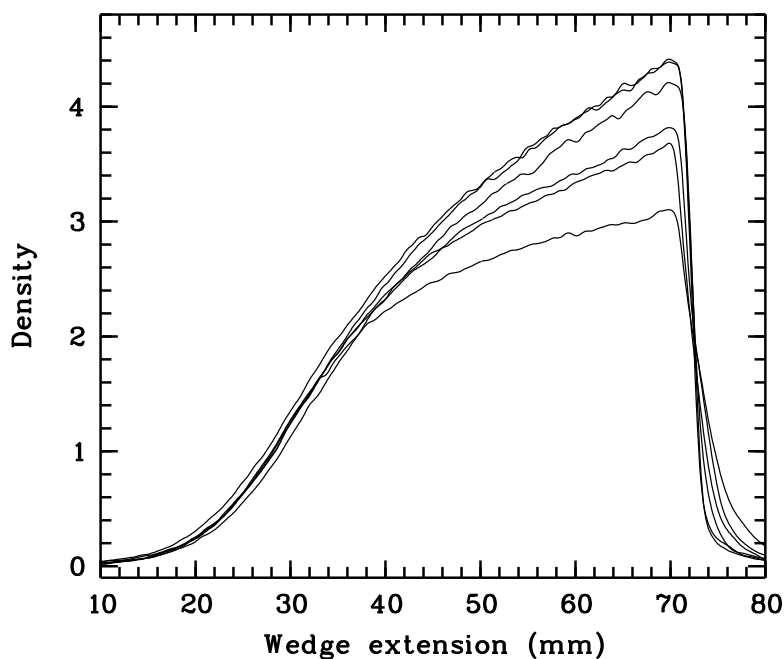


Figure 10: Spread of characteristic curves of several plates

for the Tautenburg Schmidt plates where the sky background is far from negligible due to the vicinity of several towns.

The characteristic curve of the photographic emulsion varies between plates. This means that the photometric calibration must be done separately for each plate. To make matters worse, the characteristic curve varies even between different areas on one plate, making absolute calibration impossible. Because of this, photometric precision above a certain level can only be reached by relative photometry within small fields

Probably because of chemical effects ("exhaustion" of the chemical agents for large areas of high density) during development and fixation of plates, the characteristic curve at one point of a plate is also dependent on the average blackening in the vicinity. This means that the characteristic curves for point sources and extended sources will be different; for an example see Fig. 11 where the density at PSF core of a bright star exceeds the maximum (saturation) density as determined from the (extended) calibration wedge. The simple calibration wedges or calibration spots commonly used to determine the characteristic curve of a plate are not suitable for calibrating an astronomical exposure. Instead, a calibration wedge containing linear and/or pointlike sources, easily obtained by overlaying a calibration wedge with an etched metal mask, should be used.

Because of the problems described above, the calibration wedge was not used for photometric calibration in this work.

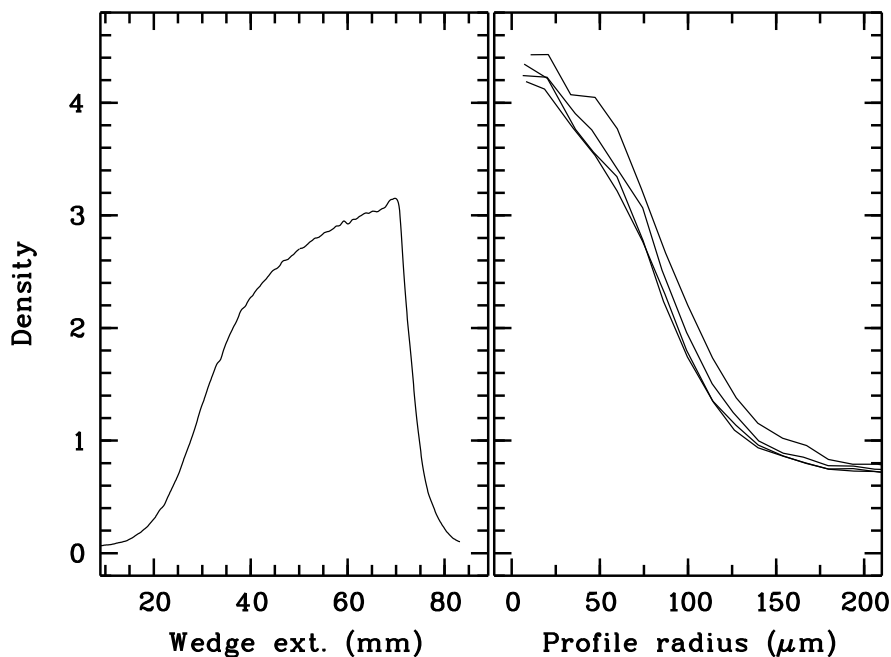


Figure 11: Photographical density for extended areas (plate wedge; left panel) and pointlike sources (stars; right panel), taken from the same plate

4.3.2 Plate background

Plate background results from light contamination (sky brightness) and from chemical effects and imperfections within the photographic plate. There are large-scale effects over the entire plate (e.g. from telescope vignetting, differential desensibilization of hypered plates, thickness variations of the photographic emulsion) and also small-scale effects. For a proper data analysis for photometry this plate background must be subtracted. Hence, size, form and amount of the variations must be studied.

Figure 12 shows an examples of large-scale background variations. Besides a general trend plate center–plate border and gradual variations several examples of non-contiguous steplike changes can be seen. This means that a simple, polynomial global background model can not be used to model the background. Instead, a method to determine a local average background is necessary.

For a determination of the necessary and appropriate size of the local area where the background should be calculated the small-scale fluctuations must be taken into account. If the background area is chosen too small the pixel noise introduces unnecessary statistical errors; if the background area is chosen too large it is not able to follow non-contiguous medium-scale variations.

After a thorough visual inspection of our scan data, a background annulus ring width of 200 μm was chosen.

Point sources on the Tautenburg Schmidt plates have extensions (FWHM) from 35 μm (faint object, good seeing) to well over 200 μm (bright star, bad

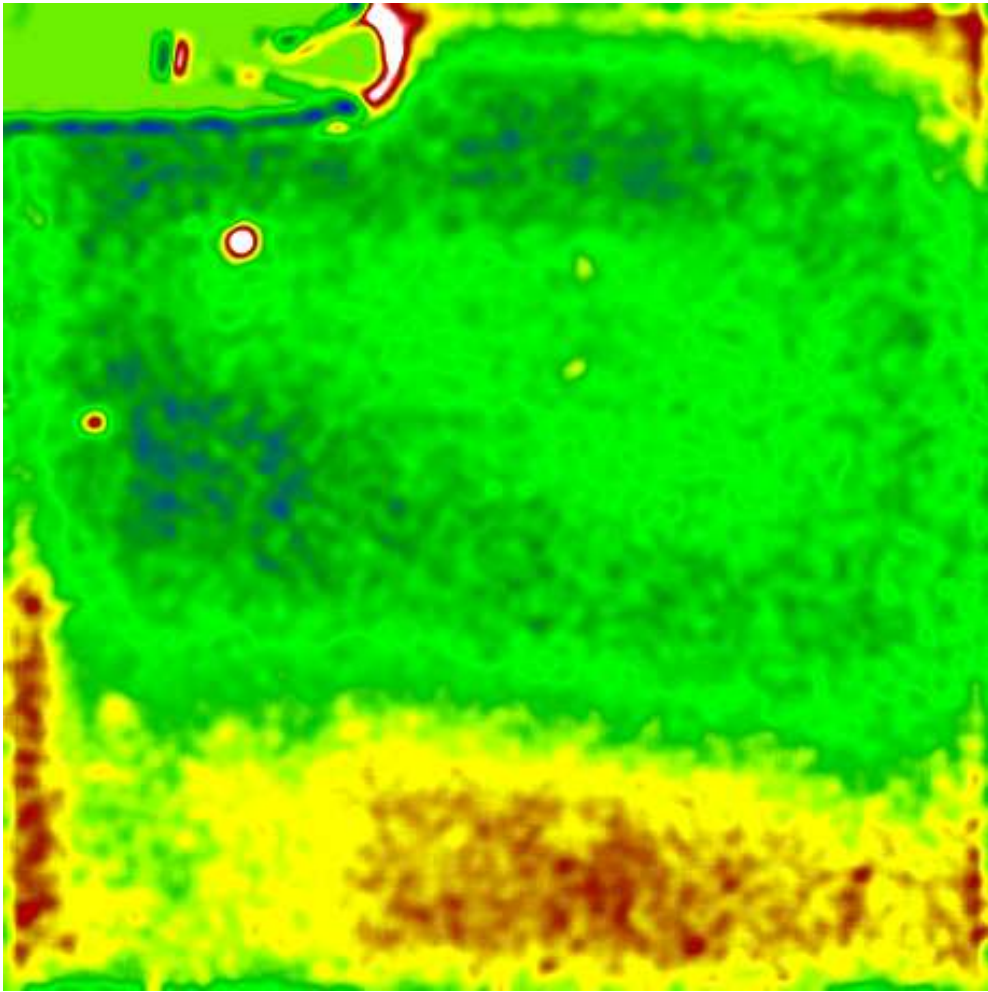


Figure 12: Large-scale plate background variations

seeing). The plate background of a point source is calculated by averaging a circular annulus. Because the background annulus must not be disturbed by the corresponding point source, the inner radius depends on the brightness of the point source; keeping the inner radius independent of the source's brightness would move the annulus unreasonably far out for faint sources.

It is therefore best to use the measured density profile to calculate a radius where the density of the source has become low enough so as not to disturb the local plate background any more. The outer radius can then be calculated either by using a constant width or a constant area of the annulus.

4.4 Astrometric properties of the Tautenburg Schmidt plates

For interpretation of any data derived from Schmidt plates it is of fundamental importance to locate objects on the plate, i.e. to transform object positions between sky coordinates and coordinates as measured on the plate.

4.4.1 Coordinate transformations

The transformation between sky coordinates (right ascension, declination) of an object and rectangular coordinates as measured on the Schmidt plates is done in two steps:

- A transformation between sky coordinates and idealized plate coordinates, where distortions introduced by the telescope optics, telescope and plate misalignments and the terrestrial atmosphere are neglected. Transformation parameters are the sky coordinates A, D of the plate center and the focal length f of the telescope. The transformations between the idealized plates coordinates ξ, η and the sky coordinates α, δ are

$$\xi(\alpha, \delta) = f \frac{\cos \delta \sin(\alpha - A)}{\cos D \cos \delta \cos(\alpha - A) + \sin D \sin \delta}$$

$$\eta(\alpha, \delta) = -f \frac{\sin D \cos \delta \cos(\alpha - A) - \cos D \sin \delta}{\cos D \cos \delta \cos(\alpha - A) + \sin D \sin \delta}$$

and

$$\alpha(\xi, \eta) = A - \arctan \frac{\frac{\xi}{f}}{\cos D - \frac{\eta}{f} \sin D}$$

$$\delta(\xi, \eta) = \arcsin \frac{\sin D + \frac{\eta}{f} \cos D}{\sqrt{1 + \left(\frac{\xi}{f}\right)^2 + \left(\frac{\eta}{f}\right)^2}}$$

- A transformation between the idealized plate coordinates and actually measured plate coordinates. This is done by using a polynomial transformation between plate standard coordinates ξ, η and actually measured coordinates x, y . The transformations are

$$\xi(x, y) = a_{11} + a_{12}x + a_{13}y + a_{14}x^2 + a_{15}y^2 + a_{16}xy$$

$$\eta(x, y) = a_{21} + a_{22}x + a_{23}y + a_{24}x^2 + a_{25}y^2 + a_{26}xy$$

and

$$x(\xi, \eta) = a_{31} + a_{32}\xi + a_{33}\eta + a_{34}\xi^2 + a_{35}\eta^2 + a_{36}\xi\eta$$

$$y(\xi, \eta) = a_{41} + a_{42}\xi + a_{43}\eta + a_{44}\xi^2 + a_{45}\eta^2 + a_{46}\xi\eta$$

To determine the $2 * 2 * 6 = 24$ parameters a_{ij} , a set of astrometric standard stars must be used. The plate coordinates x_k, y_k are measured for those stars and the plate standard coordinates ξ_k, η_k are calculated from the known positions. Then, with

$$\chi_\xi^2 = \sum_k (\xi(x_k, y_k) - \xi_k)^2$$

$$\chi_\eta^2 = \sum_k (\eta(x_k, y_k) - \eta_k)^2$$

$$\chi_x^2 = \sum_k (x(\xi_k, \eta_k) - x_k)^2$$

$$\chi_y^2 = \sum_k (y(\xi_k, \eta_k) - y_k)^2$$

i.e.

$$\chi_\xi^2 = \sum_k ((a_{11} + a_{12}x_k + a_{13}y_k + a_{14}x_k^2 + a_{15}y_k^2 + a_{16}x_k y_k) - \xi_k)^2$$

$$\chi_\eta^2 = \sum_k ((a_{21} + a_{22}x_k + a_{23}y_k + a_{24}x_k^2 + a_{25}y_k^2 + a_{26}x_k y_k) - \eta_k)^2$$

$$\chi_x^2 = \sum_k ((a_{31} + a_{32}x_k + a_{33}y_k + a_{34}x_k^2 + a_{35}y_k^2 + a_{36}x_k y_k) - x_k)^2$$

$$\chi_y^2 = \sum_k ((a_{41} + a_{42}x_k + a_{43}y_k + a_{44}x_k^2 + a_{45}y_k^2 + a_{46}x_k y_k) - y_k)^2$$

we minimise the χ^2 -sums by setting the partial derivatives after the a_{ij} equal to zero and solve the resulting set of linear equations.

4.4.2 Astrometric standard stars

In order to calculate the transformation between plate standard coordinates and plate coordinates a set of standard stars from an astrometric catalog must be used. To determine the best choice for the used catalog, the following criteria were evaluated for several astrometric catalogues:

- positional precision, precision of proper motions and timebase of proper motions. These values, taken together, determine the precision of the derived position at the epoch of the observation
- magnitude range of catalogue stars. The magnitude range of the astrometric reference stars should be close to the magnitude range of the observed objects to avoid magnitude errors of the positions
- star density of the used catalogue. The number of reference stars should be as high, their distribution across the Schmidt plates as uniform as possible
- availability of supplemental information, e.g an indication if a star is a double or multiple system.

After evaluation of three all-sky astrometric reference catalogues, namely the SAO-catalogue (Roman et al. 1983), the HST guide star catalogue GSC (Lasker et al. 1990) and the PPM catalogue (Roeser and Bastian 1988), the PPM (positions and proper motions) astrometric catalogue was chosen as the catalogue to be used in this work. The main reasons were the greater precision when compared to the SAO and GSC catalogues, the availability of proper motion data and the greater reliability compared to a catalogue derived from a single-epoch scan of photographic plates like the GSC.

From the PPM catalogue, a set of reference stars was extracted according to the criteria listed above and reduced to equinox J2000, epoch 1990.75. There are 40 to 60 scanned reference stars on each Schmidt plate. The magnitude range of the selected stars is 9 mag to 11.9 mag; the reference stars have a typical positional precision at the epoch of the observation of 0.58 arcsec. Bright stars (brighter than 9 mag), double and multiple systems and stars with large standard deviations of the catalogue positions were excluded.

4.4.3 Discussion of astrometric results

Although astrometric precision is not a primary aim of this work, a knowledge of the attained precision is important for judging the precision of the measured position of an object and possibly even for judging the reliability of an identification; although the optical positions are much more precise than the X-ray ones, this may not be true for some of the used auxiliary data.

As part of the astrometric reduction process, during determination of the plate constants as introduced in the previous chapter, the residuum of all astrometric standard stars (i.e. the difference between the coordinates as measured on the photographic plates and the expected coordinates derived from applying the plate

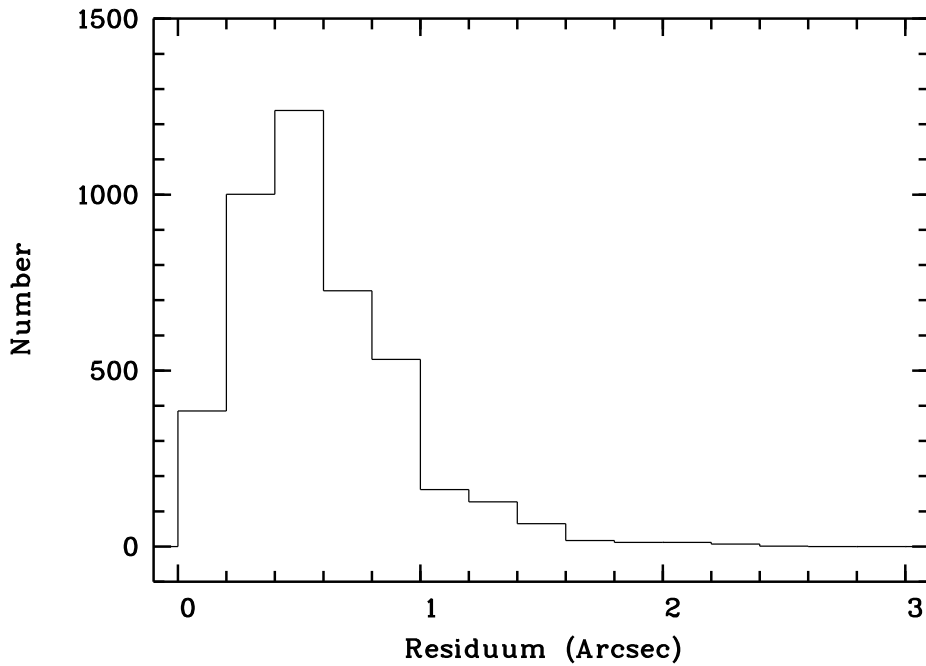


Figure 13: Histogram of astrometric positional accuracy (residua of measured vs. expected plate positions of astrometric standard stars). The mean residuum is 0.57 arcsec.

transformations to the coordinates from the astrometric catalogue) is calculated. Using the complete data from all used astrometric standard stars on all plates, the mean residuum is 0.57 arcsec.

Calculating the mean standard deviation for the astrometric position from the PPM catalogue, i.e. taking into account the uncertainty of a star's position at the epoch of the catalogue observation and the uncertainty in the proper motion also contained in the catalogue, the mean precision of the catalogue positions at the epoch of our measurement is 0.58 arcsec.

Taken together, this means that it is not possible to quantify any discernible error in our astrometric reduction. It is not possible to distinguish whether the reduction process is precise or if the error estimations of the PPM catalogue are unduly large. However, it is clear that there are no gross errors in our astrometric procedures.

5 Basic photometric methods

Photometry from photographic plates is a two-step process: First a magnitude index is calculated from the image data, i.e. a single numerical value characterizing the objects magnitude in the observed passband is extracted from the pixel data. In a second step this magnitude index is compared to related measurements on the same plate or on other plates ("differential" photometry) or, using standard stars, transformed into into a standard photometric system, i.e. calibrated.

For both steps a variety of methods have been studied using our scanned data and are discussed below. After a comparison of the advantages and disadvantages, a set of methods is selected for use in this work.

All variants assume that the positions of all objects are known beforehand, e.g. by visual inspection and measurement of the coordinates of objects on stacked plates – see Chapter 6.1. This is no great restriction for fields near the poles of the ecliptic – we do not expect objects with large proper motion, e.g. planetoids, there.

For each measurement, the exact center position of each object's image in the individual field is determined. This is done by measuring the coordinates of the entire set of objects within the field and comparing this set of measurements with the set of known positions from the measurements on the stacked plates. That way, faulty positions for faint or marginally detected objects, which would be a major cause of photometric errors later on, are prevented. No automated object search of any kind was performed.

Furthermore, all variants assume that the plate background has been subtracted already by methods described in Chapter 4.3.2.

Taking into account the physical nature of our X-ray counterparts, we are only interested in the variability of point sources. Hence, we can restrict ourselves to radially symmetric profiles. As the objects positions are also known, the general, non-trivial problem of fitting a nonradial (elliptic) profile with unknown position, unknown amplitude and unknown semi-major and semi-minor axes and position angle is reduced to the numerically much more simple problem of calculating the profile parameters of a radial profile with known position.

5.1 Integration of intensities

The photometric magnitude M is defined as $M = -2.512 \log I + M_0$ (photometric law of Weber-Fechner) where I is the radiation intensity of an object within the relevant passband and the constant M_0 is suitably chosen. So the magnitude of an object can be calculated in a simple way when the (time- and area-)integrated intensity is known; the integrated intensity could be measured on a photographic plate by integrating over the density values transformed using the calibration wedge.

This rather straightforward approach is not feasible because

- the density-to-intensity transformation for point sources i.e. for stars is only poorly known in spite of the existence of the calibration wedge (see Chapter 4.3.1)

- saturation effects of the photographic emulsion make the density-to-intensity transformation numerically unreliable as soon as the measured density approaches the saturation density of the plate. For plates with good seeing i.e. sharp PSFs this is the case for the center part even of medium-bright stars (15–16 mag), making the transformation unreliable in the part of the PSF that contributes most to a star’s intensity.

5.2 Density integration with fixed aperture

The drawbacks of the intensity integration described above stem mainly from shortcomings of the density-to-intensity transformation. By eliminating this step, i.e. by performing direct integration of density values, fewer assumptions about plate properties are necessary for the photometric process.

Photometry using this density integration method is done by integrating the radial density profile up to a fixed integration radius. For the digitized data, this means that the pixel density values of all pixels up to the integration radius around the center position are summed up.

The resulting integrated density value (hereafter termed *Magnitude index* is a value closely related to the photographic magnitude of an object but as yet uncalibrated.

The drawback of integration over a fixed integration radius is the limited dynamic range. The choice of integration radius determines which magnitude range can be measured precisely:

- If the radius is small, i.e. adapted for the measurement of faint stars, sufficiently bright stars will have image radii exceeding the integration radius. Because of plate saturation effects in the image center, bright stars will produce almost no variation in magnitude index.
- If the radius is large, i.e. adapted to the measurement of bright stars, the noise resulting from plate background in the integration area around faint stars will reduce the photometric precision of the magnitude index of faint stars.

For an example from our measurement data see Figs. 14 to 17 for stars and Fig. 18 for extended objects.

Because of the limitations of useful brightness range mentioned above, this method was not studied further.

5.3 Density integration with variable aperture depending on source brightness

As can be seen from the description of the drawbacks of the fixed aperture integration (Chapter 5.2), a way to adapt the integration aperture to the brightness of the measured source would be needed to overcome the limited dynamic range of the fixed aperture integration. The obvious question is how to solve the inherent

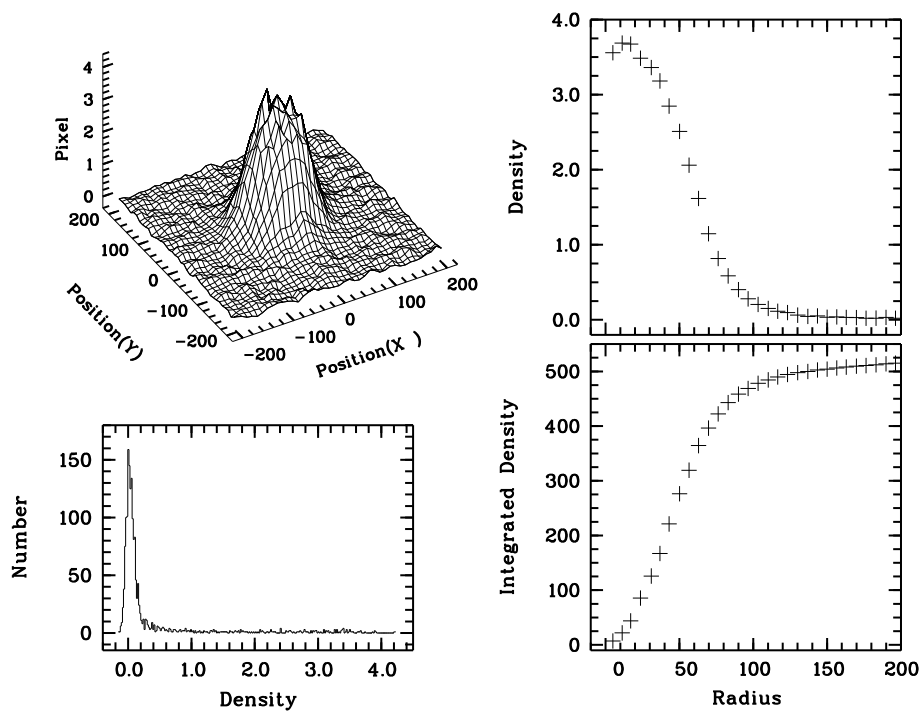


Figure 14: 3-D-plot (upper left), histogram of density distribution (lower left), Density profile function (upper right) and radially integrated density values (lower right) of a very bright star ($B=12.0$ mag)

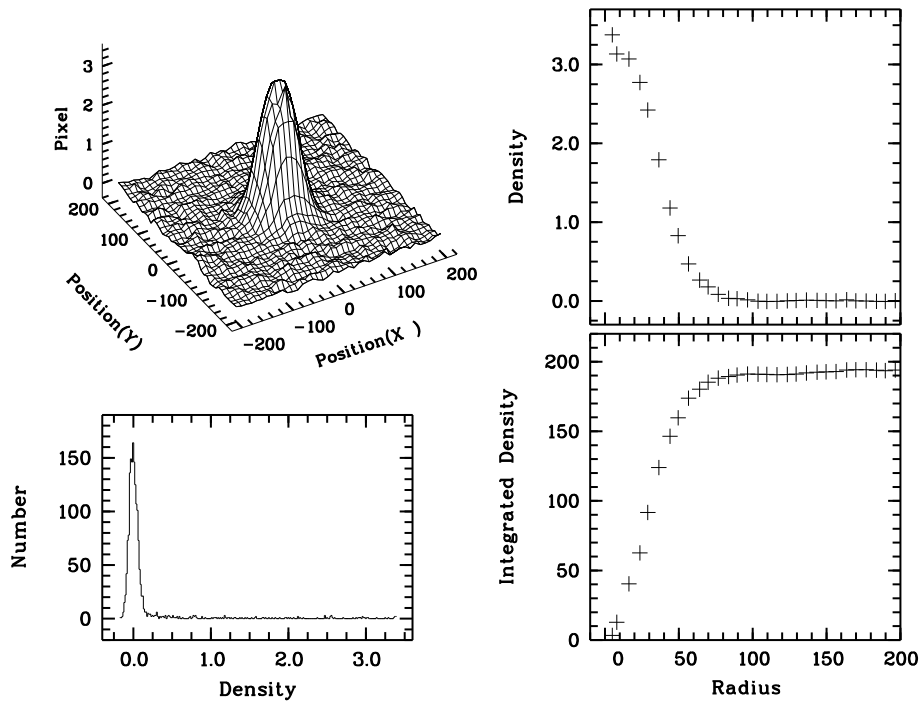


Figure 15: 3-D-plot, histogram of density distribution, profile function and radially integrated density values of a bright star (B=14.6 mag)

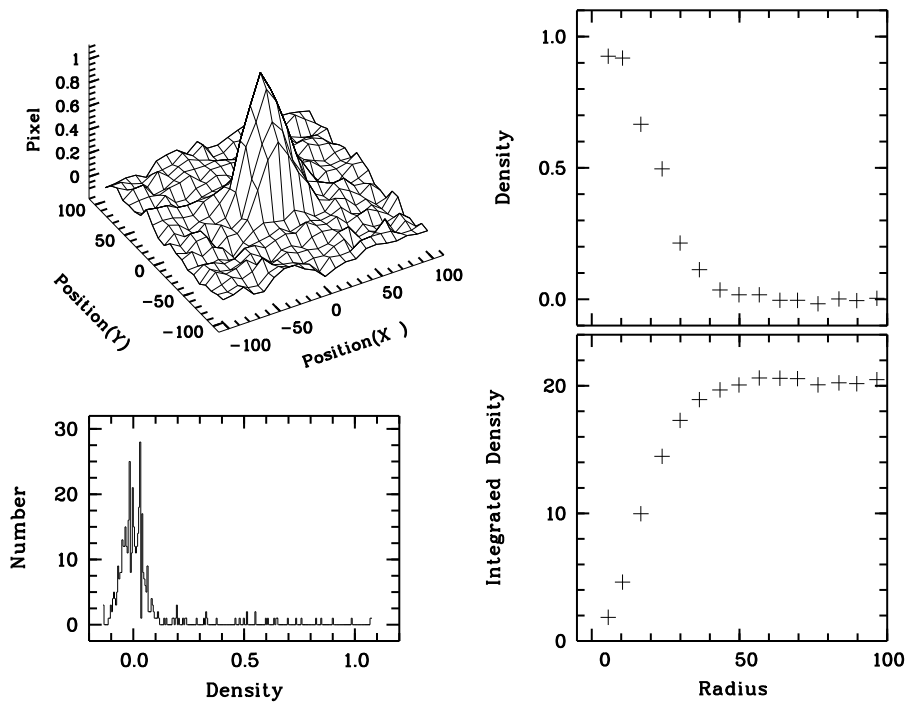


Figure 16: 3-D-plot, histogram of density distribution, profile function and radially integrated density values of a faint star (B=18.8 mag)

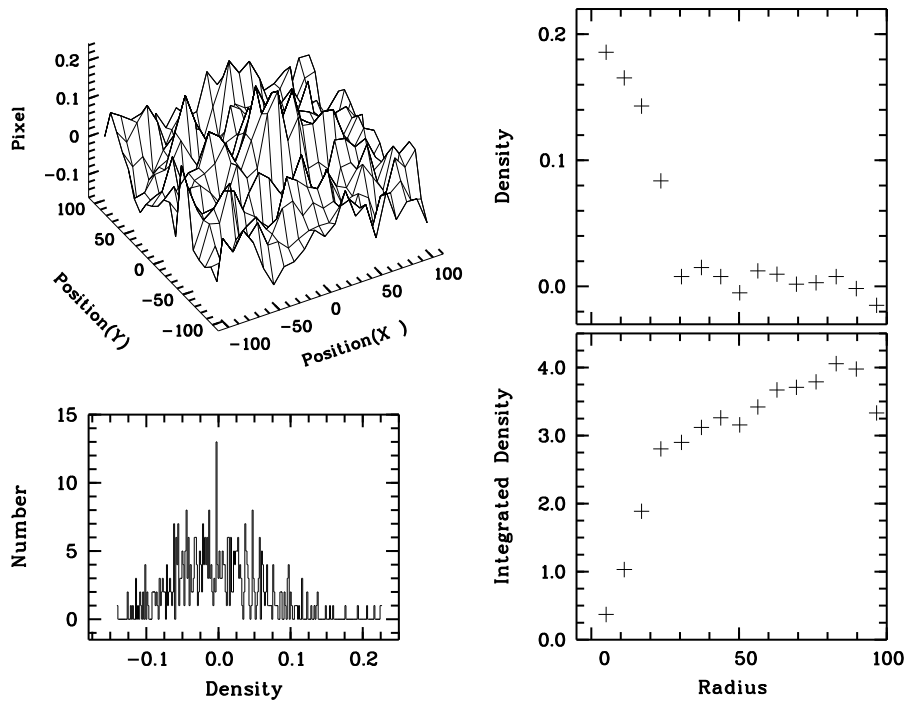


Figure 17: 3-D-plot, histogram of density distribution, profile function and radially integrated density values of a very faint star ($B=20.5$ mag)

bootstrap problem because we do not know the brightness i.e. the needed integration aperture in advance. A possible solution would be to use an iteration where we start with an intermediate size aperture and enlarge or decrease the radius depending on the magnitude index of the first result. However, ensuring convergence for faint sources is not an easy task and the needed relationship between magnitude index and needed integration aperture is not clear, nor defined uniquely; the choice of this dependency will have a profound impact on the resulting accuracy of the brightness values. A related method which derives the integration aperture from the source profile width (which depends on the source brightness) is much more promising (see Chapter 5.8).

5.4 Radial profile determination

As a first step of the profile parameter determination of every source, a profile function is measured by defining radius bins for all sources ($200 \mu\text{m}$ radius, 30 bins) and sorting all measured pixels from within a window around the source coordinates into those bins. Measured are the number of pixels within the bin, the mean radius, mean density and integrated density of all pixels within the bin. For completeness and for judging the reliability of a measurement, the number of missing pixels (e.g. because they would be located outside of the scan window of the field the source is located in) is also recorded. Areas disturbed by plate faults or dust specks are masked out manually before profile determination using a mask

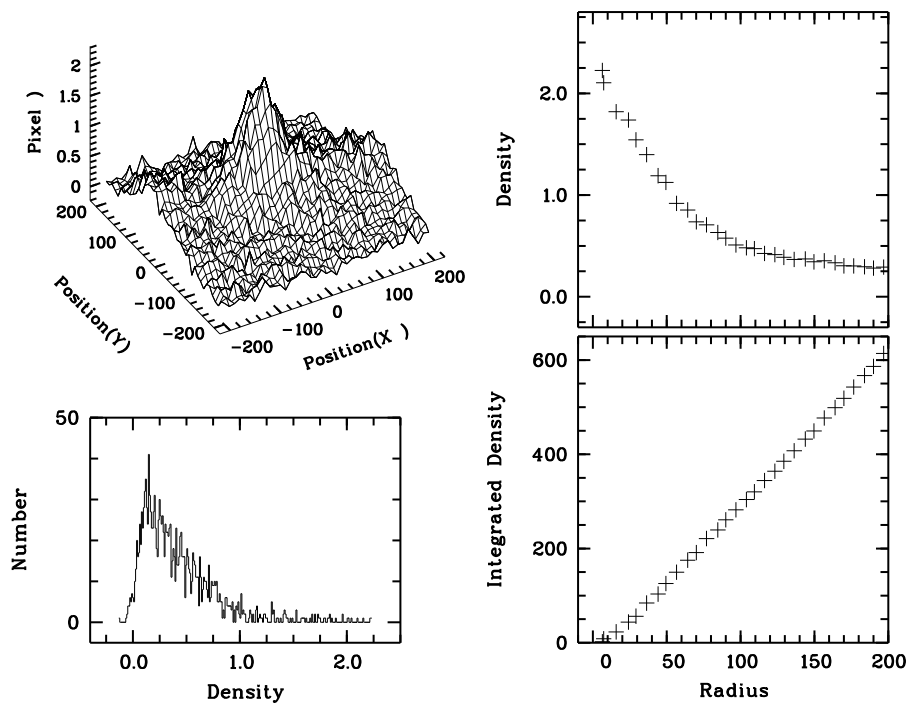


Figure 18: 3-D-plot, histogram of density distribution, profile function and radially integrated density values of an extended source (NGC 6552). Note that the integrated intensity does not converge.

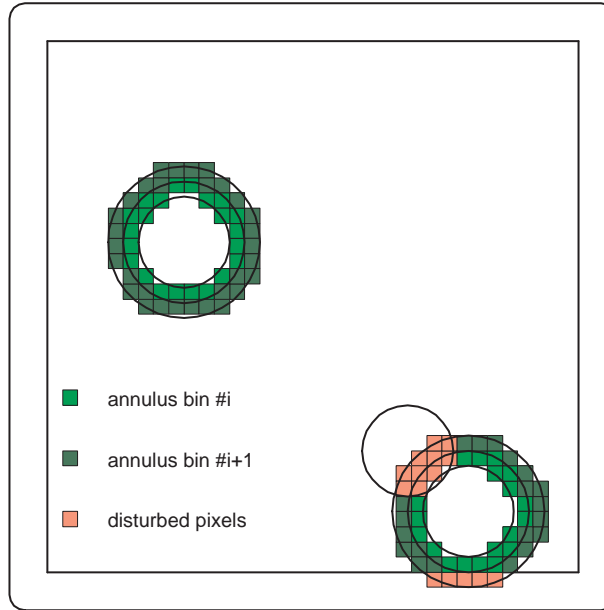


Figure 19: Schematic: determination of the radial profiles. Shown are the pixels belonging to two annulus bins (light / dark green) and pixels excluded because of disturbance by near neighbours or missing because of border placement (red)

image (see Chapter 4.2), and their pixels are eliminated rather than introducing noise into the profile. Areas disturbed by other sources are masked automatically by taking into account a "disturbance radius" which is defined for all sources on the plates depending on their brightness and profile width (Fig. 19) using an iterative process.

5.5 Profile parameter fitting

After the profile function has been measured a numerical fit to the measured values is calculated. As a first try we use a radial Gaussian (Amplitude / FWHM representation, with Amplitude H and FWHM value R)

$$G(r) = He^{-r^2/R^2}$$

which produces an acceptable fit for profiles which are not saturated (see Fig. 20, upper half). For sources for which the density at the source center is near saturation, which in our sample happens around 15 mag under good seeing conditions, the fit deteriorates, and saturation effects are beginning to show (see Fig. 20, lower half).

Normally, H and R are left unconstrained, so the amplitude and FWHM values are fitted freely from the profile data. As an improvement, it is possible to generate

”seeing-constrained” profile fits by introducing a constraint between H and R with

$$R(H) = \sum_{i=0}^3 a_i H^i$$

where the a_i are the seeing parameters of a plate which must have been determined previously as described in Chapter 6.2. This way, only one free fit parameter remains, greatly improving the robustness of the process for weak sources.

Because the constraint equation introduced above is valid only for point sources, the seeing-constrained fits can also be applied to point sources only. For extended sources (with the mean excess extension determined as described in Chapter 6.3) the extension data must be included into the constraint equation, yielding (with mean excess extension $\overline{E_{\text{FWHM}}}$)

$$R(H) = \overline{E_{\text{FWHM}}} + \sum_{i=0}^3 a_i H^i$$

This profile fit, called ”extension-constrained”, was used for all reduction processes in this work.

The weight resp. standard deviation of the individual bins within the profile function was determined by the number of contributing pixels, i.e. with N number of pixels contributing for an annulus bin

$$\sigma = 1/\sqrt{N}$$

For the fit process, the Levenberg-Marquardt algorithm ”mrqmin” routine from the ”Numerical Recipes” (Press et al. 1992) was used. The routine was slightly modified to allow the setting of boundary values for the fitted parameters to prevent physically impossible result values. and also to include a mechanism to repeat the fitting trial if those boundaries were violated.

5.6 Profile fitting including saturation effects

To produce an acceptable fit for saturated profiles the plate saturation must be modeled using an appropriate saturation function. For photographic plates the saturation function

$$D_{D_s, q}(d) = \frac{1}{\sqrt[q]{\frac{1}{d^q} + \frac{1}{D_s^q}}}$$

is used customarily (Stetson 1979) where D_s describes the saturation density of the plate and q allows to model the curvature of the transition between linear and saturated part of the characteristic curve. For $d \ll D_s$ we get $D(d) \approx d$, for $d \approx D_s$ the function $D(d)$ approaches D_s , and for $d > D_s$ $D(d) \approx D_s$. This relation is not intended to describe any physical or photographic processes. It is merely a convenient numerical way to model the principal behaviour of the photographic emulsion.

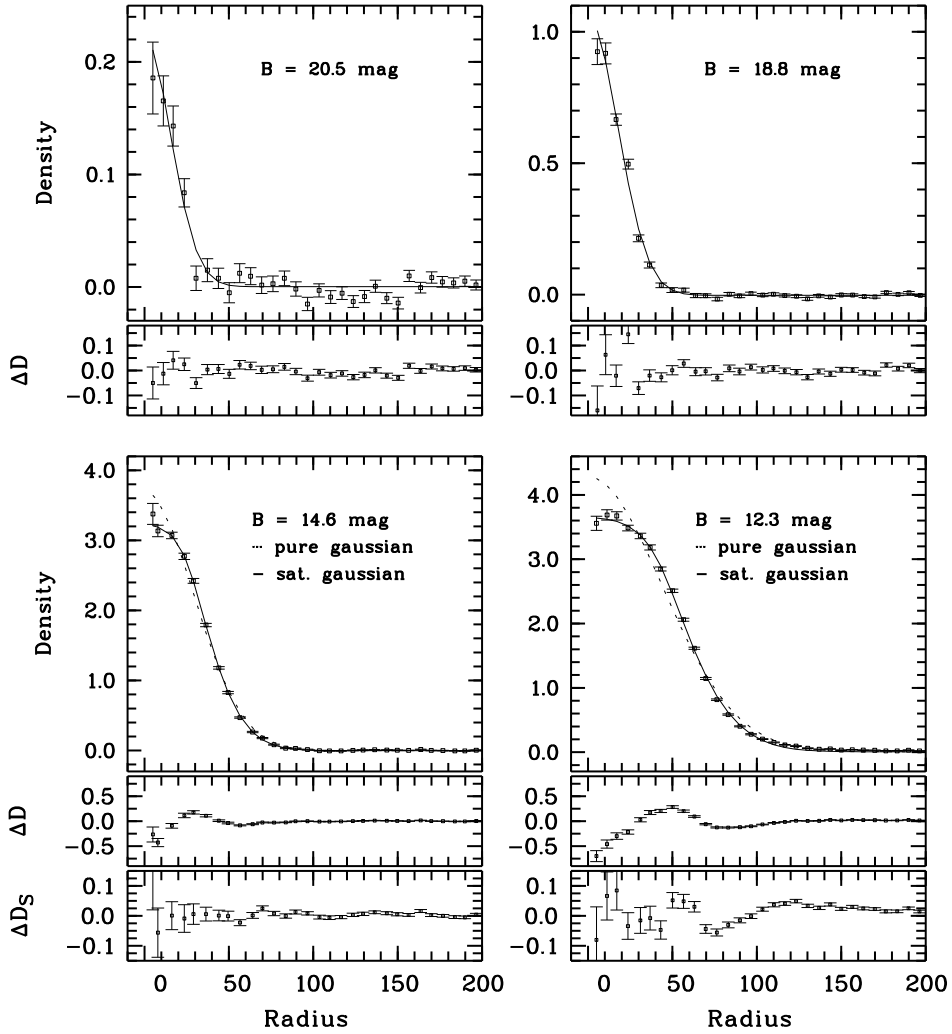


Figure 20: Quality of Gaussian fit for faint (upper panels; pure Gaussian only) and bright (lower panels; pure and saturated Gaussian) stars. Please note the different scales for the deviations ΔD (pure Gaussian) and ΔD_s (saturated Gaussian) and for faint and bright stars.

The saturated Gaussian function obtained by a composition of the Gaussian with the saturation function

$$G_{sat}(r) = D_{D_s,q}(G(r))$$

provides a much better fit for bright stars (see Fig. 20, lower panel).

5.7 Measured vs. calculated magnitude index, D–Intercept

Using the amplitude and width (H and FWHM) of the profiles a magnitude index M could be directly calculated using the integrated intensity of the profile (e.g. $M = HR^2$ for unsaturated profiles). For faint (unsaturated) profiles this value is well-defined, while the errors for H become substantial for bright, saturated profiles. As an alternative, the integrated intensity of the saturated profile could be calculated from H , R , D_s and q . The main idea behind these methods is to fit the profile and calculate the integrated intensity directly from the parameters of the fit, not from the individual pixel data.

A related method is the "Density–Intensity intercept": The measured values of Density $D(r)$ and integrated intensity $I(r)$ of a profile are plotted against each other. Using linear regression, the intersection at the intensity axis is calculated (see Fig. 21). This is just a graphical way to determine the integrated intensity at the radius of the profile where the intensity will be zero, i.e. a graphical way to determine the total integrated density.

While this works well for bright sources (although special provisions have to be made for saturated profiles, e.g., by limiting the fitted range to non-saturated densities), for faint sources the knowledge of the profile width is necessary because the inclusion of data points lying beyond the useful profile radius severely disturbs the fit. This can be seen in Fig. 22 where the inner and outer data points are distinguished in the plot. A restriction of the fit to densities above a certain limit (e.g. $0.05D$ in our example plot) does not solve the problem because this would produce unnecessarily large errors for the interception point i.e. for the fit result.

5.8 Density integration with profile-dependent aperture

Combining the results from Chapter 5.5 with the approach described in Chapter 5.3, i.e. using the fitted profile width to determine the aperture radius, a density integration with an aperture radius dependent on the source brightness has been implemented. The radius is defined as $r = k \times \text{FWHM}$, where k is chosen suitably in order to include as much of the source flux as possible without including too much sky background and increasing the probability of disturbances by nearby stars unnecessarily.

How the FWHM value that determines the integration radius is calculated – i.e. whether it is fitted freely or constraints between H and FWHM are used – is of no concern for the integration. This means that this integration can easily be used with constrained fits as described in Chapter 5.5.

The dependency of the results, in particular concerning the precision, on the integration radii was checked by integrating sets of stars from different plates,

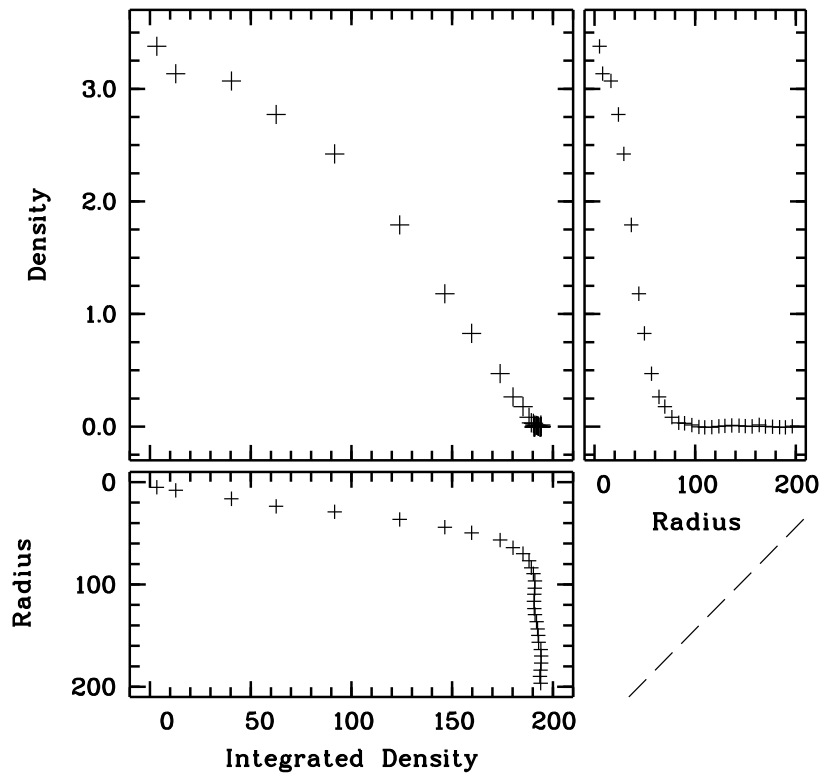


Figure 21: Density intercept for a bright source (14.6 mag). The graph can be generated from the measured representations of the profile (radius vs. density; upper right panel) and the calculated representation of the integrated density (radius vs. integrated density; lower panel, transposed) by eliminating the radius values. The graph of density vs. integrated density (upper left panel) converges nicely towards the total integrated density of the source.

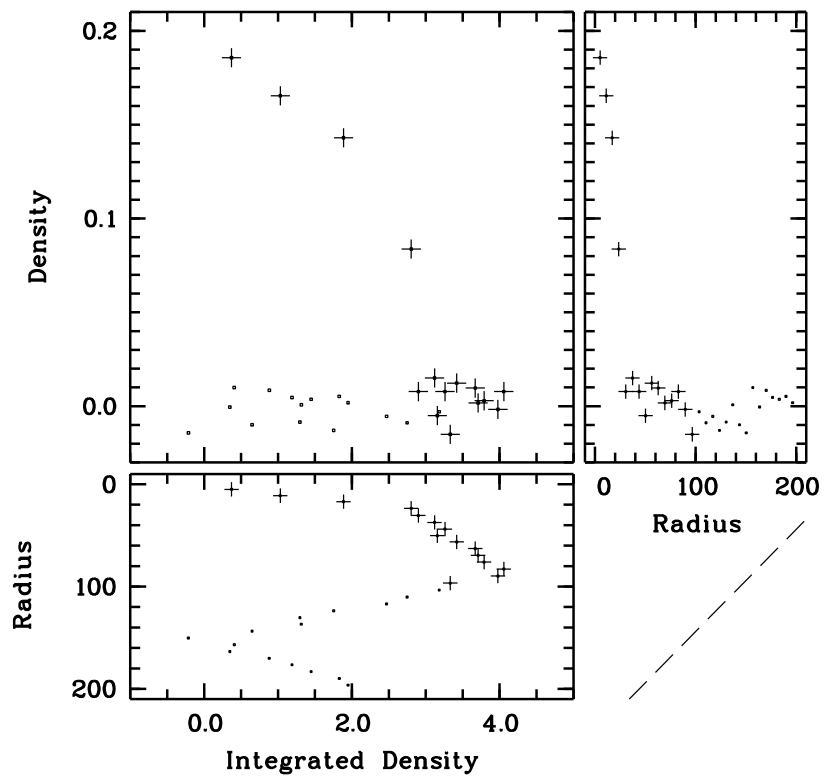


Figure 22: Density intercept for a faint source (20.5 mag). Shown are the data points for radii $< 100\mu m$ (crossed) and for the outer radii $> 100\mu m$ (dotted). Note how the Density-Intensity fit deteriorates for the outer radii.

calibrating the results with standard photometric sequences and comparing the scatter for different integration radii. Repeating this for integration radii from 0.8 to 2 FWHM, it was found that the dependency was very slight; a suitable value was found to be $k = 1$, i.e. the aperture radius was set to 1 FWHM for all photometric reductions in this work.

5.9 Discussion of the different integration methods

The drawbacks of the intensity integration and fixed aperture density integration methods have been discussed in Chapters 5.1 and 5.2 and will not be repeated here.

Because of the undefined brightness–aperture relationship and because a better way to define the aperture is available, the method of density integration with aperture depending on source brightness (Chapter 5.3) was not used.

Although the DI–intercept method (Chapter 5.7) looks promising at first sight, the necessity to limit the fit data to a certain profile radius, i.e. the necessity to *determine* the profile parameters first, makes this method a variation of the density integration with profile-dependent aperture. For point sources, it is mostly a matter of taste whether to integrate the total flux ”graphically” like with the DI–intercept method based on profile-dependent data points (Chapter 5.7) or to integrate the available data up to a certain, equally profile-dependent radius (like in the density integration with profile-dependent aperture, Chapter 5.8); any differences in the result would be incorporated into the photometric calibration.

The calculation of the magnitude index from fitted profile parameters (see Chapter 5.6) is another similar method in which the magnitude index is not derived directly from the measured data but is calculated from fitted data derived from the measurements. Both methods work well for point sources but are not able to incorporate constraints e.g. from plate seeing or source extension data (see Chapter 6.4).

Contrary to that, the profile-dependent aperture integration method described in Chapter 5.8 lends itself easily to introduce constraints based on seeing and extension parameters.

This method was therefore selected to generate the magnitude indices used for the further steps of the photometric process.

5.10 Calibration of magnitude indices

The magnitude indices measured as described above must be transformed into photographic magnitudes in the passband of the photographic plate by calibrating them against a photometric sequence, e.g. one obtained by photoelectric or CCD photometry. To avoid color effects, the passband of the photometric sequence should be as close to the passband of the photographic plate as possible.

The magnitude index as measured on a plate is compared to the photometric reference magnitude of the photometric standard stars; i.e. calibration happens in a log–log space. For simplicity, a low-order polynomial is chosen for the calibration function. To limit the effects of extrapolation beyond the available magnitude

range (including "extrapolation" to objects fainter than the faint end of the calibration sequence), the polynomial is constrained such that it is linear with a slope of unity at the faint end of the calibration sequence; it is extended beyond the faint end of the sequence by the same unity-slope polynomial without higher orders, implying a linear relationship in the intensity regime.

With M_p the photographic magnitude, n the chosen degree of the fit polynomial, I_m the magnitude index of an object and I_f the magnitude index of the faint end of the photometric reference sequence, this means

- for $I_m \leq I_f$, i.e. for objects brighter than I_f :

$$M_p = \sum_{i=0}^n a_i (I_m - I_f)^i \quad a_1 = 1$$

- for $I_m > I_f$, i.e. for objects fainter than I_f :

$$M_p = a_0 + I_m - I_f$$

The determination of the parameters a_i is performed by solving the linear equation resulting from the optimization problem obtained by inserting the known values of M_p , I_m and I_f of the calibration sequence and minimizing the resulting errors.

The calibration between magnitude index and photometric magnitude derived from one field on a photographic plate can not be used to calculate the photometric magnitudes of other fields on the same plate. The calibration is valid only locally but not valid (or rather: valid only with severe restrictions in accuracy) globally on the entire plate. This can be seen easily by overlaying the measurements of two photometric sequences on one plate (Fig. 23). The local calibration differs by up to 0.8 mag.

The photometric standard stars used in this work were CCD-sequences in the NEP area kindly provided by L. Cordis (then at the Hamburger Sternwarte). In total, there are 5 standard fields located in the 5 Schmidt plate areas, with standard stars ranging from 14 mag to 20.5 mag. In addition, one field with a reference star from the GSPC (Guide star photometric catalog, Lasker et al. 1988) was used.

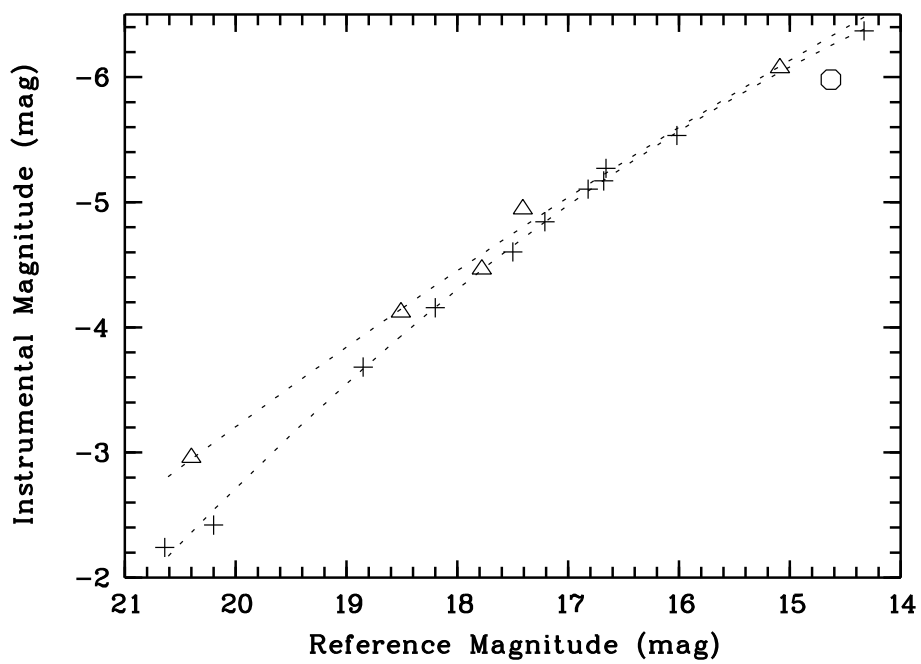


Figure 23: Photometric calibration of two standard sequences (plus signs and triangles) and one GSPC standard star (open circle) as measured on one plate. Shown are instrumental magnitudes (passband close to Johnson-B) against reference magnitudes (Johnson-B band). Note the systematic deviations.

6 Advanced topics - analysis of sets of fields

The result of the optical observation programme is a large set of plates from the same sky areas and a large set of measurements of small fields containing the same objects on those plates (Fig. 24). Using the the basic techniques for image parameter analysis as described in Chapter 5, this makes it possible to extract parameters like plate seeing and plate sensitivity as well as to recognize extended objects reliably and measure their extension. These values can then be used to make the photometry more precise by introducing *constraints* to the fit process.

6.1 Plate stacking

The large number of available plates and the large number of identical scanned fields on those plates allows us to "stack" fields, i.e. to create an average image which is much deeper than a single exposure.

The individual scanned images are initially not aligned and are also rotated with respect to each other, only slightly because of alignment imperfections if the fields are contained within one plate area, strongly if the fields are contained within two or more plate areas as is possible for fields located close to the NEP. Because of this, stacking of a field involves several steps:

- The positions of all stars on all fields are determined by fitting a Gaussian profile. This is done anyway as part of the calculation of the profile functions.
- The transformations necessary for reducing all scans of a field to a common coordinate system are determined using the measured positions of the stars.
- All scan images are aligned and rebinned to a common coordinate system.
- These scan images are averaged, producing a "stacked" i.e. much deeper image of the field.

For averaging the plates, both mean and median filtering were investigated; median filtering was chosen because of its greater robustness against plate faults. All images were background-subtracted before averaging; no correction for different exposure times or different signal-to-noise between plates was performed. This is less than optimal in terms of the resulting signal-to-noise of the stacked plate but sufficient for our cause, the reliable identification of weak sources on a set of – in terms of exposure times, viewing conditions and plate quality – rather uniform plates. For a more elaborate discussion of the topic of plate stacking see Knox et al. (1998).

As an example of the results of the stacking process, see Fig. 25 where a field taken from one (exceptionally good) Tautenburg plate, a blue DSSII-Image (Digitized Sky Survey, II. Epoch) and the stacked image from all (32) available Tautenburg scans from this field of the same field (1RXS J180023.9+634953) are shown in comparison. Please note how the stacked image is comparable in depth (sensitivity) and better in background uniformity (less image noise) when compared to the DSSII-image. The corresponding exposure times are 26 min / 55 min / 15.5 hour (Tautenburg single exposure / DSSII / Tautenburg stacked images

sum of exposure times). The direct comparison of Tautenburg and DSSII (i.e. Palomar) Schmidt plates is, as expected, heavily in favour of the DSSII-images because of the usage of hypersensitized plates and more favourable observation conditions (higher altitude and better seeing, lower sky background) and consequently longer exposure times.

The stacked images of all fields were used to identify all sources by visual inspection and to measure the coordinates of all sources. These coordinates were then used for photometry of sources on the individual plates.

Stacked images of all scanned fields are included in Appendix G.

6.2 Seeing effects and determination of plate seeing

The large number of objects scanned on each plate (on average, 50 fields per plate x 30 stars per field, i.e. 1500 objects), their uniform spatial distribution over the plate and the wide range of available magnitudes (from 12 mag to plate limit, i.e. 20.5 – 21.5 mag depending on plate quality) allows a precise determination of the plate seeing conditions.

After measurement of the profile functions for all objects in all scan fields on one plate, the H and FWHM parameters are computed using an unconstrained Gaussian fit, without taking plate saturation into account. In Fig. 27 those parameters are plotted against each other for two different plates taken under different seeing conditions. Only objects with $H > 0.2$ are plotted because the unconstrained fit deteriorates for faint stars and the scatter in FWHM becomes large. A 3rd-degree polynomial fit between H and FWHM is then calculated up to a limiting value of $H = 3$ where the errors introduced because of saturation effects become substantial. These fit parameters are needed later in the photometric process to create constraints for H and FWHM; the limiting value for $H \rightarrow 0$ of the FWHM, expressed in arcseconds, is the seeing value of the plate.

The seeing values of all used Tautenburg Schmidt plates were calculated in the reduction process and are listed in Tab. 1.

6.3 Extended Objects

Extended sources show up in the H -FWHM-plot as objects lying to the right of the fit curve, having higher FWHM than is normal for their H value (see marked object in Fig. 27)

Although pointlike (stellar and quasi-stellar) objects make up the majority of our sources, either as optical counterparts of X-ray sources or as comparison stars, there is a distinct population of extended objects. For a histogram of the extension of sources on the Tautenburg Schmidt plates see Fig. 29.

It is important that we are able to recognize an object as extended because

- the mere fact that an X-ray counterpart is extended has an important impact on the discussion of the object properties and the object's nature
- the photometric properties of extended objects are different from the properties of point sources and must be taken into account e.g. when discussing variability.

Extended objects are not suitable as comparison stars, and the variability aspects must be discussed with special care for X-counterparts. Now, how do we recognize that an object is extended ?

- For extended objects with a Gaussian profile, the FWHM is larger than what would be expected for a stellar (pointlike) object of the same brightness and of the same profile height. The reduced χ^2 of the Gaussian profile fit, i.e. the deviation of the profile from Gaussian form, is inconspicuous.
- For extended objects with non-Gaussian profiles, the reduced χ^2 of the Gaussian profile fit is larger than expected for the H /FWHM-combination. The FWHM of the fitted Gaussian profile is larger than for a stellar object of the same H /FWHM-combination.

Taken together, this means that in the plot FWHM vs. H , an extended or non-Gaussian profile object shows up lying to the right of the loci of the stellar, pointlike objects (see Fig. 27: Determination of plate seeing) in both cases. For a reliable determination of the extension of an object the excess FWHM (measured – expected FWHM) is calculated for all existing measurements of an object on all plates. For the resulting plot see Fig. 28.

The extension of an object, i.e. the mean excess FWHM, is then calculated and stored for each object for later use; in particular, as an input value for constrained profile fits (see Chapters 5.5, 5.8 and 6.4), for judging the usability of an object as a standard star for differential photometry (see e.g. Fig. 33), and also for discussion of the physical properties of X-ray counterparts (Appendix E). The distribution of optical extensions of all objects on the Schmidt plates is shown in Fig. 29.

6.4 Constrained fits for object parameter determination

For normal sources, the profile-fitting and the methods described in Chapter 5.8 work quite well without any prior knowledge about the profile parameters. However, for faint sources where the profile is not well-defined and may not be well-shaped any more, a large scatter in the fitted FWHM results. This can be seen from Fig. 26 where the FWHM values begin to scatter for sources with profile height $H \leq 0.5$, i.e. with approximately 18-19 mag. For sources below $H = 0.2$ the scatter in FWHM becomes intolerably large, and for really faint sources there is also a small fraction of objects where unfortunate profile shapes (which are unlikely but possible and therefore, in large data sets, bound to occur) pose problems like negative profile heights and impossibly large FWHM which produce outliers in the resulting FWHM and also pose numerical problems.

Because the integration radii used for intensity determination depend on the profile FWHM, faulty FWHM values or FWHM values with a large scatter produce errors in the measured intensity i.e. in the photometry of the measured objects.

However, when plate seeing and the object extensions have been determined as described in Chapters 6.2 and 6.3, it is possible to introduce constraints to the fitting process, resulting in much more well-behaved results even for faint objects.

Seeing-constrained fits The seeing graph depicted in Fig. 26 not only allows to determine the seeing value of a plate (as the limit of the FWHM for faint sources, as described in Chapter 6.2). For pointlike, i.e. non-extended Gaussian sources, a 3rd-order polynomial fit from the seeing graph between the profile parameters H and FWHM also allows to eliminate one of these remaining two free parameters (the background value has already been subtracted) from the Gaussian fit to the measured profile data points. With that constraint, all sources are forced to the seeing FWHM, and the above-mentioned numerical problems for faint sources resulting from ill-defined measurement data are resolved.

Seeing- and extension-constrained fits By using the extension values measured for all objects as described in Chapter 6.3, the constraint described above can also be used for extended sources. The input relationship between H and FWHM is merely expanded to include the object extension i.e. the mean excess FWHM of an object as described in Chapter 6.3 and Fig. 28.

The improvement in photometric precision was checked by comparing the results of photometric reduction using unconstrained and Seeing/extension-constrained profile fits. The precision gain for constrained profile fits was found to be about 0.1 mag for faint sources ($B = 20$ mag), naturally decreasing for brighter sources but still notable for sources with $B = 17$ mag.

6.5 Determination of plate sensitivity

To determine the sensitivity i.e. the plate limit of a certain plate, we calculate the magnitude of a star that would be visible at 4σ detection level.

As a first step, the noise level of the plate is measured by calculating the width of the distribution of the plate density D in unexposed sky regions. For this purpose, the area of the background annuli as described in Chapter 4.3.2 is routinely used for each star measured on the photographic plates. As a result, we have a large sample of undisturbed background areas, distributed widely over the plate, for all plates. For a related example of the density histogram, see the lower left panel in Fig. 17 where the density distribution for a faint star is shown.

Using the width of this density distribution, we calculate the magnitude index that corresponds to 4σ i.e. 4 times the standard deviation of this distribution. Then, first transforming this "local" magnitude index into the mean common system of the plate (see Chapter 7.2) and then using the calibration equations to transform this magnitude index into a true photometric magnitude (Chapter 5.10), local 4σ sensitivities are calculated all over the plate.

The mean value of those local sensitivities, averaged over all measurements from one plate, is then taken as the 4σ plate sensitivity of this Schmidt plate. These values have been calculated for all Schmidt plates used in this work and are listed in Tab. 1 in Appendix C.

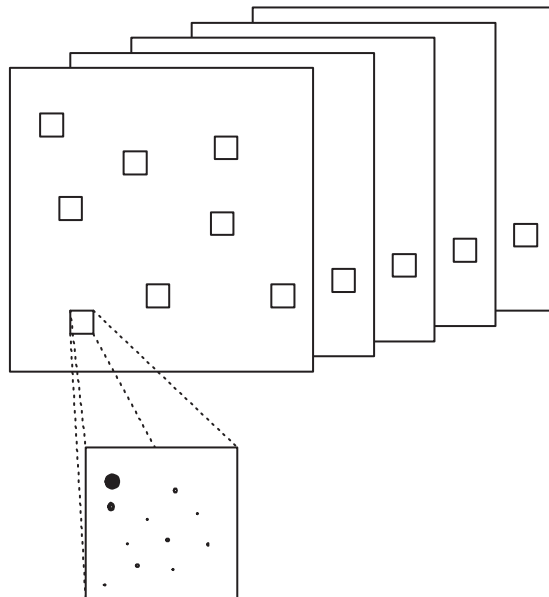


Figure 24: Hierarchy of plates – scan fields – objects, for one sky area (i.e. plate center). Each measured object belongs to a certain small field within a certain Schmidt plate; the combination Schmidt plate – field no. – object no. uniquely defines one measurement. The individual fields are measured on all plates, so there is a large set of measurements for each object.

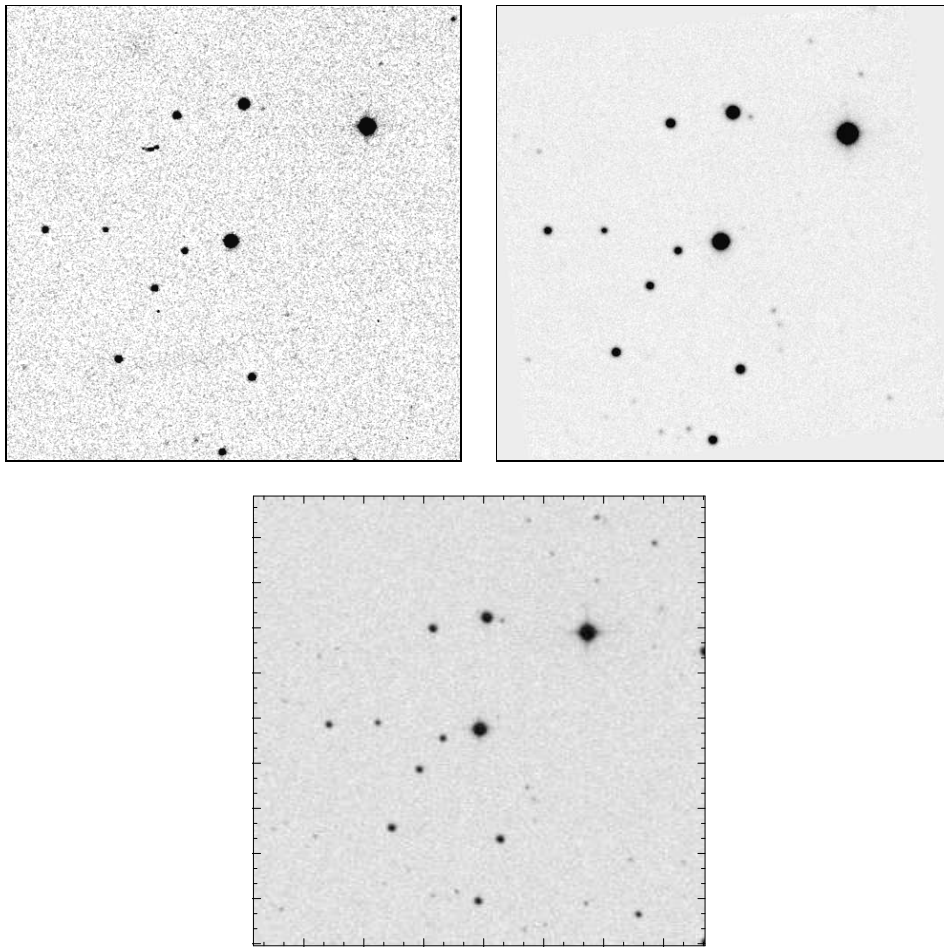


Figure 25: Effect of plate stacking: Single scan (Plate T7310: exposure 26 min), stacked image (32 Tautenburg plates, sum of exposure times: 15.5 h) and DSSII(blue)-Image (POSSII-Field XJ103: exposure 55 min) of sample field 1RXS J180023.9+634953

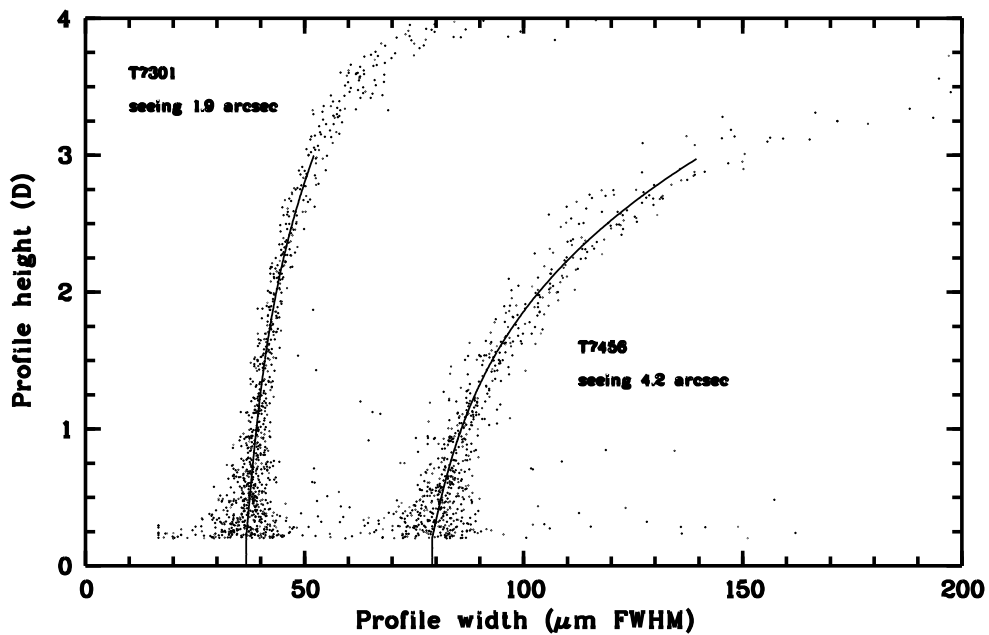


Figure 26: Seeing plot for good seeing (left) and bad seeing (right) and determination of plate seeing (fit graphs). Because of the increasing scatter in FWHM values for faint objects, measurements with profile height $H \leq 0.2$ have been omitted.

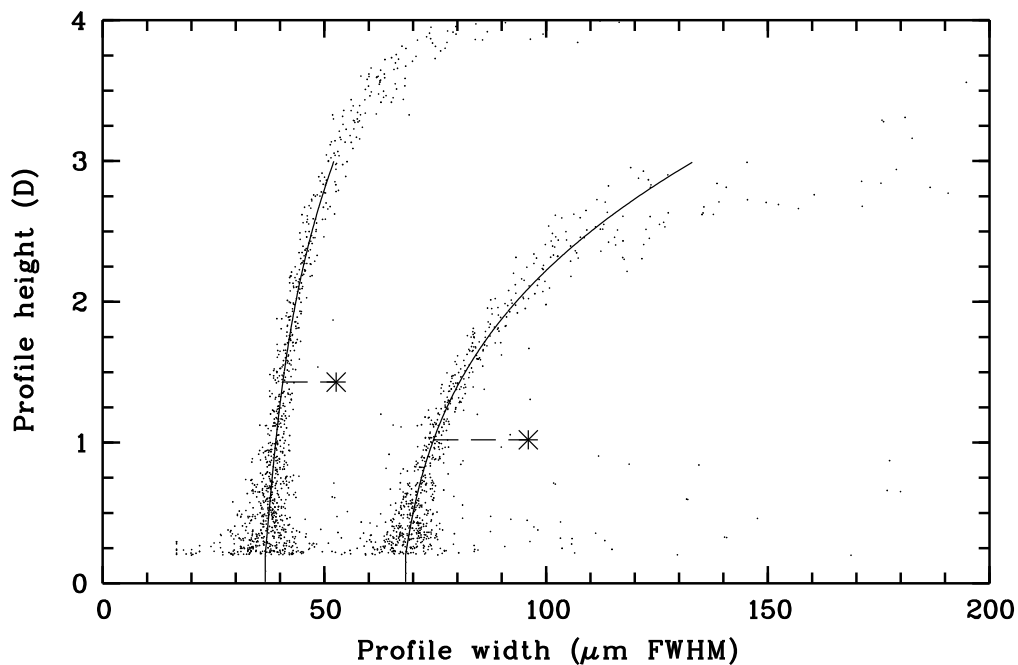


Figure 27: Plate seeing and extended objects; the seeing fit and one (the same) extended object are marked. Because the seeing is worse for the plate at the right, the flux is spread over a larger area, and the profile height is consequently lower.

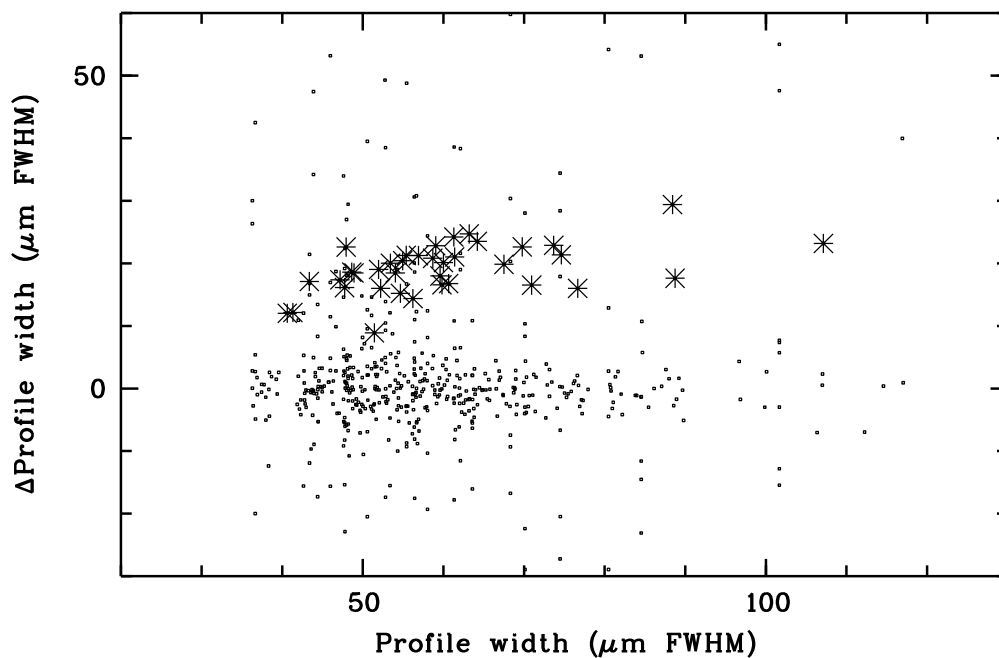


Figure 28: Object extension plot for one sample object (1RXS J175505.8+651951): shown is the excess FWHM (y-axis) vs. the measured FWHM (x-axis). All measurements from the small field surrounding the X-ray source, taken from all plates, are shown (small dots). The majority of objects is pointlike and has an excess FWHM close to zero; faint objects where the profile fit is not well determined produce a scattering of non-zero FWHM values. The data points for one extended object are marked (double crosses) and have a mean excess of $19 \mu\text{m}$ i.e. 1 arcsec

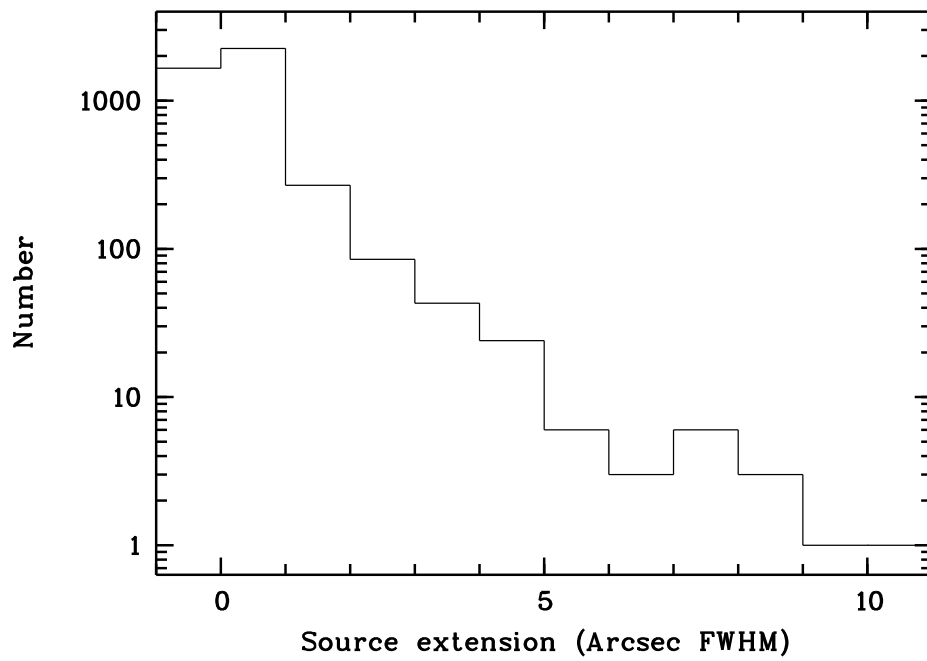


Figure 29: Distribution of the optical extension of ALL objects measured on the Tautenburg plates, including bright galaxies

7 Variability analysis

In order to perform a variability analysis of the targets, we need to compare photographic magnitudes measured at different times, i.e. on different plates. Because of the shortcomings of the photographic plates as described in Chapter 4.3, a simple, direct comparison of magnitude indices of the same field on different plates, even when corrected for exposure time, does not make much sense.

A slightly more refined approach is to calibrate one plate using whatever photometric standard stars or fields are available for that plate, using a mean calibration for the entire plate. Because the calibration varies depending on the location on the plate, the resulting photographic magnitudes of objects in one field will have systematic errors. The photographic magnitudes of one object observed on different plates will have a significant scatter (of the order of the systematic errors), masking out variability with amplitudes below the typical systematic error of the calibration differences within one plate of 0.5 – 0.8 mag.

The best approach, therefore, is to do differential photometry on a field-to-field base, using the fact that although some sources within our field will (hopefully) show a variable magnitude, most objects will be constant. These constant objects can be used to define a transformation of magnitude indices between two or more fields to allow comparison of magnitudes and measure variability, without knowing the exact photometric magnitude in any photometric system. This approach will be elaborated in Chapter 7.1

Additionally, it is possible to define a common system of all plates and to calculate transformations between the common system and the photometric system of the individual plates. The magnitude indices of the mean system can then be calibrated against photometric references as described in Chapter 7.2, effectively generating precise differential photometry as well as photometric magnitudes of all measurements which are, however, subject to the above-mentioned systematic errors.

7.1 Matching small fields

Described here is a general method for matching sets of measurements on small fields. This method can be used for differential photometry but can also be extended to do inter-plate alignment of photometric measurements.

The complete set of measurements of all stars in all used fields on all used plates can be represented by the set of magnitude indices m_{ijk} where i denotes the individual plate index (i.e. describes on which plate the measurement was taken), j the field index (which of the small fields on the plate was measured) and k the individual star within the small field. *Matching* the measurements of magnitude indices on two plates means to define a set of transformations T between plates

$$m_{i_1jk} = T(i_1, i_2, j)(m_{i_2jk})$$

where i_1 and i_2 denote the two different plates and j and k denote the field and individual star within these plates.

The first step of the process is to define a common (mean) system of all used plates, by using the mean magnitude index of all measurements of an object (using the median value would also be possible but was not investigated). In the notation introduced above,

$$\overline{m}_{jk} = 1/n \sum_i m_{ijk}$$

is calculated for all stars (all values of k) in a small field with index j , with n being the number of measurements existing of the individual star on all plates. For the transformation between the common system and the individual measurements, a p -degree polynomial P_p with

$$m_{ijk} = P_p(\overline{m}_{jk}) = \sum_{l=0}^p a_{lij} \overline{m}_{jk}^l$$

is used. To determine the transformation coefficients a_{lij} , a polynomial regression analysis is performed for each plate (index i) and each small field (index j) such that the errors for

$$\chi_{ij}^2 = \sum_k \frac{1}{\sigma(\overline{m}_{jk})^2} (m_{ijk} - P_p(\overline{m}_{jk}))^2$$

are minimized, where $\sigma(m)$ is the standard deviation of the measurement as depending on source brightness.

Minimising the errors as a function of the parameters a_{lij} leads to a system of linear equations for the a_{lij} . By solving this system of equations, the coefficients are calculated and the transformations are determined.

Some care must be taken when choosing the polynomial degree of the fit and determining the standard deviation as a function of source brightness.

Polynomial degree of fit For determination of the optimum polynomial degree, tests were made with $n = 1 \dots 3$. Because the improvement from $n = 2$ to $n = 3$ is only marginal, a quadratic polynomial is used to avoid the drawbacks that accompany higher-order polynomials (oscillation between sampling points, numerically less stable behaviour when extrapolated). For fields in which the X-ray counterparts are bright stars, we reverted to a linear polynomial which is more properly defined when there are few stars to define the fit in the relevant magnitude range (which is typical for bright stars) and also more stable when some slight extrapolation is necessary (which is often the case for fields with bright X-ray counterparts).

It should be noted that because our small fields contain typically 30–40, and very rarely less than 20 stars, the polynomial coefficients are always properly defined by the system of transformation equations.

Weight determination of the measurements What weight function i.e. what standard deviation of the measurement as a function of source brightness should be used is not immediately clear. Because of the complicated and multi-step reduction process, an analytical derivation of this weight function was not attempted. We must therefore try to derive the error function by other means.

The chosen approach was to make some assumption concerning the standard deviation as a function of magnitude and see what this assumption leads to in the reduction process. To list the two extreme positions, we can either assume that

- all measurements are weighted equally (constant standard deviation) if we are interested mainly in a good graphical impression of the result of the matching process or if we have no clear idea of how the measurement errors might depend on the magnitude index. This might also be a good approximation for bright, saturated stars but, of course, neglects the higher measurement errors of fainter stars
- the measurements are weighted according to their photon counting statistics, i.e. weight $\sim I$ or standard deviation $\sigma \sim \frac{1}{\sqrt{I}}$ where the intensity I is derived from the magnitude index. This approximation would be applicable when using linear detectors like CCDs but neglects photographic saturation effects for bright stars.

Assuming both extreme positions, we reduced the entire data set. The resulting residua and standard deviations (see Fig. 31) were used to calculate new average standard deviations as a function of magnitude $\sigma(M)$. This standard deviation as a function of magnitude index can then be used as an input for a next iteration step of data reduction, leading again to a new function $\sigma(M)$.

Starting with both initial assumptions $\sigma_0(M)$ as given above, we find that the function $\sigma(M)$ quickly (in 3–4 steps) converges from both sides to a mean $\sigma(M)$ as given in Fig. 32. This mean $\sigma(M)$ is used as the function determining the weighting of the polynomial fit and, when the transformations as described in Chapter 5.10 are applied, also gives the mean precision (as expressed by the standard deviation) of the processing method as a function of the photographic magnitude. The precision of individual plates will deviate from this mean function. Therefore the standard deviation as a function of magnitude index is calculated individually for each plate.

The straightforward case: single-field reduction When the set of stars is situated within a single field and the polynomial degree and weight function are known, the reduction procedure is executed as follows:

- The mean magnitude index is calculated for all sources.
- The standard deviation, i.e. the weight of the individual measurement within the fit, is calculated as function of mean magnitude index and of the plate. The weight of known or suspected optical variables is set to zero.
- The set of linear equations resulting from the transformation equations is solved, giving the coefficients a_{lij} . These are used to transform all measurements, including those with zero weight which were not used for the fit, into the mean common system of the respective small field.

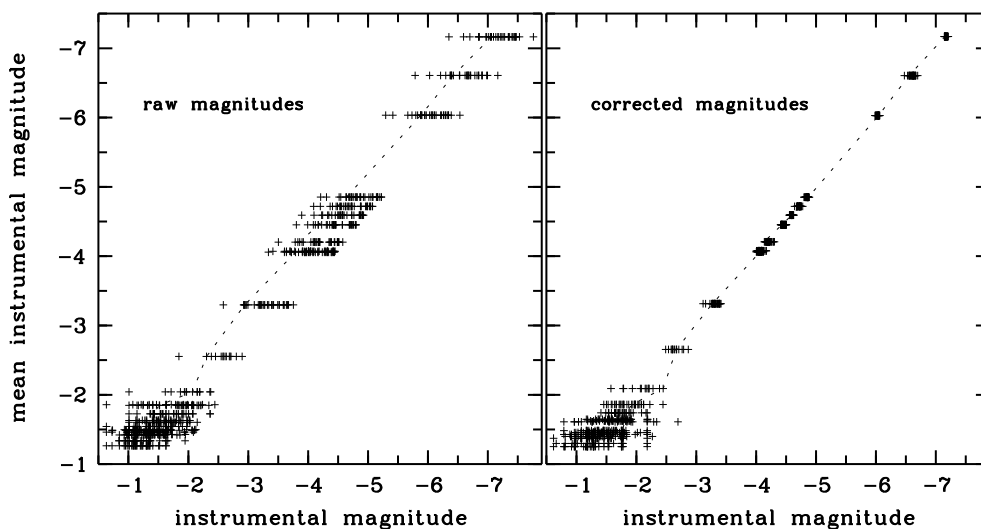


Figure 30: Transformation of the raw magnitudes into the mean common system. One set of measurements from a randomly chosen field is marked by a dotted line. Note the increasing scatter for fainter magnitudes i.e. greater numerical values of the magnitude (lower left corner)

- The reduced χ^2 of each object is calculated by comparing the standard deviations of all measurements within the common system, i.e. after transformation, with the average i.e. expected standard deviation for this mean magnitude index. Objects for which the reduced χ^2 exceeds a certain limit are flagged as optically variable.
- If variable sources still happened to be included in the standard stars used for the fit, the entire procedure was repeated, if necessary several times, until all variable stars were eliminated from the fit.

The individual stages of the process are shown in Figs. 30 (transformation of the raw magnitudes into the mean common system), 31 and 32 (individual and mean errors i.e. weight function), and 33 (resulting scatterplot including reduced χ^2). The scatterplot as the final result (Fig. 33) allows us to judge the variability data of a X-ray counterpart and the objects of the surrounding field. For a description of the meaning of all panels of the scatterplots see Fig. 33.

For each of the source fields, this variability / scatter-plot was created to judge the reliability of the variability data from this field and the variability properties of the X-ray counterparts. Some typical examples are shown in Fig. 33 to 36.

7.2 Reduction of all plates and all fields into a common system

The method described in the previous chapter allows us to analyse the variability of objects reliably and precisely within a small field without any assumptions or knowledge regarding the "true" photometric magnitude of the objects. While this

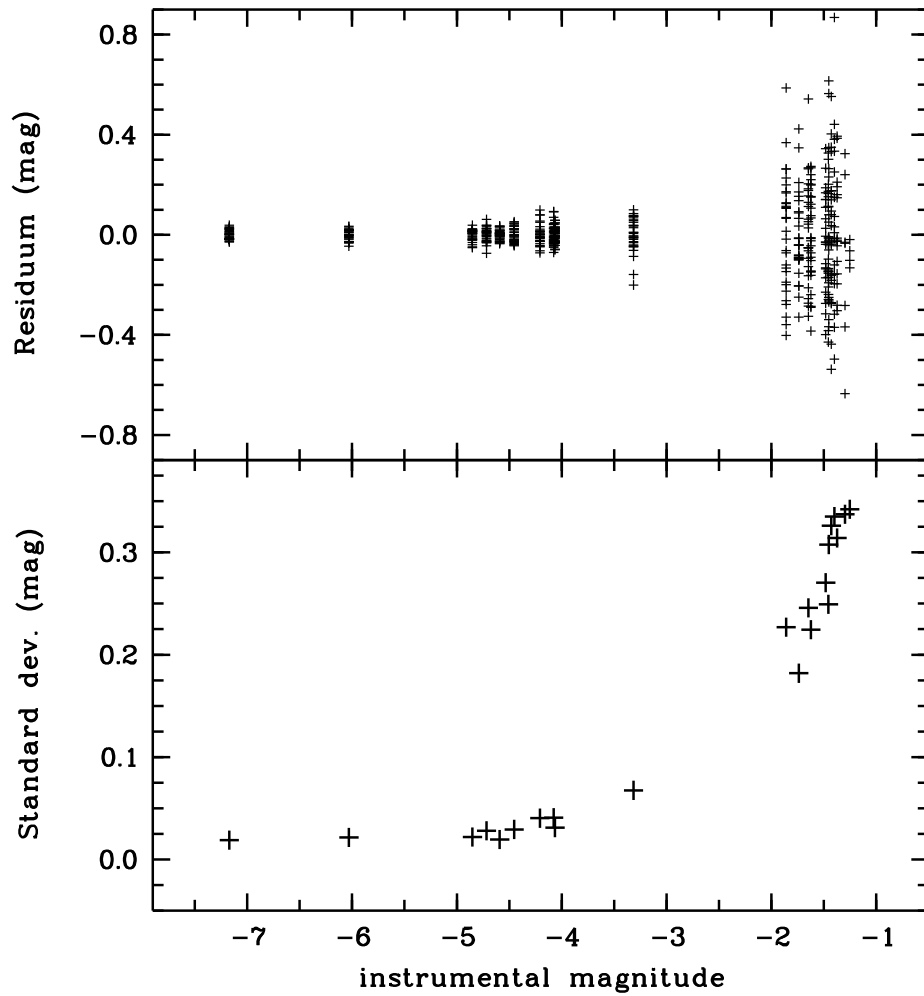


Figure 31: Determination of residua (upper panel) and standard deviation (lower panel) as a function of instrumental magnitude, calculated from one randomly chosen field. First, the residua are calculated as the difference between the mean instrumental magnitude and the measured instrumental magnitude, for each individual measurement. Then, the standard deviation of the measurement for the respective instrumental magnitude is calculated as the standard deviation of the residua.

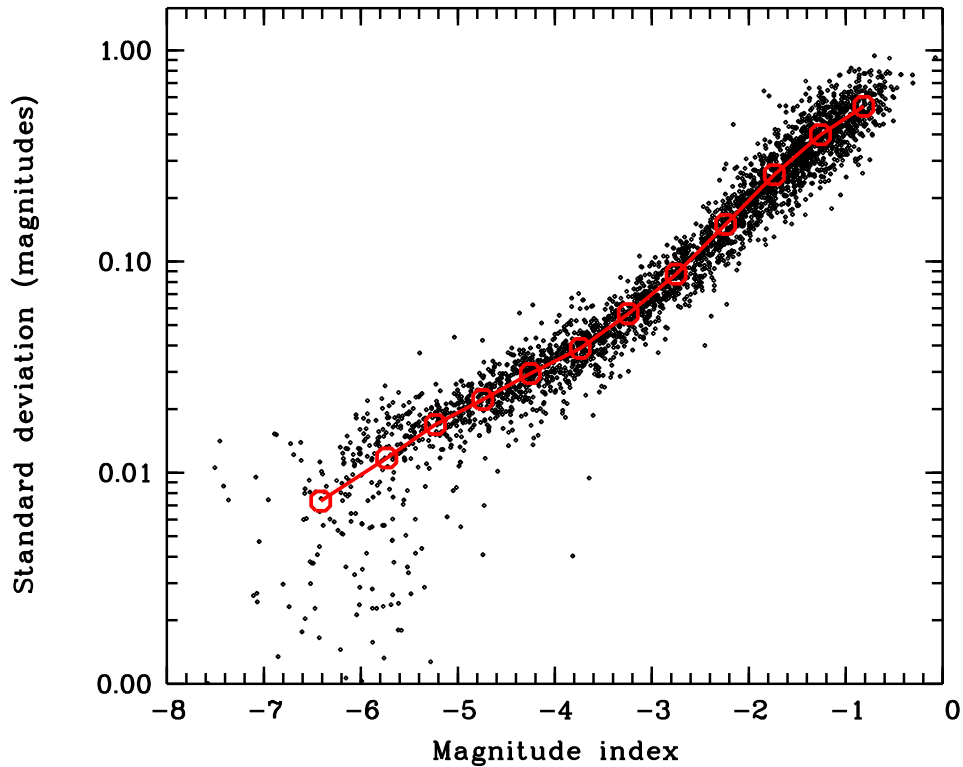


Figure 32: Determination of the mean standard deviation as a function of instrumental magnitude from the residua. Each dot represents the individual measurements of one star on a set of plates, i.e. is the result of the reduction process as depicted in Fig. 31. The individual measurements of a set of stars with a certain range of (instrumental) magnitudes are then averaged to give an average precision as function of (again, instrumental) magnitude (shown in red).

This computation can be done for one small field – which is important for weighting the individual measurements – or it can be done for *all* stars within our set of measurements – yielding an average overall precision of our reduction process.

The greater scatter of the standard deviations of brighter stars (left side of the diagram) is an artefact of the transformation process; a pair of bright stars within one field is transformed so that the higher weight of the brighter star forces the transformation in such a way that the brighter star has a scatter i.e. a standard deviation which is too low, while the standard deviation of the fainter star is too high. This effect can only be partly compensated by the weight adjustments described in Chapter 7.3.

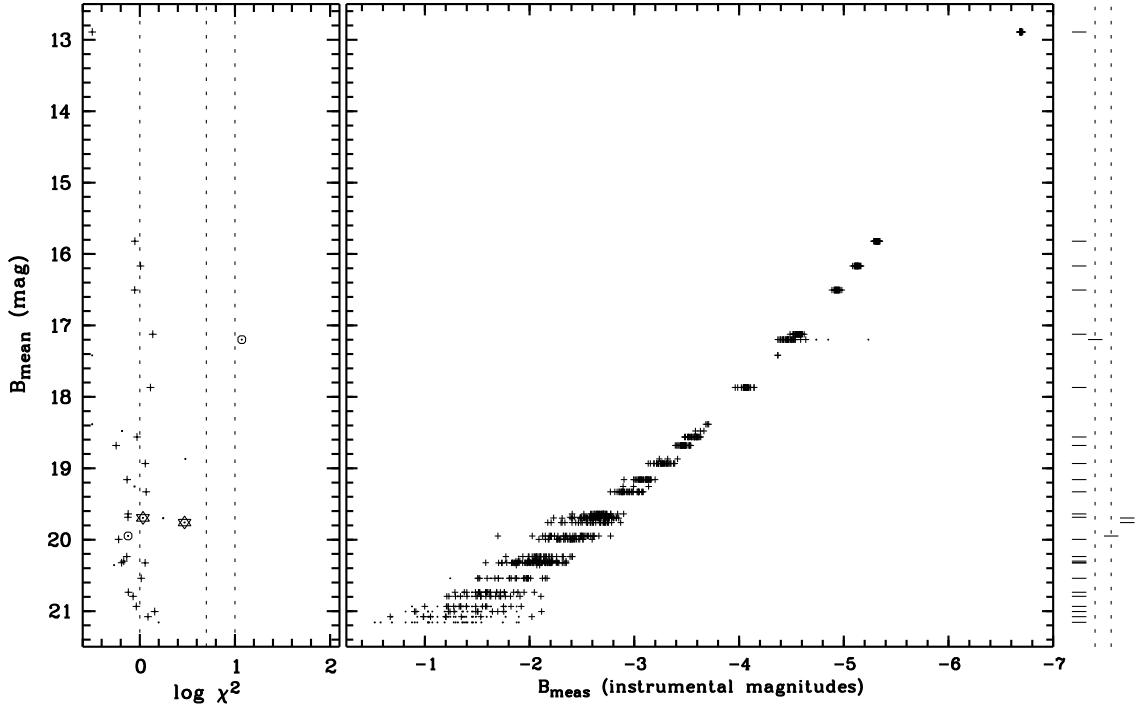


Figure 33: Scatterplot for the detection of variable objects, for field 1RXS J180251.3+660540. There are two X-ray counterpart candidates (marked with an asterisk within the left panel, at $B = 19.7$ and 19.8 mag); the slightly fainter one, an AGN at $z = 0.207$, is variable, with $\chi^2 = 3.0$.

In the large center panel, the individual photometric measurements (transformed into the mean common system) are plotted. Variable objects stand out by their large scatter (unusually wide distribution of the data points when compared to reference stars of comparable brightness) or by single deviating values (flares). The x-axis shows the instrumental magnitude (magnitude index), the y-axis shows calibrated photometric magnitude. Normal data points are plotted as small "+"-symbols; data points which have low confidence (e.g. disturbed by plate faults or near neighbours, near plate borders) are shown dotted.

The panel at the left side shows the reduced χ^2 (log scale) of all objects. Normal, non-variable objects have χ^2 near one (first dashed line); The χ^2 -values 5 and 10 are also marked by dashed lines. Normal comparison stars are plotted as small "+"-symbols; the X-ray counterparts (or candidates when there is no unambiguous identification) are plotted as asterisks. Objects which should be disregarded for variability analysis are shown as small dotted circles "⊙" (extended or variable objects not related to the X-ray emission) or dots (disturbed sources with too few measurements to allow a reliable statistical analysis). All χ^2 -values are plotted with a cut-off value of 100.

At the right side of the plot, a marker shows the classification of the sources as a normal source (left of the two dashed lines), variable non-extended object (on the left dashed line), extended object (on right dashed line) or X-ray counterpart or candidate (right of the two dashed lines).

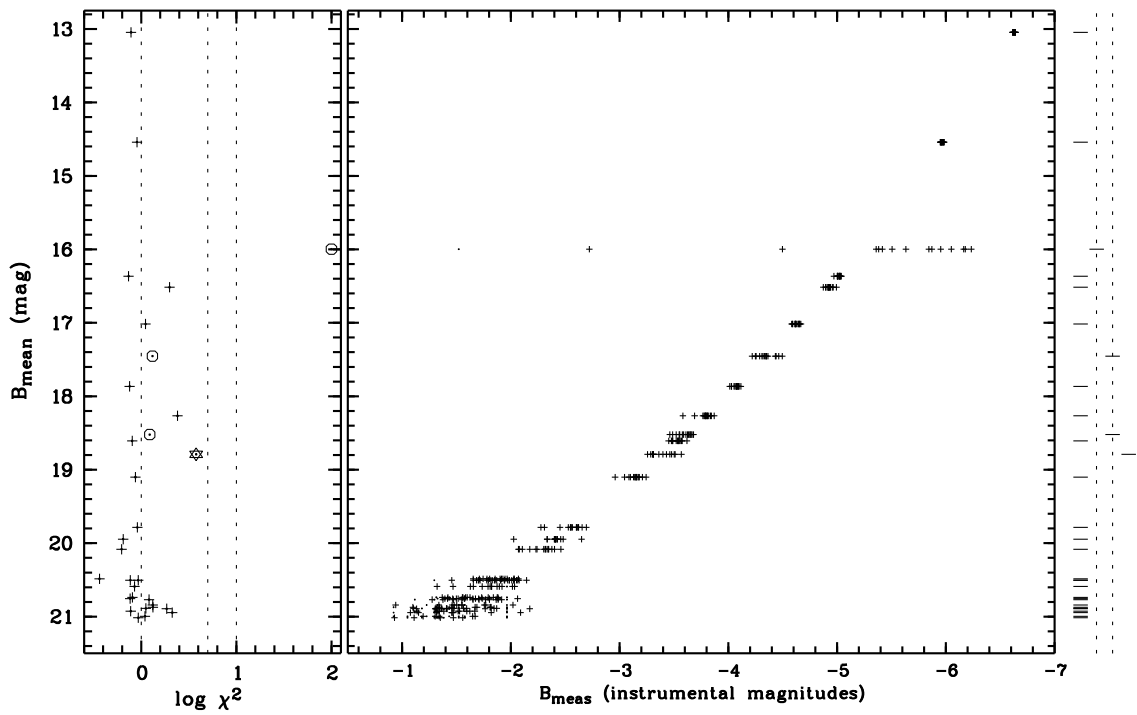


Figure 34: Scatterplot for the detection of variable objects, for field 1RXS J182320.1+641924. The X-ray counterpart (marked with an asterisk, at $B = 18.8$ mag), an AGN at $z = 0.5766$, is variable with $\chi^2 = 3.8$. The field also contains the variable star IY Dra, at a mean $B = 16$ mag

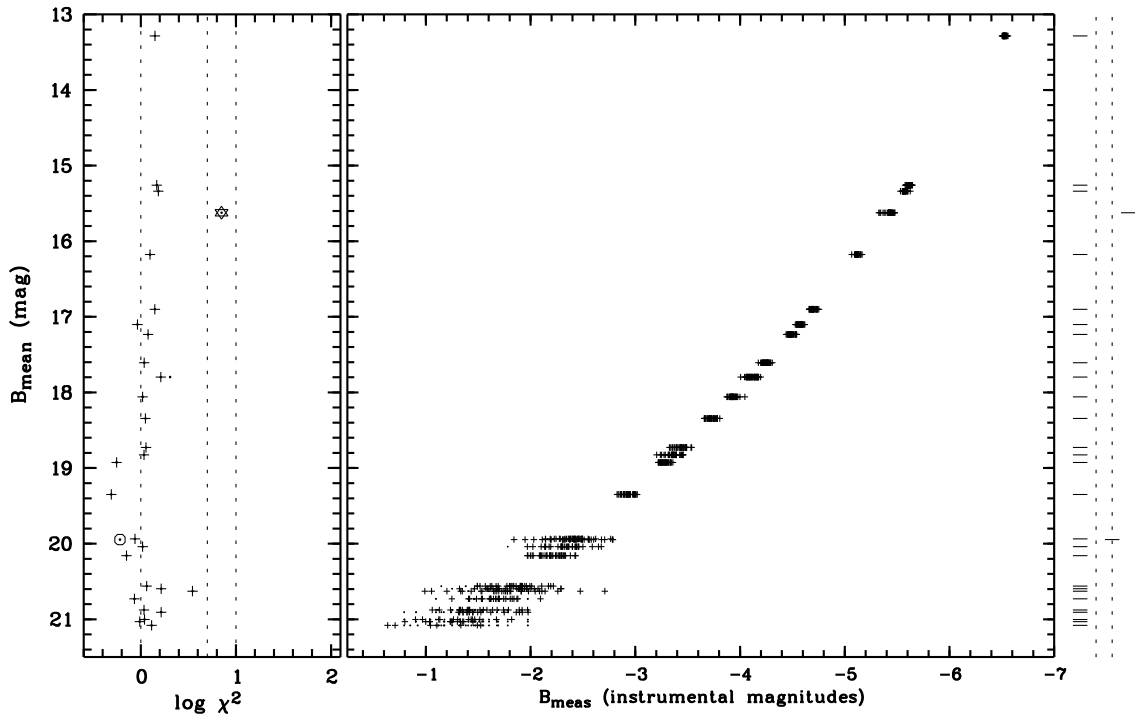


Figure 35: Scatterplot for the detection of variable objects, for field 1RXS J180328.4+673806, containing the variable Seyfert1 KAZ 102

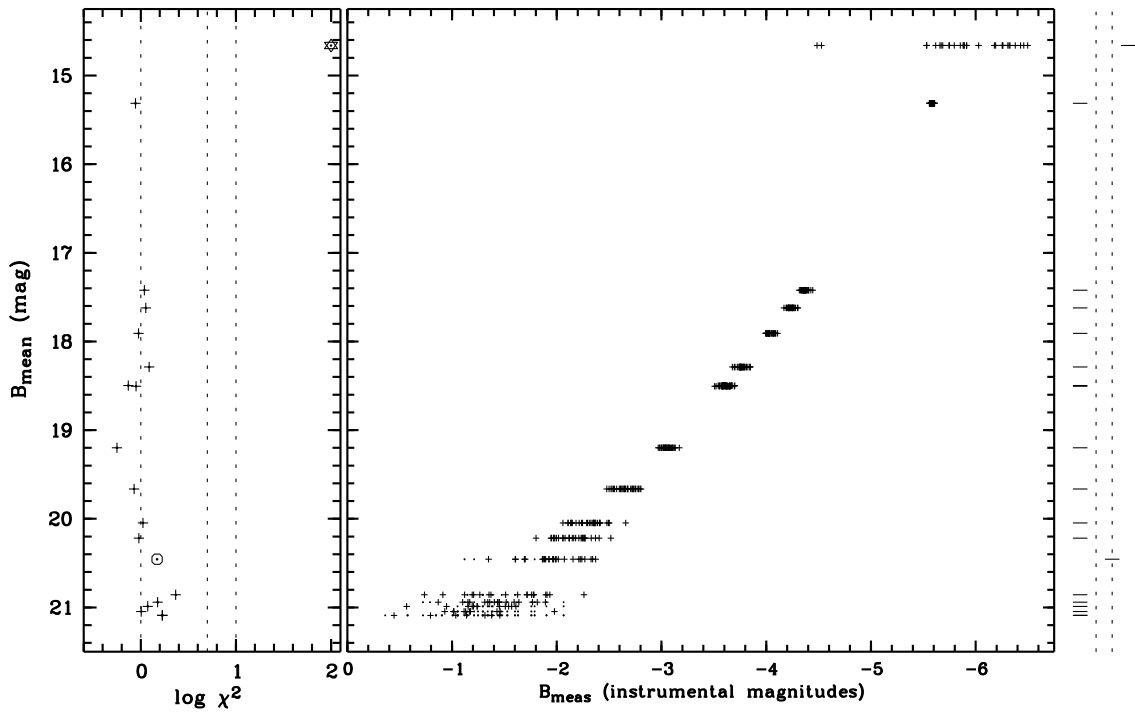


Figure 36: Scatterplot for the detection of variable objects, for field 1RXS J180413.4+675412, containing the CV MS 1804.3+6753

is optimally adapted to the shortcomings of photographic plates and allows precise differential photometry, a way to determine the "true" photometric magnitude of an object – even to a lesser degree of precision than the differential photometry – is clearly desirable.

There is no strict way to achieve this, because the photometric calibration that can be obtained for fields where CCD- or photoelectric standards are available can not be transferred to the remaining areas of the plate. Speaking in terms of the transformation equations, the transformation coefficients a_{ij} as calculated above are valid only locally on each plate, i.e. depend on plate **and** field index. Strictly speaking, there is no common system (transformation between individual measurements of magnitude index and mean magnitude) for a set of plates with identical plate centers i.e. the same ensemble of scanned small fields; rather, each small field has its own transformation and its own photometric calibration.

A useful and sensible simplification is to assume the same photometric transformation system for all fields, i.e. that the calibration of all fields is identical to a mean system. This neglects systematic errors, e.g. differences in sensitivity from plate center to plate border because of telescope vignetting. The calibration to photographic magnitude is therefore still subject to the systematic errors described above; however, the precision of the differential photometry is not degraded. The transformation equations used above then assume the simple form

$$m_{ijk} = a_{0ij} + a_{1ij}\overline{m}_{jk}$$

which has the added advantage that the inversion is very simple.

That way, we first perform differential photometry in small fields, reaching the full attainable precision, and afterwards transform the measurements into a mean system, with true photometric magnitudes subject to some systematic errors.

The case is somewhat more complicated for our measurements because our data is taken from five different but overlapping sky areas. The overlap between the center area and any of the four off-center areas is 1/4 of the plate area, while the overlap between any two off-center areas is practically zero. Reduction of all plates from all five areas to a common system is therefore done in three steps:

- First, all fields on all plates from the center area are reduced into a mean common system.
- Then, all fields from the four off-center areas which are also located within the center area are reduced to the mean common system. In other words, the fields within the plate overlap are used to transfer the mean common system from the center area to the off-center areas.
- Finally, the fields within the remaining area of the off-center plates (3/4 of the plate) are transformed to the same system as the fields from the overlap area of the plate which were already reduced to the mean common system.

That way, all measured fields from our data set are reduced to a common photometric system, and we have "true", calibrated photometric magnitudes in all fields on our plates without having to sacrifice the precision of the differential photometry.

7.3 Bright stars

Bright stars pose a special problem for several reasons:

- One of the basic assumptions underlying the photometric reduction process is that sources show simple, radially symmetric profiles. This assumption is not true for bright stars because diffraction spikes and haloes are beginning to show for stars brighter than about 13 magnitudes.
- Photometry of bright stars is prone to saturation effects, and these effects are seeing-, i.e. plate-dependent. For faint stars where the density at the profile center does not reach saturation, the seeing merely determines the area the source flux is spread over. However, for bright stars on a plate with good seeing, flux is concentrated in a smaller area, and is "lost" to the detection process because of plate saturation. Thus, the form of the transformation is seeing-dependent at the bright end only, and because of the scarcity of bright sources the resulting curvature is neither well-defined nor modeled precisely by the low-order polynomials used for the transformation.
- Bright stars are scarce in our scanned fields. Because the reliability of the transformation from plate system to the mean common system at a certain magnitude depends on the availability of enough comparison stars at this magnitude, there is less trust in this transformation for bright stars.
- The weight of a measurement in the fitting process increases with the brightness of the source. Therefore, a single bright star at the bright end of the mean vs. measured brightness diagram tends to act as a fixpoint for the transformation graphs, effectively "nailing" all transformations to this point. This effect is especially noticeable when two bright stars are located within one field; typically, the higher weight of the brighter star will produce a small χ^2 for the brighter star and an uncommonly large χ^2 for the fainter star. To avoid this undesirable effect, the weight W_1 of the brightest star in any field is decreased to W_{1c} depending on the weight i.e. brightness difference to the next brightest star with weight W_2 as

$$W_{1c} = W_1(W_2/W_1)^\alpha$$

which results in $W_{1c} = W_1$ for $\alpha = 0$ (weight is unchanged), $W_{1c} = W_2$ for $\alpha = 1$ (weights of brightest and second brightest star is identical), and $W_2 < W_{1c} < W_1$ for $0 < \alpha < 1$ (weight of brightest stars is adjusted). A suitable value for α was found by reducing several fields with bright stars with a set of test values for α and examining the resulting scatterplots, resulting in an adopted value of $\alpha = 0.8$.

Taken together, this means that the photometric errors increase and the general reliability of the variability analysis decreases for bright stars. However, this is not of major concern because the vast majority of the X-ray counterparts in general and all extragalactic ones are faint sources.

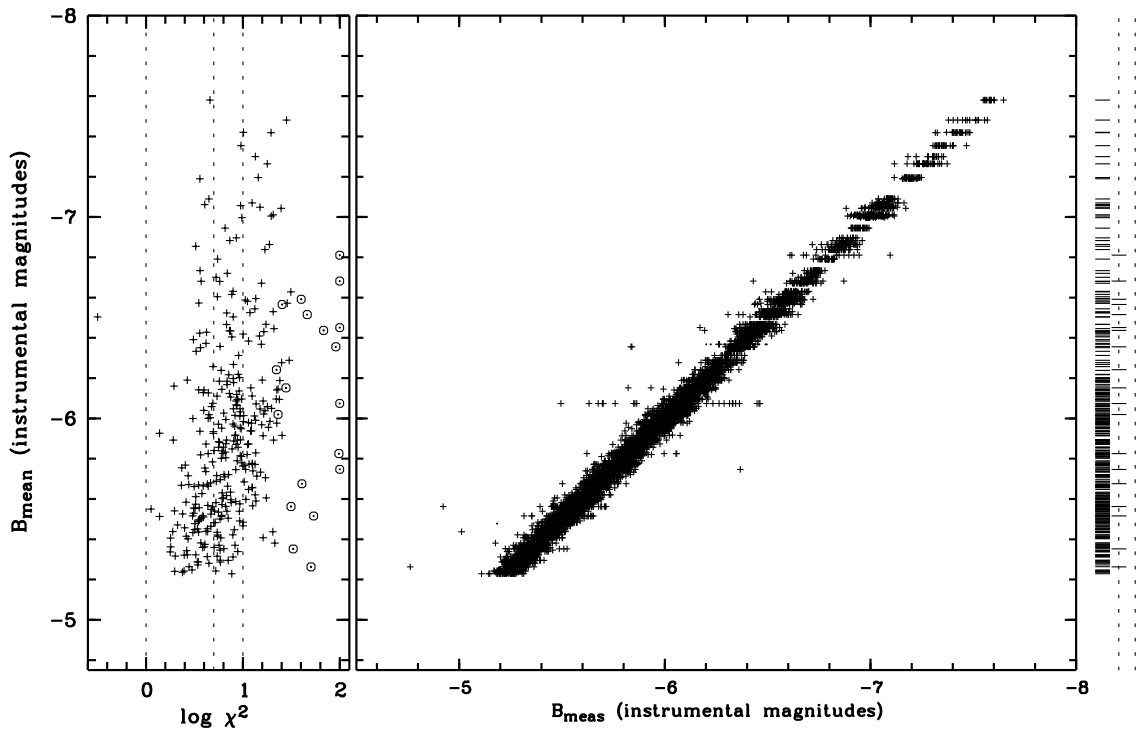


Figure 37: Scatterplot for the detection of bright variable objects, with special processing. Because the processing is no longer restricted to comparison of small fields, the χ^2 of all objects (which is computed with reference to the standard deviation for the small-field reduction) is significantly larger than normal. However, variable sources still stand out clearly and are marked with the symbol "o" in the left panel respectively with a right-shifted bar in the right panel. The layout and content of the panels is the same as in Fig. 33.

In order to detect variability in bright stars (with magnitudes from 10 to 16 mag), an additional processing step was introduced. The corresponding fields were collected and variability analysis was performed as if the objects in these fields were contained within one field. This corresponds to the "slightly more refined approach" mentioned in the beginning of Chapter 7, with a direct comparison of objects across the entire plate. The resulting scatterplot is shown in Fig. 37. Although the results are not as reliable as for the normal variability analysis and all χ^2 -values are well above the expected value for normal single-field analysis because of the larger calibration scatter (see Chapter 5.10), a population of variable objects clearly stands out.

7.4 Evaluating the effects of near neighbours

The determination of source profile and magnitude index as described in Chapters 5.4 and 5.8 is based on the assumption that the star images on the photographic plates are undisturbed by near neighbours. The local determination of plate background and the automatic exclusion of areas disturbed by near neighbours from the profile calculation (Chapter 5.4) helps to minimize effects due to the failure of this assumption but can not undo the damage if two sources are lying very close to each other or if a faint source is located close to a bright star. This is because the photographic plate is a highly non-linear detector and does not allow precise subtraction of disturbing profiles as would be possible for linear detectors, e.g. CCDs.

The general effect of a close neighbour is to increase the measurement errors of the photometric reduction process, increasing the χ^2 of the variability analysis and producing "false" variability. The magnitude of the effect depends on the distance between disturbed and disturbing source and on the brightness of the disturbing and the disturbed sources, primarily on the brightness difference. The seeing influence how pronounced the effect is for a certain plate but is incorporated in the χ^2 of the magnitude index which is calculated over all measurements.

To check if the magnitude index χ^2 (i.e. the variability) of a disturbed source is genuine, i.e. exceeds what is usual for close neighbours with this set of distance and brightness values, a comparison data base was built from the measured data. First, from the complete list of source positions generated from the stacked plates (see Chapter 6.1), a list was created of all fields which contained the nearest neighbour for all stars and all neighbours up to a certain radius (2.5 arcmin). This list, containing almost 6000 entries with χ^2 of the disturbed star and angular separation and magnitudes of disturbed and disturbing star, is used to compare the variability index, i.e. the χ^2 of the magnitude index of a certain star, with the complete set of measurements of all pairs of close neighbours with comparable magnitude pairings.

For an example see Fig. 38 where the "disturbed" and the "disturbing" objects have a brightness of 20 ± 0.5 and 15 ± 0.5 mag. For source separations above 12–15 arcsec, no influence of the brighter star on the reliability of the fainter object's photometry is visible; the values used to classify the variability cluster around the value expected for undisturbed measurements ($\log \chi^2 = 0$). For separations below

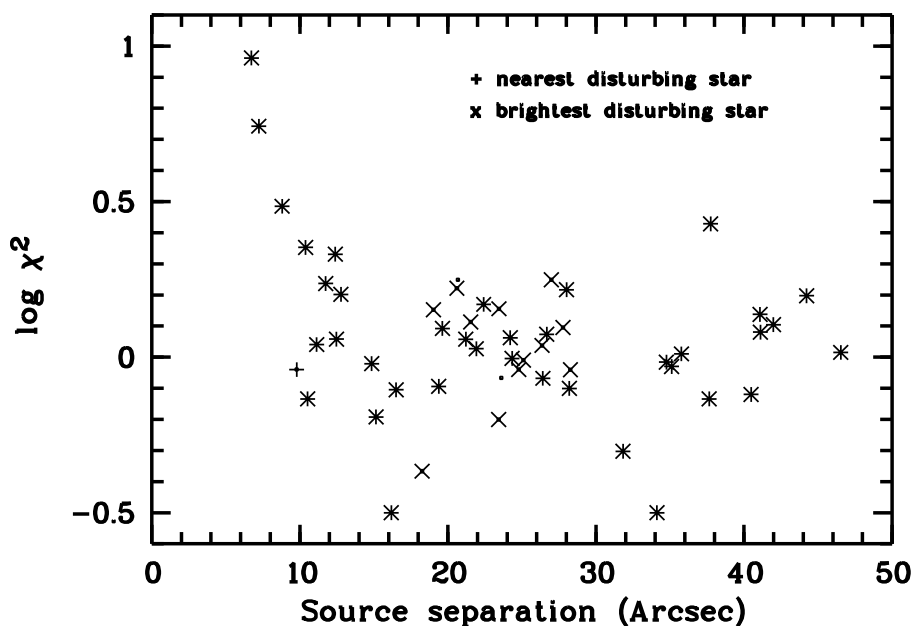


Figure 38: Apparent variability produced by disturbances from near neighbours. Shown are all measurements from the Tautenburg plates where the "disturbed" and the "disturbing" objects fall into a certain brightness range. In this example, the effect of a 15 mag disturbing star on a 20 mag object is shown. As expected, the effect of a 15 mag disturbing star on a 20 mag object is shown. As expected, the apparent variability, determined by the χ^2 of the disturbed sources, increases with decreasing source separation. The values of the χ^2 and especially the magnitude of the increase for small separations depends strongly on the brightness ranges for "disturbed" and the "disturbing" objects, mostly on the brightness difference.

10–12 arcsec the effect becomes increasingly important, resulting in a χ^2 that is e.g. ten times the expected value for a separation of ~ 6 arcsec.

For *really* bright disturbing stars, brighter than 12–13 mag, additional visual checks are necessary because the disturbed object could lie close to a diffraction ring or spike.

7.5 Discussion of the results of the photometry

In this chapter the precision, errors and results of the photometric techniques are discussed and compared with results from the literature.

7.5.1 Photometric precision

Because of our use of a two-step reduction process, it is very important to separate the errors of the differential photometry and the errors of the transformation process into the mean common system.

- The errors of the differential photometry limit the precision of the measured χ^2 of the magnitude index that is used to measure the degree of variability of an object. In other words, the errors of the differential photometry limit the capability of our survey to find variable objects, and it is of utmost importance to keep these errors as low as possible.
- The errors of the transformation process into the mean common system limit our capability to measure the "true" photometric magnitudes of objects within the photometric system defined by the standard fields. However, the precision of the differential photometry and the sensitivity of the variability survey are not affected at all.

The derivation of the standard deviation of the differential photometry has already been discussed in Chapter 7.1. The resulting mean precision of the differential photometry as a function of magnitude is shown in Fig. 39. At the faint end, the precision is still better than 0.3 mag for stars close to the 4σ plate sensitivity limit at 21.0 – 21.5 mag, reaching 0.1 mag for stars slightly brighter than 20 mag and going down below 0.02 mag for stars brighter than 16 mag. For stars brighter than about 14 mag, the precision and the reliability of the measurements are degraded by the effects described in Chapter 7.5.2; this affects the mean precision, i.e. the graph of Fig. 39, for stars brighter than about 14 mags, and results in a constant photometric precision at the bright end of the graph.

The individual errors of single plates will differ, but this is taken into account during the reduction process.

For an estimation of the errors of the transformation process, two approaches were taken:

- It is very rare for a Schmidt plate to contain only one photometric sequence. Most plates contain two sequences, some even three. It is then possible to measure the systematic differences between the photometric calibration of those sequences. See Fig. 23 for an example. Repeating this for all plates allows us to establish a statistics of the calibration differences.
- During the reduction of all photometric measurements into the mean common system, the transformation coefficients of the mean magnitude indices of each small field into the common system are calculated. The transformations will vary slightly between the fields on one plate. This means that the same numeric value of the measured magnitude index when measured in different fields will be transformed into slightly different photometric magnitudes. By comparing the effects of the transformations between the fields over a sensible magnitude range (12 – 20 mag) an estimation of the systematic errors is possible.

Both methods deliver similar results. The average systematic error of the photometric magnitudes over the above mentioned brightness range is 0.2 mag (standard deviation), while values larger than 0.5 mag are reached only for a few exceptional fields.

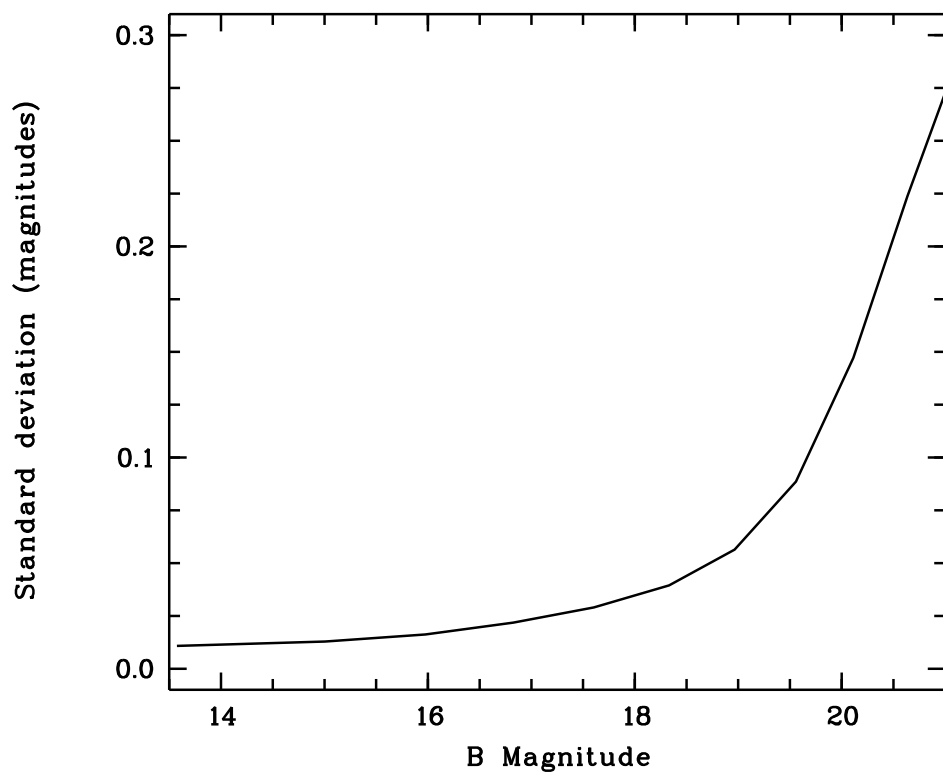


Figure 39: Mean photometric precision, averaged over ALL plates. Because of the effects described in Chapter 7.5.2, no precisions are given for magnitudes brighter than 14 mag.

7.5.2 Photometric errors for bright stars

The problems of determining the magnitude index of bright stars that result from the saturation of the star profiles can be solved quite satisfactorily (see Chapter 5.6). However, there is a fundamental problem for differential photometry with small fields (i.e. a limited number of comparison stars) in that in many fields one bright star will dominate the fit and make the transformations unreliable at the bright end.

For an example, see Fig. 33 where the brightest star in the field has about 13 mag and the 2nd brightest star is about 3 mags fainter. As a result of the "leverage" that the bright star exerts on the transformations of the individual plates, it has a very low scatter and consequently a very low reduced χ^2 . This would be the case even if this brightest star would be moderately variable; the only hint could be a moderate increase of the χ^2 -values of the fainter stars of medium brightness (16 – 18 mag). So, we must conclude that in this brightness configuration it is not possible to recognize a variability of the brightest star reliably. This is, to a lesser degree, also true if the brightness difference is lower than the 3 magnitudes that we encounter in this example. For a reliable transformation (and reliable χ^2 -values) of bright stars we need a configuration where the two brightest stars within one field have a comparable magnitude.

Changing the weight function (i.e. adjusting the standard deviation as a function of magnitude) does not solve this problem. In the example shown above, the scatter of the bright star would still be significantly lower if the weight function would be constant, even if the weight of the brightest star would be moderately *lower* than that of the fainter stars.

Because the amount of this effect depends on the brightness configuration (mainly on brightness and brightness differences of the two or three brightest stars) within the individual fields, there is no possibility to solve this problem in a satisfactory, general way. We have tried to lessen the effect by introducing a weight factor that depends on the brightness difference of the two brightest stars (see Chapter 7.3), but the result is not optimal for all cases. So, when judging the variability of bright objects from the scatterplot of one field, it is important to be aware of this effect.

The effect explained above not only makes the χ^2 -values of bright stars unreliable; it also affects the determination of the weight function of the transformations, i.e. the standard deviation as a function of magnitude, for bright stars.

7.5.3 Properties of the Tautenburg Schmidt plates

The plate seeing and plate sensitivity are routinely calculated as part of the reduction process. The resulting distributions are shown in Figs. 40 and 41. The plate seeing varies between 1.9" and 5.4", with a mean value of 2.8", while the 4σ plate sensitivity typically varies between 20.5 mag and 21.5 mag (mean value 21.1 mag) for the plates used.

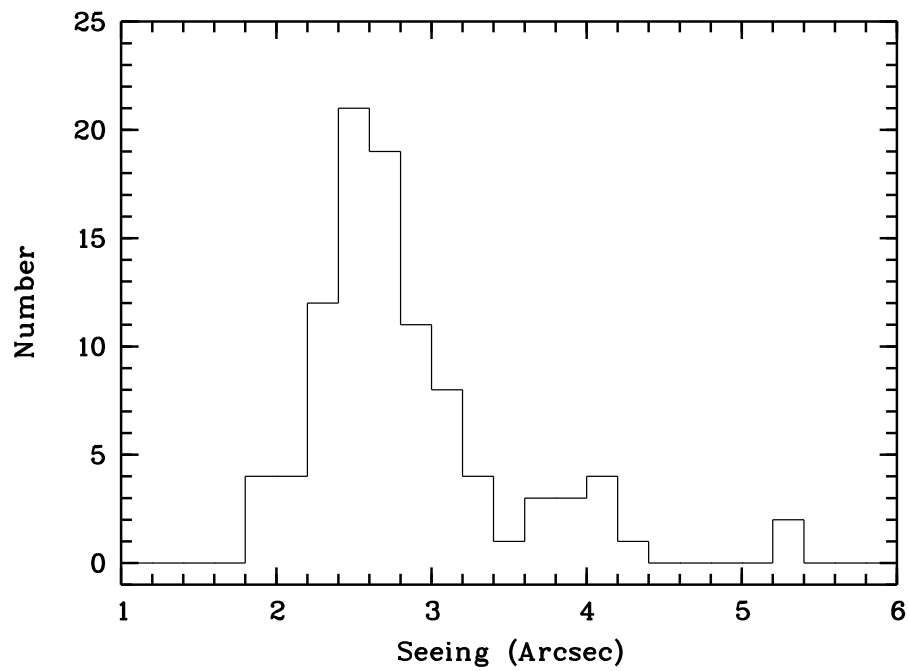


Figure 40: Distribution of seeing values of the Tautenburg plate sample

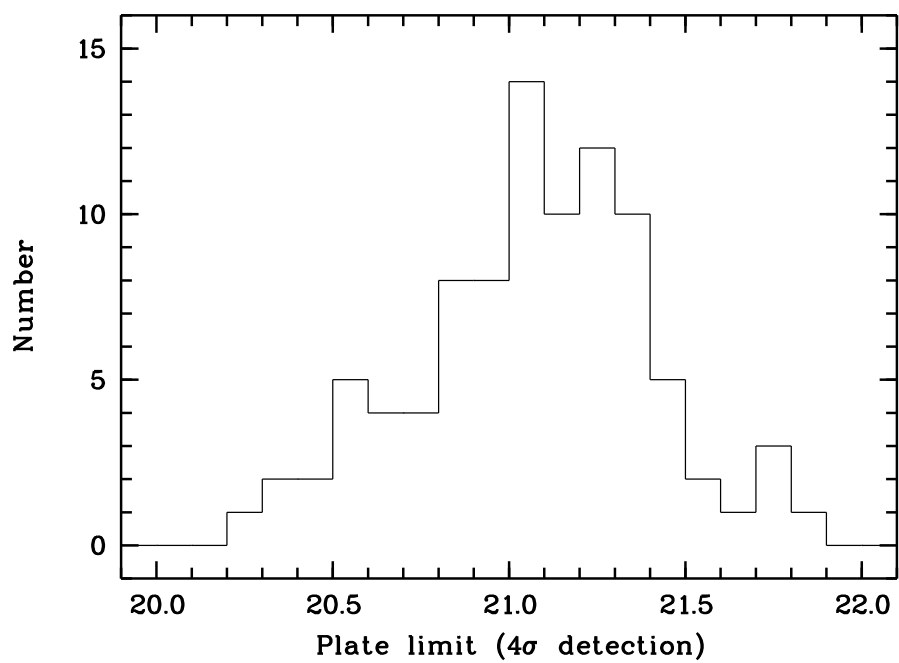


Figure 41: Distribution of plate sensitivity of the Tautenburg plate sample, for 4σ detection of sources

7.5.4 Comparison with similar studies

There are several examples in the literature for variability surveys with a timebase of several years, mostly based on photometry of series of Schmidt plates. Below, these surveys are listed with remarks on plate quality, limiting magnitude, reduction method, and precision. When comparing the results of our photographic photometry and the attained precision with data (and precisions) from literature, our results compare quite favorably.

Demers and Irwin (1987) report a survey for long-period variable stars on a set of 21 UK Schmidt telescope plates. The exposure times and the limiting magnitude of the used plates are comparable to ours. With the used photometric techniques (digitization of the plate on the Cambridge APM, differential photometry) the published standard deviations are, when compared to our measurements, equal for faint stars (0.12 mag for 20 mag objects), and worse for brighter stars (0.03 mag vs. 0.015 mag for 16 mag objects, see Fig. 39).

Cristiani et al. (1990) In this work a set of 15 Schmidt plates of SA 94 from the UK and ESO La Silla Schmidt telescope has been digitized and the variability of 90 known QSO has been checked in a statistical way. The timebase of the used plates is 7 years.

The used plate material should be substantially better than our plates (substantially longer exposure time and generally more favourable observing conditions at the telescope sites; no details are published). Comparing the achieved precision is not trivial because no sensitivity or χ^2 values are published, instead a "variability index" is defined such that the 5% of the objects with the largest scatter in magnitude are assumed to be variable objects, where the percentage is arbitrarily chosen; the variability index has the dimension and function of a precision in magnitude. This sensitivity of the variability survey is about 0.15 for 20 mag objects (compared to our standard deviation of about 0.12 mag for 20 mag objects) but does not fall substantially below 0.08 magnitudes even for bright stars (see Fig. 1 in Cristiani et al. 1990). Looking at our Fig. 39, their resulting precision is at best comparable, more often substantially worse (depending on the object magnitudes) when compared to the results that were achieved in this work, the main reason probably being that the authors choose not to perform differential photometry.

Hook et al. (1994) report the results of a study of variability of optically selected quasars near the south galactic pole. The used plate material – 12 plates with a timebase of 16 years – was taken with the UK Schmidt telescope and is of a considerable better quality than the plate material that was available for our work (limiting magnitude 21.3 – 22.4 mag). The plates were digitized with the Cambridge APM, with differential photometry within small fields being performed afterwards.

The resulting precision as given in Table 2 of Hook et al. (1994) is quite bad for bright stars (0.14 mag vs. 0.015 mag/our work for 16 mag objects), decreasing to 0.05 mag for 19 mag stars which is the same level of precision reached by our work and then slightly rising again, with the comparison being in favour of Hook et al. (1994) for fainter stars (0.07 mag vs. 0.12 mag/our work for 20 mag objects), most probably because of the better plate material.

Scholz et al. (1997) describe a search for QSO based on optical variability and proper motion of objects. A total of 57 Schmidt-plates in the B band and 28 plates in the U and V band, with a timebase of 32 years, were digitized with the Cambridge APM plate scanner. All plates were taken with the 2m Schmidt-telescope of the Karl-Schwarzschildt-observatory, and the B plates are taken mostly with the same emulsion/filter combination as the plates used in our work; in summary, the plate material is very similar to the one used by us.

Differential photometry was performed on sub-fields of the measured plates, however with a rather large size of the areas (15' square). It may be due to this fact that the resulting precisions, while being comparable to ours for faint stars (standard deviation 0.2 mag for objects with 20.5 mag brightness), stays constant for objects brighter than 18 mag and does not fall significantly below 0.1 mag (Fig. 6 in Scholz et al. 1997).

Brunzendorf and Meusinger (2001) have analyzed 162 B Schmidt plates and 46 U-, V- and R-Schmidt plates, all taken with the 2m Schmidt-telescope of the Karl-Schwarzschildt observatory, with exposure times, emulsions and limiting magnitudes of the B plates similar to our plate material. The plates were digitized with the scanner of the Tautenburg observatory (TPS, Tautenburg plate scanner). The resulting data were analysed with the MRSP software package from the Münster Redshift project.

For the photometric reduction, differential photometry was not used. Instead, each plate was reduced separately using photometric standard fields and a geometrical correction was included using fourth-order polynomials in both coordinates. The resulting corrections reach up to 0.5 mag.

The resulting standard deviation (see Fig. 5 in Brunzendorf and Meusinger 2001) is quite bad for faint stars (> 0.3 mag for 20 mag objects), is greater than 0.1 mag for 18 mag stars (compared to 0.03 mag in our work) and does not fall significantly below 0.1 mag for brighter stars.

Brunzendorf and Meusinger (2002) Using the same plates as in Brunzendorf and Meusinger (2001) but with a refined reduction procedure, improved photometric precisions are reached. However, even the improved standard deviations (Fig. 2 in Brunzendorf and Meusinger 2002) are still larger than the values reached in our work (0.05 mag vs. 0.015 mag/our work for 16 mag objects; 0.2 mag vs. 0.12 mag/our work for 20 mag objects).

Groot et al. (2003) This is the "faint sky variability survey" (FSVS), performed with the 2.5m Issac-Newton telescope at La Palma, using the wide-field camera, a 6kx6k CCD camera mounted at the prime focus of the telescope.

Although the detector is quite different, the used photometric techniques are similar to the ones we use: Fixed and variable PSF (point spread function) aperture photometry and differential photometry where, however, the differential magnitudes are not transformed by a polynomial but are compared to the mean magnitude of an ensemble of stars within one field.

When comparing the used telescope, the observing conditions at the observation site (typical seeing $1'' - 1.3''$) and especially the used detector, it is no big surprise that our variability survey can not compete with such a project regarding depth and precision. The limiting magnitude of observations is ~ 24 mag, and for 20 mag objects the standard deviation of magnitude measurements is 0.01 mag (compared to 0.12 mag for our variability survey).

Where our survey still *is* competitive is in the possible sky coverage: Because the used (large !) CCD detector covers only 0.29 degrees square per 10-minute B observation, more than 20h observation time would be needed for 36 degrees square, the area used in our survey, for a "snapshot" of a single epoch.

We also searched for contemporaneous optical measurements of objects from our variability survey for an additional check of the reliability of our measurements. Time-resolved optical photometry from the literature was found to be available for two bright AGN:

1RXS J180328.4+673806, Kaz 102 This bright Seyfert1-galaxy (B=15.6 mag, $z=0.136$) was observed in the X-ray-, UV and optical band during the RASS by Treves et al. (1995) as part of a multi-wavelength campaign. The observations in the B-band have a timespan of slightly more than one year (modified Julian date 48135 – 48505). The agreement of our data with the published CCD observations is quite good, with a slight (0.1 mag) systematic offset that is well within our error estimation. Although the time coverage of the CCD observations is somewhat patchy, the variability trends in both observations show good agreement, see Fig. 42.

1RXS J182157.4+642051, 1E 1821+64.3 This bright QSO (B=14.2 mag, $z=0.297$) was observed in the X-ray-, UV and optical band during the RASS by Ulrich et al. (1992) as part of a multi-wavelength campaign. The optical observations span a rather short time (modified Julian date 48125 – 48235) with observations in the B-, R-, I- and g-Bands. During this time the optical flux within those bands was constant at the $\sim 5\%$ -level. Our optical data (consisting, however, of only 2 observations during the timespan mentioned above) are consistent with this observation – see Appendix F. Shortly after the observations of Ulrich et al. (1992) our data show a sharp increase in brightness by more than 0.1 mag.

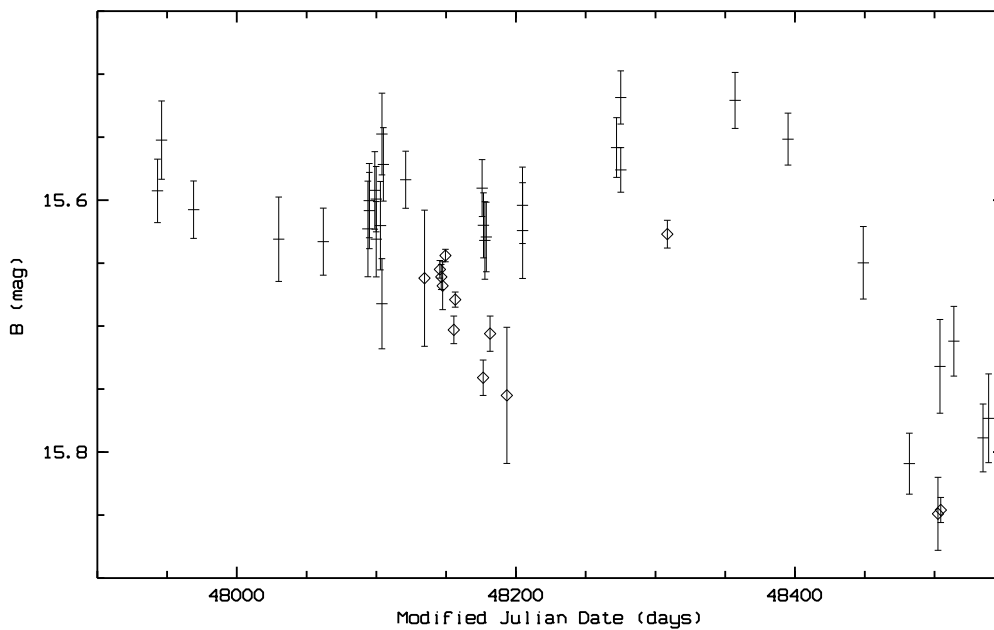


Figure 42: Comparison of photographic and CCD lightcurve for 1RXS J180328.4+673806 / Kaz 102. The data points plotted with lozenges are from the B (Lick observatory only) data of Treves et al. (1995). The CCD photometric errors are 0.01 – 0.05 mag, compared to 0.02 – 0.04 mag for our Schmidt plate data. There is a slight systematic offset of 0.1 mag between the CCD and photographic data, in accordance with our error estimation of the photometric transformation.

To summarize these results, we find that our photometric precision is most often better than works based on a comparable plate material, and is competitive even for studies which are based on far better plate material. No evidence for erroneous results was found from comparisons with CCD measurements.

8 The NEP X-ray sources – identifications, variability and physical properties

While the previous Chapters 4 to 7 discussed the photometric techniques and the overall photometric results, this chapter is focused on the identification contents of the source sample, the identification and physical nature of the individual optical counterparts and the results of the variability analysis of the optical counterparts.

The definition of the X-ray source list which forms the basis for the identification part of this work was already described in Chapters 2.3 and 2.4.

8.1 Identification of X-ray counterparts

Because of the large size of our sample (167 sources) and the involved amount of necessary observations and telescope time, it was decided not to pursue a large-scale identification programme. However, to get as much information as possible for all objects from our source list, a study of available catalogs, identifications and literature was performed.

Using the publicly available digitized POSSII data, 5 arcmin square finding charts in the blue, red and infrared passbands (B-, R- and I-plates) were printed for *all* sources, with each finding chart centered on the X-ray centroid position. For all *scanned* fields, finding charts from stacked Tautenburg Schmidt plates, with a superimposed X-ray error circle, were printed and compared to the POSSII charts.

The entire source list was cross-referenced to the NED and SIMBAD online catalogues (database epoch: 12/2003), searching for all objects within 5 arcmin around the X-ray position. The resulting matches were checked for a possible physical connection with the X-ray source; the radius where a physical connection was considered depended on the positional precision and resolution of the detection of the SIMBAD or NED object. The physical mechanisms on which a possible correspondence would be based were also considered, so for radio sources the possible existence of radio lobes around the X-ray / optical position was also taken into account.

From the available literature, the ROSAT North Ecliptic Pole survey (published in e.g. Mullis 2001, Gioia et al. 2003) proved most valuable for the identification of the X-ray sources, especially regarding the existence of spectroscopic identifications. Overlay plots of the ROSAT NEP survey identifications (Mullis 2001, Fig. 4.12) were created and our identification and finding charts were checked against the identifications, finding charts and X-ray contour plots from Gioia et al. (2003) and Mullis (2003).

The available data were collected individually for each object and are contained in Appendix D to G, with variability data and remarks where appropriate. Additionally, in Chapter 8.5 some especially noteworthy objects are discussed in more length. See Tab. 3 for a list of all counterparts.

8.2 Identification contents of the NEP X-ray sample

As a result of the identification procedure described in Chapter 8.1, our sample is composed as follows (IDs of primary counterpart candidate only in the few cases where more than one candidate exists):

- 79 (47 %) AGN
- 44 (26 %) stars (47 / 28 % including probable stars, with some doubts remaining)
- 1 (0.6 %) cataclysmic variable star
- 1 (0.6 %) white dwarf
- 22 (13 %) galaxy clusters (25 / 15 % including suspected galaxy clusters)
- 2 (1.2 %) BL Lac objects
- 3 (1.8 %) galaxies
- 2 (1.2 %) planetary nebulae
- 7 (4.2 %) objects of unknown or composite physical nature

As can be seen, almost the entire sample is identified by spectroscopic IDs. For a comparison of these results with similar studies from literature see Chapter 8.4.

The magnitude and redshift distribution of the optical counterparts of our sample are shown in Figs. 43 and 44. The optical B magnitudes range from 13.6 mag (NGC 6552, a large Sb-galaxy with a Seyfert2-type spectrum) to and beyond the plate limit of the Tautenburg Schmidt plates at approx. 21.5 mag; as expected, most counterparts are faint ($B > 18$ mag). As for redshift, most sources have $z < 0.5$, all but one source have $z < 2.2$; the source with the highest redshift of $z = 4.32$ is 2RXP J175930.1+663848 / RX J1759.4+6638 (from Henry et al. 1994) which is situated within our survey area but, with $I = 20.1$, $B > 21.9$, too faint to be visible on the Tautenburg Schmidt plates.

The completeness of the X-ray sample has already been discussed in Chapter 2.3 (see also Fig. 6). In short, the sample is complete down to a limit of 0.05 cts/sec (the sensitivity limit of the RASS BSC), is mostly complete down to a limit of 0.01 cts/sec, but, due to the used selection criteria, also contains sources very much fainter than that, down to fluxes fainter than 0.001 cts/sec.

Regarding possible optical extension of the counterparts, we also checked for an unusual proportion of extended sources among the X-ray counterparts (excluding, of course, galaxy clusters), finding none (see Fig. 45).

8.3 Variability of optical counterparts

After variability analysis of the optical data was performed on all scanned fields as described in Chapter 7 (see especially Fig. 33), objects with large χ^2 ($\chi^2 \geq 2$, with slight variations on the limit, depending on the overall quality of the scatterplot in an individual field) were flagged as variable. Additionally, a search for objects with flares was performed by checking the scatterplots and lightcurves of known

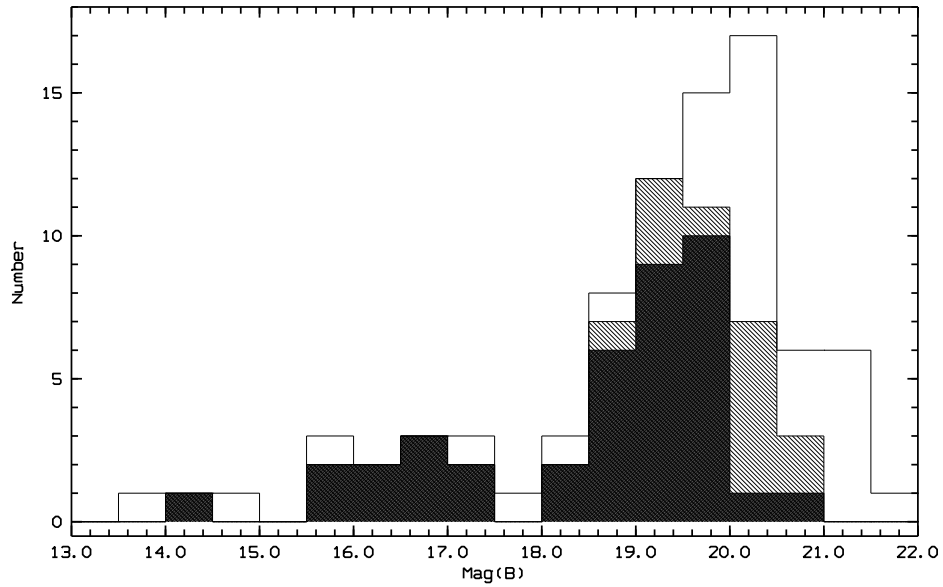


Figure 43: Magnitude distribution (B magnitude) of extragalactic X-ray counterparts, for X-ray point sources (i.e. excluding stars and galaxy clusters). The hatched areas show the portion of sources with confirmed optical variability (dark hatching) and probable optical variability (light hatching).

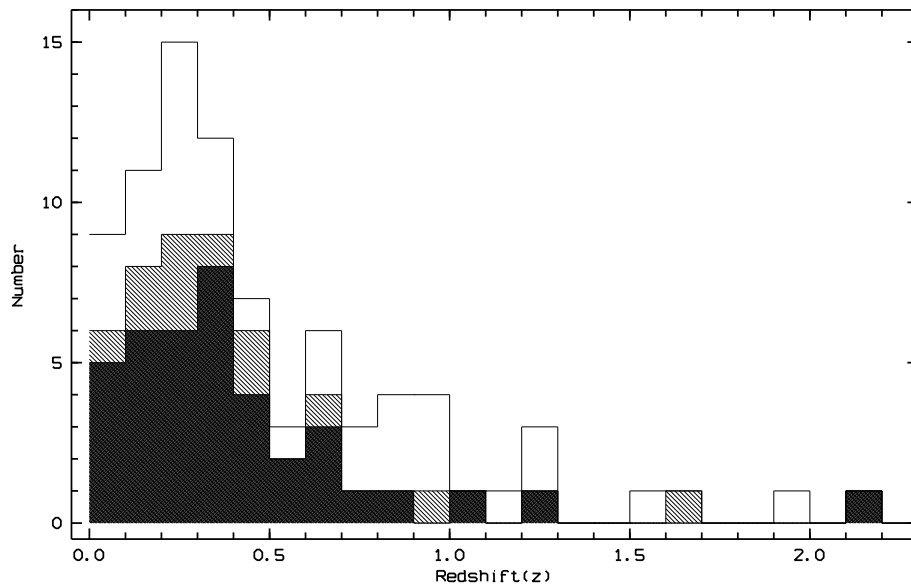


Figure 44: Redshift distribution of extragalactic X-ray counterparts, for point sources (i.e. excluding galaxy clusters). The hatched areas show the portion of sources with confirmed optical variability (dark hatching) and probable optical variability (light hatching). One QSO (2RXP J175930.1+663848) with $z = 4.32$ is not contained in this histogram because of its outstanding high redshift.

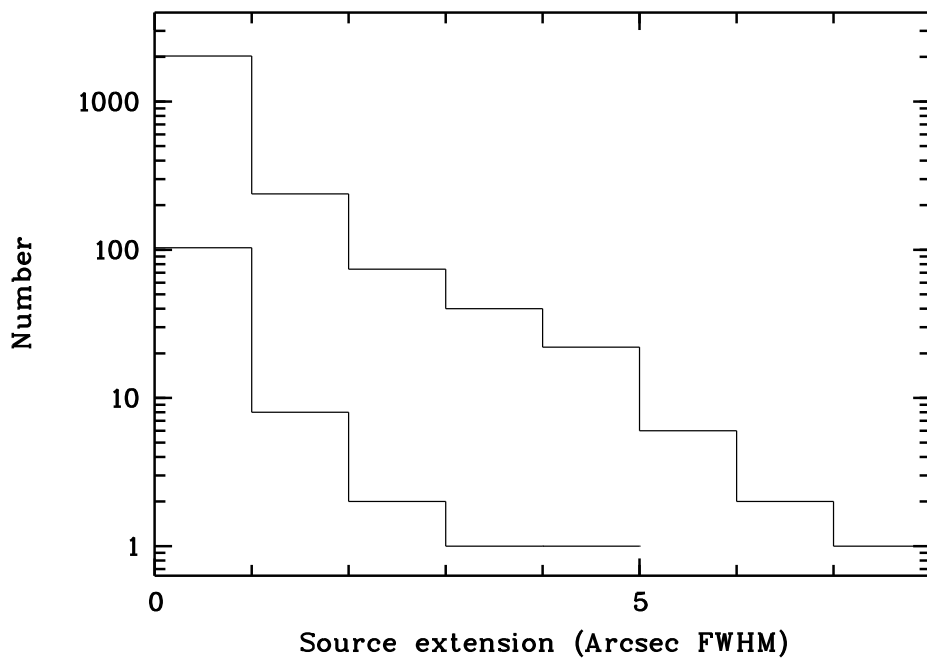


Figure 45: Histogram of source extensions, for all objects measured on the Tautenburg Schmidt plates (upper graph; bright galaxies excluded) and for the X-ray counterparts only (lower graph; galaxy clusters excluded). There is a small population of extended X-ray counterparts but in general X-ray counterparts are not more extended than "normal" objects.

or suspected X-ray counterparts visually (however, no flare object was found that was not already flagged by its χ^2). In Table 3 all variable objects are flagged, and the mean brightness of the optical counterpart and the measured χ^2 is also noted.

For some objects, additional optical data from the literature were available. This includes time-resolved photometric data for bright QSOs (e.g. KAZ 102) and Hipparcos/Tycho lightcurves for bright stars; two prominent examples are mentioned and discussed in Chapter 7.5.4. The availability of Hipparcos/Tycho data is mentioned in Appendix E where applicable.

The lightcurves of all variable objects are included in Appendix F. Additionally, a "hall of fame", containing the most striking examples of variable objects, is shown in Figs. 47 to 57. Shown are 8 AGN, one dMe-star with flares, one cataclysmic variable, and one variable star with a Mira-like lightcurve; please note that the Mira star is **not** a RASS X-ray source but was found serendipitously.

As was hoped, a large fraction of optically variable objects could be found among the X-ray counterparts. Regarding the individual classes of variable X-ray counterparts, we find – at the level of photometric precision as shown in Fig. 39 and with a timebase of 30 month –

- out of 79 AGN
 - 37 (47 %) with confirmed variability
 - 10 (13 %) with probable variability
 - 22 (28 %) not variable within the given measurement accuracy
 - 10 where no statement is possible.
- out of 47 stars (confirmed and highly probable counterparts)
 - 8 (17 %) with confirmed variability
 - 5 (11 %) with probable variability
 - 18 (38 %) not variable within the given measurement accuracy
 - 16 where no statement is possible.

In general, X-ray counterparts are found to be significantly more optically variable than the general population of objects found on the Schmidt plates (see Fig. 46). In a related representation, Figs. 43 and 44 show the distribution of variable extragalactic objects over optical magnitude and redshift.

Looking at the probability of variability, the lightcurves, and at the manner of variability of the different classes of objects, the following observations can be made:

- For stars as X-ray counterparts, a significant proportion (17 % with confirmed / 11 % with probable variability) of objects shows optical variability. Irregular, fast variability with risetimes on the order of days strongly dominates. There is just one object (1RXS J173804.9+650933, an M-star) out of the 8 stars with confirmed variability where the lightcurve possibly shows

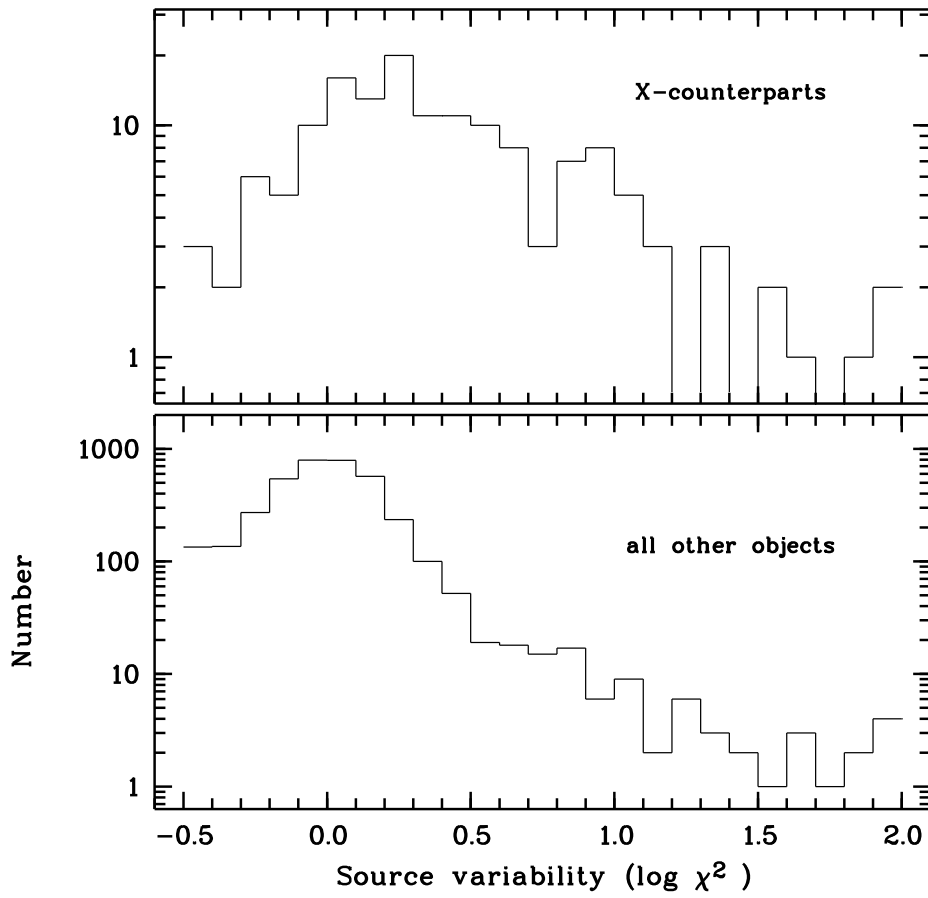


Figure 46: Histogram of source variability, for the X-ray counterparts only (upper diagram) and for all remaining objects measured on the Tautenburg Schmidt plates (lower diagram). There is a distinct population of variable objects among the X-ray counterparts. In general, variability is more common (or more pronounced) among the X-ray counterparts.

trend-like or long-term variability; however, the trends are not very pronounced.

As most stars which are X-ray counterpart are rather bright ($B = 12 - 15$ mag), the restrictions concerning photometric precision for bright stars as detailed in Chapter 7.5.2 apply.

- For the AGN among our X-ray counterpart, variability seems to be the rule, with almost two thirds of the objects showing confirmed or probable variability where a statement is possible at all. Indeed, it seems highly likely that with a longer timebase or improvements in the photometric precision this proportion would still increase.

Regarding the manner of variability, all objects show irregular variability, with observed risetimes from several days to hundreds of days; an analysis of the structure functions (see de Vries et al. 2003, Giveon et al. 1999, Hughes et al. 1992) of the optical variability as derived from the lightcurves would be needed to put this onto a more quantitative footing.

- Of the two BL Lacs in our sample, one is too faint for reliable photometry, and the other one shows probable but not confirmed variability. Anyway, the sample size of two objects allows no sensible comparisons or predictions.

We may compare our results with those of Cristiani et al. (1990), where 33 % of the studied QSOs turn out to be variable on a timebase of 7 years and 20 % variable on 2 years timebase. These considerably lower numbers compared with our findings reflect the differences in the precision of the surveys and in the photometric techniques.

8.4 Comparison with similar studies from the literature

As described in Chapter 1.4, the identification contents of an X-ray selected source sample depends mainly on galactic latitude of the sample's sky area and on the spectral response of the X-ray telescope. In this chapter we compare available works with our findings.

For the Einstein observatory extended medium sensitivity survey (Stocke et al. 1991), a composition of

- 51.1 % AGN
- 25.8 % galactic stars
- 12.2 % galaxy Clusters
- 4.3 % BL Lac objects
- 2.1 % normal galaxies
- 0.6 % cooling flow galaxies
- (3.9 % unidentified objects)

was found from identification of a sample of 835 X-ray sources, from analysis of 1435 IPC fields with a galactic latitude $|b| > 20^\circ$. The used telescope / detector (imaging proportional counter, IPC) combination, with an energy range from 0.4 – 4 keV, has a somewhat harder spectral response than the ROSAT telescope.

For the ROSAT north ecliptic pole survey (Henry et al. 2001, Gioia et al. 2003), the corresponding numbers were

- 49.0 % AGN
- 34.3 % stars
- 14.4 % galaxy clusters
- 1.8 % BL Lac
- 0.2 % galaxies
- 0.2 % planetary nebulae
- (0.4 % unidentified objects)

from a sample of 445 X-ray sources, observed in a contiguous sky area of 80.7 degrees square around the NEP, i.e. at high galactic latitude. The used telescope / detector combination is identical to the one used in our work, and the sample sky area is also very similar, embracing the area used in our survey; the survey area is more than double that of ours. Most (but, due to the different methods of source selection, not all !) of the objects from our source list are also contained in the ROSAT NEP survey. However, the purpose of this survey is somewhat different, being more focused on the detection of X-ray selected galaxy clusters and the cosmological implications of their properties.

In a different work from Zickgraf et al. (1997), Appenzeller et al. (1998) and Krautter et al. (1999), where RASS (i.e. ROSAT) sources in six study area with different galactic latitude were identified, the corresponding identification numbers were

- 42.1 % AGN (37.6 % QSOs, Seyfert galaxies and LINERS, 4.5 % BL Lac)
- 40.7 % stars
- 11.6 % galaxy clusters
- 3.9 % galaxies
- (1.7 % unidentified objects)

from a total of 674 sources. The basic observational data are identical to the one used by us; however, there is no overlap in sky area, and there are no "shared" sources with our work.

Comparing these proportions with the numbers found for this work in Chapter 8.1 and keeping in mind the restrictions and selections done and the differences in X-ray passband and galactic latitude of the source samples, we find no significant differences, nor did we expect to.

8.5 Discussion of individual objects

In this chapter, some objects of special interest or objects where additional information seems useful will be discussed in more detail.

1RXS J173627.2+682031 This bright B=10.7 mag star may be variable but no suitable comparison stars for differential photometry are available within the field. Because of this, the reduced χ^2 can not be relied on. However, special processing for bright stars makes variability at least possible, and time-resolved Hipparcos/Tycho data is available.

1RXS J173804.9+650933 M-Star, B=16.7 mag, X-ray flare variability was detected during RASS (see Fuhrmeister and Schmitt 2003); the counterpart is also optically variable, and the lightcurve is available in Appendix F. This object is the only star among the optically variable X-ray counterparts that seems to show long-term variability.

1RXS J173955.8+650007 SAO 17595, a bright variable star, B=9.33 mag, spectral type K0, with high proper motion. X-ray trend variability was detected during the RASS (see Fuhrmeister and Schmitt 2003). No variability data is available from this work, as the field was not scanned due to the brightness of the X-ray counterpart. However, time-resolved Hipparcos data is available, and the star is flagged as variable in the Hipparcos catalog.

1RXS J174609.6+673721 The X-ray counterpart, the bright Seyfert1 AGN MS1746+6738, is located on a spike and diffraction pattern of a nearby bright (B=10.0 mag) star. No reliable photometry or variability analysis is possible.

1RXS J174726.8+662628 An AGN at $z=0.1391$. See notes in Gioia et al. (2003): The galaxy south of the X-centroid is also an AGN at the same redshift and could possibly contribute to the X-ray emission.

1RXS J174838.8+684211 MRK507, a narrow-line Seyfert-1 galaxy with permitted FeII-lines, at $z=0.559$. The source is blended with a second object at a separation of 2", just visible on the best Tautenburg Schmidt plates (seeing 2.1"). Regarding the nature of the companion, there is some confusion in the available literature. While Halpern and Oke (1987) maintain that the companion is a star with spectral type G, Gioia et al. (2003) found H α emission lines in a spectrum of the companion, with z close to the redshift of the primary, which would make it a companion AGN or at least a companion galaxy.

1RXS J175713.9+654702 A dMe-star, with magnitude B=16.8 mag; spectrum kindly provided by A. Schwope (AIP). A nearby AGN could also contribute to the X-ray emission (see Gioia et al. 2003).

1RXS J175801.0+640932 SAO17709, a bright star with B=11.2 mag and spectral type G. X-ray flare variability was detected during the RASS (see Fuhr-

meister and Schmitt 2003). The Schmidt plate data do not show optical variability, and the star is not flagged as variable in the Tycho catalogue.

1RXS J180009.9+683557 This blue $B = 14.5$ mag star, also known as KUV 18004+6836 or WD 1800+686, of type sdO, is possibly variable. The evidence is not conclusive: The in-field comparison indicates variability, but the photometric measurements of the X-ray counterpart are slightly disturbed by a nearby, bright extended galaxy (MCG +11-22-020).

Although it may seem unlikely for a white dwarf to show optical variability, there are several examples from Fuhrmeister and Schmitt (2003) where white dwarfs show variability in the X-ray domain, the most likely reasons being companion stars (i.e. the white dwarf is a member of a double star system) or dark spots on the surface of the white dwarf. Further investigations into the nature of the variability of this object therefore seem indicated.

1RXS J180216.3+641546 G227-22, a dMe star with $B=15.0$ mag, with high proper motion. X-ray flare variability was detected during the RASS (see Fuhrmeister and Schmitt 2003). The optical data show an outburst by more than 1.2 mag with a rise time of less than a day on MJD 48540 (Oct. 1991).

1RXS J180328.4+673806 Kaz 102, a well-known variable bright (mean brightness $B=15.6$ mag) Seyfert 1 at $z = 0.136$. For time-resolved multifrequency photometric data see Treves et al. (1995).

1RXS J180413.4+675412 A cataclysmic variable, EX Dra, very strongly variable, with a magnitude range of $B=13.4$ mag down to 17.2 mag.

1RXS J180606.7+681308 This source has been identified as a combination of a galaxy cluster with an AGN (Gioia et al. 2003). Four out of six galaxies with spectra are emission-line galaxies, one with broad emission lines. However, at the position given in Gioia et al. (2003) ($18^{\text{h}}06^{\text{m}}4.8^{\text{s}} +68^{\circ} 13'8''$, J2000) for this object, nothing can be found on DSSII finding charts or Tautenburg Schmidt plate images. We identify the broad emission line galaxy with the nearest object found at $18^{\text{h}}06^{\text{m}}4.8^{\text{s}} +68^{\circ} 13'16''$, i.e. $8''$ away. This object, designated 1RXS J180606.7+681308a in our object list, with a mean brightness of $B=20.4$ mag, is also slightly variable with $\chi^2 = 2.1$. Somewhat brighter and more variable is the object 1RXS J180606.7+681308b, with a mean brightness of $B=19.6$ mag and with $\chi^2 = 3.7$.

1RXS J180643.4+682200 A blend of two stars ($B=14.7$ mag / 17.4 mag), with $4.7''$ separation. The position angle between the probable X-ray source, the brighter star, and the nearby star has been changing between DSSI and DSSII / Tautenburg Schmidt plates. However, no further information from SIMBAD or from the literature is available.

1RXS J180849.9+663431 A bright ($B=16.9$ mag), radio-loud AGN with broad emission lines, at $z = 0.697$. Our results provide a nice lightcurve.

- 1RXS J180930.2+662033** A faint (B=19.9 mag), slightly variable AGN at $z=0.635$. A nearby K-star (B=20.7 mag) is also a possible X-ray counterpart or contributor.
- 1RXS J181341.6+673150** This source has been identified as an AGN with broad emission lines in Gioia et al. (2003); the optical counterpart is found not to be variable in our survey. However, when looking at the X-ray contour plots from the RASS data (see Mullis 2003, object RXJ1813,6+6731), it seems unlikely that this object is responsible for the X-ray emission alone. The X-ray emission seems to consist of 3-4 components, and the stronger components are not centered on the object identified as X-ray counterpart; there is no obvious counterpart for the strongest component. Additionally, many faint galaxies are visible on the DSSII-R finding charts, which could be a sign of a faint galaxy cluster.
- 1RXS J181345.6+662849** The X-ray counterpart, a faint B=20.6 mag M-star, is located near a spike and diffraction pattern of a nearby bright (B=8.4 mag) star; no reliable photometry or variability analysis is possible.
- 1RXS J181348.3+683121** This source has been identified with a bright star (B=12.1 mag) in Gioia et al. (2003). However, when looking at the RASS X-ray contour plots, a galaxy at 18h13m27,4s;+68° 30'34", found not to be optically variable, seems to be the more likely optical counterpart.
- 1RXS J181353.7+642348** HD168151, a bright star with B=5.4 mag and spectral type F5V. X-ray flare variability was detected during the RASS (see Fuhrmeister and Schmitt 2003). No variability data is available from this work, as the field was not scanned due to the brightness of the X-ray counterpart. However, time-resolved Hipparcos data is available; the star is not flagged as variable in the Tycho catalog.
- 1RXS J181829.0+674127** HS 1818+6740, a bright (mean B=16.8 mag) blue QSO at $z=0.314$. X-ray trend variability was detected during the RASS (see Fuhrmeister and Schmitt 2003). The optical lightcurve shows a clear increase in brightness by about 0.15 mag, around MJD 48400, with a rise time of about 100 days.
- 1RXS J181857.3+661135** G258-33, a dMe / flare star. The optical position given in Gioia et al. (2003) is probably incorrect.
- 1RXS J181955.5+663619b** A star, B=14.8 mag, also detected as VLA radio source VLA-NEP J1820.0+6636; see Brinkmann et al. (1999).
- 1RXS J182157.4+642051** 1E 1821+64.3, a bright (B=14.2 mag) QSO at $z = 0.297$. For time-resolved multifrequency photometric data see Ulrich et al. (1992).
- 1RXS J182215.8+640307** Possibly a faint cluster. Several galaxies are visible on DSSII-R, one redshift measurement is available (see Tripp et al. 1998)

1RXS J182431.5+634956 Possibly a star; the NORAS position (Böhringer et al. 2000) of this counterpart is probably incorrect – no object is found at the given position on DSSII or Tautenburg stacked plates. Identification and position are taken from Gioia et al. (2003).

1RXS J182447.0+650924 There is some confusion regarding the physical nature of the X-ray counterpart. Two candidates, with a separation of 5" and with mean magnitudes of 16.3 mag and 18.8 mag, are found at the position of the X-centroid. The brighter candidate is identified in different works as a stellar blue-excess object with H-dominated spectrum (KUV 18246+6508, see Wegner and McMahan 1988; this identification also seems to be taken up by Gioia et al. 2003) and alternatively as an AGN with $z=0.303$ (HS 1824+6507, see Engels et al. 1998, Jaunsen et al. 1995). Since the object is also optically variable in a manner typical of AGN and because the near companion introduces the possibility of confusing the AGN with a star, we assume the counterpart to be an AGN. Furthermore, the spectrum published in Engels et al. (1998) helps to disperse any remaining doubts.

1RXS J182932.3+690509 A bright, $B=12.9$ mag star. The X-ray contour plot from Mullis (2003) makes a faint non-variable object with $B=20.4$ mag south of the bright star also look like a probable counterpart.

1RXS J182943.5+674910 A faint, formerly unknown variable AGN with broad emission lines (identified in Gioia et al. 2003), with $B=19.9$ mag and $z=0.4783$. The optical variability is not pronounced, with the lightcurve showing a faint start at the beginning of the optical observations, a prolonged brightness plateau about 0.3 mag brighter during the greater part of the optical observations and a fast fading by about 0.4 mag at the end of the observations, with a fading time of about 10 days. Fuhrmeister and Schmitt (2003) report a periodic variability in X-ray from RASS data, with a period of 476.2 h. However, there is no evidence of this period when folding the optical data.

V J181958.6+652023 This variable object, a small galaxy with a bright core, was found as a counterpart to an X-ray source from an intermediate X-ray source list. However, the source is not contained in the final source lists, so it should be treated as a serendipitous discovery of a variable object, but not as an X-ray counterpart. Because of the variability, the identification as an AGN is quite probable.

IY Dra This variable star was serendipitously found within the field of 1RXS J182320.1+641924; it is not a RASS X-ray source. It is strongly variable, with a magnitude ranging from more than $B=14$ mag to below detection limit of the Schmidt plates, at 20.9 mag, and with a period of about 400 days.

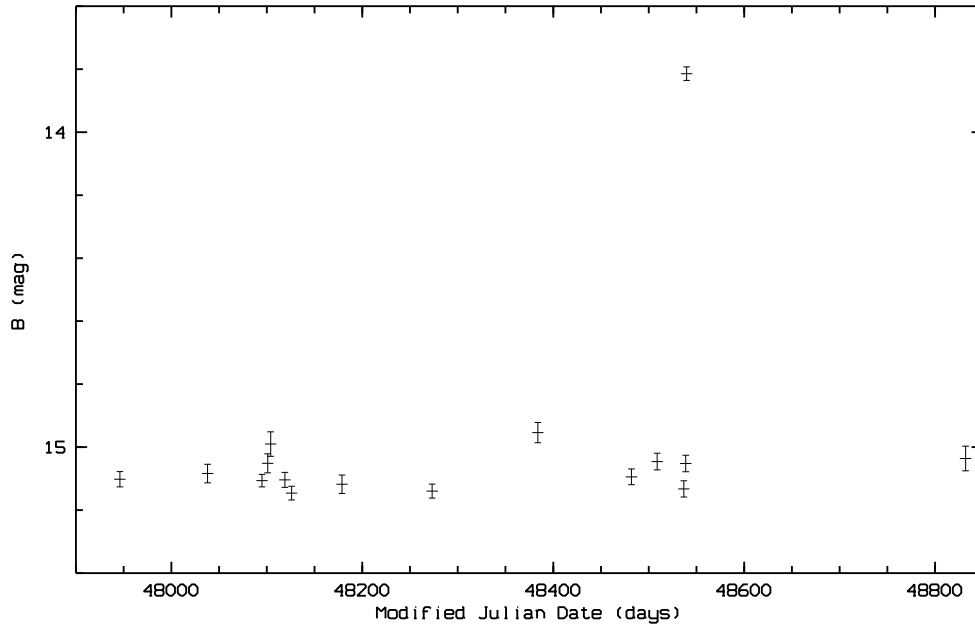


Figure 47: Lightcurve of 1RXS J180216.3+641546 / G227-22, a dMe-star, with one large and one small optical flare

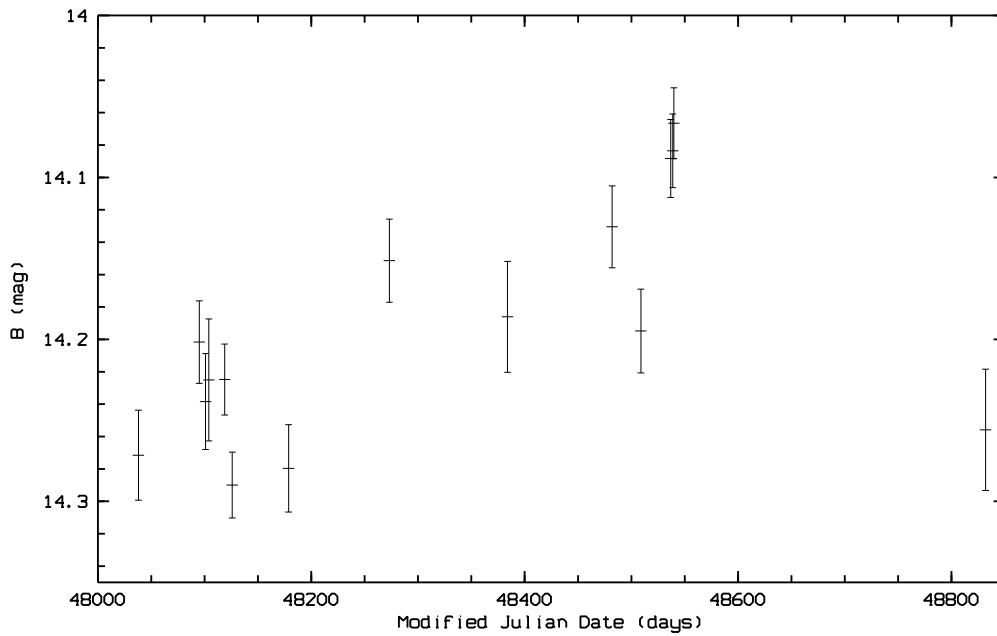


Figure 48: Lightcurve of 1RXS J182157.4+642051 / 1E 1821+64.3, a bright variable QSO

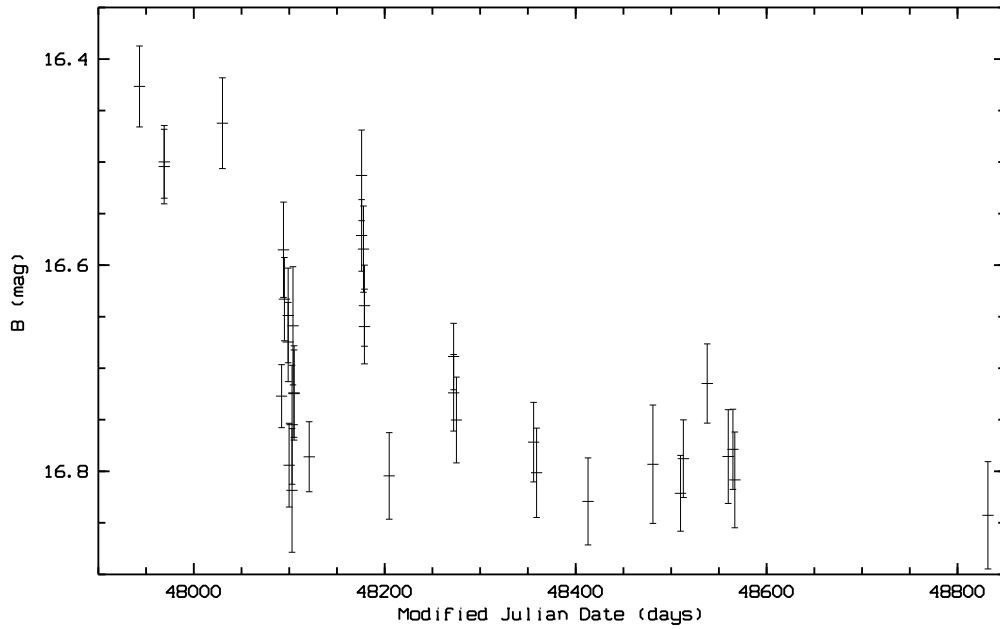


Figure 49: Lightcurve of 1RXS J175505.8+651951 / IPC17549.6521, a small Sab galaxy with a variable core

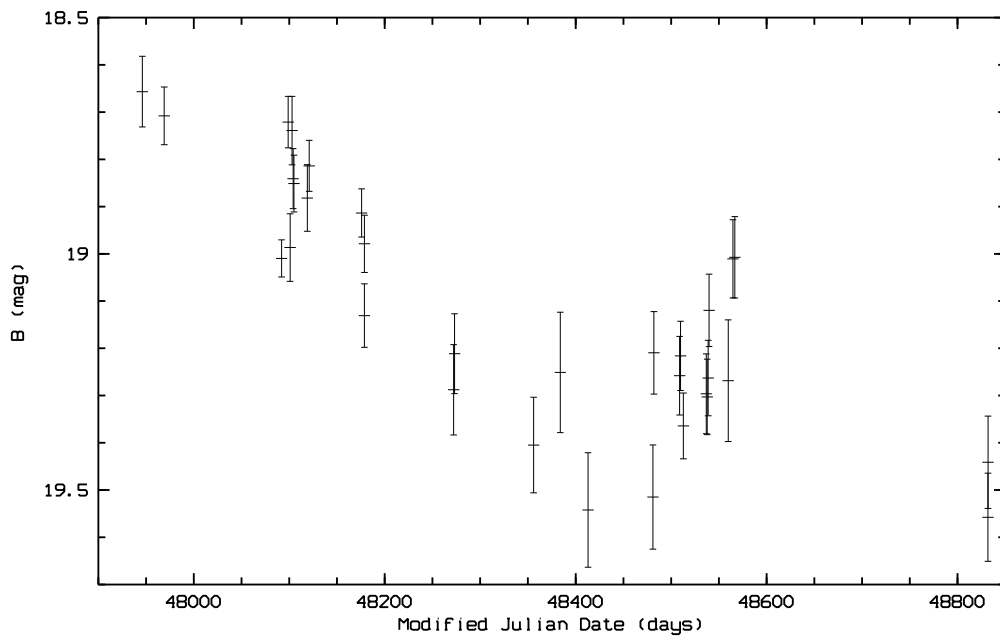


Figure 50: Lightcurve of 1RXS J180026.2+635719, a strongly variable AGN at $z = 0.6828$

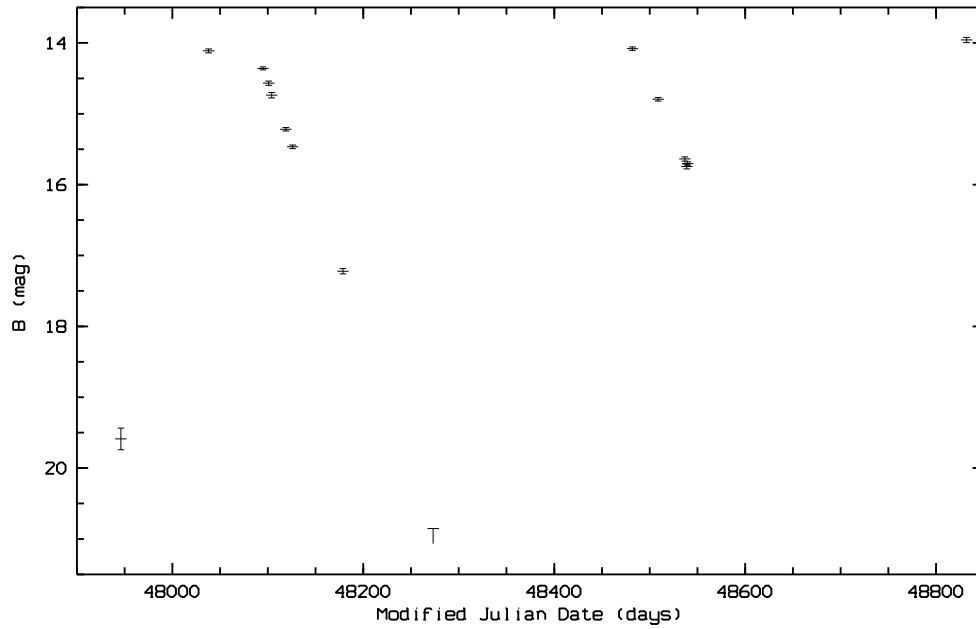


Figure 51: Lightcurve of IY Dra, a strongly variable star found serendipitously; this star is *not* a RASS X-ray source

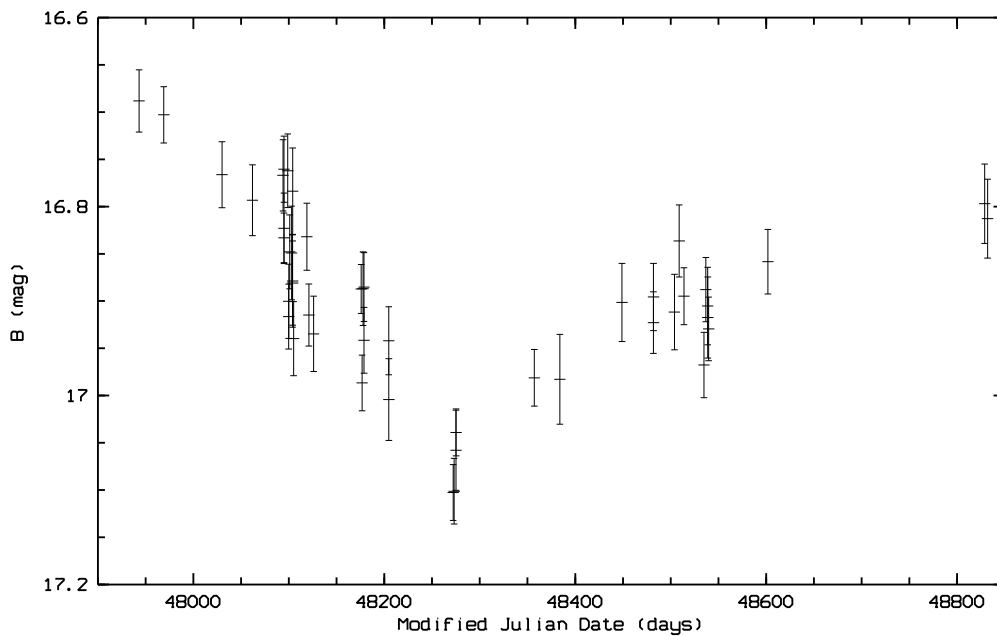


Figure 52: Lightcurve of 1RXS J180849.9+663431, a radio-loud AGN with broad emission lines at $z = 0.697$

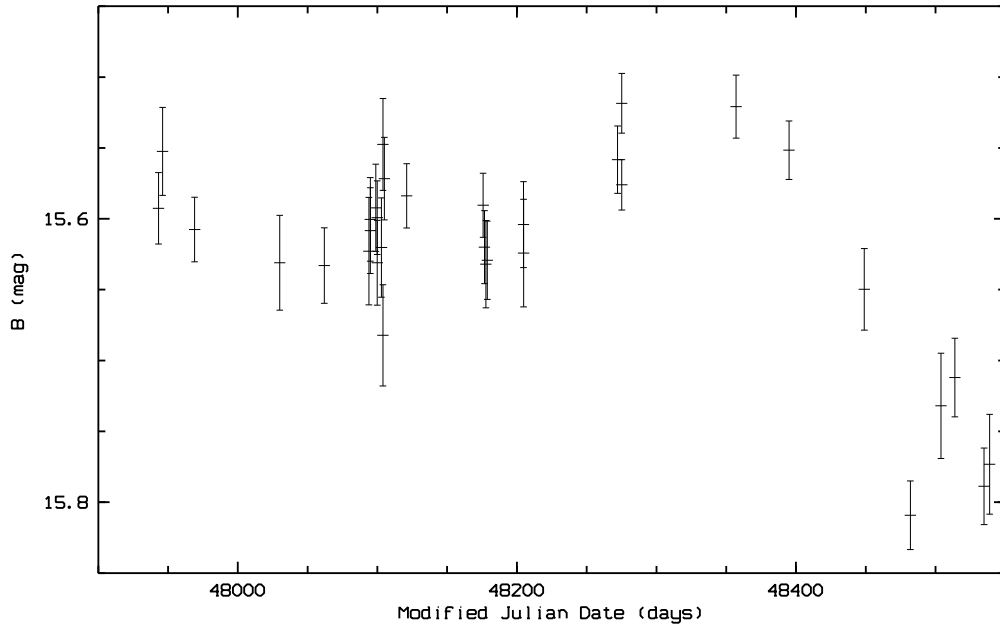


Figure 53: Lightcurve of 1RXS J180328.4+673806 / Kaz 102, a bright Seyfert1-galaxy

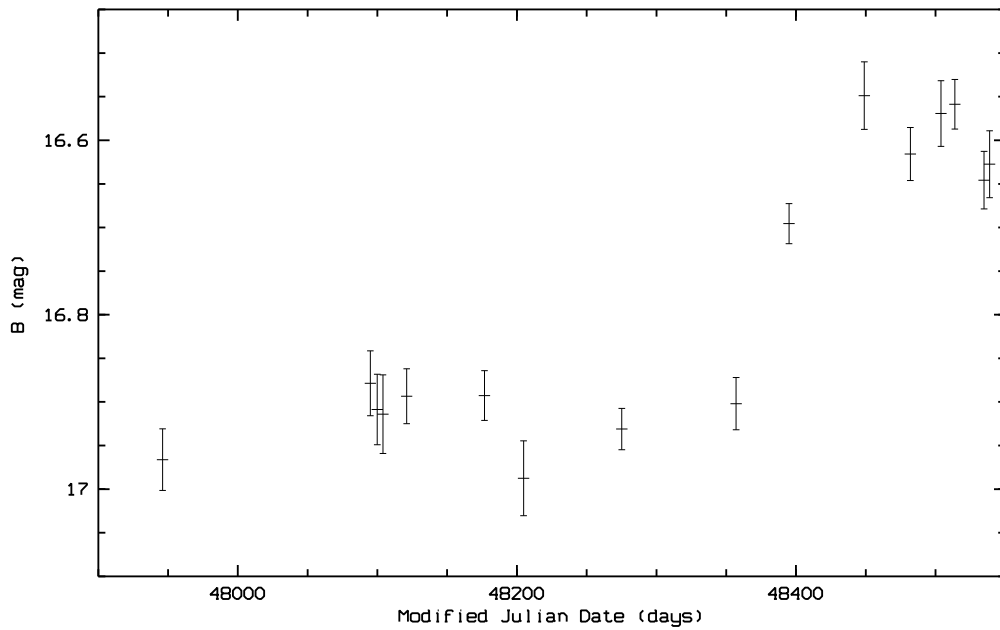


Figure 54: Lightcurve of 1RXS J181829.0+674127 / HS 1818+6740, a bright QSO which is also variable in the X-ray domain

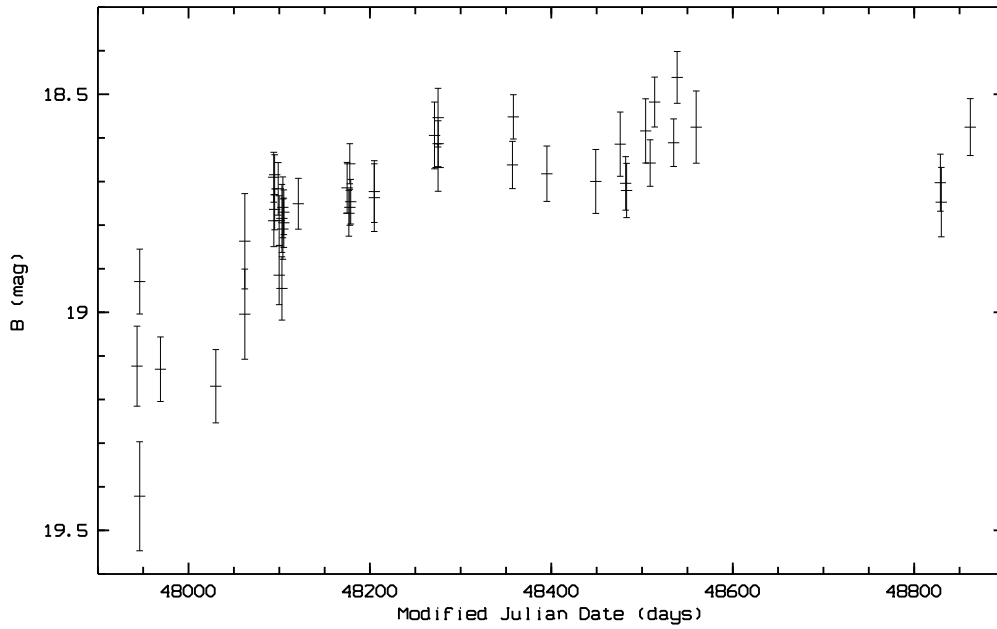


Figure 55: Lightcurve of 1RXS J175813.2+674319, an AGN with broad emission lines at $z = 0.2045$

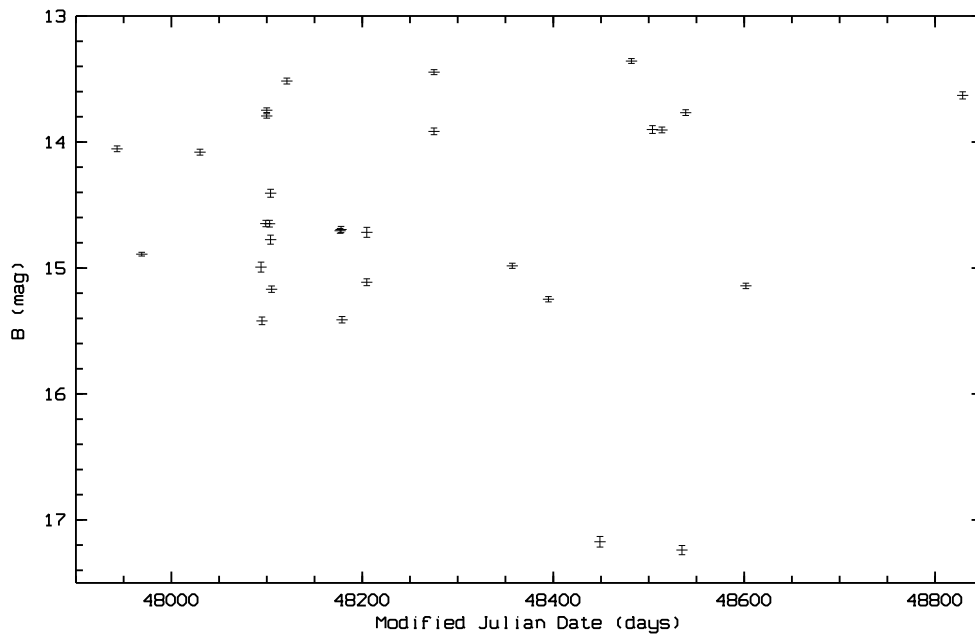


Figure 56: Lightcurve of 1RXS J180413.4+675412 / EX Dra, a cataclysmic variable

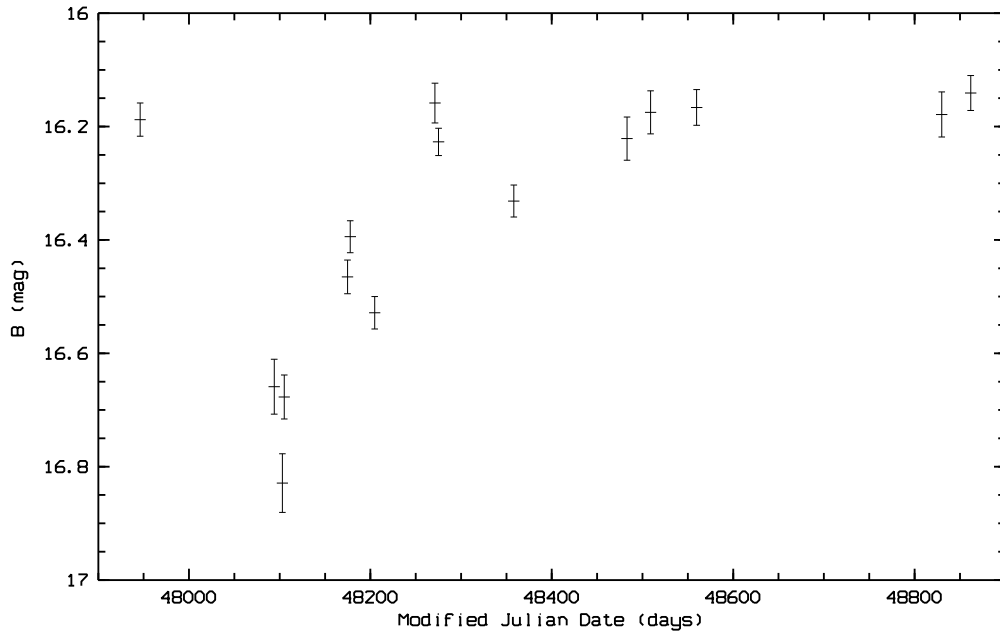


Figure 57: Lightcurve of 1RXS J174700.3+683626 / Kaz 163, a narrow-line Seyfert1-galaxy at $z = 0.63$

9 Outlook

This chapter is mainly a list of items that have **not** been performed in this work, the main reason being time. Among them, improvements in the photometric techniques and a continuation of the study of the physical parameters of the identified variable sources are the most obvious ones.

9.1 Further improvements in photometry and variability analysis

Although the average star density is low in our fields and stars normally are not disturbed by near neighbours, close blends, i.e. with stars lying so close to each other that their profiles overlap at least partially, do occur. The chosen approach to deal with close blends, namely to reject disturbed areas for the profile calculation (see Chapter 5.4) in order to minimize the effects on the photometric results, has not proven really successful for close blends, and a way to estimate the disturbances due to neighbouring stars, depending on separation and brightness pairings, had to be devised (see Chapter 7.4). More advanced techniques that attempt to iteratively model the individual contributions to the total (blended) profile should be tried, see e.g. Stetson (1987).

In addition, for *really* close blends where the elimination of disturbed areas leaves too little undisturbed remaining area for the profile measurements (and even the more advanced techniques may have difficulties in unraveling the contributions), it may make more sense to be content to measure the total flux. That way, the apparent variability induced in both contributors by varying decomposition of the blended profiles into two contributors is eliminated, and at least non-variable blends can be identified.

The problems introduced into the fit process by the presence of bright stars within the fields have been discussed in Chapter 7.5.2. To overcome these problems, further studies into new transformation and weighting techniques seem indicated.

The use of the arithmetic mean to calculate the average magnitude of an object is not the ideal choice for weak objects near the detection limit of a plate. Here more advanced techniques using "survival statistics" (Feigelson and Nelson 1985, Isobe et al. 1986) or Monte Carlo simulations are needed to prevent an overestimation of the mean magnitude and an underestimation of the degree of variability.

As a method to find and parametrize the optical variability of X-ray counterparts, the plain χ^2 -criterion has been used, in conjunction with a careful evaluation and visual checks of the scatterplots of the individual fields. However, more refined methods like the KS(Kolmogorov-Smirnov)-test are available and could be used.

9.2 Physical parameters of the extragalactic NEP X-ray sources

As for the physical parameters of the observed AGN, only fundamental observable properties like redshift and optical magnitude have been observed or collected from other works. An obvious next step is the calculation of intrinsic physical

parameters like X-ray luminosity and absolute magnitude. To parametrize the time-related properties of the optical variability, the structure function (see de Vries et al. 2003, Giveon et al. 1999, Hughes et al. 1992) should be calculated.

Using these data, correlations between e.g. redshift, absolute magnitude and structure function properties should then be studied.

9.3 Using time-resolved X-ray data

Much hope was set on correlating the time-resolved X-ray data that were available from the RASS with the time-resolved optical observations that are described in this work. However, due to technical difficulties arising in the variability and flux analysis of the X-ray data, almost nothing of this has proved possible.

The problems are partly due to the reduction software (more precisely: the used EXSAS procedures), partly to the ROSAT survey geometry and the peculiarities of small number counting statistics ("survivor statistics") and are described in detail in Fuhrmeister and Schmitt (2003). The sad result is that the reliability and precision of the X-ray variability analysis suffers greatly in the vicinity of the poles of the ecliptic, exactly the regions where the RASS coverage is deepest and longest. Although a solution to these problems should be possible, no attempt has yet been made. A collaboration with MPE scientists was envisaged when this project was initiated. In spite of the delays on both sides, the synthesis of the scientific results of the optical and the X-ray studies is still a desirable goal.

In this work I have provisionally compared the variability properties of sources in X-rays and of their counterparts in the optical domain, looking for objects that are variable in both bands. As the precision and granularity of the X-ray variability data is very restricted and mainly consists of a statement if the source is variable according to a certain set of search algorithms (no brightness, no timescales, no degree of variability), some improvement would clearly be needed.

A considerable number of the sources has not only been observed in the RASS, but also in pointed observations. However, extended time coverage is available only for a few sources, and only a very limited X-ray variability analysis would be possible using pointed observations.

9.4 A closer look at interesting objects

Now that the optical variability properties of a large set of X-ray selected AGN at the NEP have been studied, it is possible to point out objects where further studies seem especially valuable.

This includes the bright, strongly variable and already well studied sources Kaz 163 (1RXS J174700.3+683626), Kaz 102 (1RXS J180328.4+673806) and 1E 1821+64.3 (1RXS J182157.4+642051). The bright (B=16.8m) source HS 1818+6740 (1RXS J181829.0+674127) however, which is strongly variable in the optical domain and is also found to be variable in the X-ray domain – and is thus ideally suited for correlated X-ray and optically variability studies, including studies of the accretion region using "reverberation mapping" – seemingly has not attracted much attention so far. Equally, the slightly fainter and less variable but

more distant ($z=0.697$) source 1RXS J180849.9+663431 seems a good target for further variability studies.

By an analysis of the absolute magnitudes and the variability structure function (i.e. variability timescales) of all variable objects from our source list, even more interesting objects which would merit further studies could be found by selecting objects with out-of-the-ordinary properties (e.g. especially small or large absolute magnitudes, especially fast or slow variability timescales).

A Bibliography

References

- Antonucci, R. (1993). Unified models for active galactic nuclei and quasars. *ARA&A*, 31:473–521.
- Appenzeller, I., Thiering, I., Zickgraf, F.-J., Krautter, J., Voges, W., Chavarria, C., Kneer, R., Mujica, R., Pakull, M., Rosso, C., Ruzicka, F., Serrano, A., and Ziegler, B. (1998). Identification of a Complete Sample of Northern ROSAT All-Sky Survey X-Ray Sources. III. The Catalog. *ApJS*, 117:319–+.
- Appenzeller, I., Zickgraf, F.-J., Krautter, J., and Voges, W. (2000). Identification of a complete sample of northern ROSAT all-sky survey X-ray sources. VII. The AGN subsample. *A&A*, 364:443–449.
- Argyle, R. W., Morrison, L. V., Irwin, M. J., and Bunclark, P. S. (1991). Photographic astrometry of radio stars. *MNRAS*, 250:576–580.
- Ashby, M. L. N., Hacking, P. B., Houck, J. R., Soifer, B. T., and Weisstein, E. W. (1996). A Massive $Z = 0.088$ Supercluster and Tests of Starburst Galaxy Evolution at the North Ecliptic Pole. *ApJ*, 456:428–+.
- Becker, R. H., White, R. L., and Edwards, A. L. (1991). A new catalog of 53,522 4.85 GHz sources. *ApJS*, 75:1–229.
- Böhringer, H. (1992). Private communication. Target lists and Identification data for NEP X-ray sources.
- Böhringer, H., Voges, W., Huchra, J. P., McLean, B., Giacconi, R., Rosati, P., Burg, R., Mader, J., Schuecker, P., Simić, D., Komossa, S., Reiprich, T. H., Retzlaff, J., and Trümper, J. (2000). The Northern ROSAT All-Sky (NORAS) Galaxy Cluster Survey. I. X-Ray Properties of Clusters Detected as Extended X-Ray Sources. *ApJS*, 129:435–474.
- Boller, T., Voges, W., Dennefeld, M., Lehmann, I., Predehl, P., Burwitz, V., Perlman, E., Gallo, L., Papadakis, I. E., and Anderson, S. (2003). 1ES 1927+654: Persistent and rapid X-ray variability in an AGN with low intrinsic neutral X-ray absorption and narrow optical emission lines. *A&A*, 397:557–564.
- Bower, R. G., Hasinger, G., Castander, F. J., Aragon-Salamanca, A., Ellis, R. S., Gioia, I. M., Henry, J. P., Burg, R., Huchra, J. P., Böhringer, H., Briel, U. G., and McLean, B. (1996). The ROSAT North Ecliptic Pole Deep Survey. *MNRAS*, 281:59–70.
- Briel, U. G., Aschenbach, B., Englhauser, J., Freyberg, M., Hasinger, G., Gruber, R., Hippmann, H., Pfeffermann, E., Predehl, P., Schmitt, J. H. M. M., Schwentker, O., Voges, W., Zimmermann, U., George, I. M., Snowden, S. L., Turner, T. J., David, L., Harnden Jr., F. R., Kearns, K. E.,

- Zombeck, M. V., Barstow, M. A., Osborne, J. P., Pye, J. P., Watson, M., West, R. G., and Willingale, R. (1997). ROSAT User's Handbook. URL <http://wave.xray.mpe.mpg.de/rosat/doc/ruh>.
- Brinkmann, W., Chester, M., Kollgaard, R., Feigelson, E., Voges, W., and Hertz, P. (1999). Radio-loud ROSAT sources near the North Ecliptic Pole. *A&AS*, 134:221–240.
- Brunzendorf, J. and Meusinger, H. (1999). The galaxy cluster Abell 426 (Perseus). A catalogue of 660 galaxy positions, isophotal magnitudes and morphological types. *A&AS*, 139:141–161.
- Brunzendorf, J. and Meusinger, H. (2001). A QSO survey via optical variability and zero proper motion in the M 92 field. I. QSO candidates and selection effects. *A&A*, 373:38–55.
- Brunzendorf, J. and Meusinger, H. (2002). A QSO survey via optical variability and zero proper motion in the M 92 field. IV. More QSOs due to improved photometry. *A&A*, 390:879–890.
- Burg, R., Giacconi, R., Huchra, J., MacKenty, J., McLean, B., Geller, M., Hasinger, G., Marzke, R., Schmidt, M., and Truemper, J. (1992). Discovery of intermediate redshift galaxy clusters in the ROSAT NEP field. *A&A*, 259:L9–L11.
- Carrera, F. J., Barcons, X., Butcher, J. A., Fabian, A. C., Stewart, G. C., Toffolatti, L., Warwick, R. S., Hayashida, K., Inoue, H., and Kondo, H. (1993). The subdegree angular structure of the X-ray sky as seen by the GINGA satellite. *MNRAS*, 260:376–384.
- Cristiani, S., Vio, R., and Andreani, P. (1990). Long-term variability of a complete sample of quasars. *AJ*, 100:56–59.
- de Ruiter, H. R., Parma, P., Stirpe, G. M., Perez-Fournon, I., Gonzalez-Serrano, I., Rengelink, R. B., and Bremer, M. N. (1998). Bright galaxies from WENSS. I. The minisurvey. *A&A*, 339:34–40.
- de Vries, W. H., Becker, R. H., and White, R. L. (2003). Long-Term Variability of Sloan Digital Sky Survey Quasars. *AJ*, 126:1217–1226.
- Demers, S. and Irwin, M. J. (1987). The long-period variables of Fornax. I - Search, discovery and periods. *MNRAS*, 226:943–961.
- Demers, S., Irwin, M. J., and Kunkel, W. E. (1985). Automated photometry of NGC 3109. *AJ*, 90:1967–1981.
- Engels, D., Hagen, H.-J., Cordis, L., Koehler, S., Wisotzki, L., and Reimers, D. (1998). The Hamburg Quasar Survey. II. A first list of 121 quasars. *A&AS*, 128:507–523.

- Feigelson, E. D. and Nelson, P. I. (1985). Statistical methods for astronomical data with upper limits. I - Univariate distributions. *ApJ*, 293:192–206.
- Froebrich, D. and Meusinger, H. (2000). A search for LSB dwarf galaxies in the M 81 group on digitally stacked Schmidt plates. *A&AS*, 145:229–242.
- Fuhrmeister, B. and Schmitt, J. H. M. M. (2003). A systematic study of X-ray variability in the ROSAT all-sky survey. *A&A*, 403:247–260.
- Gaidos, E. J., Magnier, E. A., and Schechter, P. L. (1993). A catalog of QSO candidates from a BVRI CCD survey of the North Ecliptic Pole. *PASP*, 105:1294–1307.
- Gioia, I. M., Henry, J. P., Luppino, G. A., Clowe, D. I., Böhringer, H., Briel, U. G., Voges, W., Huchra, J. P., and MacGillivray, H. (1995). Discovery of a large gravitational arc in the X-ray cluster A2280. *A&A*, 297:L75+.
- Gioia, I. M., Henry, J. P., Mullis, C. R., Böhringer, H., Briel, U. G., Voges, W., and Huchra, J. P. (2003). The ROSAT North Ecliptic Pole Survey: the Optical Identifications. *ApJS*, 149:29–51.
- Gioia, I. M., Maccacaro, T., Schild, R. E., Stocke, J. T., Liebert, J. W., Danziger, I. J., Kunth, D., and Lub, J. (1984). The medium sensitivity survey - A new sample of X-ray sources with optical identifications and the revised extragalactic log N-log S. *ApJ*, 283:495–511.
- Gioia, I. M., Maccacaro, T., Schild, R. E., Wolter, A., Stocke, J. T., Morris, S. L., and Henry, J. P. (1990). The Einstein Observatory Extended Medium-Sensitivity Survey. I - X-ray data and analysis. *ApJS*, 72:567–619.
- Giveon, U., Maoz, D., Kaspi, S., Netzer, H., and Smith, P. S. (1999). Long-term optical variability properties of the Palomar-Green quasars. *MNRAS*, 306:637–654.
- Groot, P. J., Vreeswijk, P. M., Huber, M. E., Everett, M. E., Howell, S. B., Nelemans, G., van Paradijs, J., van den Heuvel, E. P. J., Augusteijn, T., Kuulkers, E., Rutten, R. G. M., and Storm, J. (2003). The Faint Sky Variability Survey - I. Goals and data reduction process. *MNRAS*, 339:427–434.
- Grupe, D., Thomas, H.-C., and Beuermann, K. (2001). X-ray variability in a complete sample of Soft X-ray selected AGN. *A&A*, 367:470–486.
- Hacking, P. and Houck, J. R. (1987). A very deep IRAS survey at L = 97 deg, B = 30 deg. *ApJS*, 63:311–333.
- Halpern, J. P. and Oke, J. B. (1987). Narrow-line Seyfert galaxies with permitted Fe II emission Markarian 507, 5C 3.100, and I ZW 1. *ApJ*, 312:91–100.
- Hasinger, G. (1991). Private communication. Target lists and Identification data for NEP X-ray sources.

- Hasinger, G., Truemper, J., and Schmidt, M. (1991). Results on the X-ray background and sources from the ROSAT medium sensitivity survey. *A&A*, 246:L2–L5.
- Hawkins, M. R. S. (1986). On the nature of objects detected as faint long-term variables. *MNRAS*, 219:417–426.
- Hawkins, M. R. S. and Veron, P. (1993). The quasar luminosity function from a variability-selected sample. *MNRAS*, 260:202–208.
- Heckman, T. M. (1980). An optical and radio survey of the nuclei of bright galaxies - Activity in normal galactic nuclei. *A&A*, 87:152–164.
- Henry, J. P., Gioia, I. M., Böhringer, H., Bower, R. G., Briel, U. G., Hasinger, G. H., Aragon-Salamanca, A., Castander, F. J., Ellis, R. S., Huchra, J. P., Burg, R., and McLean, B. (1994). RX J1759.4+6638: an x-ray selected quasars at a redshift of 4.320. *AJ*, 107:1270–1273.
- Henry, J. P., Gioia, I. M., Huchra, J. P., Burg, R., McLean, B., Böhringer, H., Bower, R. G., Briel, U. G., Voges, W., MacGillivray, H., and Cruddace, R. G. (1995). Groups of Galaxies in the ROSAT North Ecliptic Pole Survey. *ApJ*, 449:422–+.
- Henry, J. P., Gioia, I. M., Mullis, C. R., Voges, W., Briel, U. G., Böhringer, H., and Huchra, J. P. (2001). Overview of the ROSAT North Ecliptic Pole Survey. *ApJ*, 553:L109–LL113.
- Hoegner, W. and Ziener, R. (1978). The Orwo ZU 2 plate with improved characteristics. *Astronomische Nachrichten*, 299:159–163.
- Hook, I. M., McMahon, R. G., Boyle, B. J., and Irwin, M. J. (1994). The Variability of Optically Selected Quasars. *MNRAS*, 268:305–+.
- Hughes, P. A., Aller, H. D., and Aller, M. F. (1992). The University of Michigan radio astronomy data base. I - Structure function analysis and the relation between BL Lacertae objects and quasi-stellar objects. *ApJ*, 396:469–486.
- Irwin, M. (1996). Detectors and data analysis techniques for wide field optical imaging. URL <http://www.ast.cam.ac.uk/~mike/puerta.ps.gz>.
- Irwin, M. J. (1985). Automatic analysis of crowded fields. *MNRAS*, 214:575–604.
- Isobe, T., Feigelson, E. D., and Nelson, P. I. (1986). Statistical methods for astronomical data with upper limits. II - Correlation and regression. *ApJ*, 306:490–507.
- Jaunsen, A. O., Jablonski, M., Petterson, B. R., and Stabell, R. (1995). The NOT gravitational lens survey for multiply imaged quasars. *A&A*, 300:323–+.
- Kümmel, M. W. and Wagner, S. J. (2000). A wide field survey at the Northern Ecliptic Pole. I. Number counts and angular correlation functions in K. *A&A*, 353:867–672.

- King, I. R. (1971). The Profile of a Star Image. *PASP*, 83:199–+.
- King, I. R. (1983). Accuracy of measurement of star images on a pixel array. *PASP*, 95:163–168.
- Knox, R. A., Hambly, N. C., Hawkins, M. R. S., and MacGillivray, H. T. (1998). Digital stacking of photographic plates with SuperCOSMOS. *MNRAS*, 297:839–848.
- Kollgaard, R. I., Brinkmann, W., Chester, M. M., Feigelson, E. D., Hertz, P., Reich, P., and Wielebinski, R. (1994). A sensitive 1.5 GHz radio survey around the north ecliptic pole. *ApJS*, 93:145–159.
- Koo, D. C. and Kron, R. G. (1982). QSO counts - A complete survey of stellar objects to $B = 23$. *A&A*, 105:107–119.
- Koo, D. C., Kron, R. G., and Cudworth, K. M. (1986). Quasars to B greater than 22.5 in selected area 57 - A catalog of multicolor photometry, variability, and astrometry. *PASP*, 98:285–306.
- Krautter, J., Zickgraf, F.-J., Appenzeller, I., Thiering, I., Voges, W., Chavarria, C., Kneer, R., Mujica, R., Pakull, M. W., Serrano, A., and Ziegler, B. (1999). Identification of a complete sample of northern ROSAT All-Sky Survey X-ray sources. IV. Statistical analysis. *A&A*, 350:743–752.
- Kron, R. G. (1980). Photometry of a complete sample of faint galaxies. *ApJS*, 43:305–325.
- Lacy, M., Hill, G. J., Kaiser, M. E., and Rawlings, S. (1993). A Complete Sample of Sources in the North Ecliptic CAP Selected at 38-MHZ - Part Two - CCD Observations and Their Implications. *MNRAS*, 263:707–+.
- Lacy, M., Rawlings, S., and Warner, P. J. (1992). A complete sample of radio sources in the North Ecliptic Cap, selected at 38 MHz. I - The radio data. *MNRAS*, 256:404–424.
- Lasker, B. M., Sturch, C. R., Lopez, C., Mallamas, A. D., McLaughlin, S. F., Russell, J. L., Wisniewski, W. Z., Gillespie, B. A., Jenkner, H., Siciliano, E. D., Kenny, D., Baumert, J. H., Goldberg, A. M., Henry, G. W., Kemper, E., and Siegel, M. J. (1988). The Guide Star Photometric Catalog. *ApJS*, 68:1–90.
- Lasker, B. M., Sturch, C. R., McLean, B. J., Russell, J. L., Jenkner, H., and Shara, M. M. (1990). The Guide Star Catalog. I - Astronomical foundations and image processing. *AJ*, 99:2019–2058.
- Loiseau, N., Reich, W., Wielebinski, R., Reich, P., and Muench, W. (1988). A survey of an area around the north ecliptic pole at 11 CM wavelength. *A&AS*, 75:67–78.

- Maccacaro, T., Gioia, I. M., Zamorani, G., Feigelson, E. D., Fener, M., Giacomoni, R., Griffiths, R. E., Murray, S. S., Stocke, J., and Liebert, J. (1982). A medium sensitivity X-ray survey using the Einstein Observatory - The log N-log S relation for extragalactic X-ray sources. *ApJ*, 253:504–511.
- Majewski, S. R., Munn, J. A., Kron, R. G., Bershad, M. A., Smetanka, J. J., and Koo, D. C. (1991). A proper motion and variability QSO survey to $B = 22.5$. In *ASP Conf. Ser. 21: The Space Distribution of Quasars*, pages 55–65.
- Meusinger, H. (2002). Tautenburg Plate Archive and Plate Scanner. URL <http://www.tls-tautenburg.de/scanner.html>.
- MPE (1997). ROSAT News, Bulletin of the MPE X-ray Astronomy Group about the ROSAT Mission, No. 52. URL http://wave.xray.mpe.mpg.de/rosat/mission/rosat_news/news52.txt.
- Mullis, C. R. (2001). The ROSAT north ecliptic pole survey. *Ph.D. Thesis*. URL <http://www.eso.org/~cmullis/research/phd/phd.pdf>.
- Mullis, C. R. (2002). The ROSAT North Ecliptic Pole Survey. *PASP*, 114:688–688.
- Mullis, C. R. (2003). ROSAT North Ecliptic Pole Survey Source Catalog. URL <http://www.eso.org/~cmullis/research/nep.html>.
- Mullis, C. R., Henry, J. P., Gioia, I. M., Böhringer, H., Briel, U. G., Voges, W., and Huchra, J. P. (2001). The North Ecliptic Pole Supercluster. *ApJ*, 553:L115–L118.
- Mushotzky, R. F., Done, C., and Pounds, K. A. (1993). X-ray spectra and time variability of active galactic nuclei. *ARA&A*, 31:717–761.
- Osterbrock, D. E. (1993). The nature and structure of active galactic nuclei. *ApJ*, 404:551–562.
- Parker, Q. A. and Malin, D. (1999). The introduction of Tech Pan film at the UK Schmidt Telescope. *Publications of the Astronomical Society of Australia*, 16:288–98.
- Press, W. H., Teukolsky, S. A., Vetterling, W. T., and Flannery, B. P. (1992). *Numerical recipes in C. The art of scientific computing*. Cambridge: University Press, —c1992, 2nd ed.
- Roeser, S. and Bastian, U. (1988). A new star catalogue of SAO type. *A&AS*, 74:449–451.
- Roman, N. G., Warren, W. H., and Schofield, N. (1983). Documentation for the machine-readable version of the SAO-HD-GC-DM cross index version 1983. *NSSDC/WDC*, 84:23418–+.
- Scholz, R.-D., Brunzendorf, J., Ivanov, G., Kharchenko, N., Lasker, B., Meusinger, H., Preibisch, T., Schilbach, E., and Zinnecker, H. (1999). IC 348 proper motion study from digitised Schmidt plates. *A&AS*, 137:305–321.

- Scholz, R.-D., Meusinger, H., and Irwin, M. (1997). A UBV / variability / proper motion QSO survey from Schmidt plates. I. Method and success rate. *A&A*, 325:457–472.
- Stetson, P. B. (1979). Photographic stellar photometry with the PDS microdensitometer. *AJ*, 84:1056–1066.
- Stetson, P. B. (1987). DAOPHOT - A computer program for crowded-field stellar photometry. *PASP*, 99:191–222.
- Stetson, P. B. (1990). On the growth-curve method for calibrating stellar photometry with CCDs. *PASP*, 102:932–948.
- Stetson, P. B. (1992). Progress in CCD photometry. *JRASC*, 86:71–88.
- Stetson, P. B. (1996). On the Automatic Determination of Light-Curve Parameters for Cepheid Variables. *PASP*, 108:851–+.
- Stilburn, J. R., Stetson, P. B., and Fisher, W. A. (1992). Improvements to PDS microdensitometer of the Dominion Astrophysical Observatory. *JRASC*, 86:140–152.
- Stocke, J. T., Liebert, J., Gioia, I. M., Maccacaro, T., Griffiths, R. E., Danziger, I. J., Kunth, D., and Lub, J. (1983). The Einstein Observatory Medium Sensitivity Survey - Optical identifications for a complete sample of X-ray sources. *ApJ*, 273:458–477.
- Stocke, J. T., Morris, S. L., Gioia, I. M., Maccacaro, T., Schild, R., Wolter, A., Fleming, T. A., and Henry, J. P. (1991). The Einstein Observatory Extended Medium-Sensitivity Survey. II - The optical identifications. *ApJS*, 76:813–874.
- Thomas, H.-C. (1991). Private communication. Target lists and Identification data for NEP X-ray sources.
- Treves, A., Fink, H. H., Malkan, M., Wagner, S. J., Wilkes, B. J., Baganoff, F., Heidt, J., Pian, E., Sadun, A., Schaeidt, S., Bonnell, J. T., Brinkmann, W., de Martino, D., Maraschi, L., Tanzi, E. G., Ulrich, M. H., and Wamsteker, W. (1995). Multifrequency observations of KAZ 102 during the ROSAT all-sky survey. *ApJ*, 442:589–596.
- Trevese, D., Pittella, G., Kron, R. G., Koo, D. C., and Bershad, M. (1989). A survey for faint variable objects in SA 57. *AJ*, 98:108–116.
- Tripp, T. M., Lu, L., and Savage, B. D. (1998). The Relationship between Galaxies and Low-Redshift Weak Ly α Absorbers in the Directions of H1821+643 and PG 1116+215. *ApJ*, 508:200–231.
- Ulrich, M., Maraschi, L., and Urry, C. M. (1997). Variability of Active Galactic Nuclei. *ARA&A*, 35:445–502.

- Ulrich, M.-H., Fink, H. H., Schaeidt, S., Baganoff, F., Malkan, M. A., Heidt, J., and Wagner, S. (1992). Multiwavelength observations of the quasar Q 1821 + 643 during the ROSAT All Sky Survey. *A&A*, 266:183–189.
- Voges, W. (1996). Private communication. Target lists and Identification data for NEP X-ray sources.
- Voges, W., Aschenbach, B., Boller, T., Bräuninger, H., Briel, U., Burkert, W., Dennerl, K., Englhauser, J., Gruber, R., Haberl, F., Hartner, G., Hasinger, G., Kürster, M., Pfeffermann, E., Pietsch, W., Predehl, P., Rosso, C., Schmitt, J. H. M. M., Trümper, J., and Zimmermann, H. U. (1999). The ROSAT all-sky survey bright source catalogue. *A&A*, 349:389–405.
- Voges, W., Aschenbach, B., Boller, T., Brauninger, H., Briel, U., Burkert, W., Dennerl, K., Englhauser, J., Gruber, R., Haberl, F., Hartner, G., Hasinger, G., Pfeffermann, E., Pietsch, W., Predehl, P., Schmitt, J., Trumper, J., and Zimmermann, U. (2000). Rosat All-Sky Survey Faint Source Catalogue. *IAU Circ.*, 7432:3–+.
- Voges, W., Henry, J. P., Briel, U. G., Böhringer, H., Mullis, C. R., Gioia, I. M., and Huchra, J. P. (2001). The ROSAT North Ecliptic Pole Survey X-Ray Data. *ApJ*, 553:L119–LL123.
- Wegner, G. and McMahan, R. K. (1988). Spectral types for objects in the KISO survey. IV - Data for 81 stars. *AJ*, 96:1933–1940.
- White, R. L. and Becker, R. H. (1992). A new catalog of 30,239 1.4 GHz sources. *ApJS*, 79:331–467.
- Zickgraf, F.-J., Thiering, I., Krautter, J., Appenzeller, I., Kneer, R., Voges, W. H., Ziegler, B., Chavarria, C., Serrano, A., Mujica, R., Pakull, M., and Heidt, J. (1997). Identification of a complete sample of northern ROSAT All-Sky Survey X-ray sources. II. The optical observations. *A&AS*, 123:103–114.
- Ziener, R. (1971). Temperaturabhängigkeit des photographischen Farbsystems der Tautenburger Schmidtkamera. *Astronomische Nachrichten*, 292:231–+.

B Acknowledgements

This work would not have been possible without the support and help of many people and institutions, and it is my pleasure to thank all of them and at the same time ask the forgiveness of those that I may have forgotten.

First I have to thank my dissertation advisor or "Doktorvater", Prof. Dr. Klaus Beuermann, without whose support, advice and neverending patience this work would not have been started and, more importantly, would never have been ended – at least not in a finite time.

At the former Institute for Astronomy and Astrophysics of the TU Berlin – now Centre of Astronomy and Astrophysics – I wish to thank Prof. Dr. Erwin Sedlmayr for his friendly support and willingness to participate in the Dissertation committee. I also thank Axel Schwöpe (now at the Astrophysical Institute Potsdam) for his help in obtaining some of the observational data.

From the Thüringer Landessternwarte Tautenburg (the former Karl-Schwarzschildt-Observatory Tautenburg), I thank F. Börngen, H. Meusinger, B. Stecklum, R. Ziener and C. Högner, U. Laux, F. Ludwig for their patient work in providing the plate material on which this work is based, and also the late S. Marx, former director of the KSO Tautenburg, whose support for this project has made these extensive observations possible.

At the Universitätssternwarte Göttingen, I remember the MIDAS-support of Klaus Reinsch and Vadim Burwitz, the discussions about trains and strange music with Dirk Grupe and the hospitality, video events and comic books of Boris Gänsicke most gratefully.

I wish to thank the staff of the MPE for their great work in providing the X-ray observational data that has been the starting point of this work (and an uncountable number of other ones). In particular, I thank H. Böhringer and G. Hasinger of MPE and H.-C. Thomas of ESO for providing RASS data in advance of publication.

To my wife Christine and my children Annika and Juliane, I extend most grateful and loving thanks for their great patience and ask their forgiveness for all those weekends and evenings when I was working.

This research has made use of the DSSII, the 2nd Digitized Sky Survey of the California Institute of Technology, which is based on photographic data obtained using the Oschin Schmidt Telescope on Palomar Mountain and the UK Schmidt Telescope.

This research has made use of the SIMBAD database, operated at CDS, Strasbourg, France, and of the NASA/IPAC extragalactic database (NED) which is operated by the Jet Propulsion Laboratory, Caltech, under contract with the National Aeronautics and Space Administration.

This work was partially funded by the DFG (grant Be 470/15-1/2).

C Plate data of used Schmidt plates

See below for a list of all used Tautenburg Schmidt plates. The table columns are

- (1) Plate number from the Tautenburg Schmidt plate archive
- (2) Date of plate exposure
- (3) Plate area as defined in Fig. 8
- (4) Plate center coordinates (equinox J2000.0)
- (5) Exposure time in minutes
- (6) Seeing value of the plate, measured in arc seconds, as derived by the methods in Chapter 6.2
- (7) Sensitivity limit of the plate for 4σ detection of objects, measured in magnitudes, as derived by the methods in Chapter 6.5

Table 1: List of all used Tautenburg Schmidt plates

Plate No.	Obs. date	Sky area	Plate center RA / DE		Exp. time	Seeing	Plate limit
(1)	(2)	(3)	(4)		(5)	(6)	(7)
7209	21.2.90	C	18 00 00	+66 34	23	2.7	21.0
7223	24.2.90	I	18 13 30	+67 54	23	3.1	20.4
7224	24.2.90	II	18 13 30	+65 14	23	3.3	20.5
7226	24.2.90	III	17 46 30	+67 54	22	3.0	20.6
7235	19.3.90	C	18 00 00	+66 34	33	3.2	21.2
7236	19.3.90	IV	17 46 30	+65 14	32	3.2	21.2
7249	19.5.90	C	18 00 00	+66 34	30	2.4	21.1
7263	27.5.90	II	18 13 30	+65 14	23	2.3	20.7
7266	19.6.90	C	18 00 00	+66 34	18	2.5	20.7
7267	20.6.90	III	17 46 30	+67 54	16	2.8	20.5
7271	20.7.90	IV	17 46 30	+65 14	28	2.8	21.3
7272	21.7.90	C	18 00 00	+66 34	27	2.2	21.5
7273	21.7.90	III	17 46 30	+67 54	28	2.3	21.7
7277	22.7.90	C	18 00 00	+66 34	28	2.5	21.7
7278	22.7.90	I	18 13 30	+67 54	30	2.4	21.8
7279	23.7.90	II	18 13 30	+65 14	30	2.7	21.7

continued on next page

Plate No.	Obs. date	Sky area	Plate center RA / DE		Exp. time	Seeing	Plate limit
7283	26.7.90	C	18 00 00	+66 34	25	2.3	21.2
7284	26.7.90	IV	17 46 30	+65 14	29	2.5	21.2
7290	27.7.90	C	18 00 00	+66 34	25	2.6	20.9
7291	27.7.90	I	18 13 30	+67 54	28	2.6	21.0
7298	28.7.90	II	18 13 30	+65 14	24	2.7	21.0
7301	30.7.90	C	18 00 00	+66 34	25	1.9	21.0
7302	30.7.90	III	17 46 30	+67 54	27	2.1	21.2
7303	31.7.90	IV	17 46 30	+65 14	28	1.9	21.2
7308	1.8.90	C	18 00 00	+66 34	27	2.0	21.4
7309	1.8.90	I	18 13 30	+67 54	26	2.1	21.4
7310	1.8.90	II	18 13 30	+65 14	26	2.0	21.5
7314	2.8.90	IV	17 46 30	+65 14	24	2.5	21.2
7316	2.8.90	C	18 00 00	+66 34	26	2.3	21.4
7317	2.8.90	III	17 46 30	+67 54	24	2.5	21.4
7320	15.8.90	II	18 13 30	+65 14	28	2.6	21.0
7325	17.8.90	IV	17 46 30	+65 14	26	3.6	21.1
7327	18.8.90	I	18 13 30	+67 54	25	3.3	21.1
7329	22.8.90	II	18 13 30	+65 14	26	2.7	21.0
7333	10.10.90	III	17 46 30	+67 54	27	2.6	21.3
7337	11.10.90	IV	17 46 30	+65 14	29	2.6	21.5
7338	11.10.90	C	18 00 00	+66 34	31	2.9	21.4
7346	12.10.90	I	18 13 30	+67 54	30	3.9	21.2
7356	13.10.90	C	18 00 00	+66 34	30	2.5	21.3
7357	13.10.90	III	17 46 30	+67 54	31	2.9	21.4
7369	14.10.90	II	18 13 30	+65 14	28	2.4	21.1
7370	14.10.90	C	18 00 00	+66 34	31	2.5	21.3
7371	14.10.90	IV	17 46 30	+65 14	31	2.6	21.2
7389	9.11.90	C	18 00 00	+66 34	29	2.7	20.9
7390	9.11.90	III	17 46 30	+67 54	30	3.0	20.8
7391	9.11.90	I	18 13 30	+67 54	32	3.0	20.8
7432	15.1.91	III	17 46 30	+67 54	32	5.4	20.6
7441	16.1.91	C	18 00 00	+66 34	32	4.2	20.9
7442	16.1.91	IV	17 46 30	+65 14	32	4.3	20.8
7456	17.1.91	II	18 13 30	+65 14	32	4.2	21.0
7475	19.1.91	C	18 00 00	+66 34	30	5.3	20.6
7476	19.1.91	III	17 46 30	+67 54	30	4.0	21.1
7477	19.1.91	I	18 13 30	+67 54	30	4.0	21.1
7486	10.4.91	IV	17 46 30	+65 14	42	3.1	21.2
7500	11.4.91	I	18 13 30	+67 54	27	2.9	21.0

continued on next page

Plate No.	Obs. date	Sky area	Plate center RA / DE		Exp. time	Seeing	Plate limit
7511	12.4.91	III	17 46 30	+67 54	40	3.2	21.5
7520	13.4.91	IV	17 46 30	+65 14	42	2.8	21.2
7530	7.5.91	II	18 13 30	+65 14	33	2.4	20.4
7549	19.5.91	I	18 13 34	+67 55	30	3.5	21.0
7553	6.6.91	IV	17 46 30	+65 14	19	3.0	20.6
7562	12.7.91	I	18 13 34	+67 55	18	2.8	20.7
7582	7.8.91	III	17 46 30	+67 54	33	2.9	20.8
7592	12.8.91	IV	17 46 30	+65 14	31	2.3	20.8
7596	13.8.91	I	18 13 34	+67 56	33	2.8	21.1
7597	14.8.91	II	18 13 30	+65 14	34	2.6	21.2
7599	14.8.91	III	17 46 30	+67 54	31	2.5	21.1
7606	16.8.91	IV	17 46 30	+65 14	28	3.7	*
7621	4.9.91	I	18 13 30	+67 54	30	2.5	20.8
7635	9.9.91	II	18 13 30	+65 14	30	2.4	21.3
7636	9.9.91	III	17 46 30	+67 54	28	2.6	21.3
7645	10.9.91	IV	17 46 30	+65 14	36	2.7	21.4
7665	13.9.91	IV	17 46 30	+65 14	32	2.9	21.4
7677	14.9.91	I	18 13 30	+67 54	37	2.6	21.3
7719	5.10.91	I	18 13 30	+67 54	32	2.6	21.3
7730	7.10.91	II	18 13 30	+65 14	32	2.4	21.0
7744	8.10.91	IV	17 46 30	+65 14	31	3.2	20.9
7753	9.10.91	I	18 13 30	+67 54	29	2.5	21.1
7755	9.10.91	II	18 13 30	+65 14	30	2.5	21.1
7767	10.10.91	II	18 13 30	+65 14	26	2.8	21.0
7776	30.10.91	III	17 46 30	+67 54	24	2.8	20.5
7778	30.10.91	IV	17 46 30	+65 14	25	3.8	20.2
7795	4.11.91	IV	17 46 30	+65 14	22	3.6	20.7
7798	6.11.91	IV	17 46 30	+65 14	25	2.8	20.7
7814	11.12.91	I	18 13 30	+67 54	27	3.0	20.4
8040	25.7.92	I	18 13 30	+67 54	33	2.5	20.7
8046	26.7.92	III	17 46 30	+67 54	40	2.4	21.1
8058	28.7.92	IV	17 46 30	+65 14	32	2.2	21.2
8059	28.7.92	II	18 13 30	+65 14	39	2.1	21.4
8094	27.8.92	III	17 46 30	+67 54	31	2.8	21.0

D X-ray data for all sources

Below is a list of the X-ray sources in the NEP area studied in this work. The table columns are

- (1) Source name, in most cases taken from the 1RXS and 2RXP catalogs
- (2) source X-ray coordinates in decimal degrees (equinox J2000.0)
- (3) precision of source coordinates, in arcsec
- (4) ROSAT exposure time in seconds
- (5) ROSAT countrate and countrate error
- (6) ROSAT hardness ratio HR1 and error in HR1
- (7) source likelihood
- (8) source extension
- (9) source extension likelihood
- (10) Flag for X-ray variability, from Fuhrmeister and Schmitt (2003)
- (11) remarks to individual sources
- (12) footnote reference

Table 2: X-ray data of all sources

Source name	Source coordinates		dPos	Exp. time	Countrate±dCtr		HR1±dHR1		srcl	ext	extl	var	Comments	Note
(1)	(2)	(3)	(4)	(5)	(6)	(7)	(8)	(9)	(10)	(11)	(12)	(13)	(14)	(15)
1RXS J173202.4+652328	263.0100	65.3913	12	4338	8.29E-03	2.22E-03	0.88	0.29	19	0	0			
1RXS J173254.5+653324	263.2271	65.5567	8	4415	3.45E-02	3.48E-03	0.78	0.08	179	11	2			
1RXS J173316.9+671228	263.3204	67.2078	8	5197	2.74E-02	2.84E-03	-0.04	0.10	136	13	4			
1RXS J173453.6+680709	263.7234	68.1193	23	6100	2.62E-02	3.21E-03	1.00	0.06	47	88	14		associated with 1RXS J173623.4+680206	1
1RXS J173505.0+640557	263.7708	64.0992	11	3009	7.93E-02	6.41E-03	0.54	0.07	148	53	61			
1RXS J173600.1+655900	264.0004	65.9835	10	4547	9.47E-03	2.12E-03	0.36	0.21	29	0	0			
2RXP J173614.2+682007	264.0592	68.3353	5	3946	6.19E-03	1.46E-03	-0.18	0.23	28	0	0			
1RXS J173614.7+650229	264.0613	65.0414	6	4156	1.02E-01	5.69E-03	0.37	0.05	710	0	0			
1RXS J173623.4+680206	264.0975	68.0350	16	6493	5.00E-02	3.88E-03	1.00	0.03	85	102	76		associated with 1RXS J173453.6+680709	1
1RXS J173627.2+682031	264.1133	68.3419	7	5788	6.21E-02	4.07E-03	-0.62	0.04	374	13	2			
2RXP J173641.8+682256	264.1742	68.3825	3	6262	1.21E-02	1.52E-03	-0.04	0.12	92	5	1			
1RXS J173657.6+684522	264.2400	68.7561	6	4848	4.66E-01	1.04E-02	-0.28	0.02	5410	10	11			
1RXS J173804.9+650933	264.5204	65.1592	8	4832	2.85E-02	3.09E-03	-0.38	0.09	125	12	2	+	X-ray flares detected in RASS	2
1RXS J173944.7+671052	264.9363	67.1813	7	6449	3.39E-02	2.78E-03	0.32	0.08	248	16	10			
1RXS J173955.8+650007	264.9825	65.0021	7	5029	3.59E-02	3.39E-03	-0.38	0.08	179	0	0	+	X-ray trend variability detected in RASS	2
1RXS J174114.4+650743	265.3100	65.1288	9	5614	1.33E-02	2.20E-03	0.24	0.15	45	8	1			
1RXS J174144.9+650427	265.4371	65.0743	12	5671	4.29E-03	1.41E-03	0.74	0.45	13	0	0			
1RXS J174212.5+663949	265.5521	66.6638	13	6938	1.33E-02	2.02E-03	0.54	0.14	43	24	4			
1RXS J174217.9+635109	265.5746	63.8525	7	4416	3.89E-02	3.81E-03	0.19	0.09	186	6	1			
1RXS J174234.2+670936	265.6425	67.1601	9	7492	1.28E-02	1.80E-03	0.15	0.14	68	13	2			
1RXS J174246.8+673553	265.6950	67.5981	17	8096	2.82E-02	2.88E-03	0.57	0.08	67	81	20			
1RXS J174302.3+660642	265.7596	66.1118	7	7137	4.66E-02	3.12E-03	0.10	0.06	406	12	8			
1RXS J174323.3+644018	265.8471	64.6718	15	5440	2.78E-02	3.21E-03	0.98	0.10	56	57	18			
1RXS J174328.1+634140	265.8671	63.6944	10	4486	4.00E-02	3.84E-03	0.62	0.10	131	29	24			
1RXS J174414.2+653455	266.0592	65.5820	7	7603	5.44E-02	3.10E-03	0.55	0.05	577	14	9			
1RXS J174526.0+691819	266.3583	69.3053	7	5354	3.91E-02	3.38E-03	0.34	0.08	215	9	1		two components ?	3

continued on next page

Source name	Source coordinates		dPos	Exp. time	Countrate±dCtr		HR1±dHR1		srcl	ext	extl	var	Comments	Note
1RXS J174555.3+645118	266.4804	64.8550	9	6425	2.11E-02	2.50E-03	0.57	0.13	95	20	3			
1RXS J174603.1+672709	266.5129	67.4526	8	9136	1.21E-02	1.55E-03	0.66	0.13	92	0	0			
1RXS J174604.2+640622	266.5175	64.1061	10	5303	4.87E-03	1.50E-03	1.00	0.22	18	0	0			
1RXS J174609.6+673721	266.5400	67.6226	6	9136	1.46E-01	4.46E-03	0.36	0.02	2380	14	20			
1RXS J174700.3+683626	266.7513	68.6074	6	6922	2.13E-01	6.04E-03	0.25	0.02	2790	13	19			
1RXS J174714.4+653230	266.8100	65.5418	10	9133	1.08E-02	1.67E-03	0.73	0.12	54	0	0			
1RXS J174726.8+662628	266.8617	66.4411	7	11104	1.38E-02	1.48E-03	0.52	0.11	127	9	1			
1RXS J174733.7+634355	266.8904	63.7321	11	5143	1.28E-02	2.51E-03	0.71	0.14	28	0	0			
1RXS J174757.4+662327	266.9892	66.3910	8	11600	1.48E-02	1.55E-03	0.38	0.10	122	14	5			
1RXS J174758.0+653835	266.9917	65.6431	7	9764	3.06E-02	2.26E-03	0.40	0.07	280	18	6			
1RXS J174822.7+640327	267.0946	64.0576	11	5781	1.55E-02	2.36E-03	0.17	0.15	50	22	4			
1RXS J174838.8+684211	267.1617	68.7032	7	7214	2.36E-02	2.38E-03	0.79	0.08	182	7	1			
1RXS J174920.5+641108	267.3354	64.1857	11	6168	1.09E-02	1.99E-03	0.07	0.17	33	14	1			
1RXS J174955.0+661116	267.4792	66.1878	9	14069	3.96E-03	8.70E-04	0.57	0.24	27	0	0			
1RXS J175014.3+681433	267.5596	68.2425	11	9094	6.95E-03	1.35E-03	0.31	0.18	29	0	0			
1RXS J175015.5+641515	267.5646	64.2542	9	6569	1.16E-02	1.97E-03	0.14	0.16	45	13	1			
2RXP J175108.6+653153	267.7859	65.5314	10	1393	1.75E-02	3.90E-03	2.68	0.81	13	27	9		weak source with questionable HR	
1RXS J175115.5+653334	267.8146	65.5595	14	12430	8.58E-03	1.50E-03	0.93	0.12	38	0	0			
1RXS J175130.9+671920	267.8788	67.3224	14	14492	1.30E-02	1.48E-03	0.92	0.05	58	45	21			
1RXS J175139.8+654040	267.9158	65.6779	12	13776	1.23E-02	1.51E-03	0.62	0.11	56	37	13		complex X-emission, extension faulty ?	
1RXS J175157.7+655120	267.9904	65.8556	8	15835	1.22E-02	1.26E-03	0.78	0.10	130	12	2			
1RXS J175257.4+644058	268.2392	64.6829	8	8765	1.25E-02	1.67E-03	-0.15	0.12	75	8	1			
1RXS J175341.7+654242	268.4237	65.7117	8	17285	7.69E-03	9.87E-04	0.80	0.12	84	0	0			
1RXS J175405.5+661354	268.5229	66.2317	7	26766	1.53E-02	1.03E-03	0.42	0.07	307	7	1			
1RXS J175441.9+680334	268.6746	68.0595	8	12121	1.45E-01	4.15E-03	0.95	0.01	752	104	872			
1RXS J175445.8+662353	268.6908	66.3981	7	28937	1.33E-02	9.28E-04	0.23	0.07	290	13	5			
1RXS J175505.8+651951	268.7742	65.3308	6	13864	9.49E-02	3.04E-03	0.20	0.03	1850	10	7			
1RXS J175545.5+675242	268.9396	67.8785	11	13835	5.07E-02	2.70E-03	0.80	0.08	139	95	216		problems with deblending extended emission	4
1RXS J175556.9+654054	268.9871	65.6818	7	20124	8.99E-03	9.99E-04	0.27	0.10	113	0	0			
1RXS J175610.0+661514	269.0417	66.2540	7	31043	8.67E-03	7.36E-04	0.40	0.08	162	14	4			
1RXS J175614.1+680707	269.0588	68.1188	7	12434	3.90E-02	2.22E-03	0.27	0.05	508	10	4			
1RXS J175631.0+651302	269.1292	65.2172	10	13744	1.18E-02	1.43E-03	0.73	0.11	82	0	0		problems with deblending extended emission	5
1RXS J175643.3+643853	269.1804	64.6482	7	10570	2.31E-02	1.94E-03	0.27	0.08	208	9	2			
1RXS J175703.7+684923	269.2654	68.8232	7	9382	2.52E-02	2.21E-03	-0.04	0.08	208	4	1			

continued on next page

Source name	Source coordinates		dPos	Exp. time	Countrate±dCtr		HR1±dHR1		srcl	ext	extl	var	Comments	Note
1RXS J175709.8+635238	269.2908	63.8774	8	8045	1.46E-02	1.91E-03	0.18	0.12	80	8	1			
1RXS J175713.9+654702	269.3079	65.7839	8	25303	6.60E-03	7.97E-04	0.40	0.10	88	8	1			
1RXS J175719.9+663139	269.3329	66.5276	11	33836	3.16E-03	4.96E-04	0.97	0.13	31	25	8			
1RXS J175734.1+684122	269.3921	68.6896	7	9857	2.05E-02	1.87E-03	0.48	0.08	213	0	0			
1RXS J175801.0+640932	269.5042	64.1589	7	8992	6.78E-02	3.27E-03	-0.06	0.04	753	14	5	+	X-ray flares detected in RASS	2
RX J1758.1+6639	269.5346	66.6525		79100	9.14E-04				29				data taken from NEP deep survey	8
1RXS J175813.2+674319	269.5550	67.7220	7	16818	1.22E-02	1.23E-03	0.41	0.09	148	7	1			
1RXS J175818.8+690631	269.5783	69.1086	12	8575	1.04E-02	1.65E-03	0.50	0.15	46	23	2			
1RXS J175819.1+673515	269.5796	67.5875	8	18916	3.07E-03	6.24E-04	0.41	0.24	32	0	0			
1RXS J175824.2+653105	269.6008	65.5182	7	18252	1.95E-02	1.36E-03	0.58	0.06	344	8	1			
1RXS J175833.4+663759	269.6392	66.6331	7	36047	5.95E-03	5.43E-04	-0.13	0.09	155	7	1		also contained in NEP deep survey	8
1RXS J175847.2+635039	269.6967	63.8443	7	8230	3.03E-02	2.50E-03	0.27	0.08	240	9	2			
2RXP J175900.1+664752	269.7508	66.7978	5	44603	2.22E-03	3.08E-04	0.55	0.15	22	8	0			
1RXS J175911.3+663521	269.7971	66.5893	9	36990	7.89E-04	2.24E-04	0.67	0.37	12	0	0		also contained in NEP deep survey	8
1RXS J175912.5+640833	269.8021	64.1425	7	9187	4.14E-02	2.66E-03	-0.18	0.06	377	9	3			
2RXP J175919.9+665135	269.8329	66.8597	7	40775	1.68E-03	3.10E-04	0.31	0.19	25	10	0			
2RXP J175930.1+663848	269.8758	66.6469	4	48268	9.06E-04	1.81E-04	0.63	0.25	16	0	0		also contained in NEP deep survey	8
2RXP J175934.4+664533	269.8933	66.7592	5	46826	8.81E-04	1.92E-04	0.66	0.27	10	0	0		also contained in NEP deep survey	8
2RXP J175937.9+664818	269.9079	66.8050	9	45256	6.19E-04	1.83E-04	1.67	0.68	11	0	0		also contained in NEP deep survey	8
1RXS J175944.3+662911	269.9346	66.4864	7	35843	4.02E-03	4.39E-04	0.44	0.12	127	6	1		also contained in NEP deep survey	8
1RXS J180001.9+664559	270.0079	66.7664	7	36425	2.11E-03	3.58E-04	-0.09	0.15	46	0	0		also contained in NEP deep survey	8
2RXP J180006.6+661950	270.0275	66.3306	9	33835	1.50E-03	3.38E-04	-0.21	0.19	10	16	2			
1RXS J180007.5+663654	270.0313	66.6151	7	33730	4.83E-03	4.93E-04	0.77	0.09	158	9	4		also contained in NEP deep survey	8
1RXS J180009.9+683557	270.0413	68.5992	6	10473	5.61E-01	7.46E-03	-0.99	0.00	9999	14	94			
1RXS J180022.1+662501	270.0921	66.4171	9	36401	9.55E-04	2.68E-04	0.58	0.42	14	0	0		also contained in NEP deep survey	8
1RXS J180023.1+661554	270.0963	66.2651	7	34301	4.85E-03	5.11E-04	0.21	0.11	130	0	0			
1RXS J180023.9+634953	270.0996	63.8314	7	8384	3.01E-02	2.40E-03	0.30	0.08	252	14	7		two components ?	3
1RXS J180026.2+635719	270.1092	63.9554	7	8679	2.05E-02	2.06E-03	0.06	0.09	165	9	1			
1RXS J180028.2+691322	270.1175	69.2228	12	8151	5.63E-02	3.49E-03	0.88	0.04	201	78	98			
2RXP J180041.5+664112	270.1729	66.6867		29332	3.16E-03		-0.13	0.07	27	0	0		also contained in NEP deep survey	8
2RXP J180046.2+665140	270.1929	66.8611	6	40288	2.21E-03	3.41E-04	0.81	0.18	17	16	3			
2RXP J180055.1+662207	270.2296	66.3686	9	46866	1.16E-03	2.62E-04	0.51	0.18	10	15	1		also contained in NEP deep survey	8
1RXS J180057.6+660058	270.2400	66.0163	7	31479	6.49E-03	6.73E-04	0.07	0.10	120	0	0			
1RXS J180115.2+662401	270.3134	66.4004	8	37185	1.21E-03	2.83E-04	0.23	0.24	20	0	0			

continued on next page

Source name	Source coordinates		dPos	Exp. time	Countrate±dCtr		HR1±dHR1		srcl	ext	extl	var	Comments	Note
2RXP J180116.7+663110	270.3196	66.5194	3	48335	1.40E-03	2.04E-04	0.68	0.19	28	0	0		also contained in NEP deep survey	8
1RXS J180121.6+665405	270.3400	66.9014	6	33480	2.65E-02	1.08E-03	0.19	0.04	1150	6	2			
NEPX1 J1801.5+6646.5	270.3542	66.7750		49100									NEPX1, "the blotch", extended structure	6
2RXP J180133.1+663208	270.3879	66.5356	3	47370	8.94E-04	1.66E-04	1.85	0.42	15	0	0		also contained in NEP deep survey	8
2RXP J180144.5+663708	270.4354	66.6192	3	47893	1.08E-03	1.91E-04	0.60	0.24	25	0	0		also contained in NEP deep survey	8
1RXS J180146.7+663840	270.4446	66.6445	6	37296	2.49E-02	9.52E-04	0.66	0.03	1490	7	7		also contained in NEP deep survey	8
1RXS J180205.9+662902	270.5246	66.4840	9	36946	1.35E-03	3.26E-04	0.34	0.24	20	0	0		also contained in NEP deep survey	8
1RXS J180216.3+641546	270.5679	64.2629	6	9529	1.44E-01	4.38E-03	-0.19	0.02	2290	9	8	+	X-ray flares detected in RASS	2
1RXS J180222.9+664750	270.5954	66.7972	7	35093	4.73E-03	5.38E-04	0.81	0.12	97	8	1			
2RXP J180236.6+664459	270.6525	66.7497	5	45136	2.72E-03	3.30E-04	0.53	0.13	27	16	6		also contained in NEP deep survey	8
2RXP J180249.3+662441	270.7054	66.4114	15	44521	2.57E-03	4.49E-04	0.85	0.12	16	38	10			
1RXS J180251.3+660540	270.7138	66.0946	7	31870	1.67E-02	9.14E-04	0.80	0.05	509	10	6			
1RXS J180305.7+644526	270.7738	64.7574	8	11004	1.83E-02	1.76E-03	-0.08	0.09	154	13	3			
1RXS J180328.4+673806	270.8683	67.6351	6	17165	2.80E-01	4.21E-03	0.46	0.01	9999	15	100			
1RXS J180354.5+654827	270.9771	65.8076	7	25149	1.58E-02	1.07E-03	0.48	0.07	317	9	4			
1RXS J180413.4+675412	271.0559	67.9033	7	13826	1.12E-02	1.29E-03	-0.10	0.10	110	0	0			
1RXS J180525.4+663859	271.3558	66.6497	8	31294	1.06E-02	8.13E-04	0.60	0.08	187	22	16		complex X-emission, extension faulty ?	
1RXS J180536.2+662452	271.4009	66.4146	7	30969	1.10E-02	8.14E-04	0.58	0.08	273	7	1			
1RXS J180541.4+643251	271.4225	64.5475	8	9229	1.21E-02	1.57E-03	0.88	0.10	96	0	0			
1RXS J180606.7+681308	271.5279	68.2189	9	10732	1.40E-02	1.67E-03	0.51	0.11	86	15	3			
1RXS J180643.4+682200	271.6808	68.3667	7	9827	2.24E-02	2.00E-03	-0.03	0.09	177	11	4			
1RXS J180651.7+653747	271.7154	65.6297	11	16351	2.30E-02	1.67E-03	0.96	0.05	158	52	45			
1RXS J180700.5+664348	271.7521	66.7301	11	28101	9.56E-03	9.51E-04	0.60	0.13	73	41	16		complex X-emission, extension faulty ?	
1RXS J180719.4+663530	271.8308	66.5918	7	27594	2.11E-02	1.16E-03	0.22	0.05	440	12	8			
1RXS J180739.7+682917	271.9154	68.4882	8	9025	1.84E-02	1.92E-03	0.04	0.10	125	5	1			
1RXS J180802.6+645225	272.0108	64.8736	10	9241	2.12E-02	2.14E-03	0.51	0.09	104	28	7			
1RXS J180825.3+643725	272.1054	64.6236	14	8151	9.69E-03	1.76E-03	0.39	0.18	33	0	0			
2RXP J180839.6+653145	272.1650	65.5294	13	1889	1.13E-02	2.83E-03	1.04	0.13	12	29	7			
1RXS J180840.7+673554	272.1696	67.5983	7	12553	2.37E-02	1.83E-03	0.17	0.08	233	13	2			
1RXS J180849.9+663431	272.2079	66.5753	7	23950	2.21E-02	1.30E-03	0.45	0.06	409	12	3			
1RXS J180851.1+653022	272.2129	65.5061	8	12959	9.59E-03	1.32E-03	0.31	0.14	73	0	0			
1RXS J180930.2+662033	272.3758	66.3425	10	19461	6.15E-03	9.21E-04	-0.05	0.13	48	14	2			
1RXS J181004.3+634424	272.5179	63.7401	9	5700	2.23E-02	2.69E-03	0.17	0.12	85	19	3			
1RXS J181112.4+654346	272.8017	65.7296	7	12382	1.28E-02	1.43E-03	0.25	0.11	120	5	1			

continued on next page

Source name	Source coordinates		dPos	Exp. time	Countrate±dCtr		HR1±dHR1		srcl	ext	extl	var	Comments	Note
1RXS J181119.1+644736	272.8296	64.7935	10	7456	1.12E-02	1.83E-03	0.41	0.16	47	11	1			
1RXS J181136.9+650704	272.9038	65.1178	8	8817	1.97E-02	2.04E-03	0.60	0.10	138	6	1			
1RXS J181208.5+635335	273.0354	63.8932	10	5254	1.45E-02	2.37E-03	0.45	0.15	47	12	1			
1RXS J181341.6+673150	273.4233	67.5307	17	9121	1.43E-02	1.97E-03	0.61	0.12	47	42	4		X-ray contour plot shows 3–4 components	1
1RXS J181345.6+662849	273.4400	66.4803	8	13108	2.64E-02	1.88E-03	0.15	0.07	222	23	29			
1RXS J181346.6+653821	273.4442	65.6392	7	10682	3.42E-02	2.22E-03	0.25	0.06	426	10	5			
1RXS J181348.3+683121	273.4513	68.5225	10	7176	5.54E-03	1.31E-03	0.92	0.25	22	5	1			
1RXS J181351.0+672811	273.4625	67.4697	9	9370	8.42E-03	1.53E-03	0.58	0.21	39	0	0			
1RXS J181353.7+642348	273.4738	64.3968	6	5748	2.42E-01	7.10E-03	-0.17	0.02	2500	11	10	+	X-ray flares detected in RASS	2
1RXS J181422.4+690804	273.5933	69.1346	13	5867	6.48E-03	1.73E-03	0.32	0.25	17	0	0			
1RXS J181517.1+665811	273.8212	66.9697	10	10072	7.05E-03	1.30E-03	0.96	0.15	36	15	3			
1RXS J181524.4+680630	273.8517	68.1083	7	7272	2.14E-02	2.20E-03	0.85	0.08	151	9	2			
1RXS J181552.4+644101	273.9683	64.6836	9	6308	1.18E-02	2.08E-03	-0.05	0.16	49	5	1			
1RXS J181648.2+650429	274.2008	65.0749	8	7824	1.16E-02	1.78E-03	-0.04	0.14	62	0	0			
1RXS J181659.5+644909	274.2479	64.8193	14	6712	1.15E-02	2.06E-03	-0.04	0.15	28	28	3			
1RXS J181746.1+682424	274.4421	68.4068	8	6360	5.12E-02	3.42E-03	0.82	0.04	268	38	70			
1RXS J181829.0+674127	274.6209	67.6908	6	7386	1.13E-01	4.42E-03	0.41	0.03	1320	5	1	+	X-ray trend variability detected in RASS	2
1RXS J181857.3+661135	274.7387	66.1931	7	9325	5.61E-02	3.10E-03	-0.49	0.04	494	14	6			
1RXS J181952.3+651035	274.9679	65.1765	7	7735	1.73E-02	2.08E-03	0.07	0.11	118	0	0			
1RXS J181955.5+663619	274.9812	66.6054	8	8613	1.21E-02	1.59E-03	0.70	0.12	91	0	0			
1RXS J182013.0+685722	275.0542	68.9563	11	5472	7.91E-02	4.78E-03	0.99	0.02	188	82	171			
1RXS J182019.7+651918	275.0821	65.3217	7	7882	6.86E-02	3.51E-03	0.08	0.04	693	14	16			
1RXS J182032.9+662029	275.1371	66.3415	11	8590	7.51E-03	1.51E-03	0.51	0.18	31	0	0			
1RXS J182123.8+655928	275.3492	65.9911	8	8168	2.20E-02	2.21E-03	-0.05	0.09	145	9	1			
1RXS J182138.8+654304	275.4117	65.7179	8	7965	1.71E-02	2.03E-03	-0.13	0.11	96	7	1			
1RXS J182146.6+635716	275.4442	63.9546	8	4354	1.35E-02	2.54E-03	0.05	0.17	47	0	0			
2RXP J182152.0+642147	275.4671	64.3631	7	809	3.50E-02	7.26E-03	-1.02	0.10	33	15	1			
1RXS J182157.4+642051	275.4892	64.3475	6	5257	1.07E+00	1.41E-02	0.24	0.01	9999	23	486			
1RXS J182215.8+640307	275.5658	64.0521	10	4527	6.99E-03	1.77E-03	0.56	0.27	21	8	1			
1RXS J182308.8+653320	275.7867	65.5556	9	7520	7.50E-03	1.49E-03	0.97	0.28	37	0	0		two components ?	7
1RXS J182320.1+641924	275.8337	64.3233	8	5229	2.19E-02	2.62E-03	0.58	0.11	118	6	1			
1RXS J182431.5+634956	276.1313	63.8322	22	4223	2.49E-02	3.68E-03	0.95	0.14	35	68	10		extension only marginally detected	
1RXS J182447.0+650924	276.1958	65.1567	6	6948	1.27E-01	4.81E-03	0.16	0.03	1570	14	22			
1RXS J182510.6+645017	276.2942	64.8381	6	6348	2.29E-01	6.48E-03	0.23	0.02	3070	10	17			

continued on next page

Source name	Source coordinates		dPos	Exp. time	Countrate±dCtr		HR1±dHR1		srcl	ext	extl	var	Comments	Note
1RXS J182546.4+690551	276.4433	69.0975	8	4393	3.62E-02	3.64E-03	0.65	0.10	147	18	8			
1RXS J182638.3+670647	276.6596	67.1131	8	6415	2.13E-02	2.36E-03	0.61	0.11	121	14	1			
1RXS J182733.6+643138	276.8900	64.5274	8	5620	1.41E-02	2.20E-03	0.43	0.14	64	0	0			
1RXS J182932.3+690509	277.3846	69.0860	13	3430	2.08E-02	3.21E-03	0.30	0.16	47	26	3			
1RXS J182943.5+674910	277.4312	67.8194	8	4671	1.58E-02	2.38E-03	0.67	0.16	78	0	0	+	X-ray periodic variability detected in RASS	2

Footnotes:

- (1) 1RXS deblending of extended structure and the resulting coordinates are doubtful
- (2) see Fuhrmeister and Schmitt (2003)
- (3) X-ray contour plot indicates the possibility of a two-component emission (foreground star set within larger background structure)
- (4) nearby 1RXS source 1RXS J175531.0+675001 is an artefact of 1RXS deblending of this extended structure
- (5) extended emission is deblended into 1RXS sources 1RXS J175631.0+651302 and 1RXS J175620.5+651145
- (6) see Hasinger et al. (1991), Burg et al. (1992)
- (7) X-ray contour plot indicates two-component emission (foreground star set within larger background structure, possibly cluster). This would also explain the (for a star) somewhat unusual hardness ratio.
- (8) see Bower et al. (1996)

E Optical data and identifications for all sources

See below for a list of the optical counterparts and available identifications for the sources given in Tab. 2. The table columns are

- (1) Source name, same as in Tab. 2.
- (2) Coordinates of the optical counterpart, for pointlike sources. No coordinates are given for extended objects like e.g. clusters. Coordinate equinox is J2000.0
- (3) Position difference optical to X-ray coordinates, in seconds of arc.
- (4) Scan flag (field was scanned on Tautenburg Schmidt plates to search for variable sources). A "*" means that the field was scanned but that the X-ray counterpart was not analysed for some reason.
- (5) Mean brightness of optical counterpart (magnitudes). Color passband is the native passband of the Tautenburg Schmidt plates. For sources that were not scanned, data from literature (or SIMBAD / NED) is used when available.
- (6) χ^2 of the optical brightness of the counterpart, as an indication of optical source variability. See also for special remarks if the χ^2 is unreliable for some reasons.
- (7) Extension flag if X-ray counterpart is optically extended
- (8) Variability flag if X-ray counterpart is judged to be optically variable. If the variability is only marginally detected, this is flagged by a question mark ("v?"). If the source is non-variable, this is shown by "-". If no variability analysis can be performed (e.g. for clusters or because a counterpart cannot be found), this column is left blank. If there is variability data from other sources or catalogs, this is marked by "(v)".
- (9) Lightcurve flag. Time-resolved optical data is available in Appendix F.
- (10) Identification, physical nature of the optical counterpart.
- (11) Redshift of the optical counterpart, for extragalactic objects.
- (12) Comments, including popular designations
- (13) Footnote reference
- (14) Discussion flag. Source is discussed in some more depth in Chapter 8.5

An unambiguous identification of the X-ray counterpart is possible for all but three of the sources. In these cases of almost equal probability of two counterparts, both candidates are listed, and the somewhat less likely candidate carries the suffix "b". Some additional cases with a less likely alternative or secondary identifications are discussed in the individual notes to objects.

Please note that the last two objects in the list are not X-ray counterparts but rather interesting variable objects that are found serendipitously within scanned fields.

Table 3: Optical data and available identifications of all sources

Source name	Source coordinates	dPos	Scan	Mag	χ^2	Ext	Var	LC	ID	z	Comments	Note	Disc.
(1)	(2)	(3)	(4)	(5)	(6)	(7)	(8)	(9)	(10)	(11)	(12)	(13)	(14)
1RXS J173202.4+652328	17 32 2.9 +65 23 30	3	+	20.2	2.8		v?	+	Gal./AGN		galaxy or AGN within cluster	13	
1RXS J173254.5+653324	17 32 54.0 +65 33 25	3	+	18.2	8.4		v	+	AGN	0.8560	4C65.21		
1RXS J173316.9+671228	17 33 18.1 +67 12 13	17	-	8.05					*		HD 160198	3	
1RXS J173453.6+680709			+						Cluster	0.0258	common cluster with 1RXS J173623.4+680206	15	
1RXS J173505.0+640557			+						Cluster	0.1411		16	
1RXS J173600.1+655900	17 36 1.9 +65 58 55	12	+	20.6	4.0		v?	+	AGN	0.4341	crowded, χ^2 unreliable	11	
2RXP J173614.2+682007	17 36 12.9 +68 20 3	8	*	20.5:					?		variability analysis not performed, no spectrum	13	
1RXS J173614.7+650229	17 36 14.4 +65 2 28	2	+	11.8	0.6		-		*		MS 1736.0+6504; bright star, χ^2 unreliable	5	
1RXS J173623.4+680206			+						Cluster	0.0258	common cluster with 1RXS J173453.6+680709	15	
1RXS J173627.2+682031	17 36 26.3 +68 20 33	5	+	10.8	1.4		v?	+	*		SAO 17568; bright star, χ^2 unreliable	3,6	
2RXP J173641.8+682256	17 36 42.2 +68 22 58	2	-	8.44					*		SAO 17570	3	
1RXS J173657.6+684522	17 36 57.1 +68 45 26	5	-	5.23					*		Ω Dra	3	
1RXS J173804.9+650933	17 38 4.7 +65 9 28	5	+	16.7	3.3		v	+	*		X-ray and optically variable	1	+
1RXS J173944.7+671052	17 39 44.7 +67 10 43	10	+	18.0	4.3	+	v	+	AGN	0.1180	MS 1739.8+6712, Seyfert 1-Galaxy		
1RXS J173955.8+650007	17 39 55.7 +65 0 5	3	-	9.33					*		SAO 17595, X- and optically variable	1,3,4	+
1RXS J174114.4+650743	17 41 15.8 +65 7 42	9	+	18.5	2.0		v	+	AGN	0.7466	AGN in cluster; see notes in Gioia et al. (2003)		
1RXS J174144.9+650427	17 41 45.6 +65 4 14	14	*			+			Galaxy		red ext. galaxy, within cluster ?	17,27	
1RXS J174212.5+663949	17 42 14.0 +66 39 34	18	+	17.1	3.2		v	+	AGN	1.2720			
1RXS J174217.9+635109	17 42 18.6 +63 51 16	8	+	18.3					AGN	0.4019	one usable plate only		
1RXS J174234.2+670936	17 42 33.8 +67 9 23	14	+	13.2	4.2		-		*		disturbed by nearby star, χ^2 unreliable	10	
1RXS J174246.8+673553			+						Cluster	0.0420	cluster containing NGC6456		
1RXS J174302.3+660642	17 43 1.9 +66 6 43	3	-	10.2					*		BD+66 1042, 2E 1742.8+6608	3	
1RXS J174323.3+644018			+						Cluster	0.1790	near Abell 2281		
1RXS J174328.1+634140			+						Cluster	0.3270	cluster with cD-galaxy and gravitational arc	18,19	
1RXS J174414.2+653455	17 44 14.6 +65 34 53	3	+	19.9	6.8		v	+	AGN	0.2550			
1RXS J174526.0+691819	17 45 24.5 +69 18 22	9	+	13.5	75.7		v	+	*			6	

continued on next page

Source name	Source coordinates	dPos	Scan	Mag	χ^2	Ext	Var	LC	ID	z	Comments	Note	Disc.
1RXS J174555.3+645118	17 45 55.6 +64 51 25	7	+	19.0	4.0		v	+	AGN	0.1790	AGN in cluster		
1RXS J174603.1+672709	17 46 1.9 +67 27 9	7	+	20.0	2.9		v?	+	AGN	0.2146			
1RXS J174604.2+640622	17 46 4.8 +64 6 16	7	+	19.0	1.4		-		?		faint cluster ?	13	
1RXS J174609.6+673721	17 46 9.0 +67 37 24	4	+	15.7	32.4				AGN	0.0410	MS1746+6738, Seyfert1; χ^2 unreliable		+
1RXS J174700.3+683626	17 46 59.6 +68 36 31	6	+	16.4	31.7	+	v	+	AGN	0.0630	Kaz 163, narrow-line Seyfert1 with companion		
1RXS J174714.4+653230	17 47 13.9 +65 32 36	6	+	21.2	0.8		-		AGN	1.5166	4C65.22, QSO with strong host galaxy contrib.		
1RXS J174726.8+662628	17 47 27.1 +66 26 24	4	+	18.7	4.2		v	+	AGN	0.1391			+
1RXS J174733.7+634355			-						Cluster	0.3280	faint cluster, not scanned on Schmidt plates		
1RXS J174757.4+662327	17 47 58.4 +66 23 27	6	+	19.0	2.9	+	v	+	Galaxy	0.1738	galaxy with narrow emission lines	26	
1RXS J174758.0+653835	17 47 57.9 +65 38 29	6	+	19.2	5.4		v	+	AGN	0.3248			
1RXS J174822.7+640327	17 48 23.3 +64 3 38	11	+	20.6	2.3		v?	+	AGN	0.9859			
1RXS J174838.8+684211	17 48 38.5 +68 42 16	5	+	15.8	9.6	+	v	+	AGN	0.0537	MRK 507; close blend of two sources		+
1RXS J174920.5+641108	17 49 19.5 +64 11 19	12	+	17.7	1.5		-		AGN	0.9836			
1RXS J174955.0+661116			-						*				
1RXS J175014.3+681433			-	20.4:					AGN	0.2310	not scanned; data from COSMOS finding charts	28	
1RXS J175015.5+641515	17 50 15.1 +64 14 57	18	+	20.3	1.1	+	-		AGN	0.2504			
2RXP J175108.6+653153	17 51 7.4 +65 31 51	8	+	14.7	6.6	+	-		Galaxy	0.0389	NGC 6505, large galaxy E/S0	9	
1RXS J175115.5+653334			+						Cluster	0.0424	cluster including NGC 6505	15	
1RXS J175130.9+671920			+						Cluster	0.0933			
1RXS J175139.8+654040	17 51 36.9 +65 40 31	20	+	20.4	1.6		-		AGN	0.8259			
1RXS J175157.7+655120	17 51 56.8 +65 51 18	6	+	20.5	7.8		v	+	AGN	0.3901			
1RXS J175257.4+644058	17 52 56.9 +64 40 55	5	+	19.4	1.7	+	v?	+	AGN	0.1230			
1RXS J175341.7+654242	17 53 42.1 +65 42 40	3	+	20.0	0.8	+	-		AGN	0.1400		18	
1RXS J175405.5+661354	17 54 4.8 +66 13 51	5	+	19.5	7.3		v	+	AGN	0.4067			
1RXS J175441.9+680334			-						Cluster	0.0770	VIIZw751, MS 1754.9+6803		
1RXS J175445.8+662353			+						Cluster	0.0879		20	
1RXS J175505.8+651951	17 55 5.6 +65 19 56	5	+	16.7	7.8	+	v	+	AGN	0.0785	IPC17549.6521, Sab galaxy		
1RXS J175545.5+675242			+						Cluster	0.0833	part of z=0.088 supercluster	21	
1RXS J175556.9+654054	17 55 56.8 +65 40 52	3	+	19.5	2.2		v?	+	AGN	0.3238			
1RXS J175610.0+661514	17 56 9.5 +66 15 9	6	+	18.6	2.1		v?	+	AGN	0.6357			
1RXS J175614.1+680707	17 56 13.8 +68 7 11	4	+	13.8	13.7		v	+	*		bright star, χ^2 unreliable	6	
1RXS J175631.0+651302			+						Cluster	0.0284	... containing MCG+11-22-014, large E/S0 galaxy	15	
1RXS J175643.3+643853	17 56 43.1 +64 39 1	8	+	17.1	1.7		-		AGN	0.2233	close blend with star, 3.3" separation		
1RXS J175703.7+684923	17 57 3.6 +68 49 20	4	-	9.69					*		SAO 17704	3	

continued on next page

Source name	Source coordinates	dPos	Scan	Mag	χ^2	Ext	Var	LC	ID	z	Comments	Note	Disc.
1RXS J175709.8+635238	17 57 9.2 +63 52 34	6	+	19.6	1.2	-			AGN	0.3220			
1RXS J175713.9+654702	17 57 14.2 +65 47 0	3	+	16.8	1.9	v?	+		*		dMe-star		+
1RXS J175719.9+663139			+						Cluster	0.6909	faint cluster; blank on Schmidt plates		
1RXS J175734.1+684122	17 57 34.1 +68 41 21	1	+	19.2	2.3	v	+		AGN	0.1814			
1RXS J175801.0+640932	17 58 1.4 +64 9 34	3	+	11.2	1.9	-			*		SAO 17709; χ^2 unreliable; X-ray-variable	1,2,5	+
RX J1758.1+6639	17 58 7.8 +66 38 57	13	-	10.3					*		BD +66 1065	2	
1RXS J175813.2+674319	17 58 14.0 +67 43 18	5	+	18.8	5.2	v	+		AGN	0.2045			
1RXS J175818.8+690631	17 58 15.9 +69 6 32	16	+	20.2	3.2	v	+		AGN	2.1572			
1RXS J175819.1+673515	17 58 18.7 +67 35 19	5	-	18.6					*		magnitude from COSMOS finding chart	28	
1RXS J175824.2+653105	17 58 24.3 +65 31 8	3	+	19.5	7.3	v	+		AGN	0.3250	faint whisp visible on object		
1RXS J175833.4+663759	17 58 34.2 +66 38 6	8	-	9.80					PN		IC 4677, NGC 6543		
1RXS J175847.2+635039	17 58 47.7 +63 50 38	4	-	8.66					*		SAO 17714	2	
2RXP J175900.1+664752	17 58 58.2 +66 47 50	12	+	20.4	1.6	-			?			13	
1RXS J175911.3+663521	17 59 12.1 +66 35 12	11	+	20.9	1.5	-			AGN	0.6300		23	
1RXS J175912.5+640833	17 59 13.6 +64 8 34	7	-	7.64					*		SAO 17717	3	
2RXP J175919.9+665135	17 59 16.8 +66 51 44	20	+	20.7	1.9	-			AGN	0.9440			
2RXP J175930.1+663848	17 59 27.9 +66 38 53	14	+	>21.9					AGN	4.3200	high-z QSO, invisible on Schmidt plates	22	
2RXP J175934.4+664533	17 59 32.2 +66 45 42	16	+	21.0	1.7	-			AGN	1.1700		23	
2RXP J175937.9+664818			+						?		very faint, unidentified in NEP deep survey	23	
1RXS J175944.3+662911	17 59 45.0 +66 29 10	4	+	20.2	1.2	-			AGN	0.3990			
1RXS J180001.9+664559	18 0 2.1 +66 45 55	4	-	11.3					*		TYC 4213- 617-1	2	
2RXP J180006.6+661950	18 0 5.5 +66 19 45	8	+	16.3	1.0	-			*?		most likely counterpart: M-star		
1RXS J180007.5+663654	18 0 7.3 +66 36 54	1	+	13.6	73.1	+			AGN	0.0260	NGC 6552, large Sb-galaxy, Seyfert 2	9	
1RXS J180009.9+683557	18 0 9.6 +68 35 53	4	+	14.5	5.9	v?	+		wD		KUV 18004+6836, sdO; χ^2 unreliable	7	+
1RXS J180022.1+662501	18 0 21.3 +66 24 58	6	+	20.2	1.6	v?	+		AGN	1.6200			
1RXS J180023.1+661554	18 0 23.8 +66 15 52	5	+	20.2	1.6	v?	+		AGN	0.4475	AGN within cluster		
1RXS J180023.9+634953	18 0 24.5 +63 49 53	4	+	13.3	20.0	v	+		*		bright star, χ^2 unreliable	6	
1RXS J180026.2+635719	18 0 26.1 +63 57 21	2	+	19.1	12.5	v	+		AGN	0.6828	highly variable AGN		
1RXS J180028.2+691322			+						Cluster	0.0821	near Abell 2295		
2RXP J180041.5+664112	18 0 40.2 +66 41 14	8	+	21.1	1.5	-			AGN	0.9400	faint, just detected	12	
2RXP J180046.2+665140	18 0 42.3 +66 51 42	24	+	20.1	1.3	-			AGN	1.9710			
2RXP J180055.1+662207	18 0 54.6 +66 22 9	4	+	20.9	1.9	-			AGN	0.8500			
1RXS J180057.6+660058	18 0 57.2 +66 0 58	3	+	14.6	4.8	v?	+		*		bright star, χ^2 unreliable	5	
1RXS J180115.2+662401	18 1 16.5 +66 24 1	8	+	20.4	1.0	-			AGN	1.2500		23	

continued on next page

Source name	Source coordinates	dPos	Scan	Mag	χ^2	Ext	Var	LC	ID	z	Comments	Note	Disc.
2RXP J180116.7+663110	18 1 14.3 +66 31 14	15	+	>21.5					AGN	0.5700	invisible on Schmidt plates	23	
1RXS J180121.6+665405	18 1 21.8 +66 54 5	1	+	12.5	2.2		-		*		bright star, χ^2 unreliable	5	
NEPX1 J1801.5+6646.5			-						Cluster	0.0900	NEPX1, "the blotch"	24	
2RXP J180133.1+663208	18 1 30.8 +66 32 9	14	+	21.7:					AGN	1.3000	invisible on Schmidt plates		
2RXP J180144.5+663708			+						Cluster	0.5700	brightness near plate limit of Schmidt plates		
1RXS J180146.7+663840	18 1 46.8 +66 38 40	1	+	21.1	1.1		-		BL Lac		faint, just detected	12	
1RXS J180205.9+662902	18 2 7.3 +66 29 6	9	+	21.0	1.1		-		AGN	0.2650	faint, just detected	12	
1RXS J180216.3+641546	18 2 16.4 +64 15 47	1	+	15.0	227		v	+	*		G227-22, dMe, X-ray variable, opt. flare found	1	+
1RXS J180222.9+664750	18 2 24.5 +66 47 35	18	*	21.0:					AGN	0.3424	faint, just detected	12	
2RXP J180236.6+664459	18 2 35.3 +66 45 6	10	+	20.4	1.0		-		*		star, very red from DSSII	23	
2RXP J180249.3+662441			+						Cluster ?		faint cluster ? Blank on Schmidt plates		
1RXS J180251.3+660540	18 2 51.3 +66 5 42	2	+	19.8	3.0		v	+	AGN	0.2070			
1RXS J180305.7+644526	18 3 5.7 +64 45 30	4	+	15.4	3.4		v?	+	*		blended, χ^2 unreliable	11	
1RXS J180328.4+673806	18 3 28.8 +67 38 10	4	+	15.6	7.1		v	+	AGN	0.1360	Kaz 102, Seyfert 1		+
1RXS J180354.5+654827	18 3 54.4 +65 48 25	3	+	20.3	1.7		v?	+	BL Lac	0.085:			
1RXS J180413.4+675412	18 4 14.3 +67 54 12	5	+	14.7	1165		v	+	CV		EX Dra, 2E 1804.3+6753, strongly variable		
1RXS J180525.4+663859	18 5 24.8 +66 39 4	6	+	19.2	2.2	+	v?	+	AGN	0.1449			
1RXS J180536.2+662452	18 5 36.0 +66 24 53	1	+	20.2	0.9		-		AGN	0.7210			
1RXS J180541.4+643251	18 5 40.5 +64 32 47	7	-	>21.0					AGN	0.7432	just faintly visible on DSSII-R		
1RXS J180606.7+681308a	18 6 4.8 +68 13 16	13	+	20.4	2.1		v?	+	AGN/Cl.	0.2953	AGN in cluster; see Gioia et al. (2003)		+
1RXS J180606.7+681308b	18 6 8.9 +68 13 10	12	+	19.6	3.7		v	+	AGN/Cl.	0.3030	AGN in cluster; see Gioia et al. (2003)		+
1RXS J180643.4+682200	18 6 43.5 +68 22 2	2	+	14.7	0.5		-		*		blended with star 17.4m, 4.7" separation		+
1RXS J180651.7+653747			+						Cluster	0.2626			
1RXS J180700.5+664348	18 6 58.2 +66 43 30	23	*	21.0:					*		variability analysis not performed	12	
1RXS J180719.4+663530	18 7 19.8 +66 35 30	2	+	13.5	1.5		-		*		bright star, χ^2 unreliable	7	
1RXS J180739.7+682917	18 7 39.6 +68 29 23	6	+	13.7	0.1		-		*		bright star, χ^2 unreliable	5	
1RXS J180802.6+645225	18 8 3.6 +64 52 29	8	+	18.9	3.1		v	+	AGN	1.0360			
1RXS J180825.3+643725	18 8 23.7 +64 37 11	17	+	15.0	1.7		-		*		χ^2 unreliable	14	
2RXP J180839.6+653145			+						Cluster ?				
1RXS J180840.7+673554	18 8 41.5 +67 36 0	8	+	12.9	10.3		-		*		bright star, χ^2 unreliable	5	
1RXS J180849.9+663431	18 8 49.5 +66 34 30	3	+	16.9	7.4		v	+	AGN	0.6970	radio-loud source; nice lightcurve		
1RXS J180851.1+653022	18 8 50.7 +65 30 19	4	+	19.5	3.8	+	v	+	AGN	0.2937	AGN within cluster		
1RXS J180930.2+662033	18 9 30.2 +66 20 21	12	+	19.9	2.4		v	+	AGN	0.6350			+
1RXS J181004.3+634424	18 10 4.4 +63 44 26	2	+	18.5	4.2		v	+	AGN	0.3770			

continued on next page

Source name	Source coordinates	dPos	Scan	Mag	χ^2	Ext	Var	LC	ID	z	Comments	Note	Disc.
1RXS J181112.4+654346	18 11 11.6 +65 43 48	5	+	19.1	3.2		v	+	AGN	0.4895			
1RXS J181119.1+644736			+						Cluster	0.4510			
1RXS J181136.9+650704	18 11 36.1 +65 6 59	7	+	19.7	0.9		-		AGN	0.8470			
1RXS J181208.5+635335			+						Cluster	0.5408			
1RXS J181341.6+673150	18 13 43.0 +67 32 23	33	+	19.9	1.8		-		AGN	0.6168	AGN in Cluster, ID doubtful		+
1RXS J181345.6+662849	18 13 47.2 +66 29 0	15	+	20.6	3.0		v?	+	*		disturbed by brighter star, χ^2 unreliable		+
1RXS J181346.6+653821	18 13 45.8 +65 38 20	5	+	18.5	11.8				AGN	0.1912	disturbed by brighter star, χ^2 unreliable	10	
1RXS J181348.3+683121	18 13 48.6 +68 31 33	12	+	12.1	0.3		-		*?		χ^2 unreliable; ID doubtful	14	+
1RXS J181351.0+672811	18 13 50.7 +67 28 6	5	+	19.3	2.8		v	+	AGN	0.3196			
1RXS J181353.7+642348	18 13 53.8 +64 23 50	2	-	5.40					*		HD168151, X-ray variable	1,3	+
1RXS J181422.4+690804			-						?		weak source, far from NEP; not scanned		
1RXS J181517.1+665811	18 15 17.5 +66 58 6	6	+	20.0	1.3	+	-		AGN	0.2287	AGN in cluster		
1RXS J181524.4+680630	18 15 25.0 +68 6 32	4	+	20.3	1.8		-		AGN	0.2390	4C68.20, Seyfert 1, Broad-line radio galaxy		
1RXS J181552.4+644101	18 15 51.8 +64 41 2	4	+	19.5	3.0		v	+	AGN	0.4116			
1RXS J181648.2+650429	18 16 49.8 +65 4 26	11	+	11.6	0.7		-		*			2	
1RXS J181659.5+644909	18 16 58.6 +64 49 35	14	+	12.9	24.5		-		*		bright star, χ^2 unreliable	5	
1RXS J181659.5+644909b	18 16 58.9 +64 49 23	26	+	20.1	2.9		-		?		spectrum unavailable		
1RXS J181746.1+682424			+						Cluster	0.2820			
1RXS J181829.0+674127	18 18 28.9 +67 41 25	2	+	16.8	23.0		v	+	AGN	0.3140	HS 1818+6740, variable in X- and optically	1	+
1RXS J181857.3+661135	18 18 56.5 +66 11 38	6	+	15.3	9.5		v	+	*		G258-33, dMe / flare star		+
1RXS J181952.3+651035	18 19 51.6 +65 10 36	4	+	19.5	1.4		-		AGN	0.1894			
1RXS J181955.5+663619	18 19 53.8 +66 36 18	9	+	14.8	1.0		-		*				
1RXS J181955.5+663619b	18 19 56.8 +66 36 15	10	+	14.8	0.6				*?		also detected as VLA radio source		+
1RXS J182013.0+685722			+						Cluster	0.0890	near Abell 2304		
1RXS J182019.7+651918	18 20 19.3 +65 19 19	3	-	8.42					*		SAO 17860	3	
1RXS J182032.9+662029	18 20 33.0 +66 20 20	10	+	19.3	4.7		v	+	AGN	0.5057			
1RXS J182123.8+655928	18 21 24.4 +65 59 29	4	+	19.5	8.6		-		*		disturbed by brighter star, χ^2 unreliable	10	
1RXS J182138.8+654304	18 21 40.1 +65 43 10	10	+	19.3	1.9		v?	+	AGN	0.2666	AGN in cluster		
1RXS J182146.6+635716	18 21 47.0 +63 57 15	3	-	10.5					*		TYC 4222- 1770-1	2	
2RXP J182152.0+642147	18 21 52.1 +64 21 53	6	+	14.6	1.3		-		PN		DS Dra, EUVE J1821+64.3		
1RXS J182157.4+642051	18 21 57.2 +64 20 35	16	+	14.2	8.9		v	+	AGN	0.2970	1E 1821+64.3, bright QSO		+
1RXS J182215.8+640307			+						Cluster ?	0.200:	faint cluster ?		+
1RXS J182215.8+640307b	18 22 14.0 +64 3 4	12	+	19.9	1.3	+			Galaxy ?	0.2000	galaxy with bright core	25	
1RXS J182308.8+653320	18 23 6.8 +65 33 13	14	-	9.21			(v)		*		HD 170154, optically variable	3,4,8	

continued on next page

Source name	Source coordinates	dPos	Scan	Mag	χ^2	Ext	Var	LC	ID	z	Comments	Note	Disc.
1RXS J182320.1+641924	18 23 19.3 +64 19 30	8	+	18.8	3.8		v	+	AGN	0.5766			
1RXS J182431.5+634956	18 24 29.6 +63 49 38	22	+	18.5	0.0		-		*		3 plates only		+
1RXS J182447.0+650924	18 24 46.4 +65 9 24	4	+	16.3	8.9		v	+	AGN	0.3030	close blend of two sources, confusion about ID		+
1RXS J182510.6+645017	18 25 10.1 +64 50 18	3	-	7.85			(v)		*		HD 170527, optically variable	3,4	
1RXS J182546.4+690551	18 25 47.4 +69 5 54	6	+	17.3	15.4	+	v	+	AGN	0.0888	galaxy with bright core in group of galaxies		
1RXS J182638.3+670647	18 26 37.5 +67 6 44	6	+	19.5	12.2		v	+	AGN	0.2870	8C1826.670, Seyfert 1, broad line radio gal.	18	
1RXS J182733.6+643138	18 27 33.9 +64 31 43	5	+	19.0	4.1		v	+	AGN	0.0977	complex structure / blend		
1RXS J182932.3+690509	18 29 31.8 +69 5 14	5	+	12.9	1.4		-		*?		ID doubtful		+
1RXS J182943.5+674910	18 29 42.0 +67 49 12	9	+	19.9	2.1		v	+	AGN	0.4783	variable in X-ray and also optically	1	+
V J181958.6+652023	18 19 58.6 +65 20 23		+	17.9	8.9	+	v	+	Gal./AGN		galaxy with bright core, no X-counterpart		+
IY Dra	18 23 17.9 +64 20 36		+	16.0	2212		v	+	Var. *		variable star, no X-counterpart		+

Footnotes:

- | | |
|---|---|
| <p>(1) see Fuhrmeister and Schmitt (2003)</p> <p>(2) Hipparcos / Tycho data available</p> <p>(3) time-resolved Hipparcos / Tycho data available</p> <p>(4) no variability data from this work but flagged in Hipparcos/Tycho data as variable star</p> <p>(5) Special processing for bright stars shows that data is compatible with non-variability</p> <p>(6) Special processing for bright stars indicates variability</p> <p>(7) Special processing for bright stars indicates no variability although in-field comparison shows variability</p> <p>(8) X-ray contour plot shows possibility of another X-ray contributor</p> <p>(9) no reliable variability analysis possible because of the optical extension</p> <p>(10) disturbance analysis shows that data are compatible with non-variability</p> <p>(11) object is disturbed by another object; variability slightly exceeds what is usual for the magnitude difference and separation</p> <p>(12) object's brightness is near plate limit of Tautenburg Schmidt plates</p> | <p>(13) no spectrum of suspected counterpart available</p> <p>(14) no suitable comparison stars, scatterplot quality is bad</p> <p>(15) see Henry et al. (1995)</p> <p>(16) see Böhringer et al. (2000)</p> <p>(17) see de Ruiter et al. (1998)</p> <p>(18) see Lacy et al. (1993)</p> <p>(19) see Gioia et al. (1995)</p> <p>(20) see Ashby et al. (1996)</p> <p>(21) see Mullis et al. (2001)</p> <p>(22) see Henry et al. (1994)</p> <p>(23) see Bower et al. (1996)</p> <p>(24) see Burg et al. (1992)</p> <p>(25) see Tripp et al. (1998)</p> <p>(26) see Gioia et al. (2003)</p> <p>(27) invisible on Tautenburg Schmidt plates</p> <p>(28) finding charts kindly provided by MPE / ROE</p> |
|---|---|

F Time-resolved photometric data

In this appendix the time-resolved photometric data of all variable X-ray counterparts are plotted.

Non-variable X-ray counterparts are not included in this appendix. Please note that the position information are the X-ray positions (in fact, they are the object designators for the X-ray object); the sky coordinates for the optical counterpart must be taken from the finding charts resp. from the identification lists.

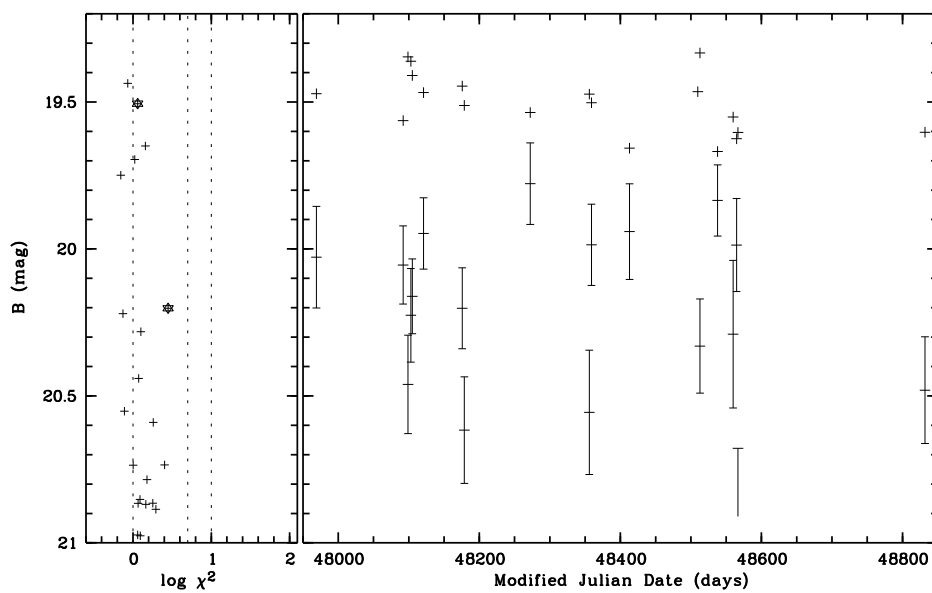
Each lightcurve plot contains the available data of the optical counterpart, with error bars or an upper limit when no lower error bar is printed. In a few exceptional cases, questionable magnitudes are also flagged by display of an upper limit. Also shown is the optical data for one comparison star, with a magnitude as similar as possible. To allow for an easier discrimination between counterpart and comparison star, the comparison star is plotted without error bars; however, because the magnitudes are comparable, the error bars will also be of a comparable value. The panel at the left shows the reduced χ^2 , plotted in a logarithmic representation, of all sources within the field with a comparable magnitude, with a cut-off value of $\chi^2 = 100$.

The photometric data for all variable sources can also be obtained in electronic form from the author (simon@uni-sw.gwdg.de or carsten.simon@alumni.tu-berlin.de) on request.

Please note that the lightcurves for V J181958.6+652023 and IY Dra, two variable objects which are no X-Ray counterparts, are also included for completeness sake.

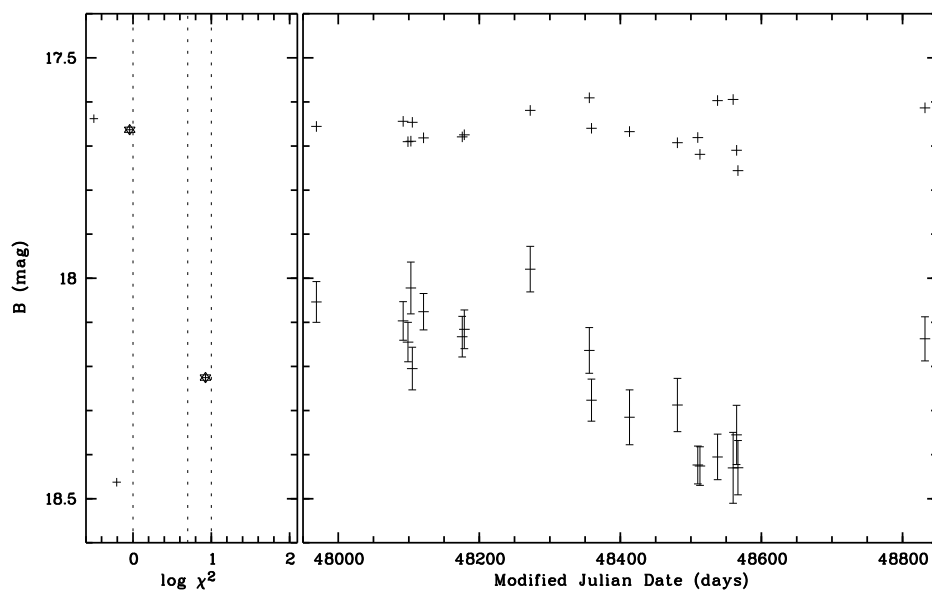
1RXS J173202.4+652328

Galaxy/AGN



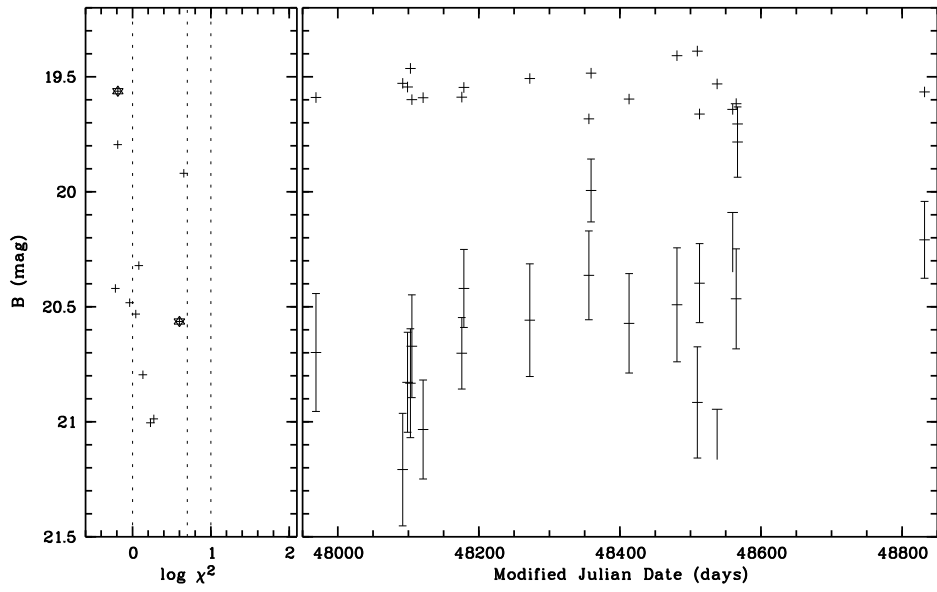
1RXS J173254.5+653324

AGN $z = 0.8560$



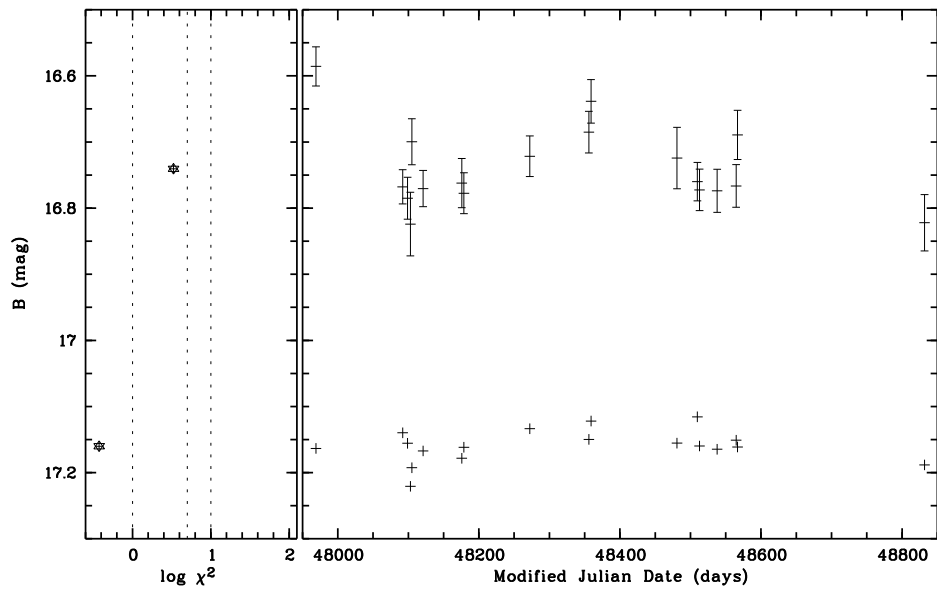
1RXS J173600.1+655900

AGN $z = 0.4341$



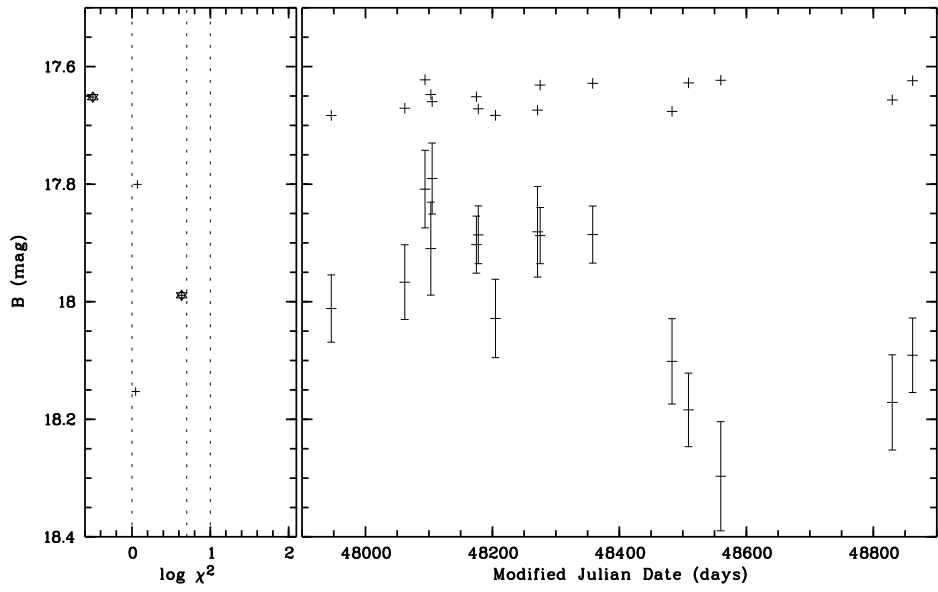
1RXS J173804.9+650933

Star



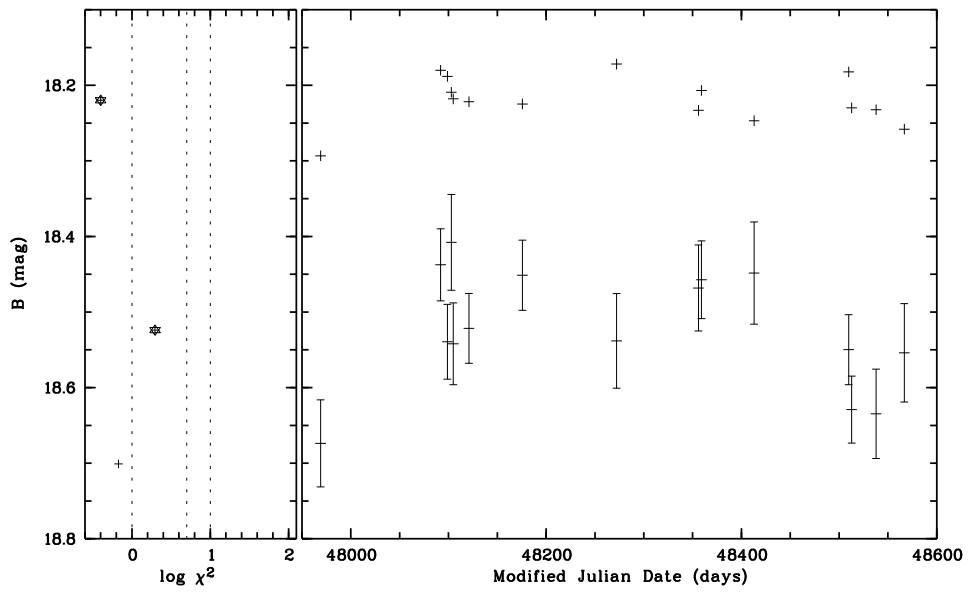
1RXS J173944.7+671052

AGN $z = 0.1180$



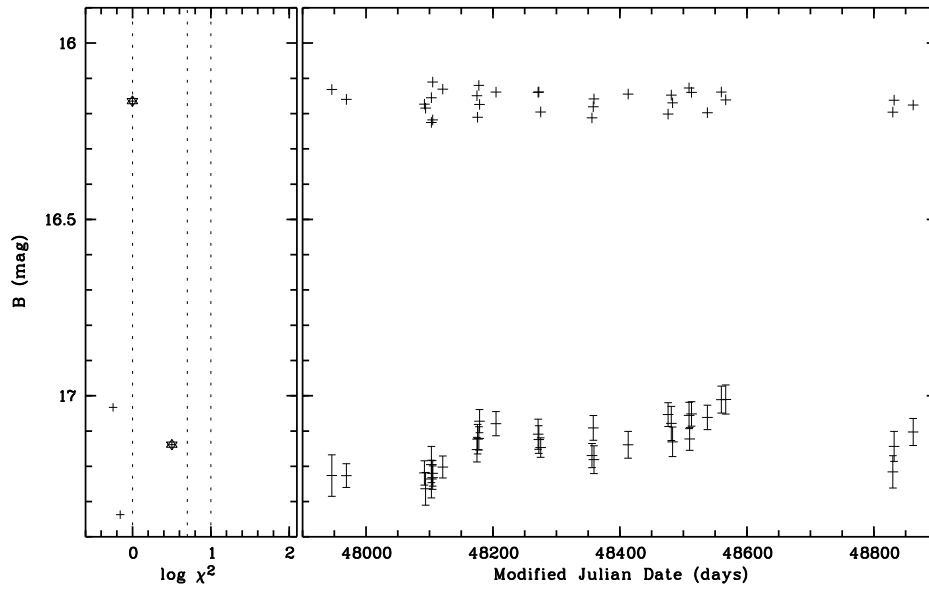
1RXS J174114.4+650743

AGN $z = 0.7466$



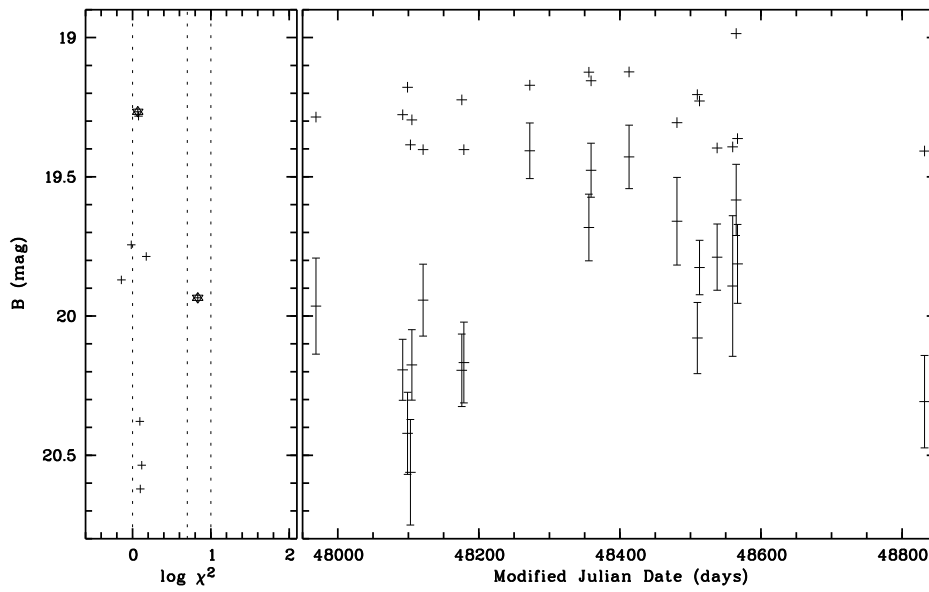
1RXS J174212.5+663949

AGN $z = 1.2720$



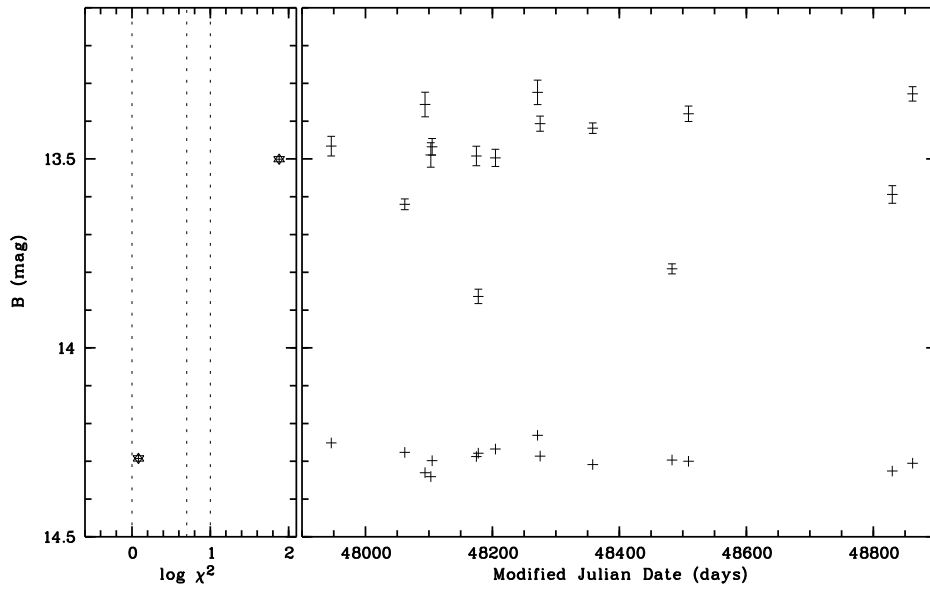
1RXS J174414.2+653455

AGN $z = 0.2550$



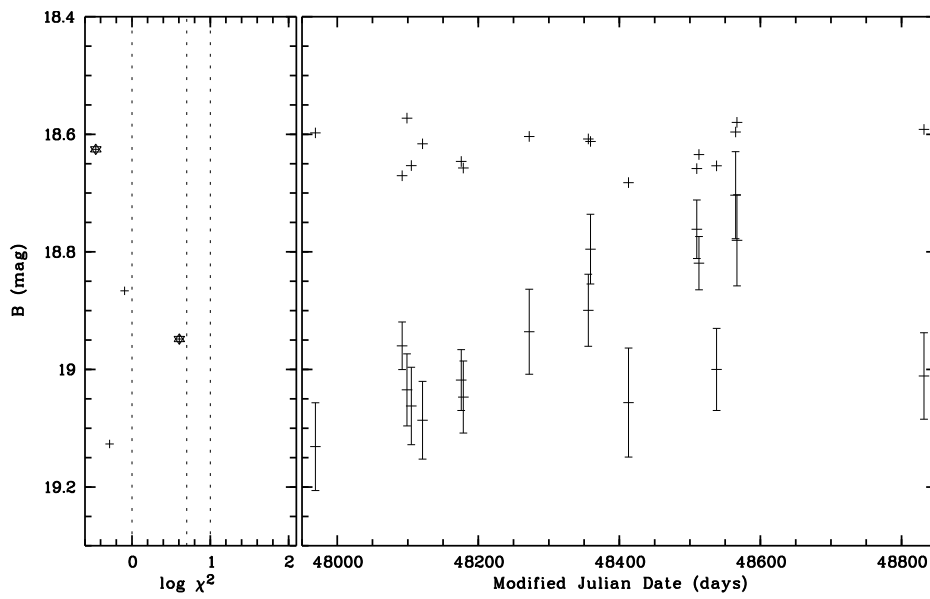
1RXS J174526.0+691819

Star



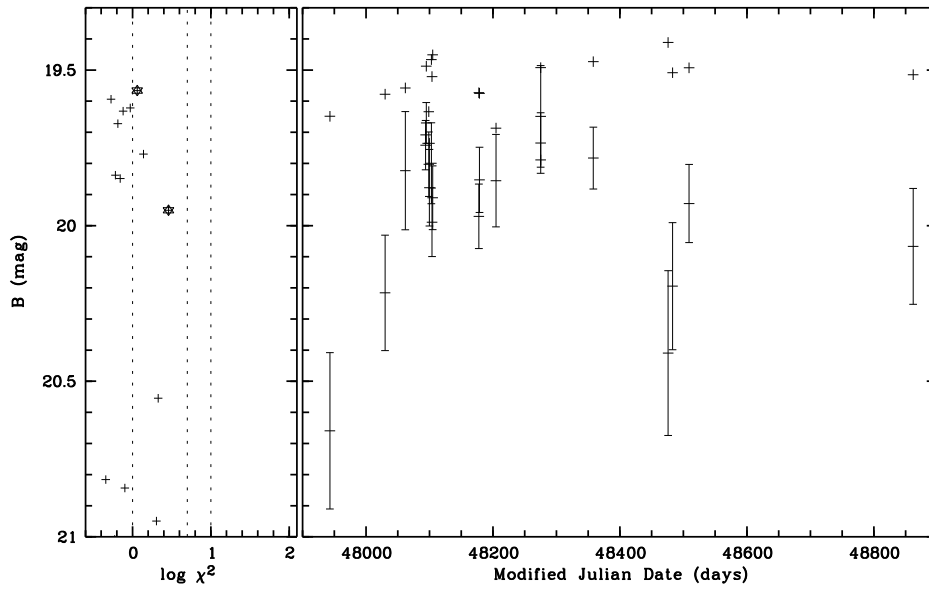
1RXS J174555.3+645118

AGN $z = 0.1790$



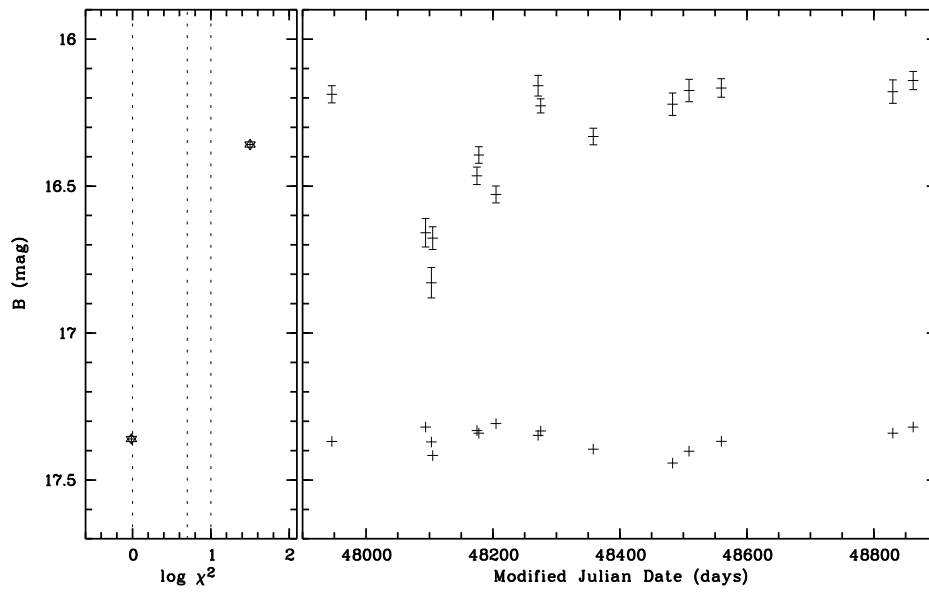
1RXS J174603.1+672709

AGN $z = 0.2146$



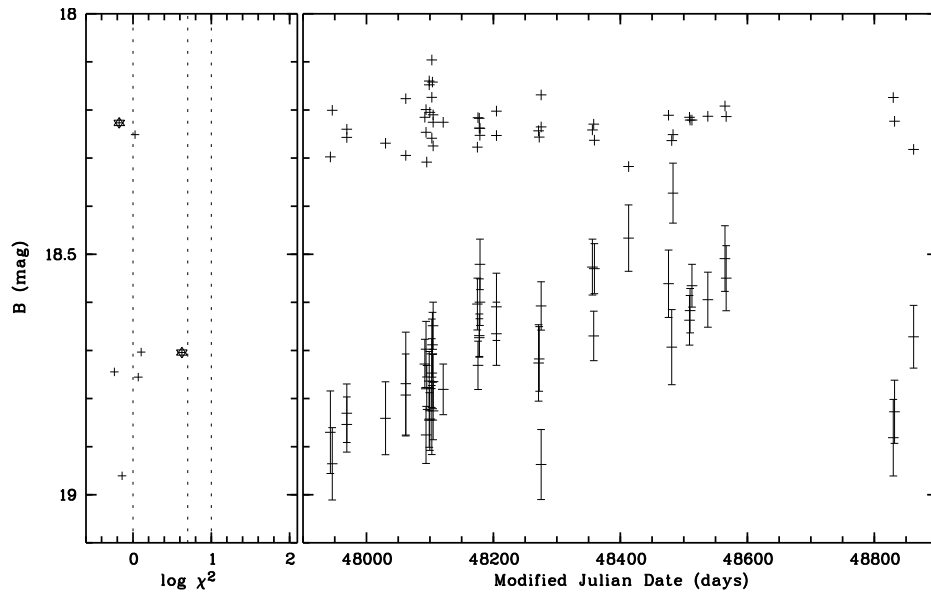
1RXS J174700.3+683626

AGN $z = 0.0630$



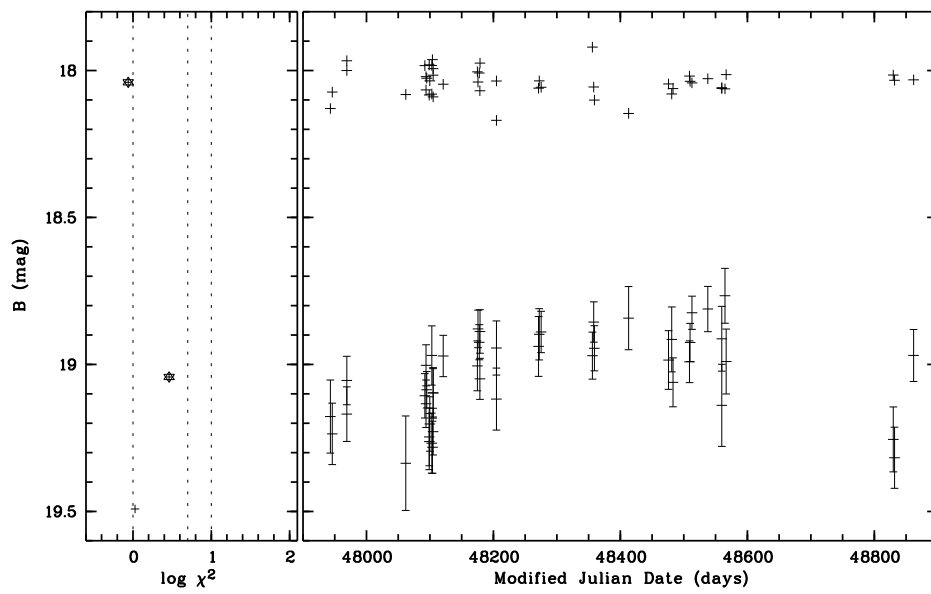
1RXS J174726.8+662628

AGN $z = 0.1391$



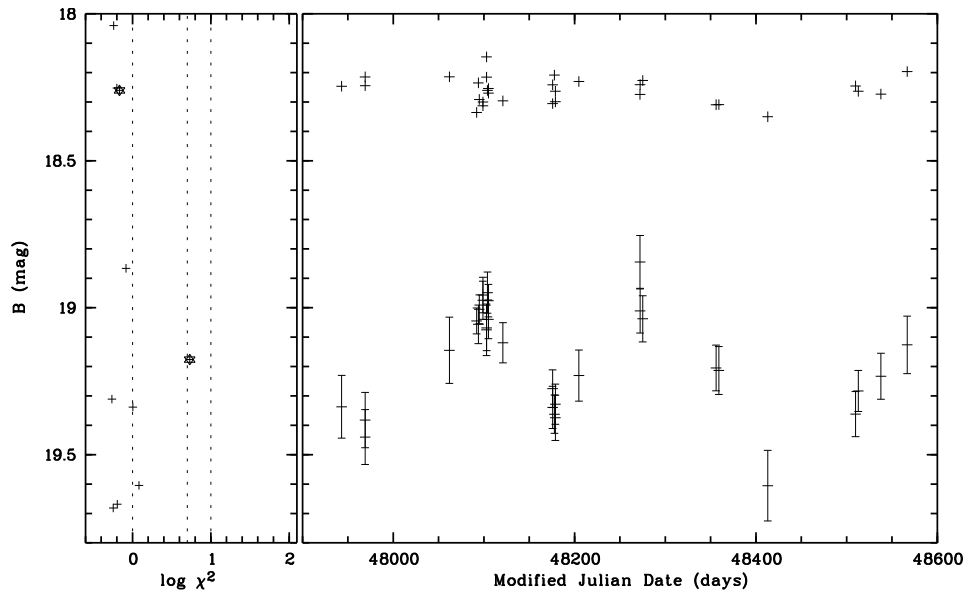
1RXS J174757.4+662327

Galaxy $z = 0.1738$



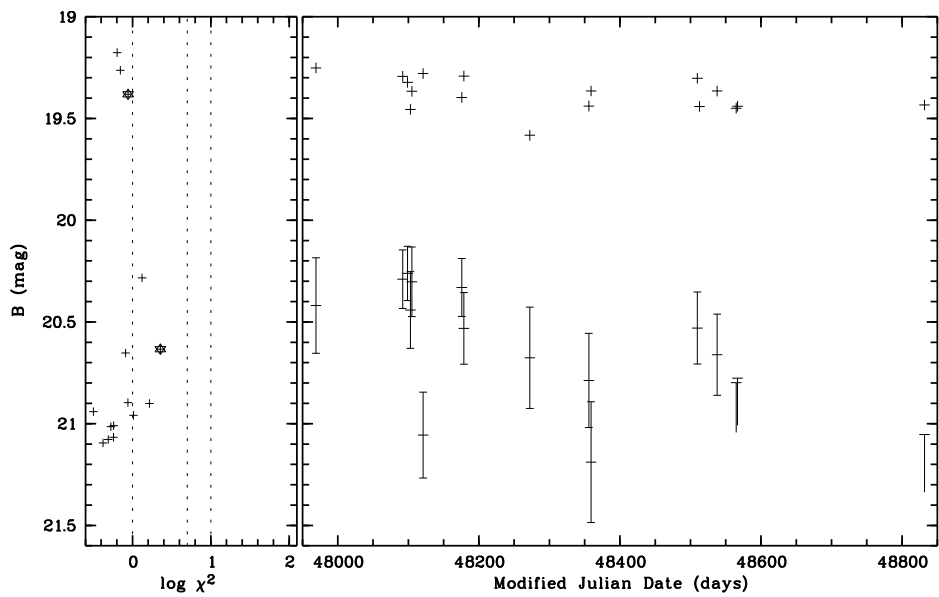
1RXS J174758.0+653835

AGN $z = 0.3248$



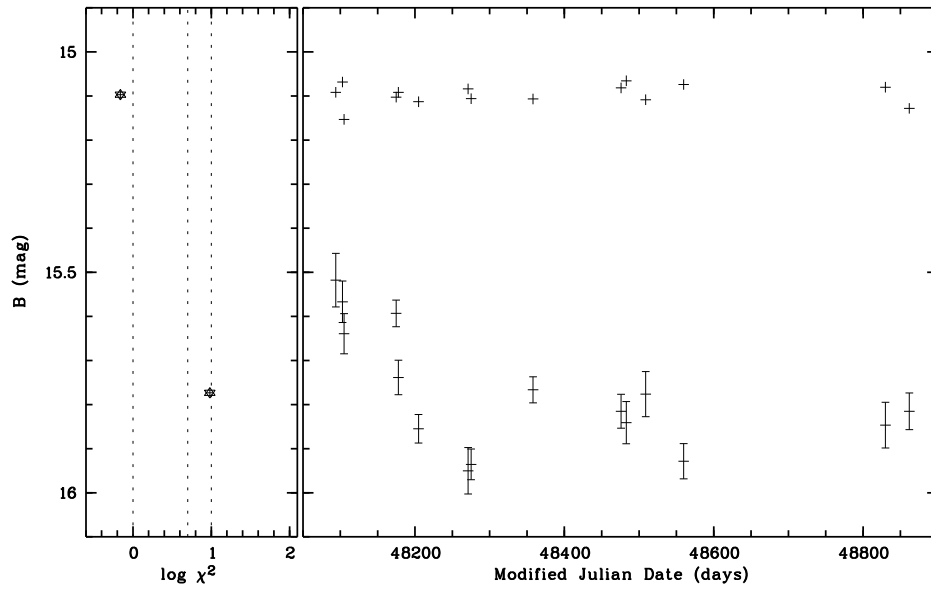
1RXS J174822.7+640327

AGN $z = 0.9859$



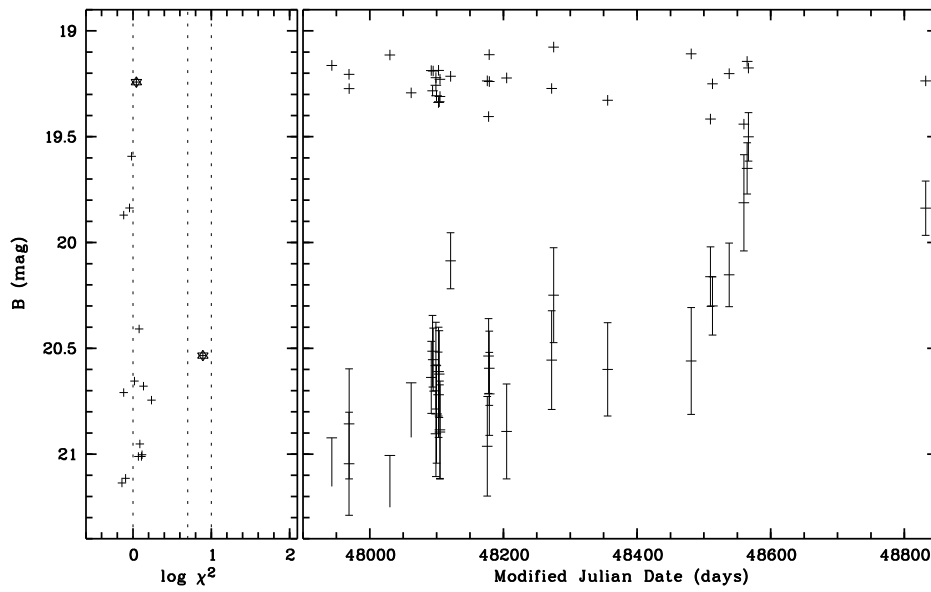
1RXS J174838.8+684211

AGN $z = 0.0537$



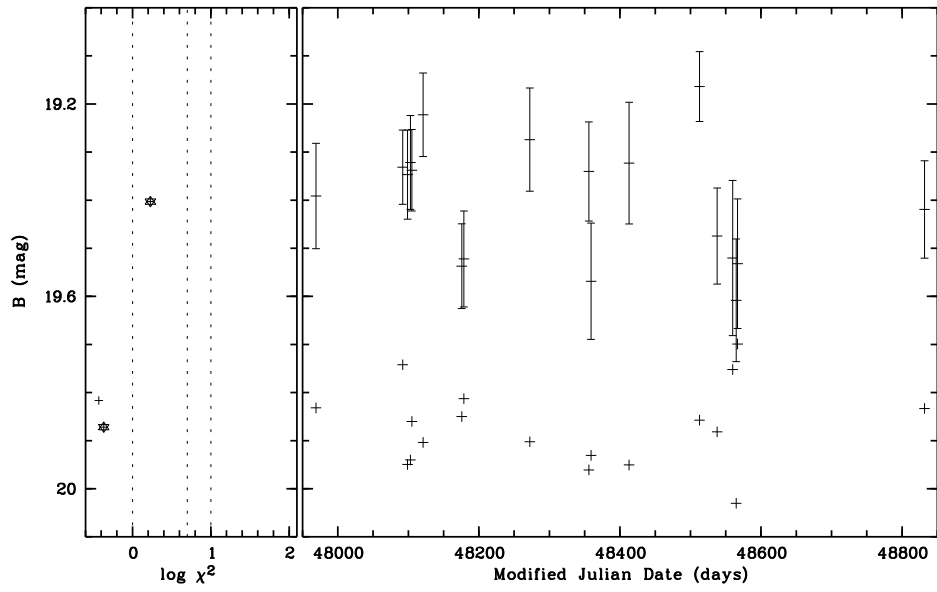
1RXS J175157.7+655120

AGN $z = 0.3901$



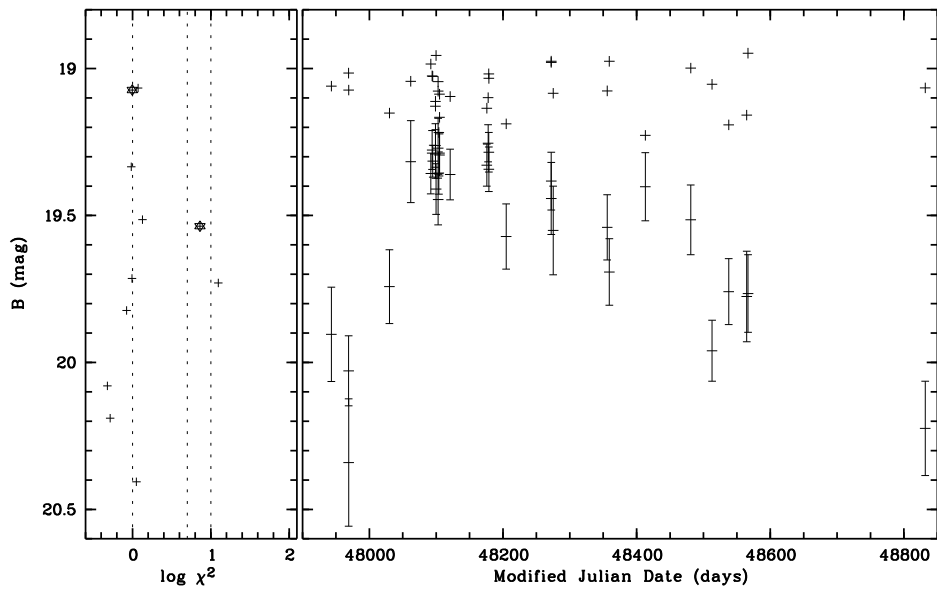
1RXS J175257.4+644058

AGN $z = 0.1230$



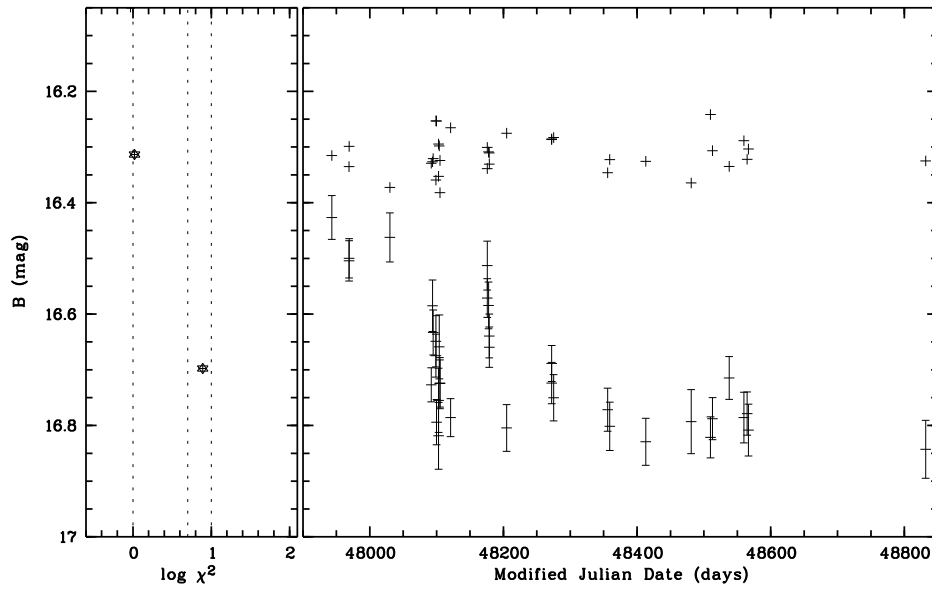
1RXS J175405.5+661354

AGN $z = 0.4067$



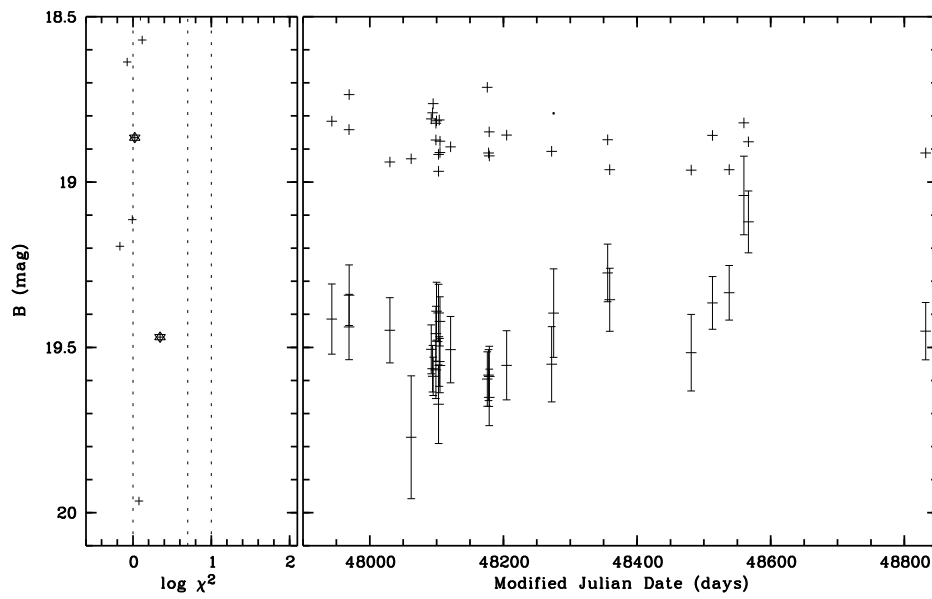
1RXS J175505.8+651951

AGN $z = 0.0785$



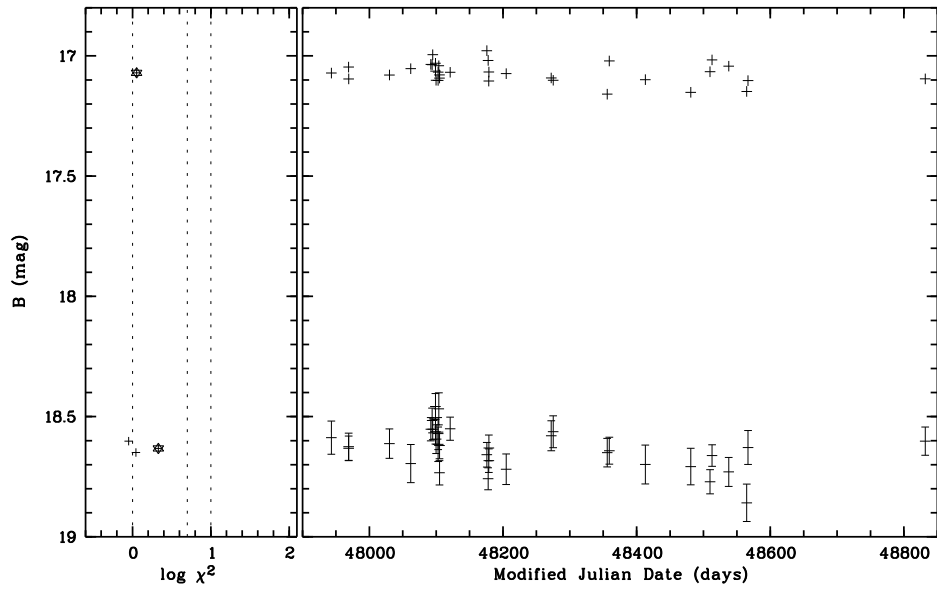
1RXS J175556.9+654054

AGN $z = 0.3238$



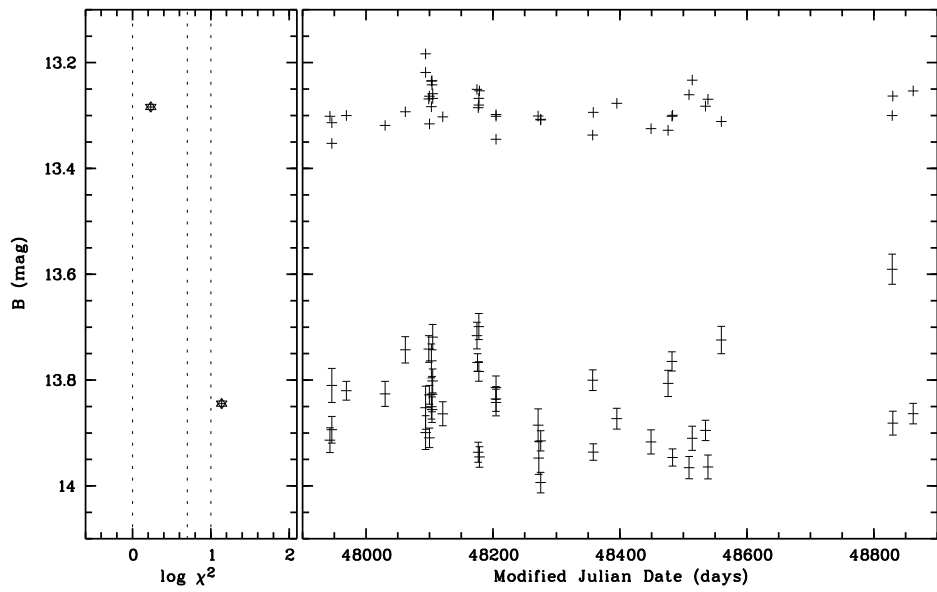
1RXS J175610.0+661514

AGN $z = 0.6357$



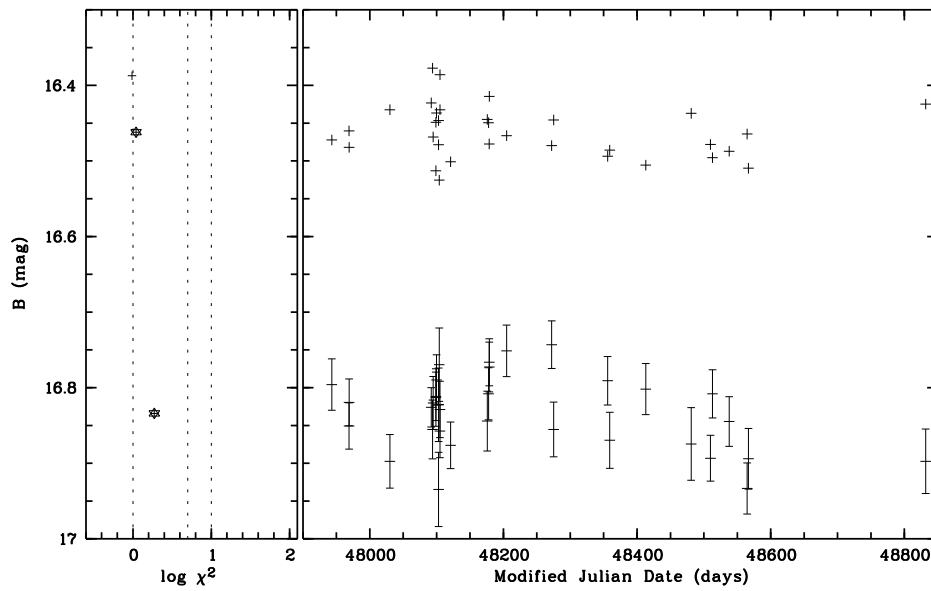
1RXS J175614.1+680707

Star



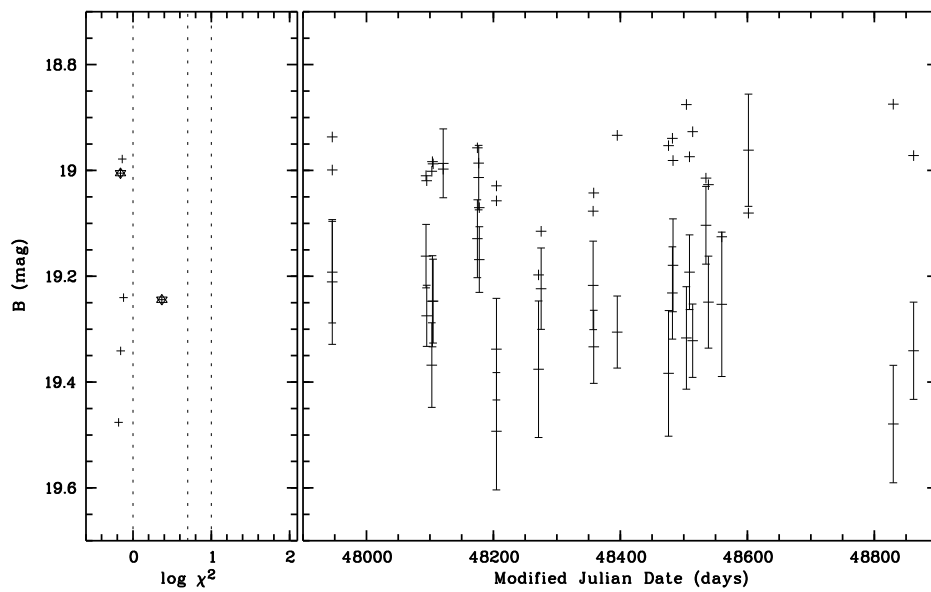
1RXS J175713.9+654702

Star



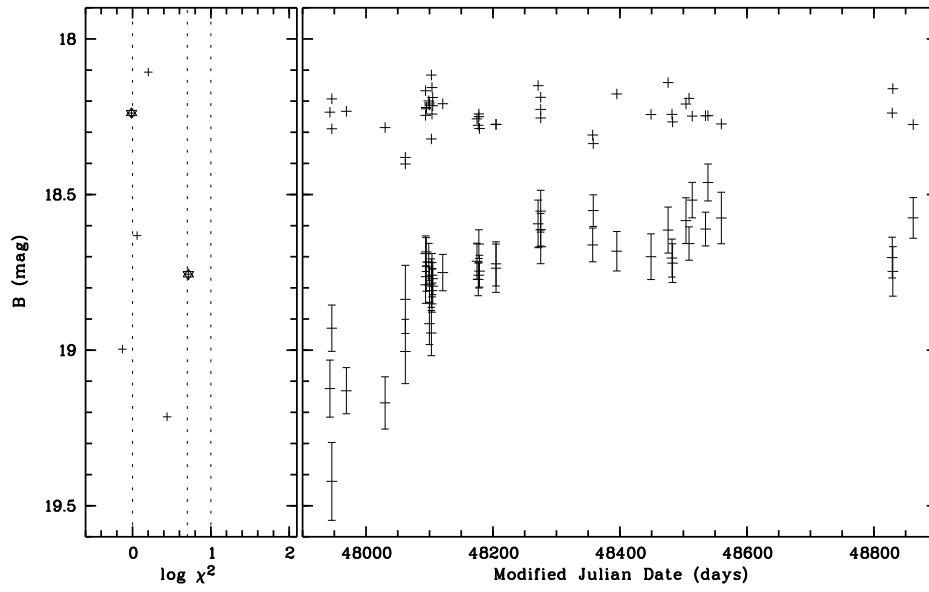
1RXS J175734.1+684122

AGN $z = 0.1814$



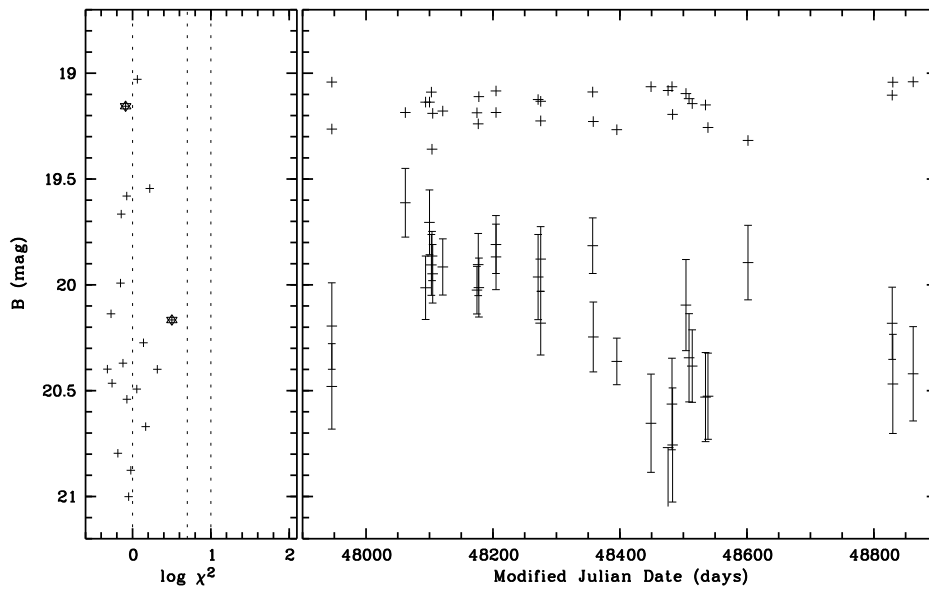
1RXS J175813.2+674319

AGN $z = 0.2045$



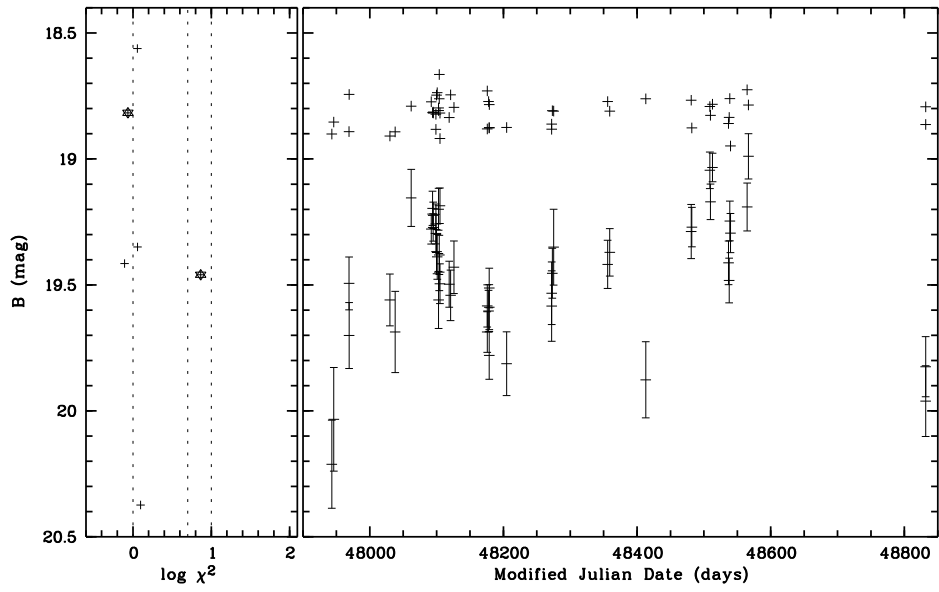
1RXS J175818.8+690631

AGN $z = 2.1572$



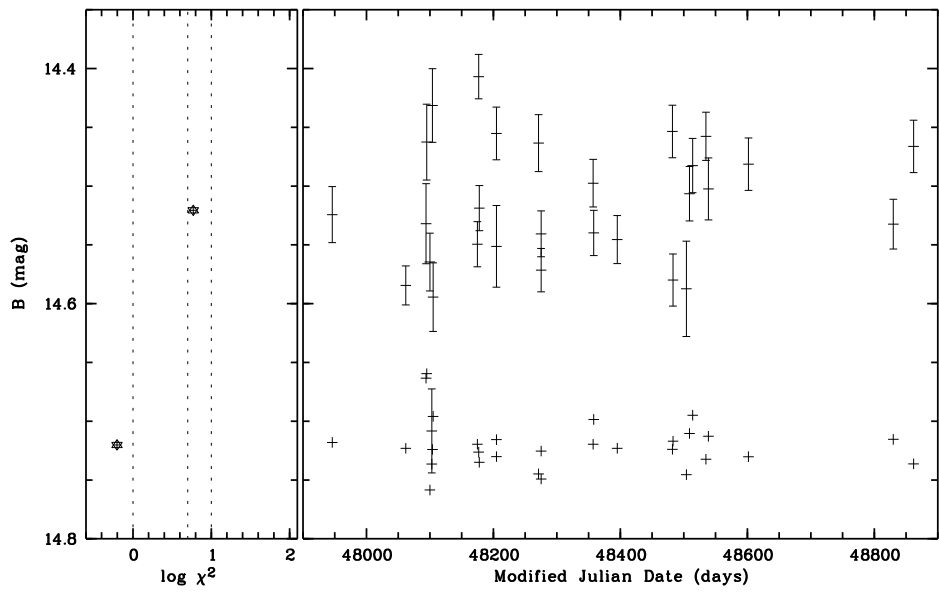
1RXS J175824.2+653105

AGN $z = 0.3250$



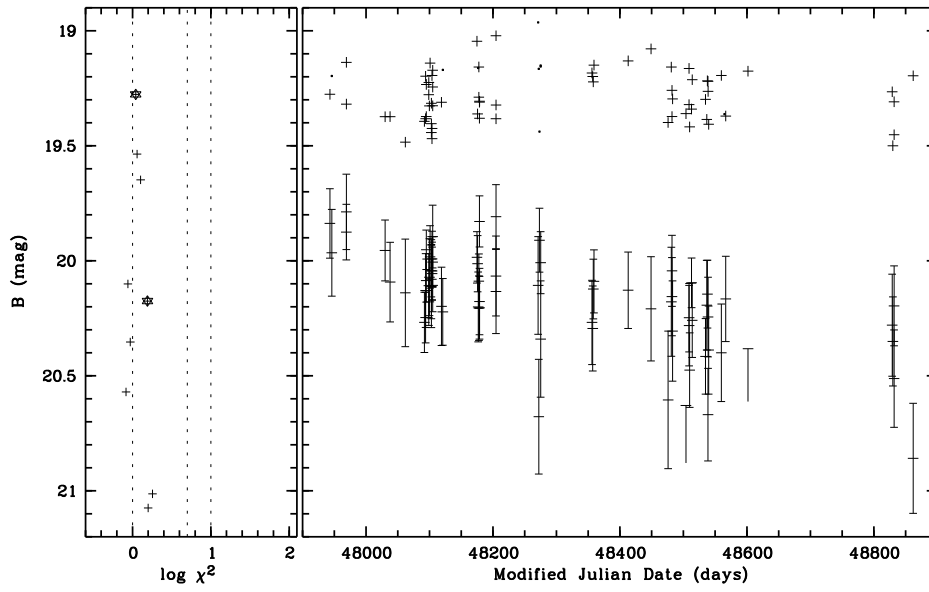
1RXS J180009.9+683557

white dwarf



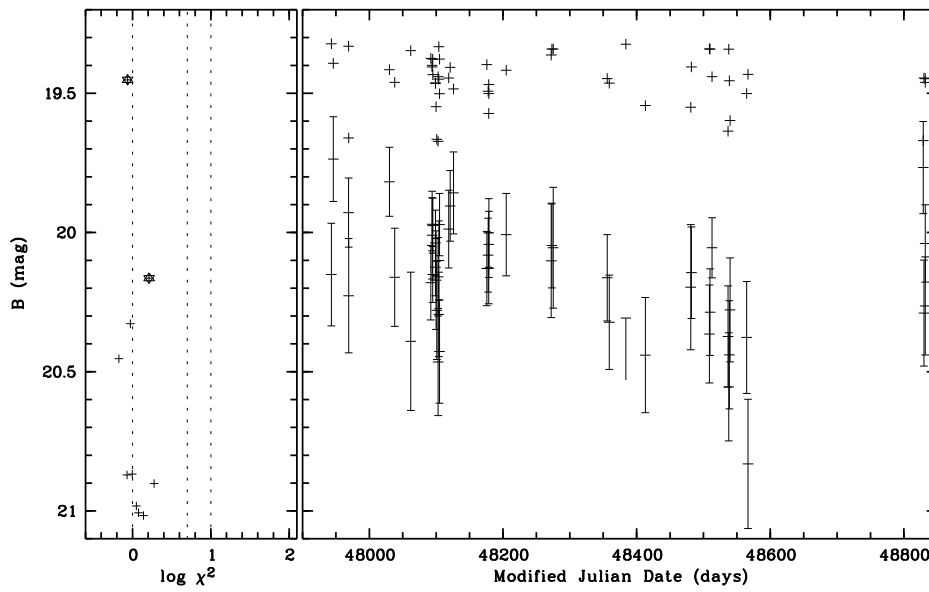
1RXS J180022.1+662501

AGN $z = 1.6200$



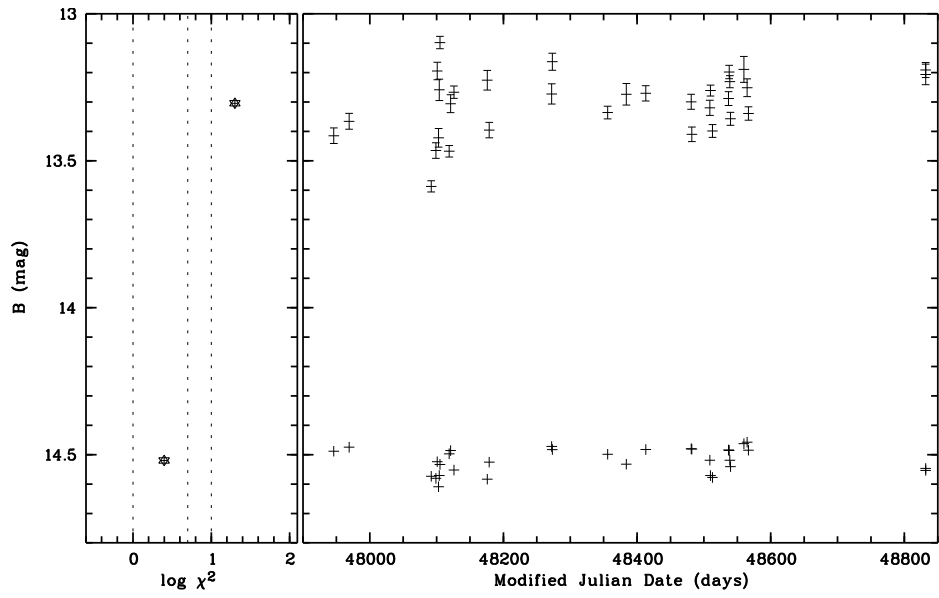
1RXS J180023.1+661554

AGN $z = 0.4475$



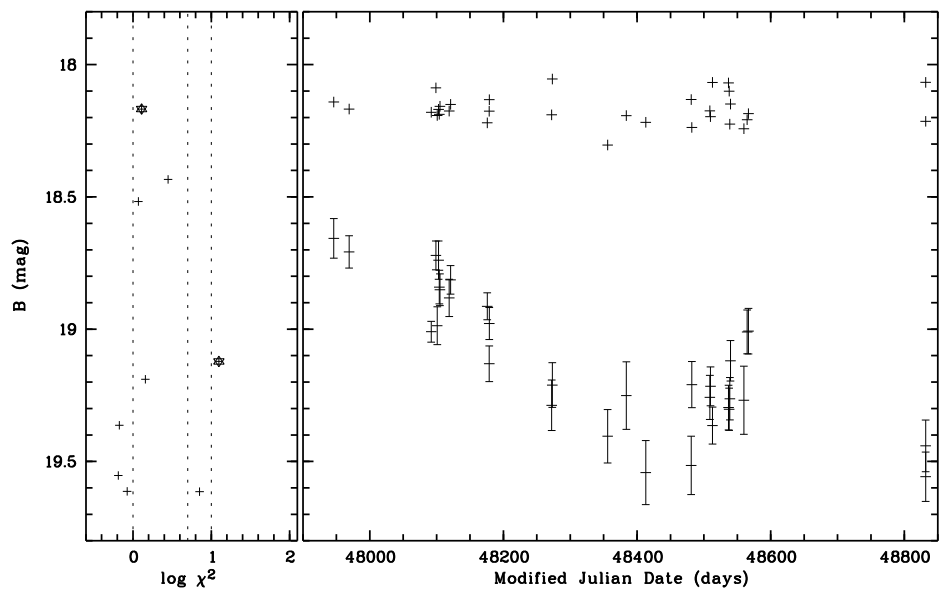
1RXS J180023.9+634953

Star



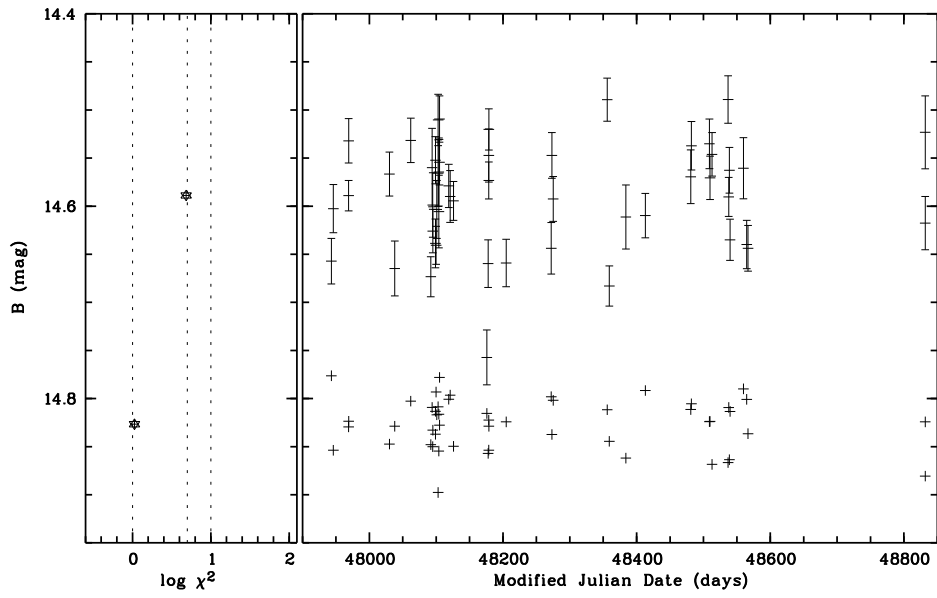
1RXS J180026.2+635719

AGN $z = 0.6828$



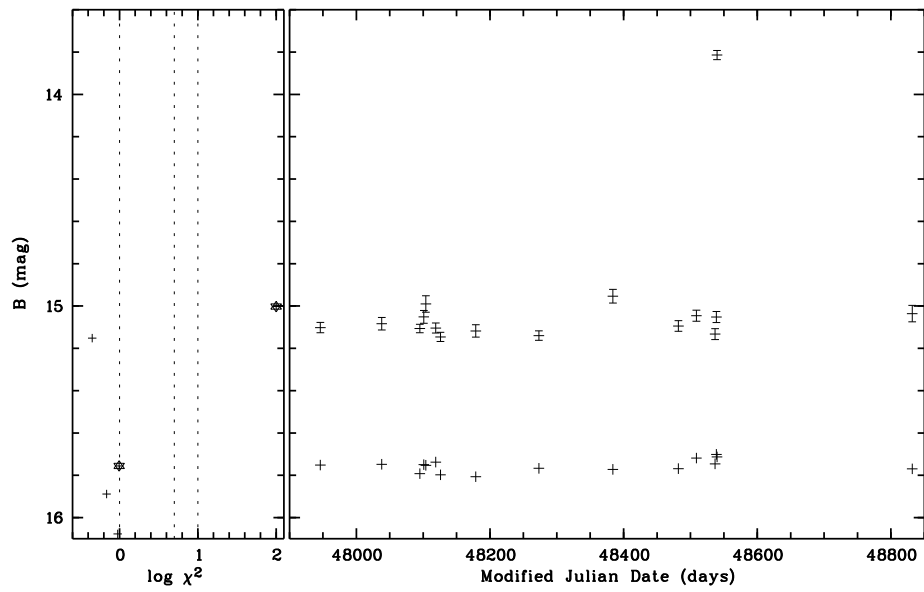
1RXS J180057.6+660058

Star



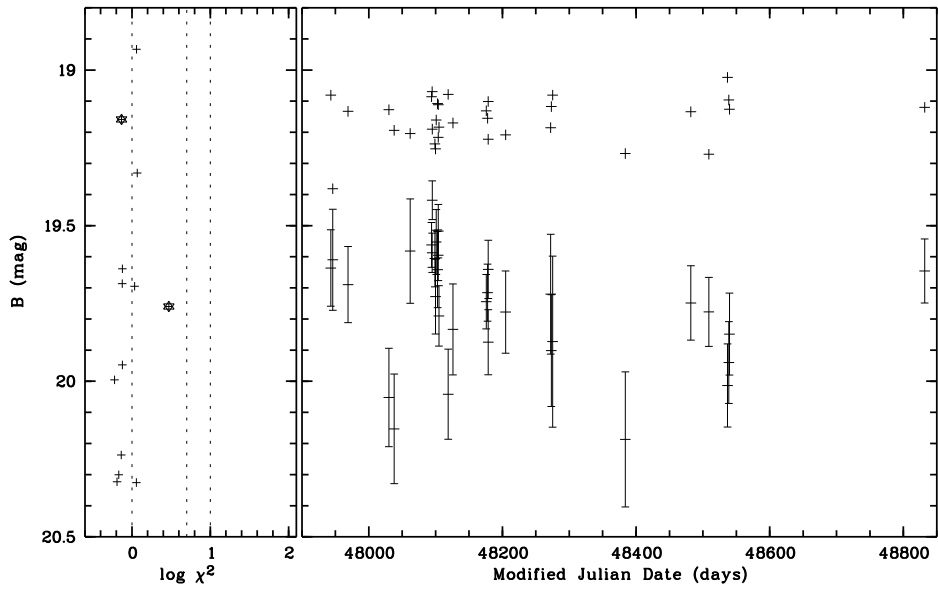
1RXS J180216.3+641546

Star



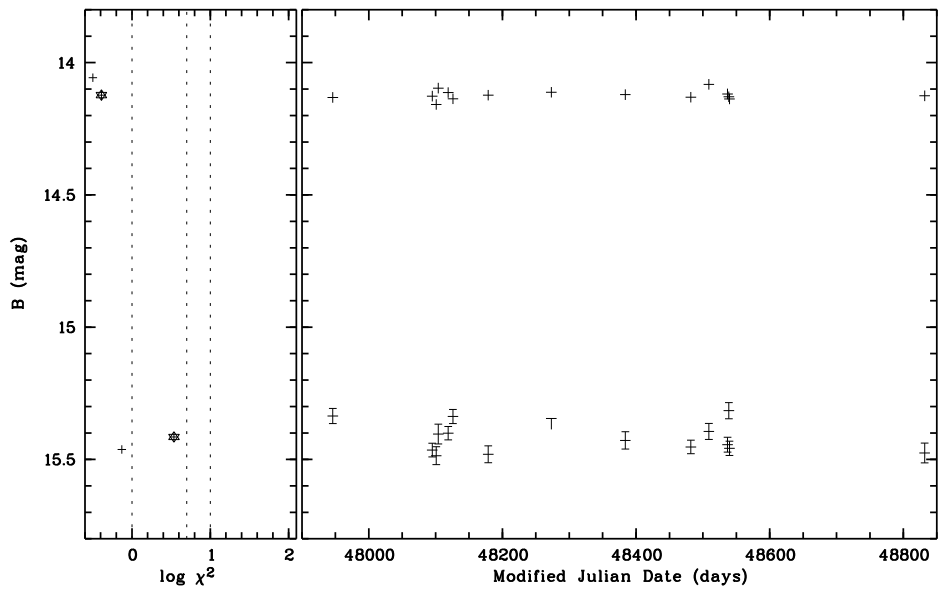
1RXS J180251.3+660540

AGN $z = 0.2070$



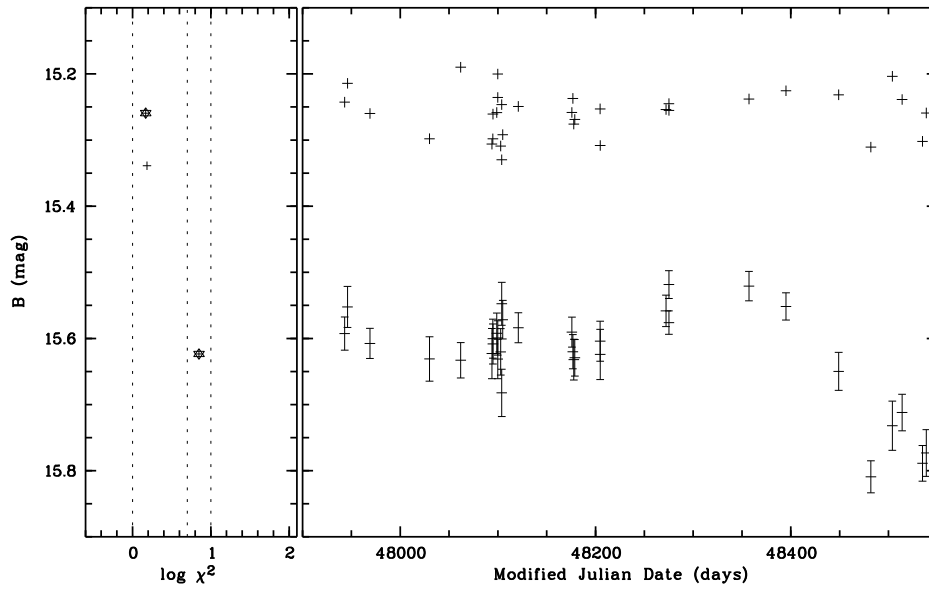
1RXS J180305.7+644526

Star



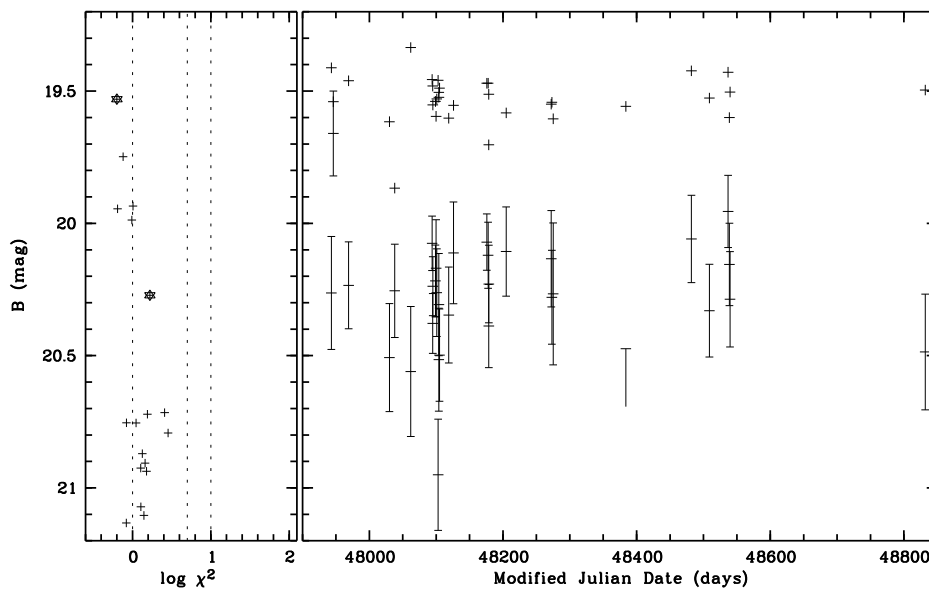
1RXS J180328.4+673806

AGN $z = 0.1360$



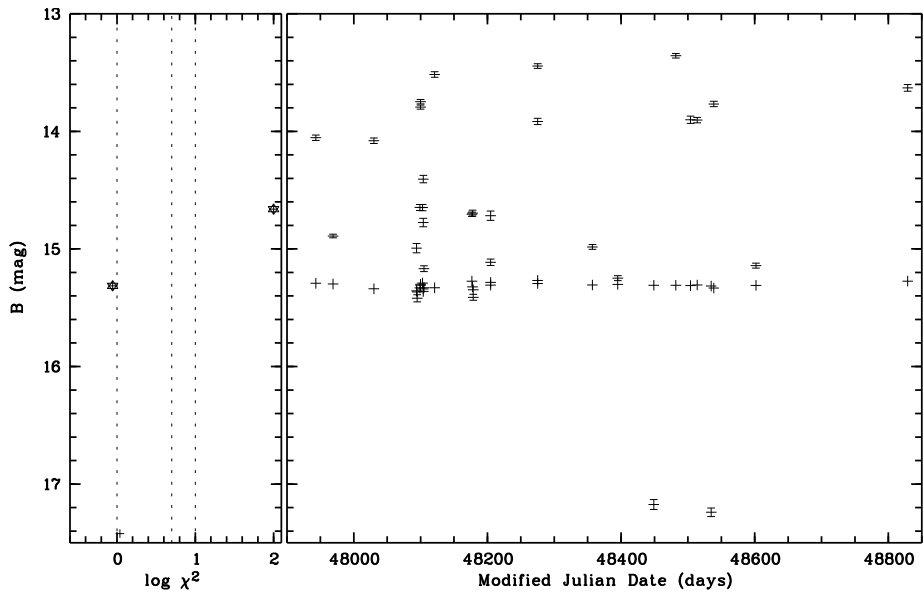
1RXS J180354.5+654827

BL Lac $z = 0.085$



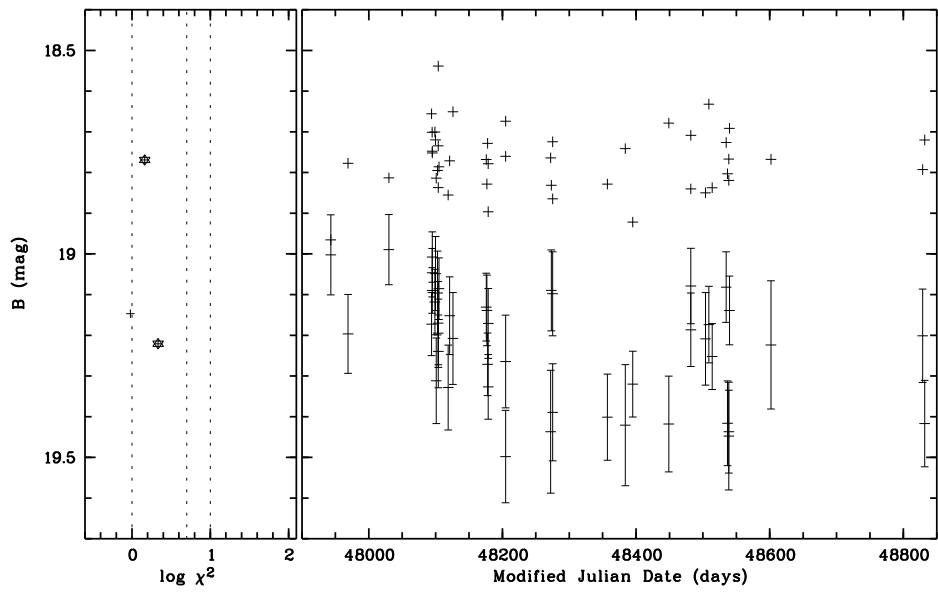
1RXS J180413.4+675412

cataclysmic variable



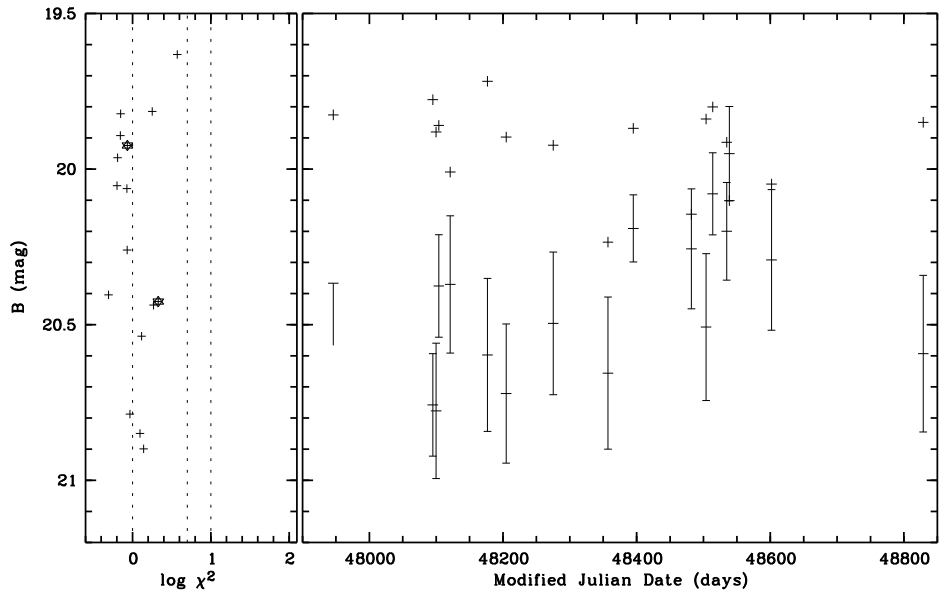
1RXS J180525.4+663859

AGN $z = 0.1449$



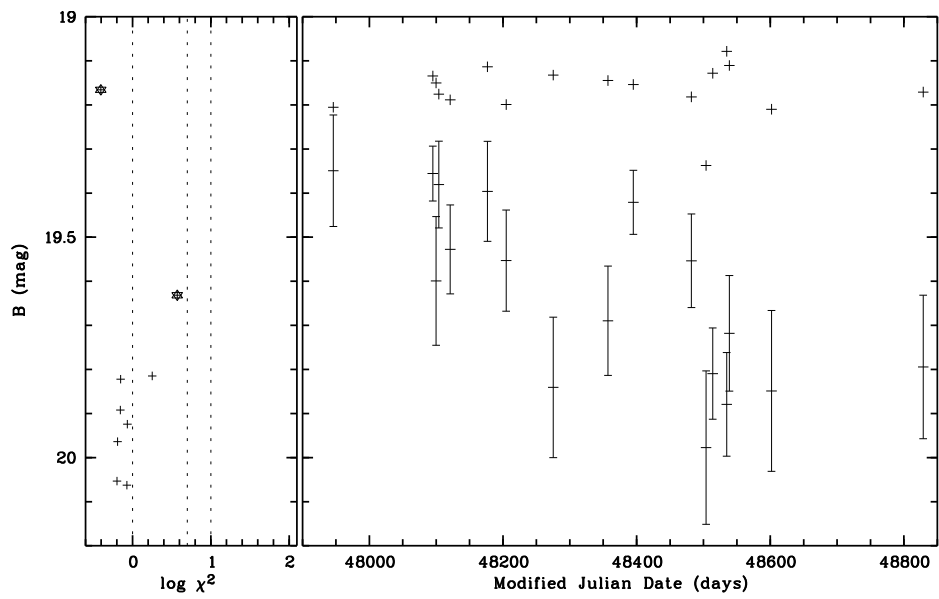
1RXS J180606.7+681308a

AGN/Cluster $z = 0.2953$



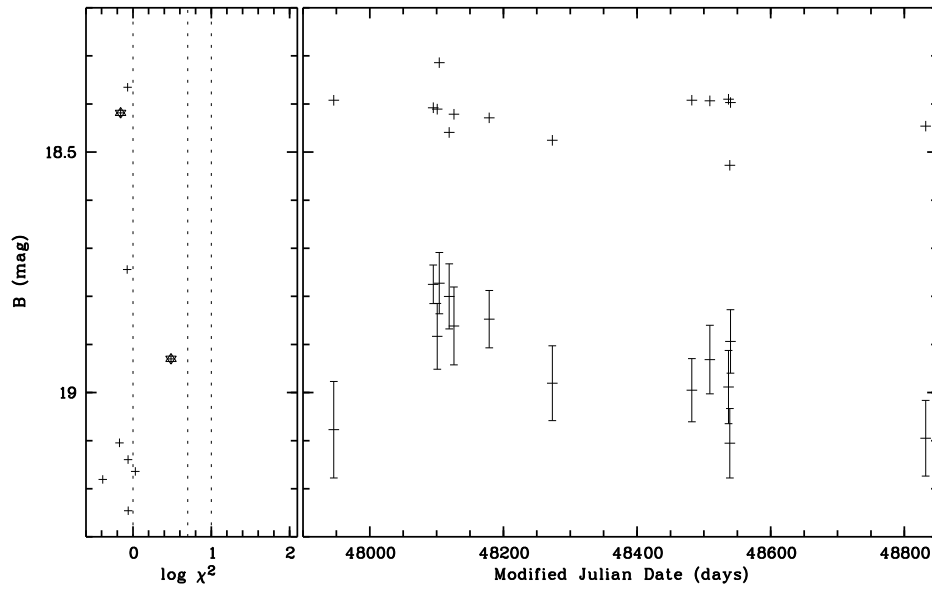
1RXS J180606.7+681308b

AGN/Cluster $z = 0.3030$



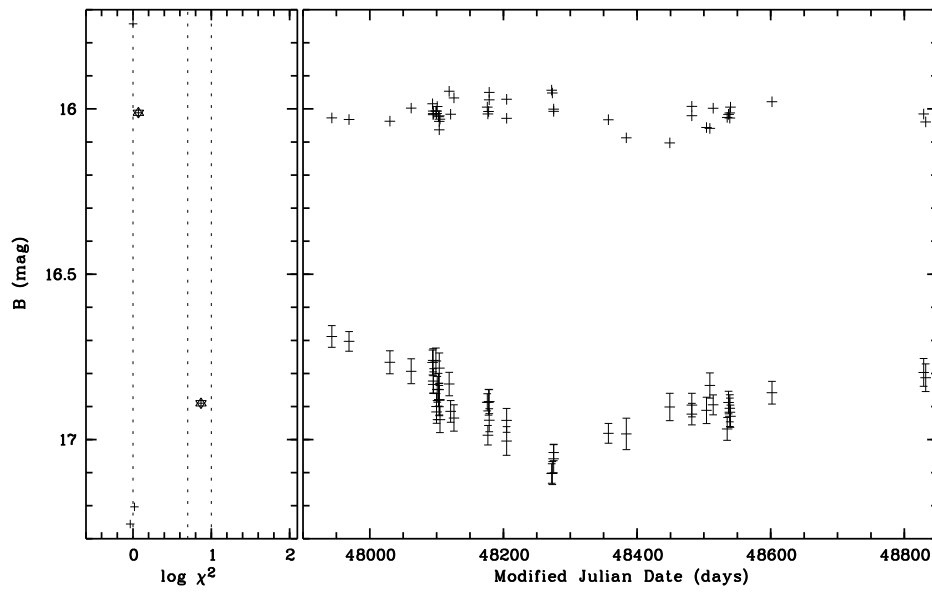
1RXS J180802.6+645225

AGN $z = 1.0360$



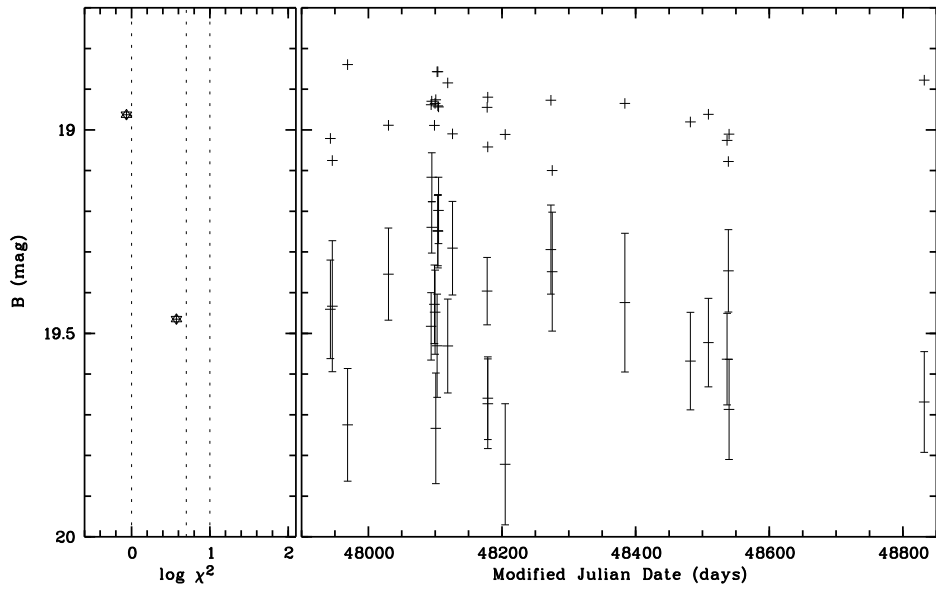
1RXS J180849.9+663431

AGN $z = 0.6970$



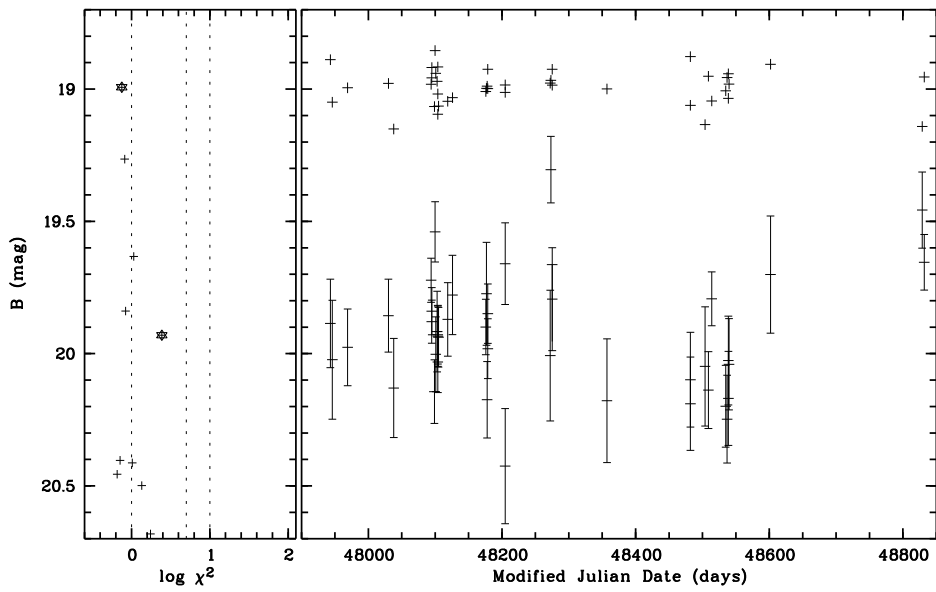
1RXS J180851.1+653022

AGN $z = 0.2937$



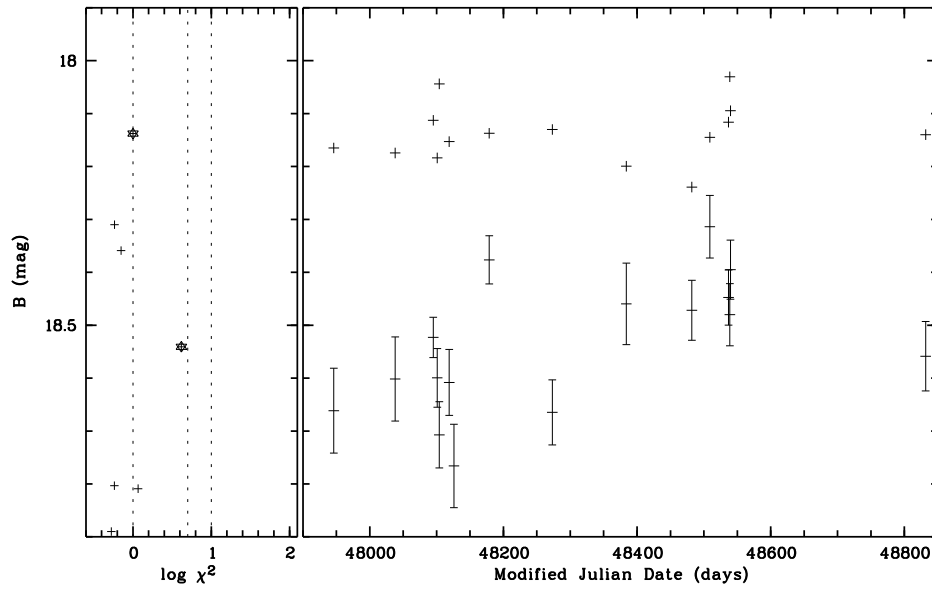
1RXS J180930.2+662033

AGN $z = 0.6350$



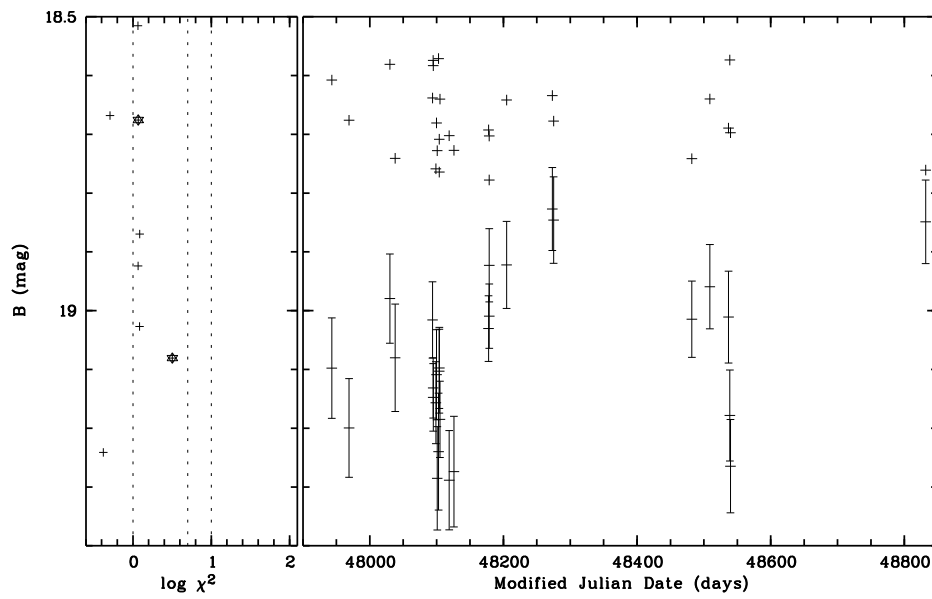
1RXS J181004.3+634424

AGN $z = 0.3770$



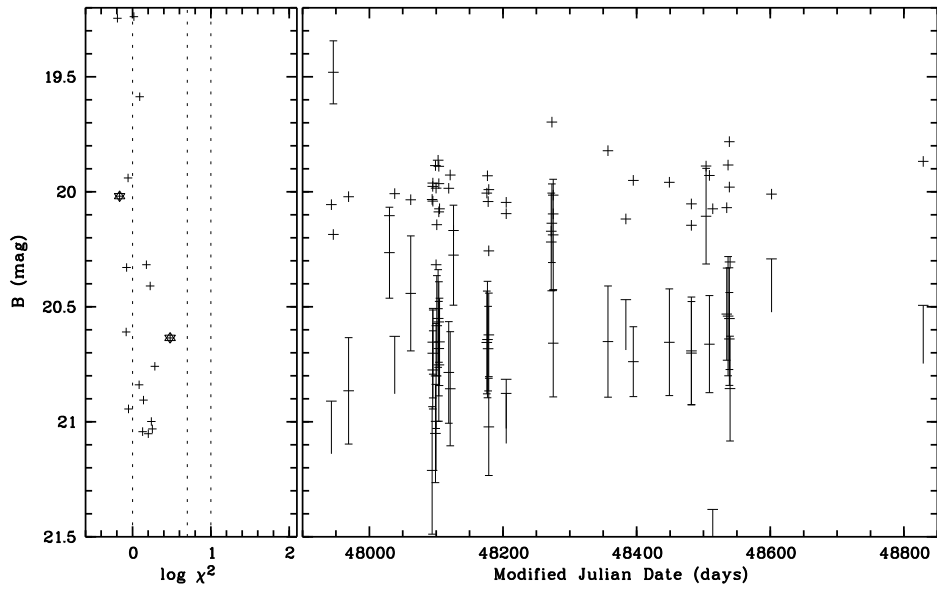
1RXS J181112.4+654346

AGN $z = 0.4895$



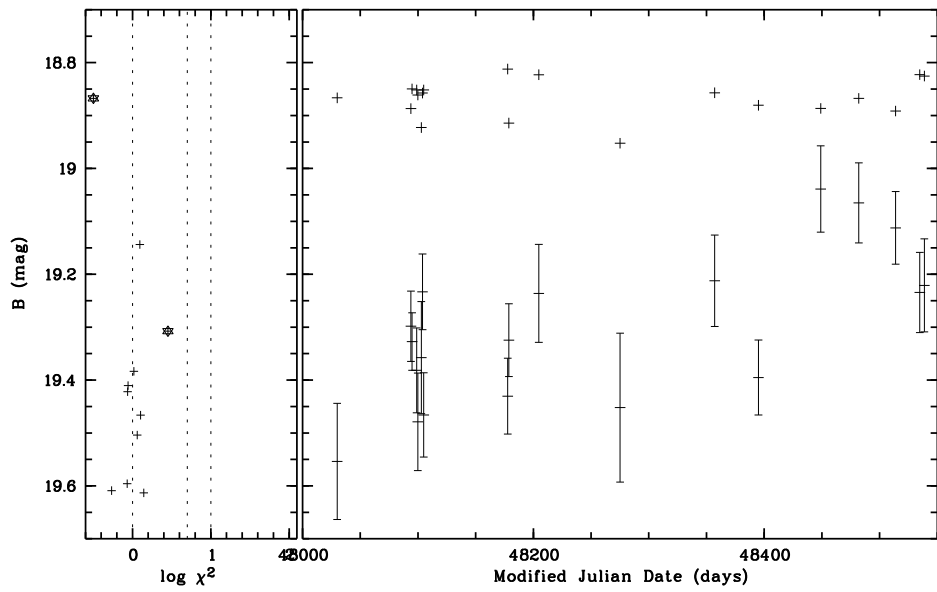
1RXS J181345.6+662849

Star



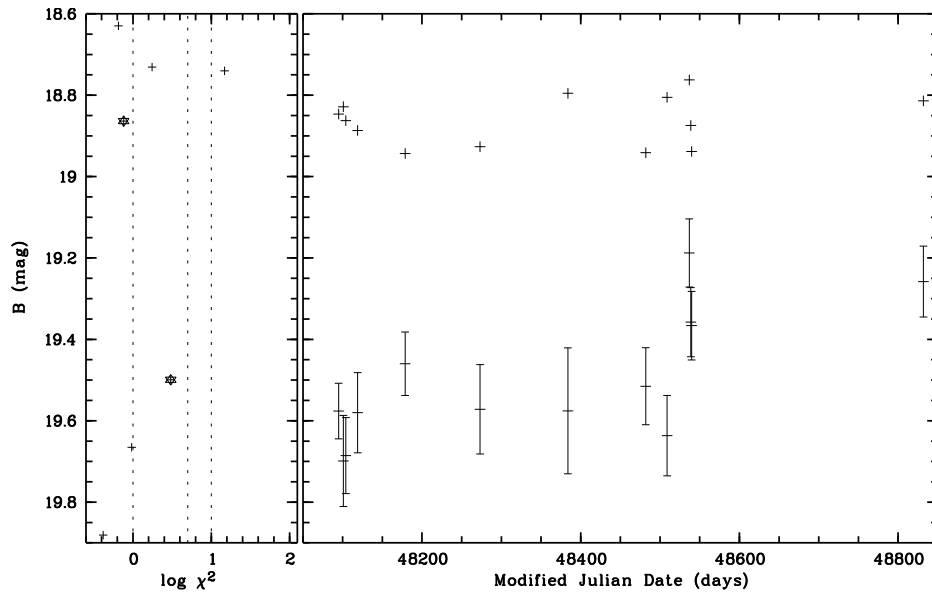
1RXS J181351.0+672811

AGN $z = 0.3196$



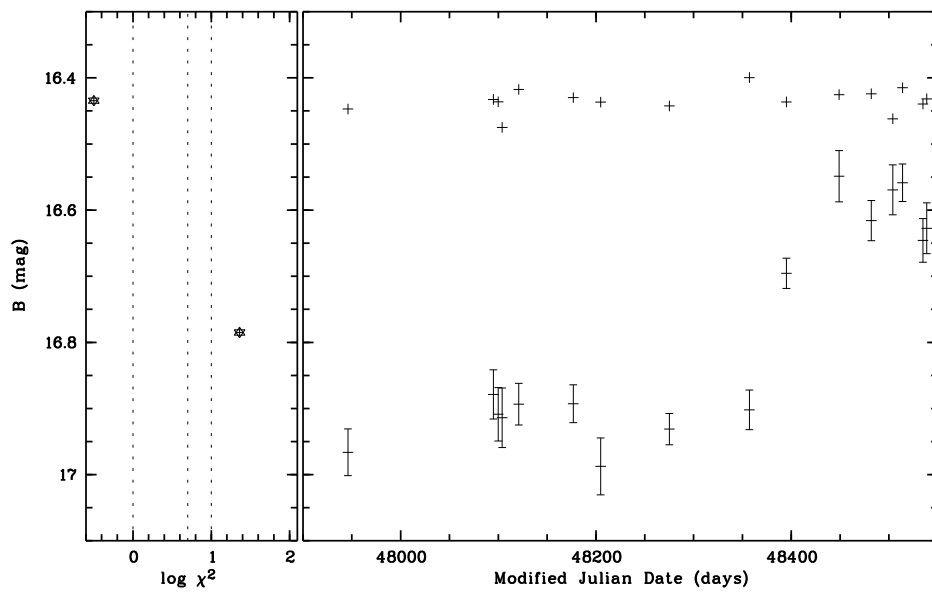
1RXS J181552.4+644101

AGN $z = 0.4116$



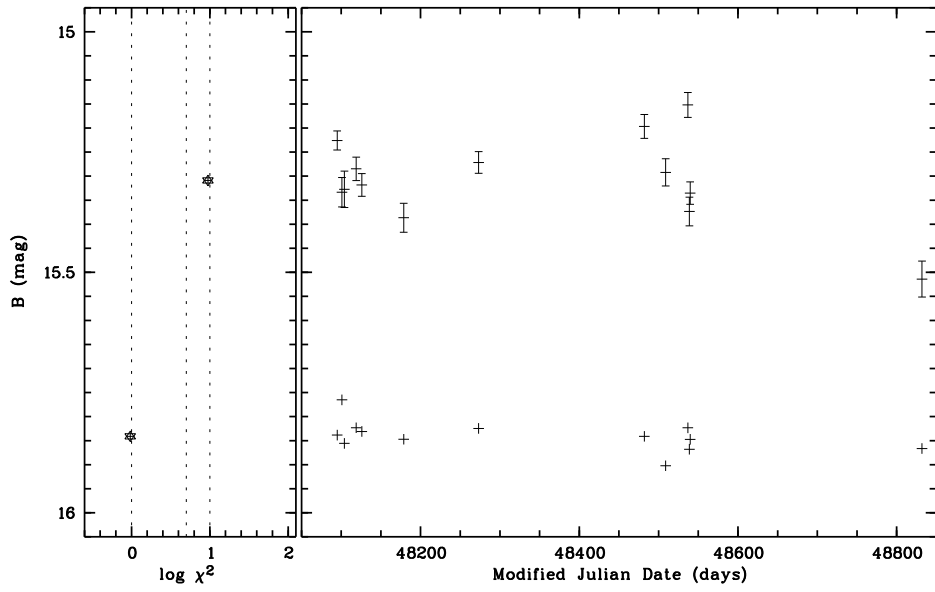
1RXS J181829.0+674127

AGN $z = 0.3140$



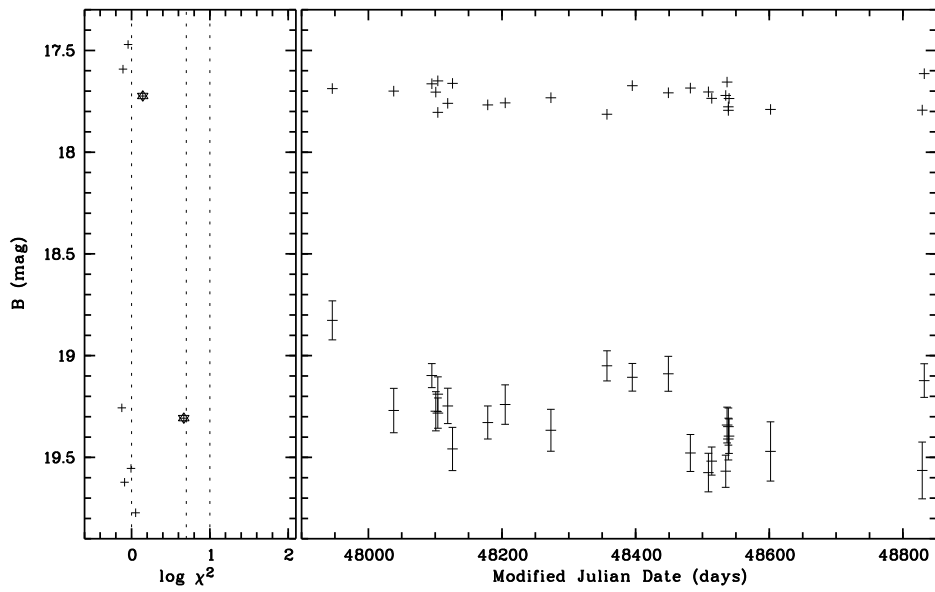
1RXS J181857.3+661135

Star



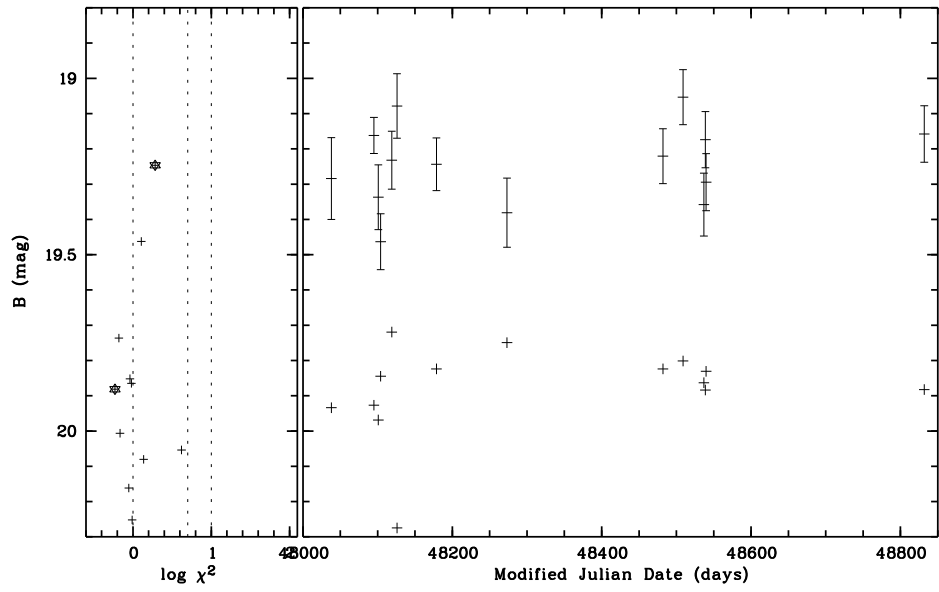
1RXS J182032.9+662029

AGN $z = 0.5057$



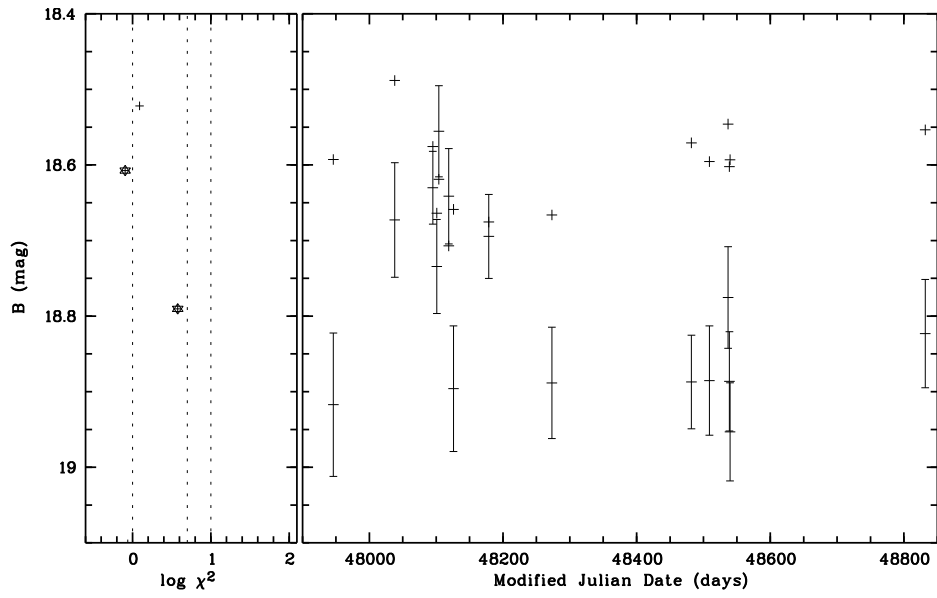
1RXS J182138.8+654304

AGN $z = 0.2666$



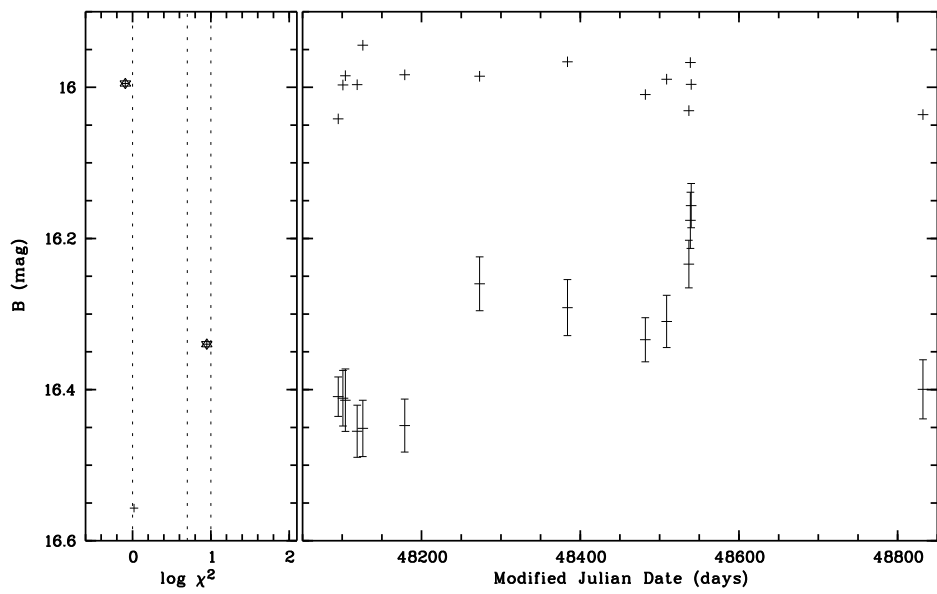
1RXS J182320.1+641924

AGN $z = 0.5766$



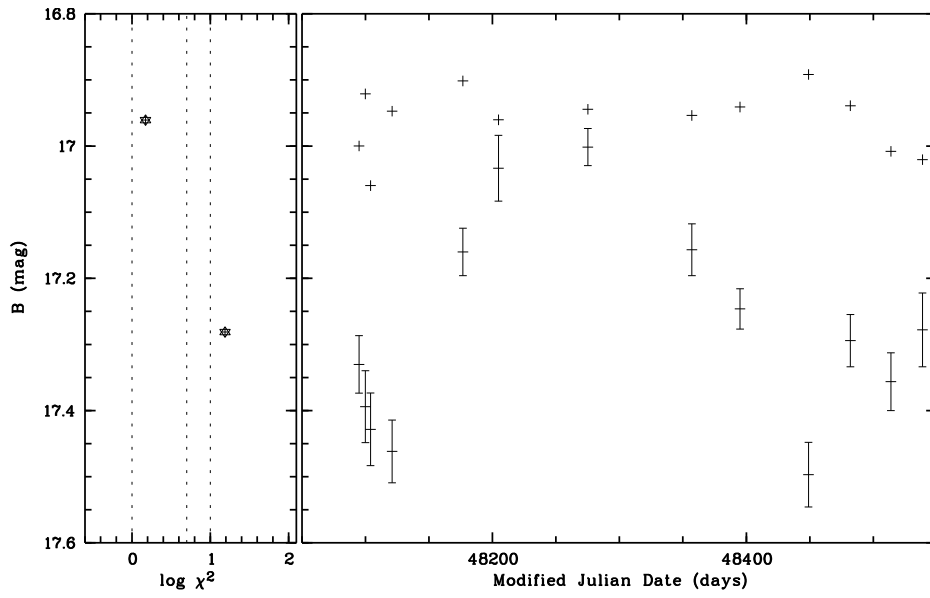
1RXS J182447.0+650924

AGN $z = 0.3030$



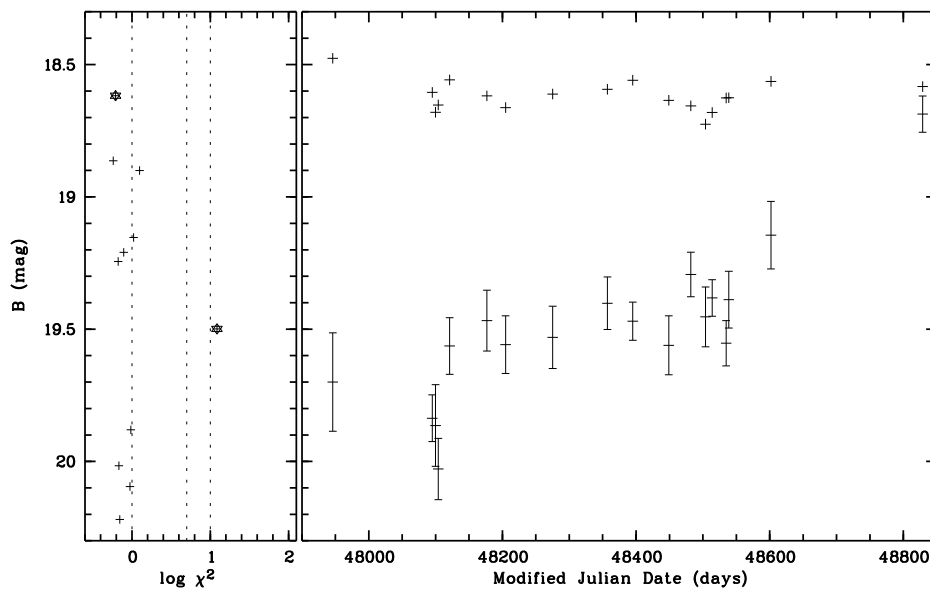
1RXS J182546.4+690551

AGN $z = 0.0888$



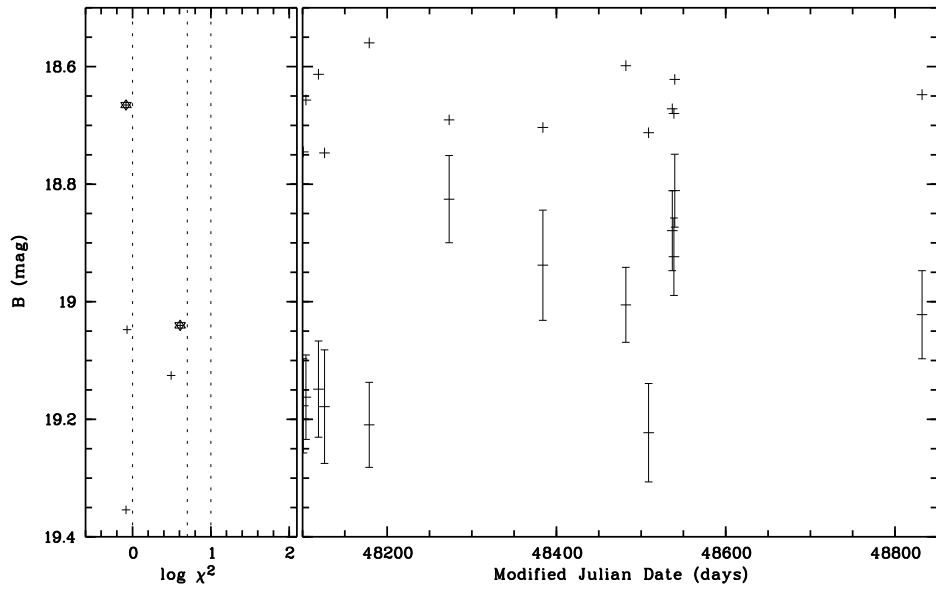
1RXS J182638.3+670647

AGN $z = 0.2870$



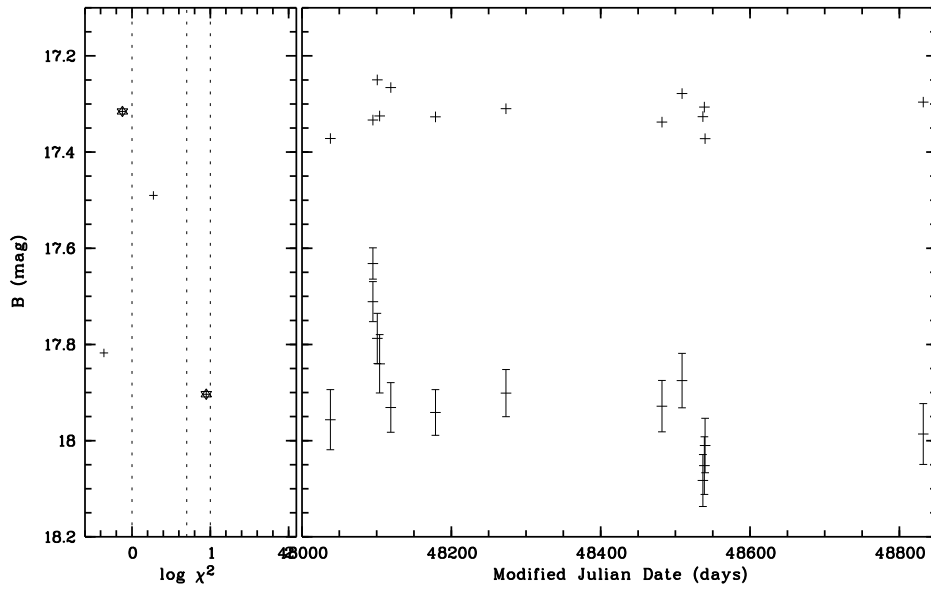
1RXS J182733.6+643138

AGN $z = 0.0977$



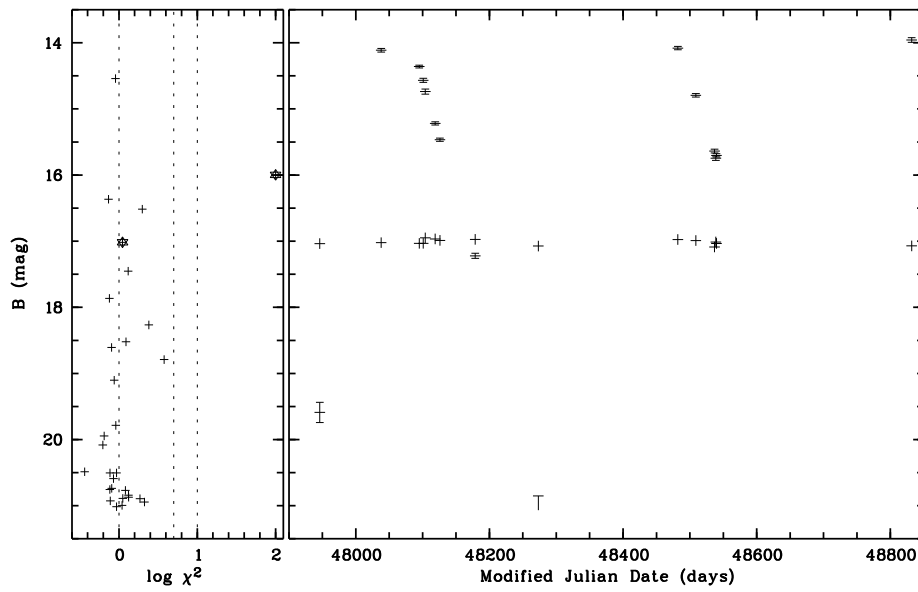
V J181958.6+652023

Galaxy/AGN, no X-counterpart



IY Dra

Star, no X-counterpart



G Finding charts

This appendix contains finding charts for each field within our study area. The layout for each field is similar and contains, on the left, a DSSII-R (Digitized Sky Survey, 2nd generation, red passband) image with sky coordinates. For a few exceptional cases where the R band image is of inferior quality, the B (blue) field is used instead. On the right is shown a stacked image generated from the Tautenburg Schmidt plates with the error circle of the X-ray position and, for extended sources (RASS extension likelihood > 10), a superimposed extension circle.

For bright stars or sources that were excluded from the variability survey, only the DSSII finding charts is available. For an explanation of the layout see below.

Also printed are the identification data, e.g. star or AGN, redshifts for extragalactic objects, magnitudes and, for point sources, the coordinates of the optical counterparts; these may differ from the coordinates given in the object designator which are derived from the X-ray coordinates.

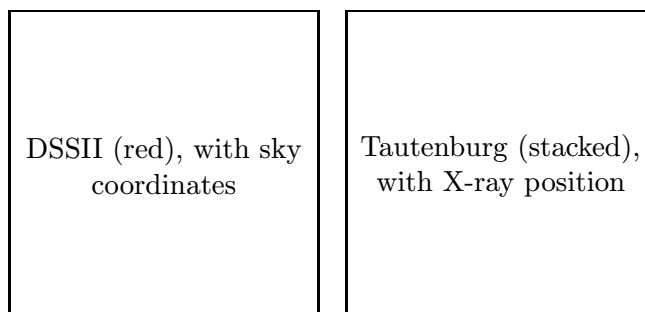
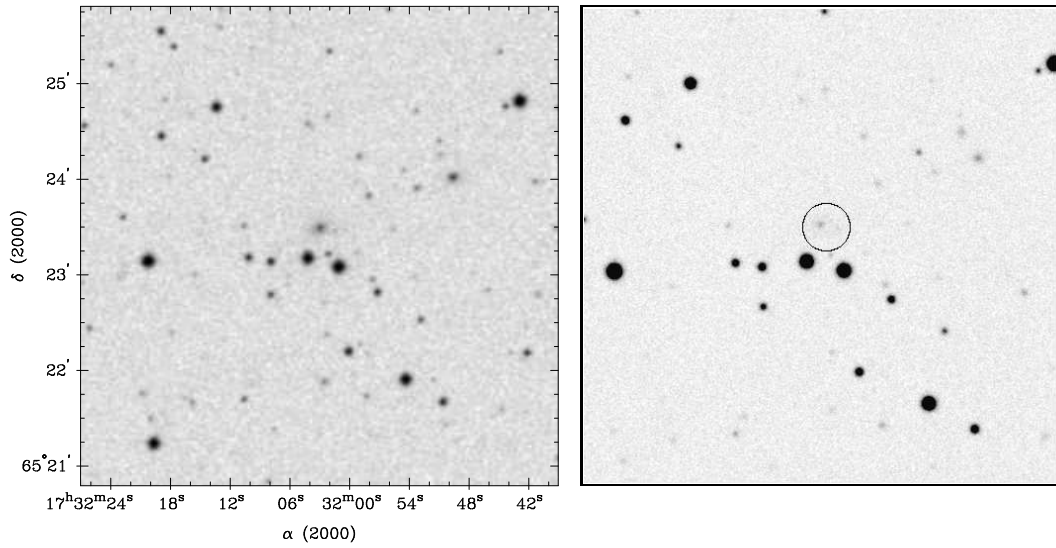


Figure 58: Finding charts layout

1RXS J173202.4+652328

Galaxy/AGN

20.2 mag



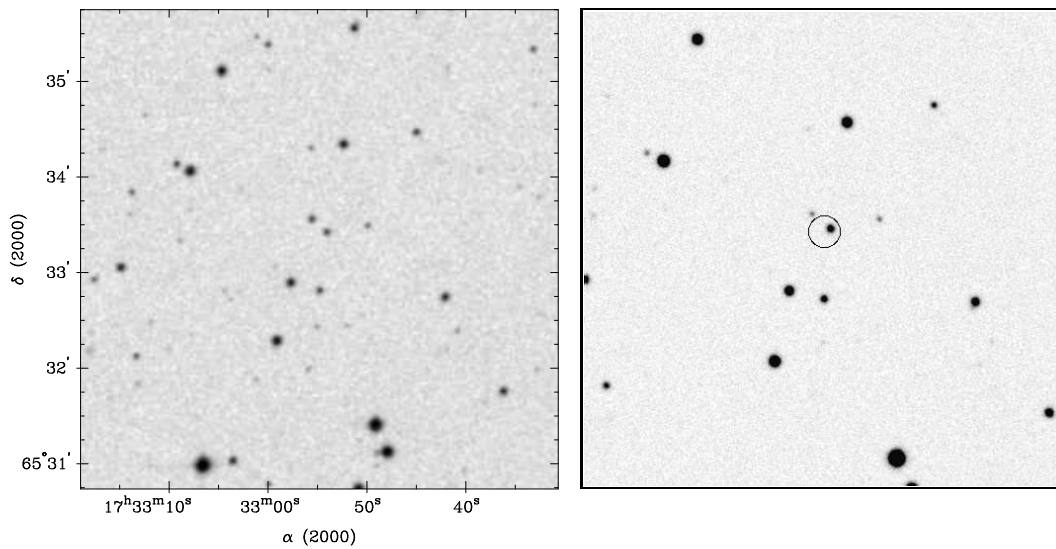
$\alpha/\delta_{\text{opt}} 17 32 2.9 +65 23 30$

1RXS J173254.5+653324

AGN

$z = 0.856$

18.2 mag

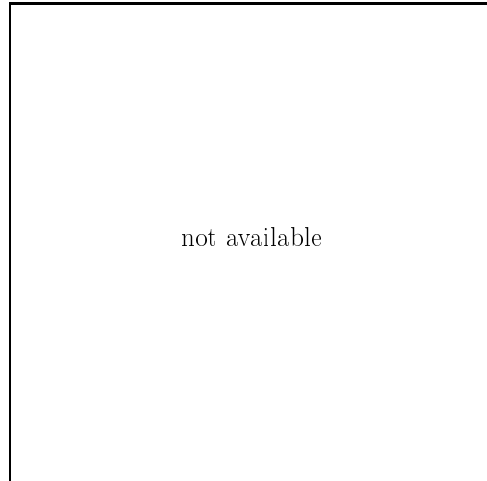
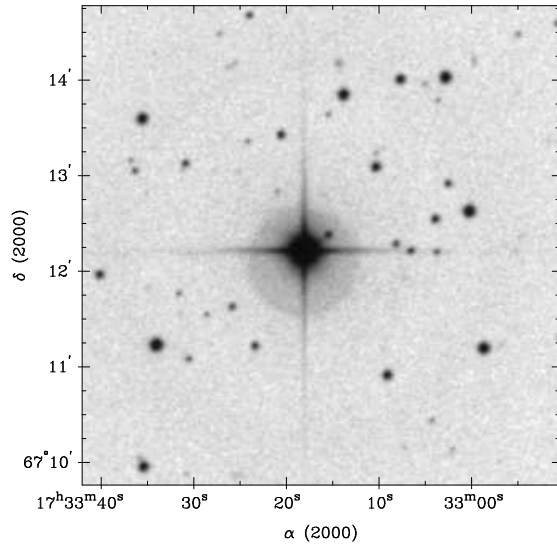


$\alpha/\delta_{\text{opt}} 17 32 54.0 +65 33 25$

1RXS J173316.9+671228

Star

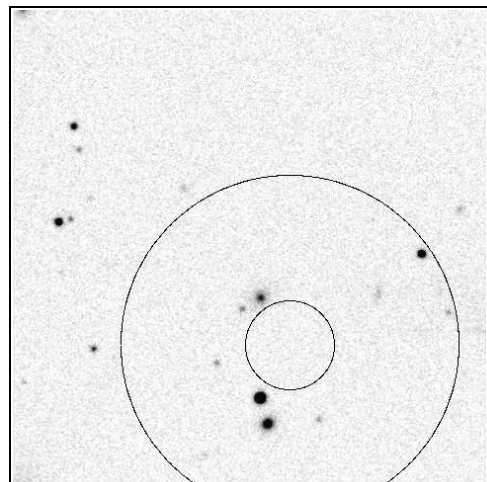
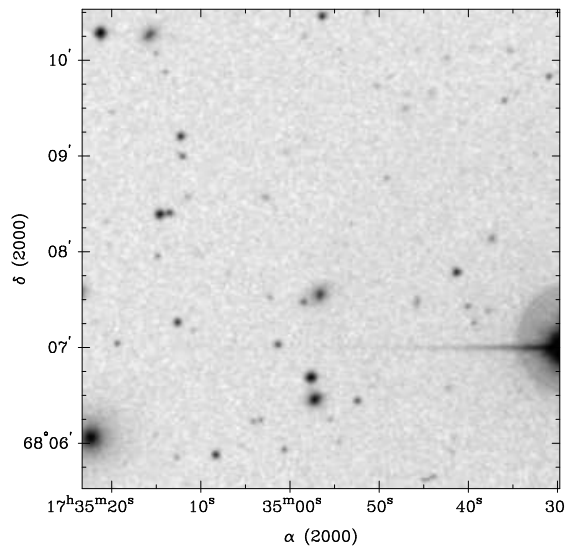
8.05 mag



$\alpha/\delta_{\text{opt}}$ 17 33 18.1 +67 12 13

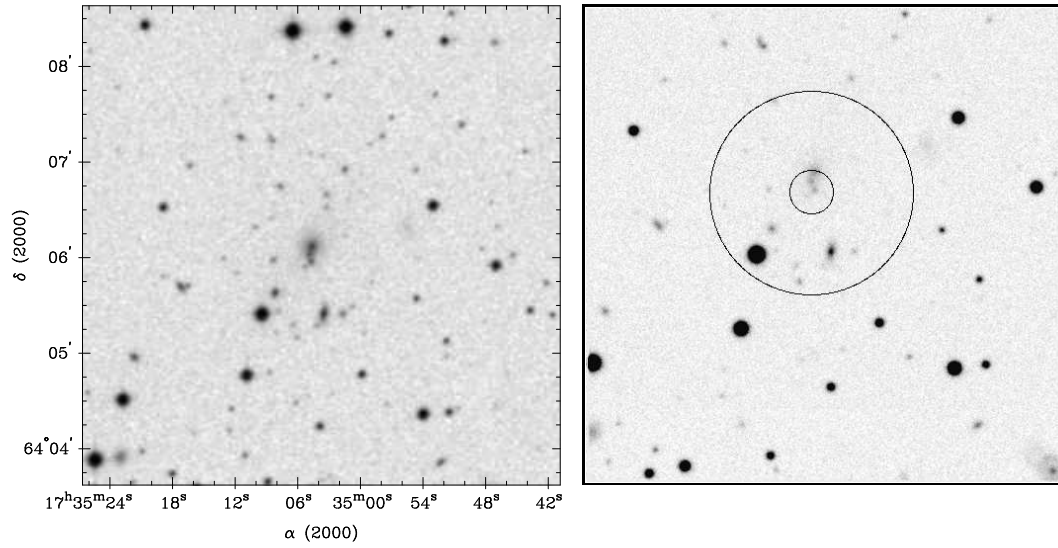
1RXS J173453.6+680709

Cluster $z = 0.0258$



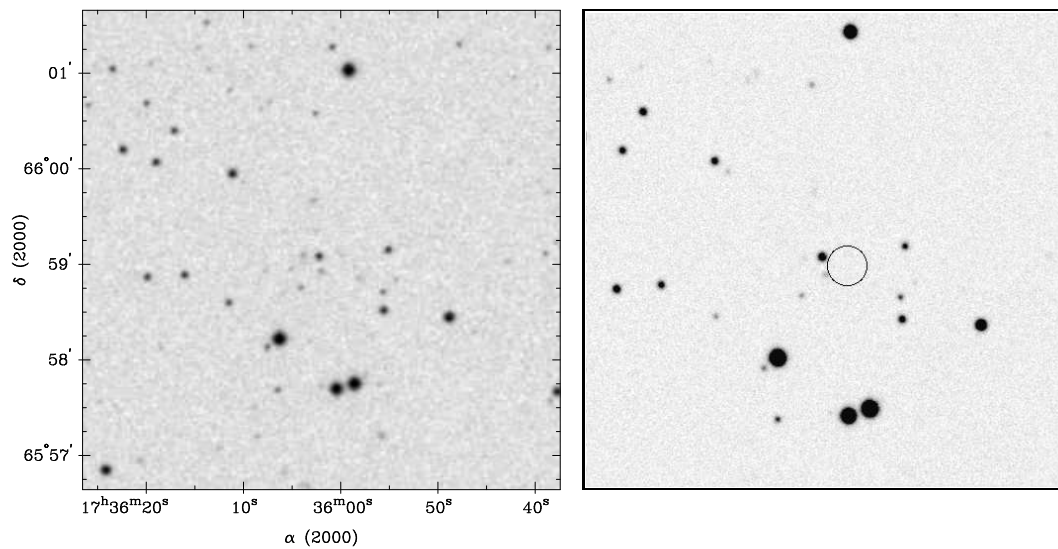
1RXS J173505.0+640557

Cluster $z = 0.1411$



1RXS J173600.1+655900

AGN $z = 0.4341$ 20.6 mag

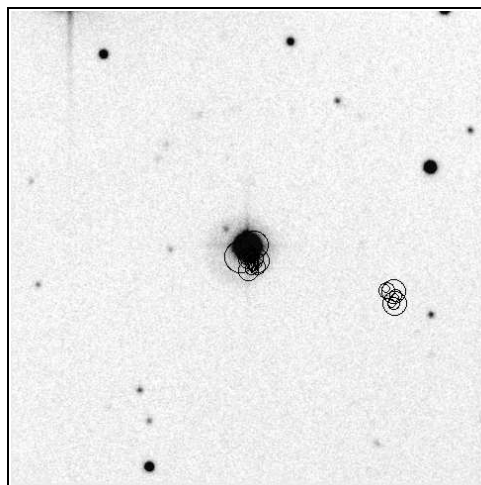
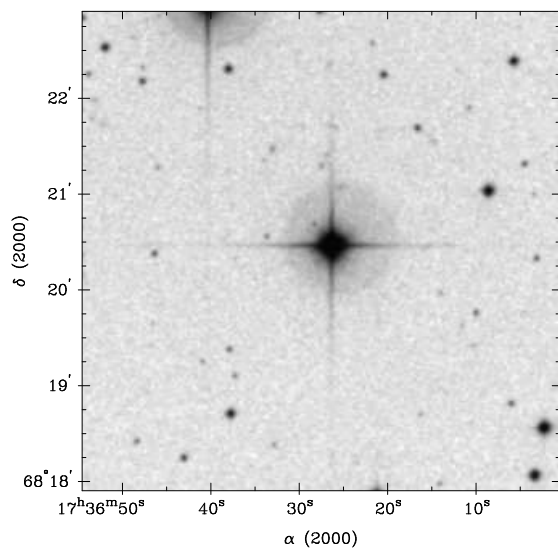


$\alpha/\delta_{\text{opt}} 17 36 1.9 +65 58 55$

2RXP J173614.2+682007

?

20.5: mag

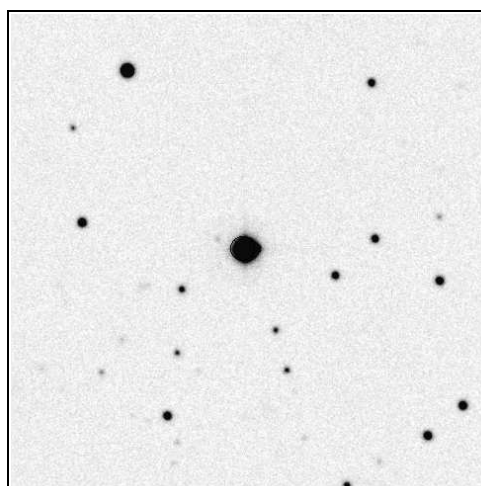
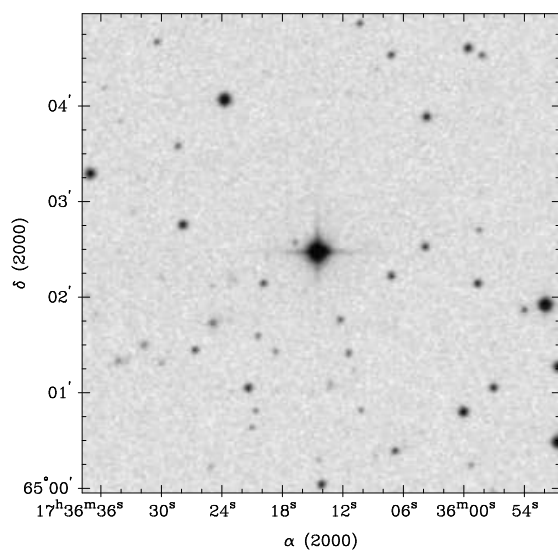


$\alpha/\delta_{\text{opt}}$ 17 36 12.9 +68 20 3

1RXS J173614.7+650229

Star

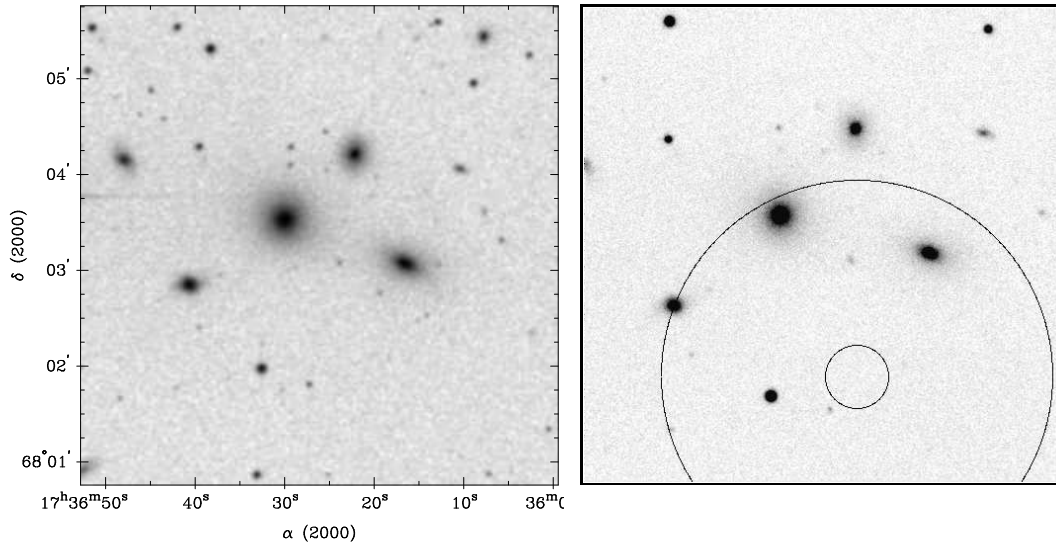
11.8 mag



$\alpha/\delta_{\text{opt}}$ 17 36 14.4 +65 2 28

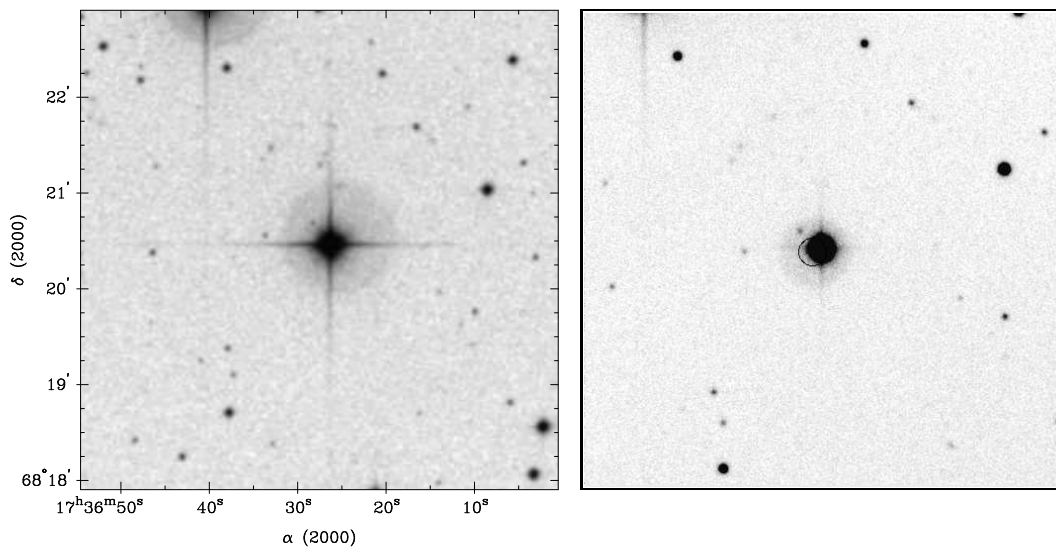
1RXS J173623.4+680206

Cluster $z = 0.0258$



1RXS J173627.2+682031

Star 10.8 mag

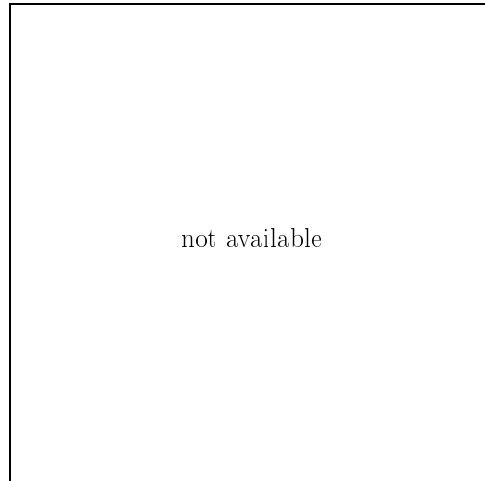
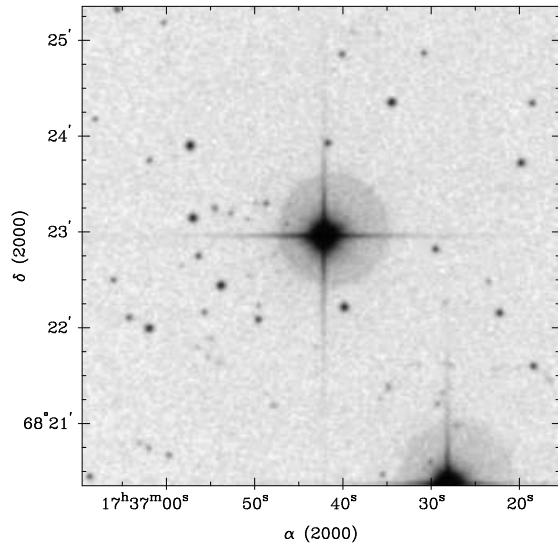


$\alpha/\delta_{\text{opt}} 17 36 26.3 +68 20 33$

2RXP J173641.8+682256

Star

8.44 mag

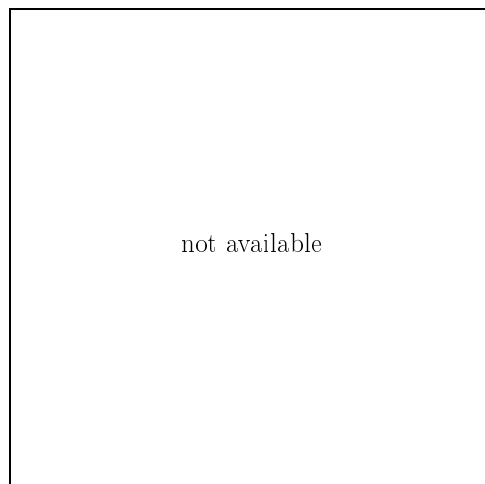
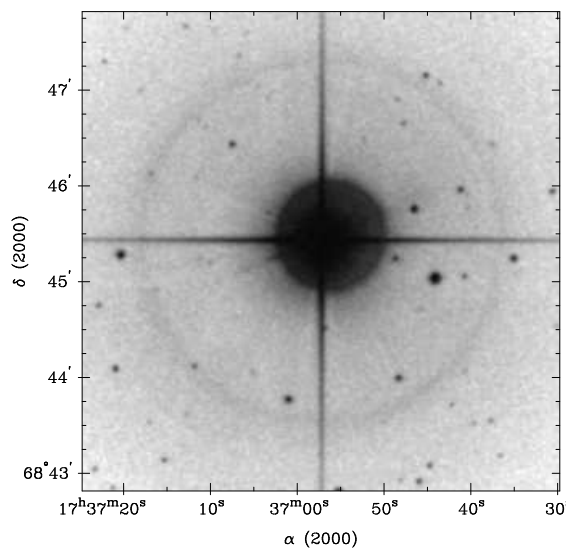


$\alpha/\delta_{\text{opt}}$ 17 36 42.2 +68 22 58

1RXS J173657.6+684522

Star

5.23 mag

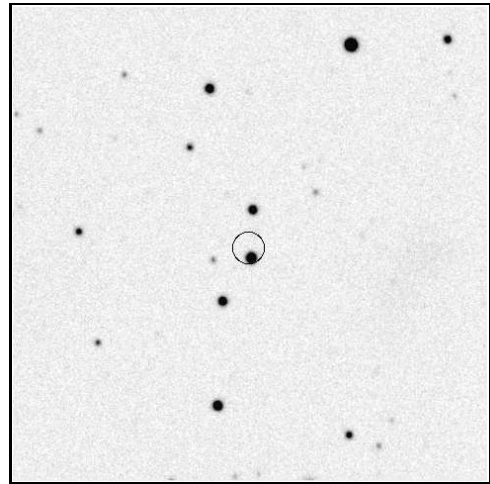
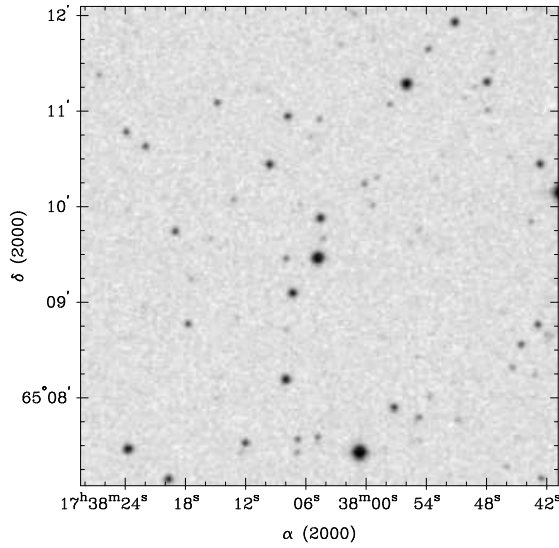


$\alpha/\delta_{\text{opt}}$ 17 36 57.1 +68 45 26

1RXS J173804.9+650933

Star

16.7 mag



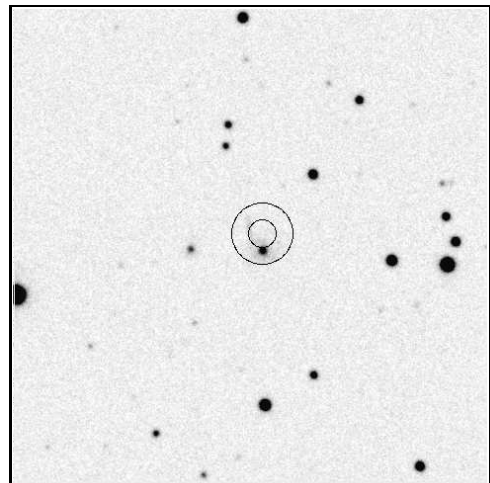
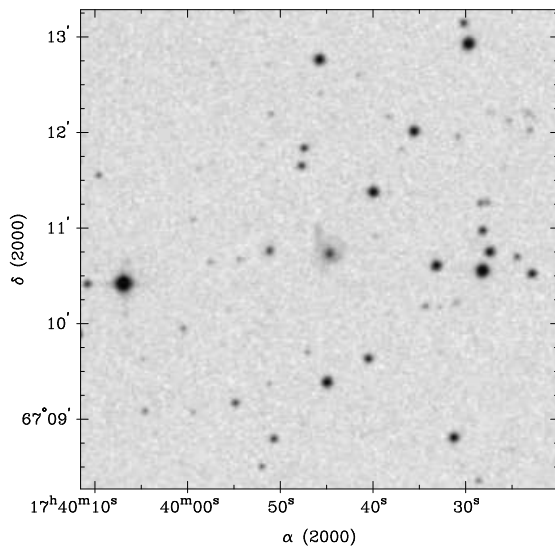
$\alpha/\delta_{\text{opt}} 17 38 4.7 +65 9 28$

1RXS J173944.7+671052

AGN

$z = 0.118$

18.0 mag

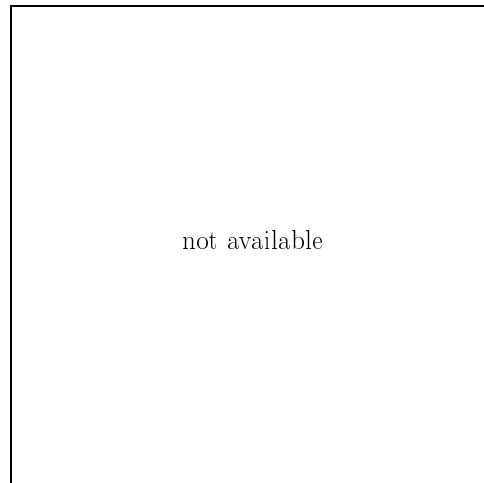
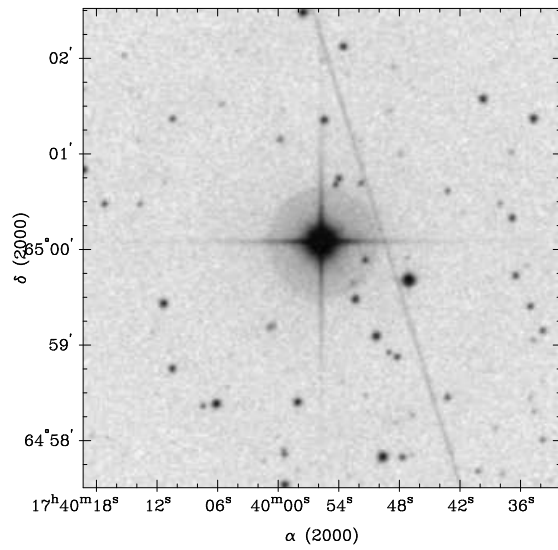


$\alpha/\delta_{\text{opt}} 17 39 44.7 +67 10 43$

1RXS J173955.8+650007

Star

9.33 mag



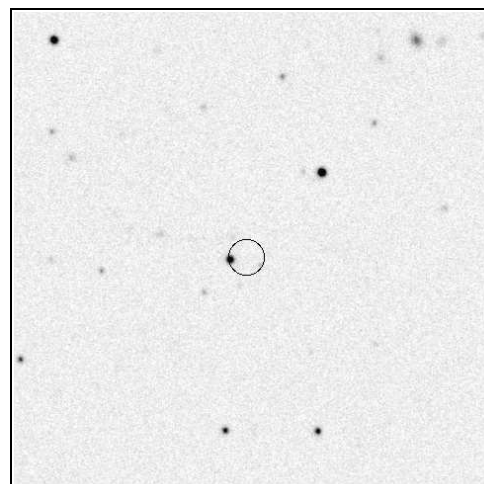
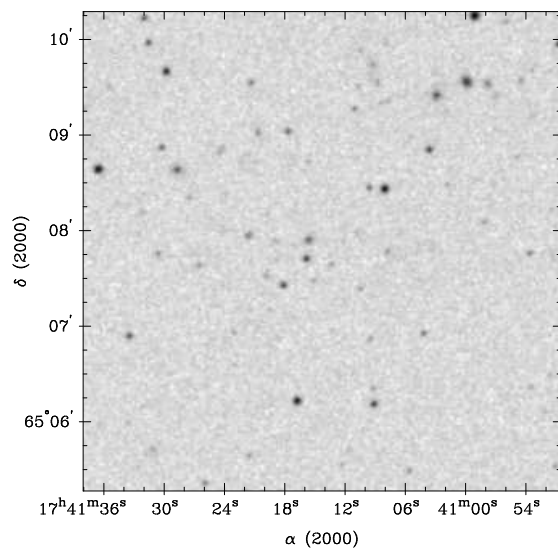
$\alpha/\delta_{\text{opt}}$ 17 39 55.7 +65 0 5

1RXS J174114.4+650743

AGN

$z = 0.7466$

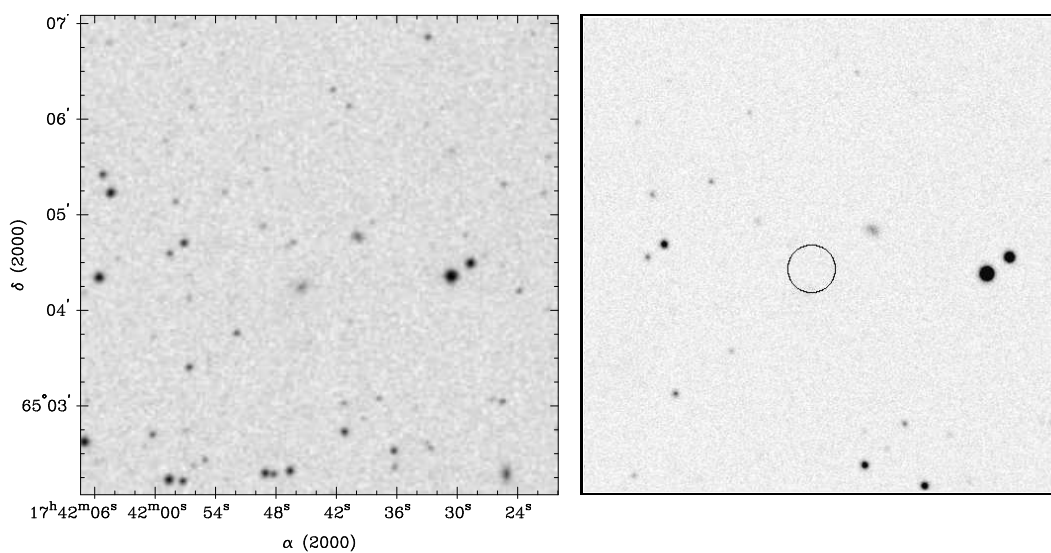
18.5 mag



$\alpha/\delta_{\text{opt}}$ 17 41 15.8 +65 7 42

1RXS J174144.9+650427

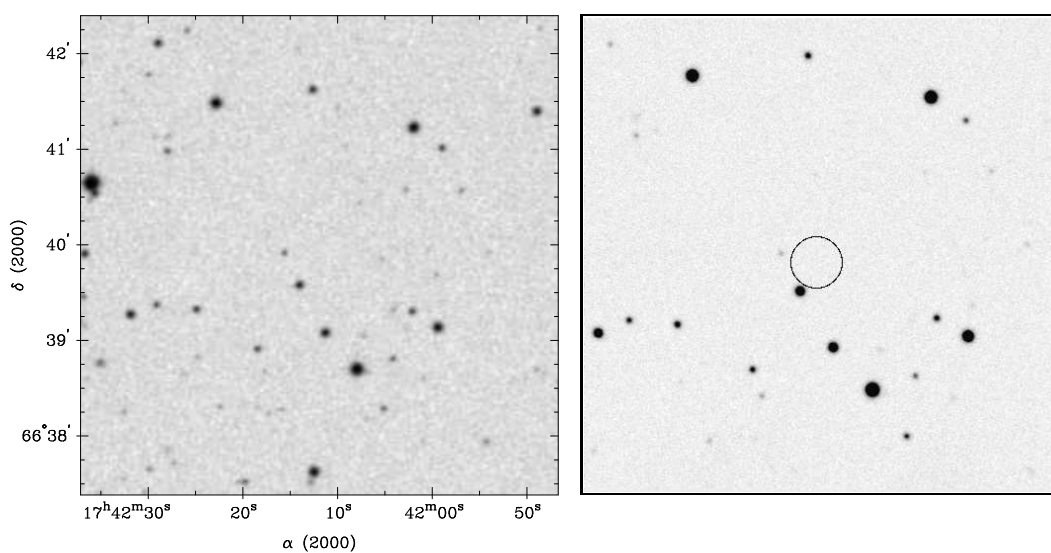
Galaxy



$\alpha/\delta_{\text{opt}} 17 41 45.6 +65 4 14$

1RXS J174212.5+663949

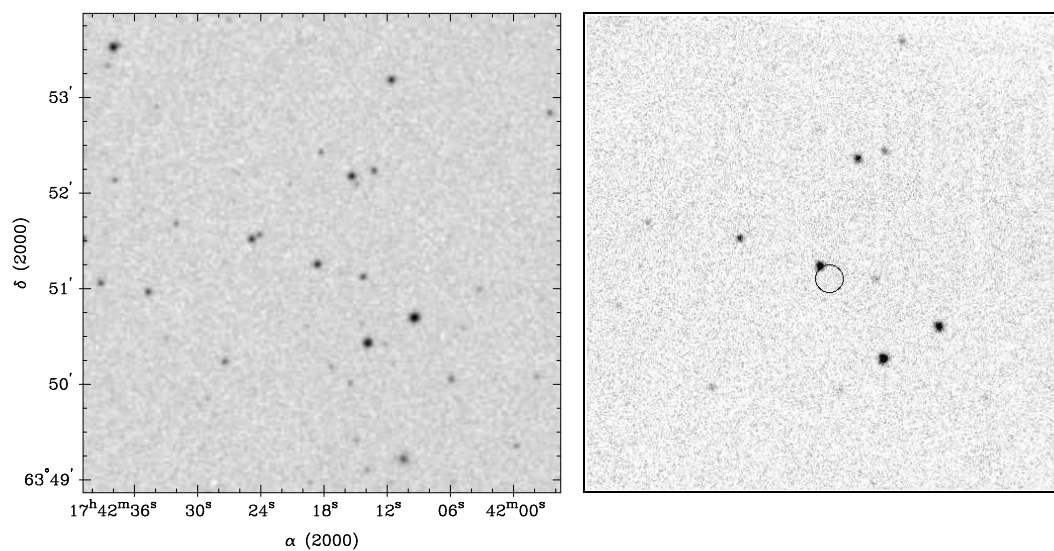
AGN $z = 1.272$ 17.1 mag



$\alpha/\delta_{\text{opt}} 17 42 14.0 +66 39 34$

1RXS J174217.9+635109

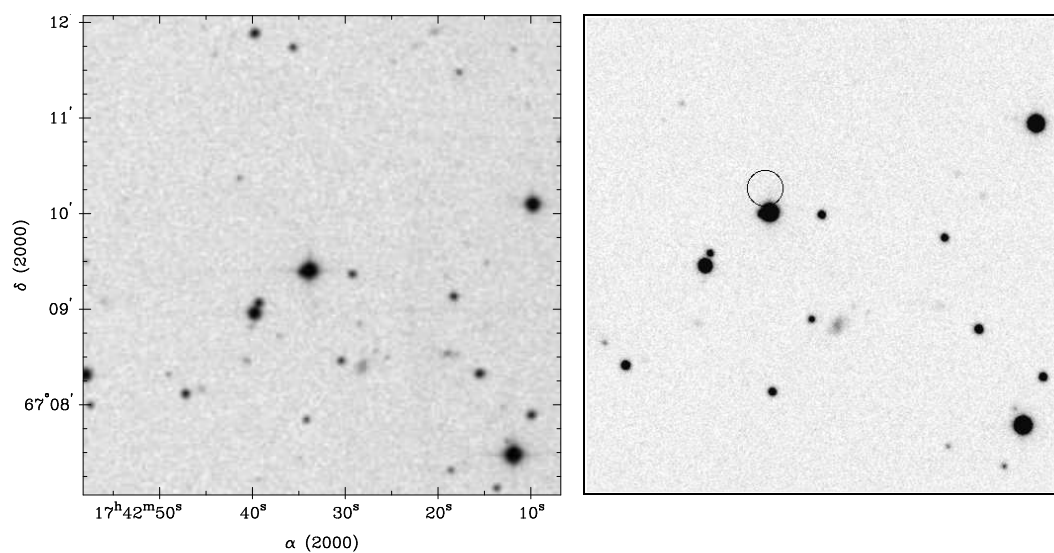
AGN $z = 0.4019$ 18.3 mag



$\alpha/\delta_{\text{opt}} 17 42 18.6 +63 51 16$

1RXS J174234.2+670936

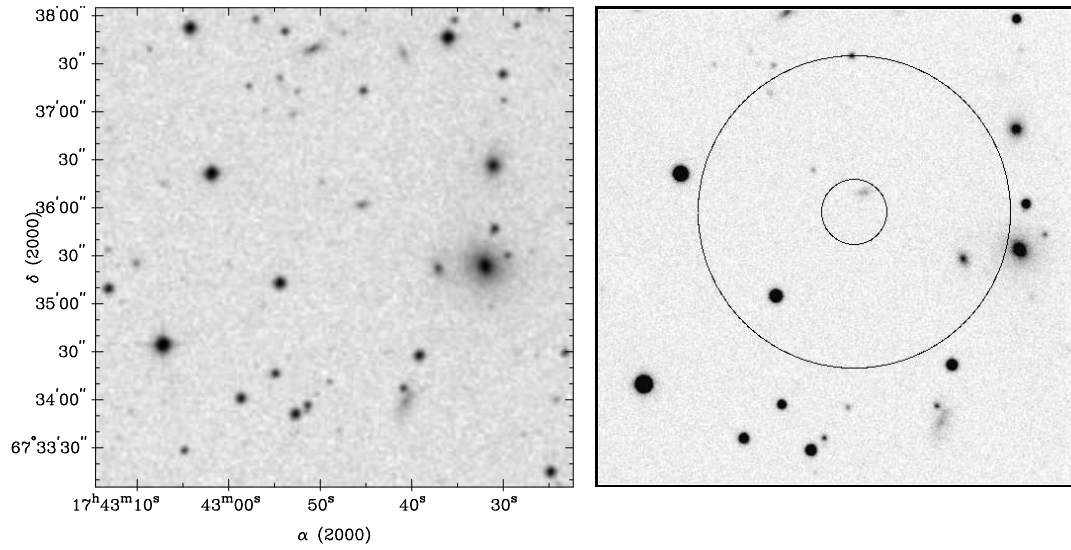
Star 13.2 mag



$\alpha/\delta_{\text{opt}} 17 42 33.8 +67 9 23$

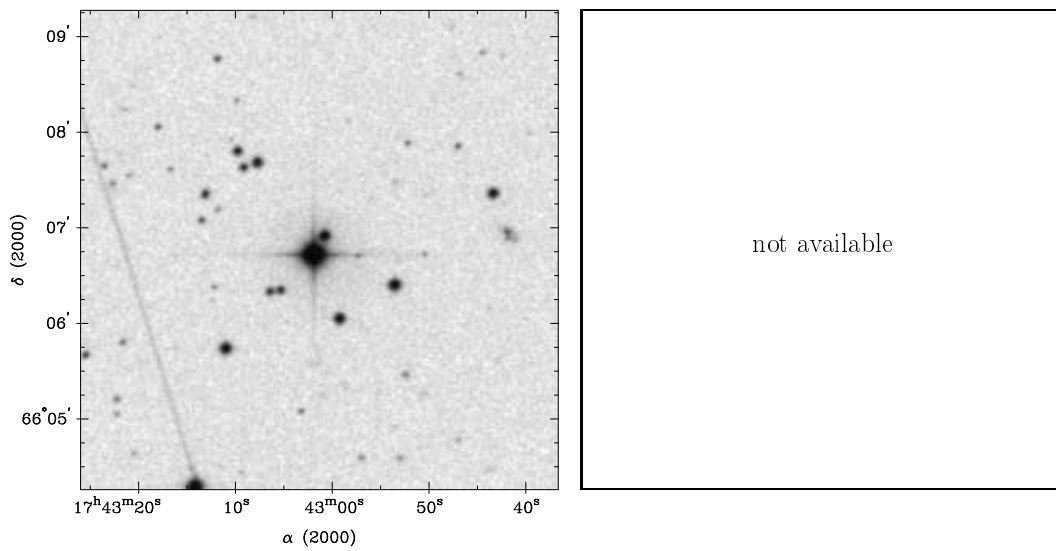
1RXS J174246.8+673553

Cluster $z = 0.042$



1RXS J174302.3+660642

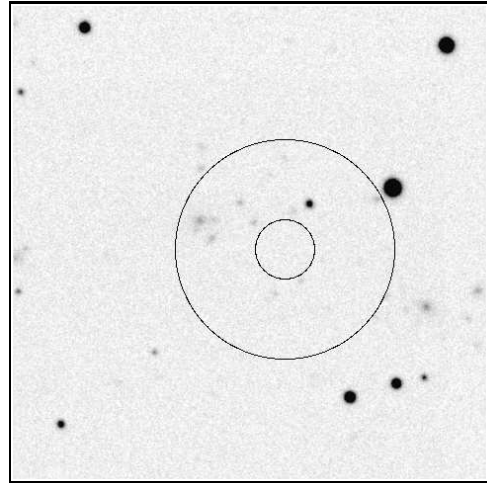
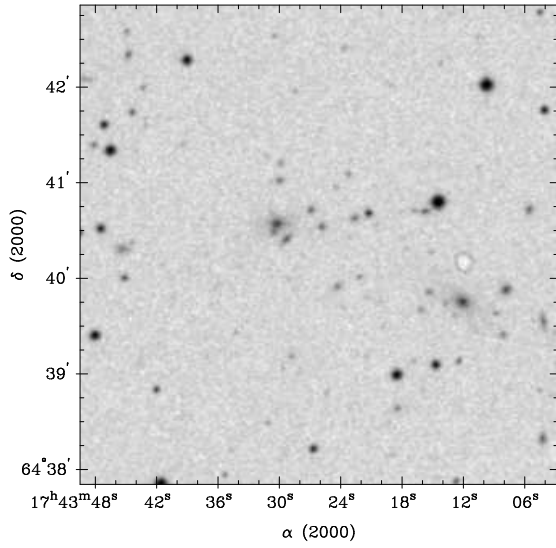
Star 10.2 mag



$\alpha/\delta_{\text{opt}} 17\ 43\ 1.9\ +66\ 6\ 43$

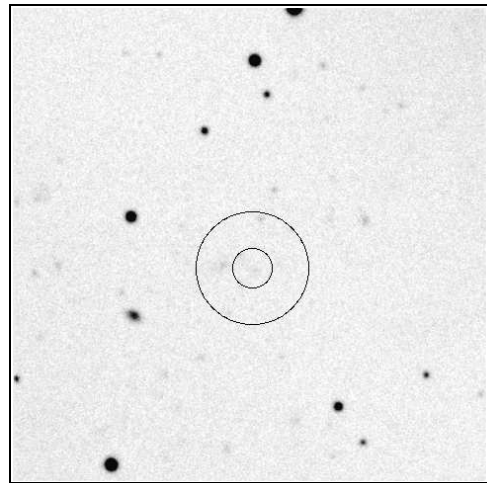
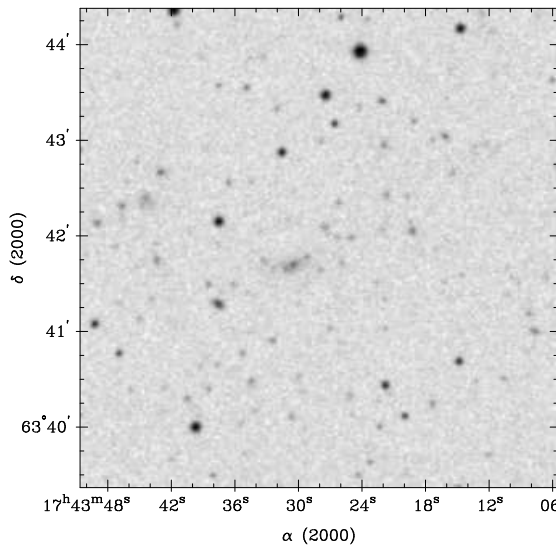
1RXS J174323.3+644018

Cluster $z = 0.179$



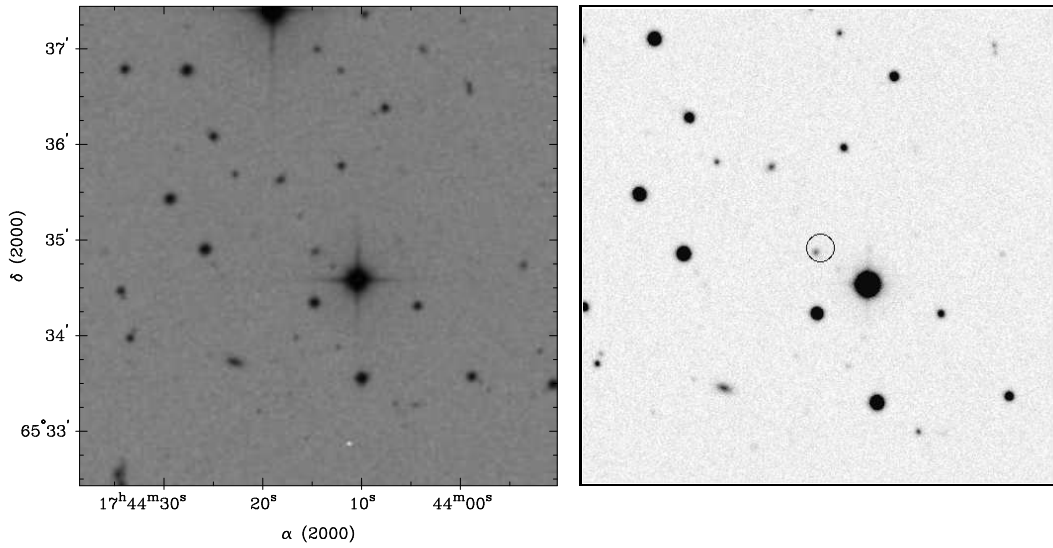
1RXS J174328.1+634140

Cluster $z = 0.327$



1RXS J174414.2+653455

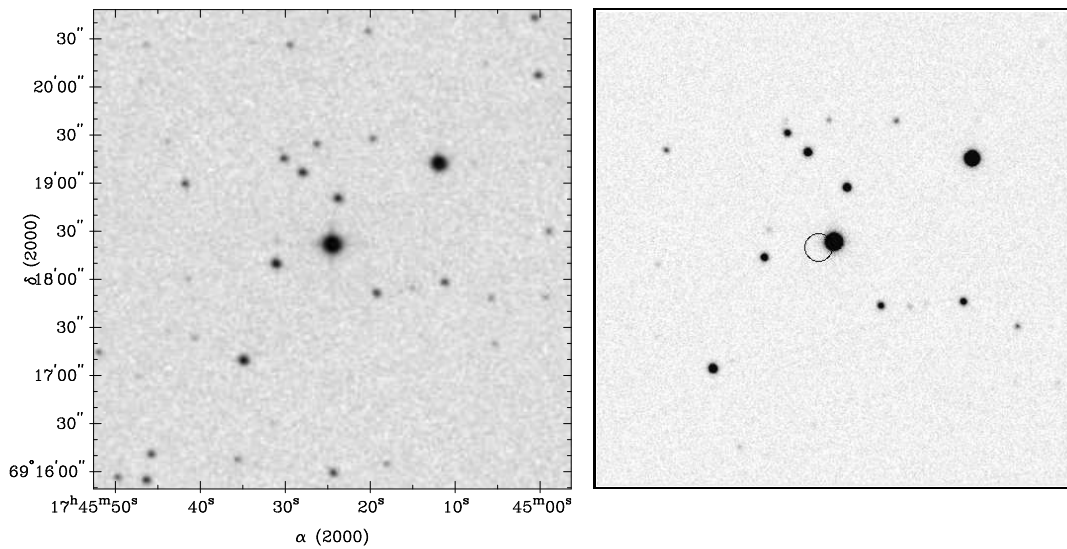
AGN $z = 0.255$ 19.9 mag



$\alpha/\delta_{\text{opt}}$ 17 44 14.6 +65 34 53

1RXS J174526.0+691819

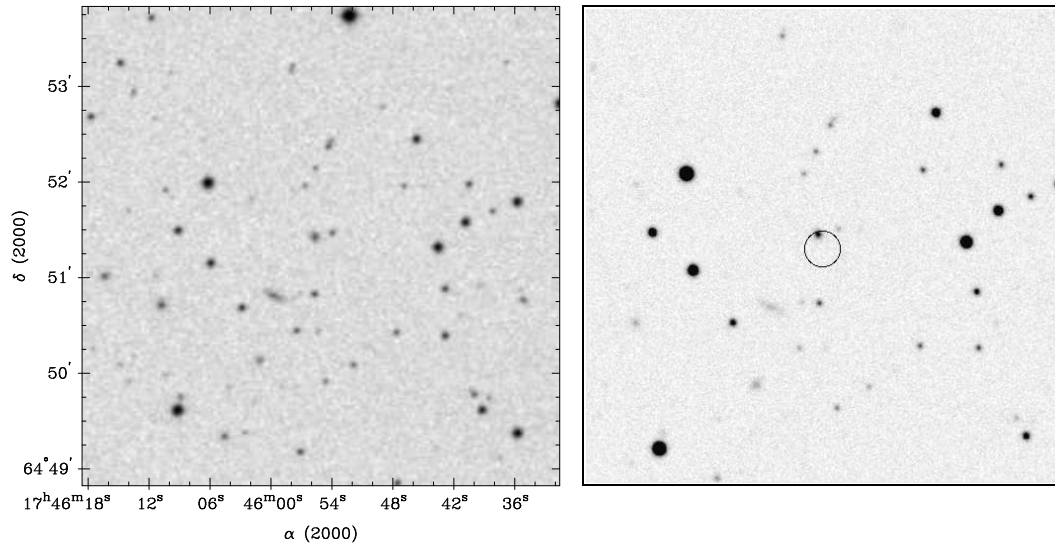
Star 13.5 mag



$\alpha/\delta_{\text{opt}}$ 17 45 24.5 +69 18 22

1RXS J174555.3+645118

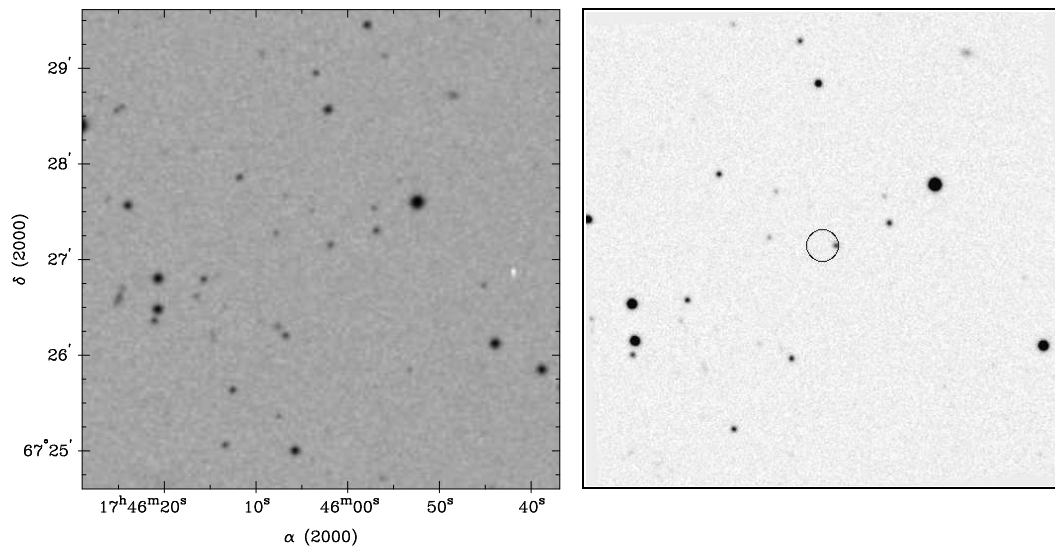
AGN $z = 0.179$ 19.0 mag



$\alpha/\delta_{\text{opt}} 17\ 45\ 55.6\ +64\ 51\ 25$

1RXS J174603.1+672709

AGN $z = 0.2146$ 20.0 mag

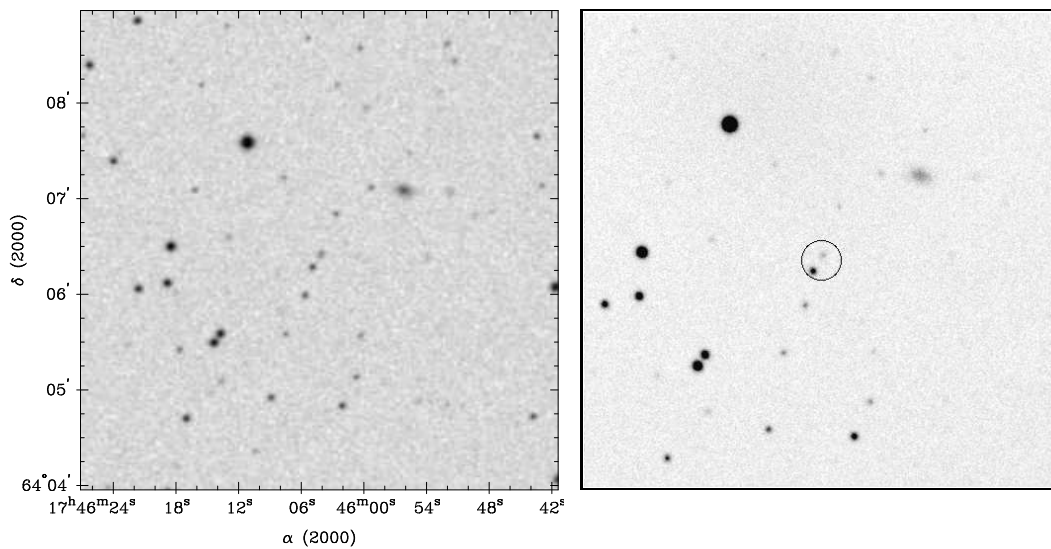


$\alpha/\delta_{\text{opt}} 17\ 46\ 1.9\ +67\ 27\ 9$

1RXS J174604.2+640622

?

19.0 mag



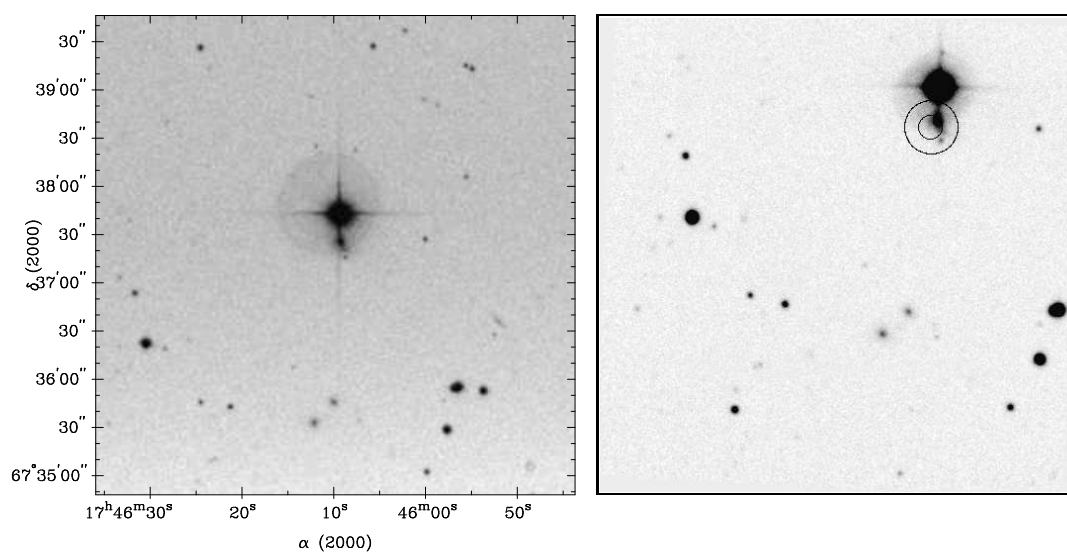
$\alpha/\delta_{\text{opt}}$ 17 46 4.8 +64 6 16

1RXS J174609.6+673721

AGN

$z = 0.041$

15.7 mag

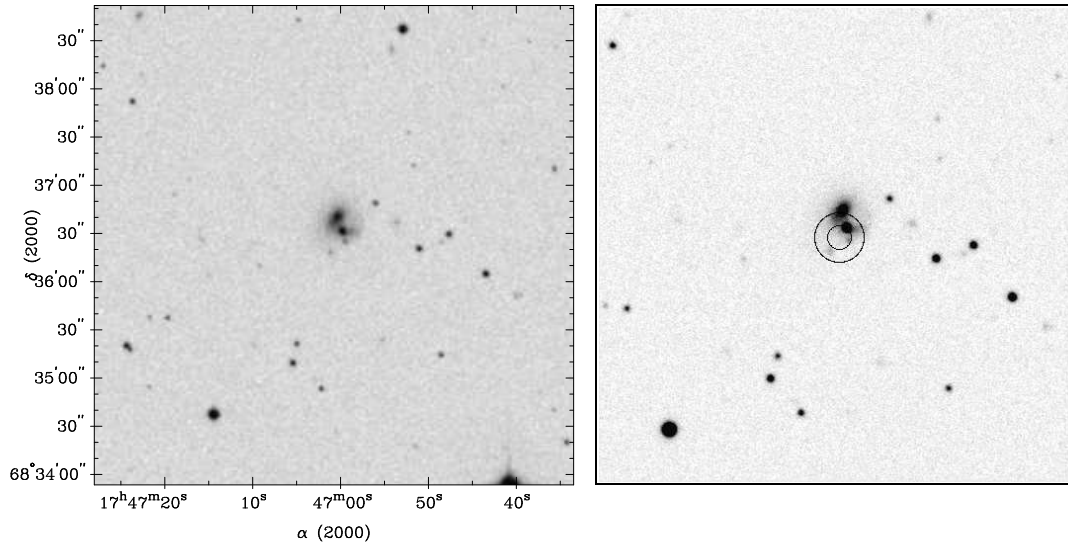


DSSII finding chart from POSSII-B

$\alpha/\delta_{\text{opt}}$ 17 46 9.0 +67 37 24

1RXS J174700.3+683626

AGN $z = 0.063$ 16.4 mag

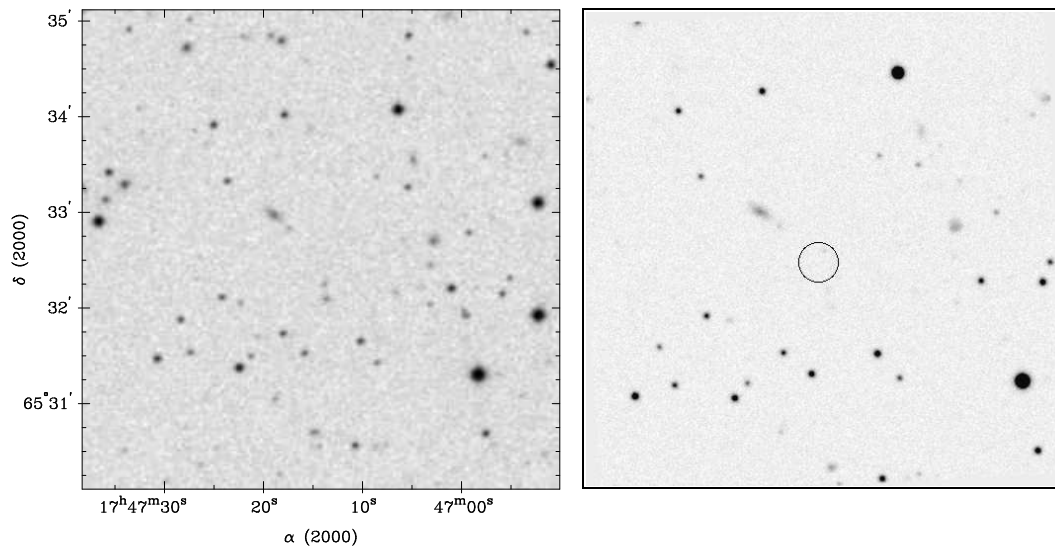


DSSII finding chart from POSSII-B

$\alpha/\delta_{\text{opt}} 17\ 46\ 59.6 +68\ 36\ 31$

1RXS J174714.4+653230

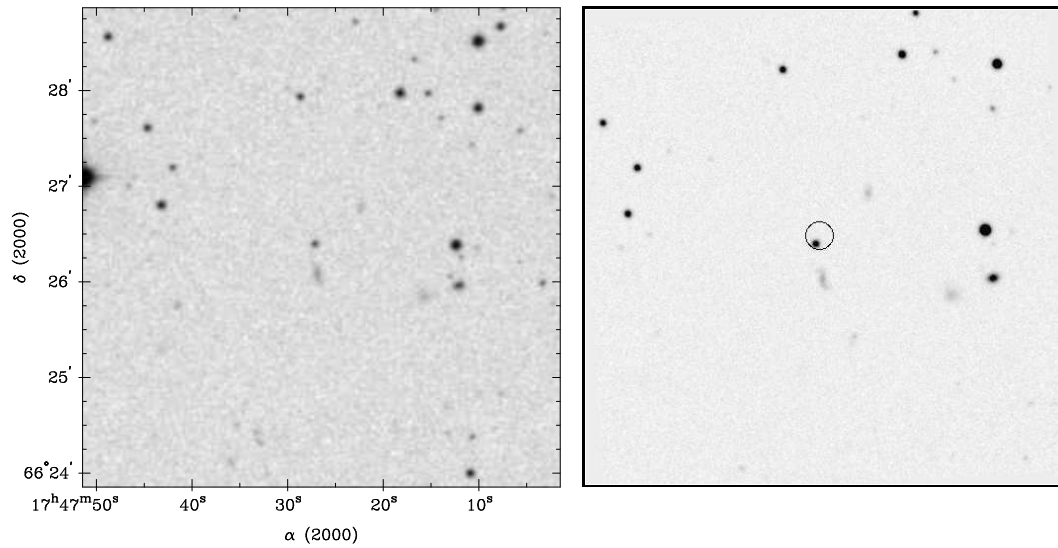
AGN $z = 1.5166$ 21.2 mag



$\alpha/\delta_{\text{opt}} 17\ 47\ 13.9 +65\ 32\ 36$

1RXS J174726.8+662628

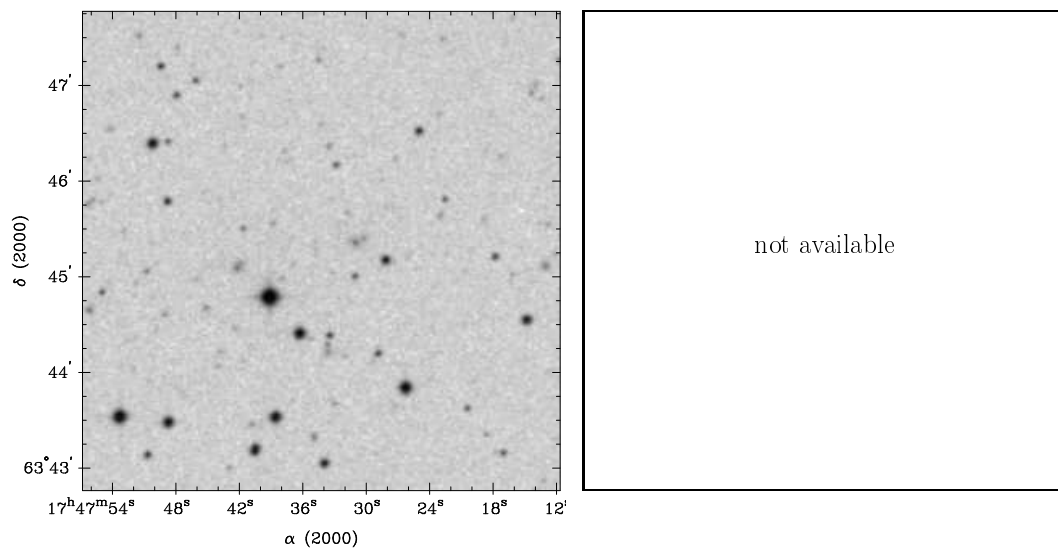
AGN $z = 0.1391$ 18.7 mag



$\alpha/\delta_{\text{opt}} 17\ 47\ 27.1 +66\ 26\ 24$

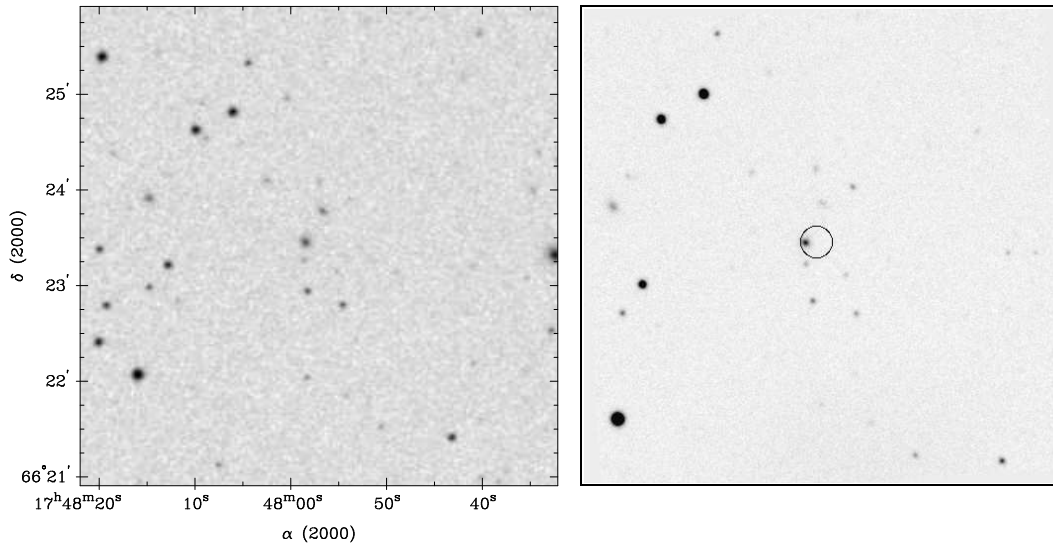
1RXS J174733.7+634355

Cluster $z = 0.328$



1RXS J174757.4+662327

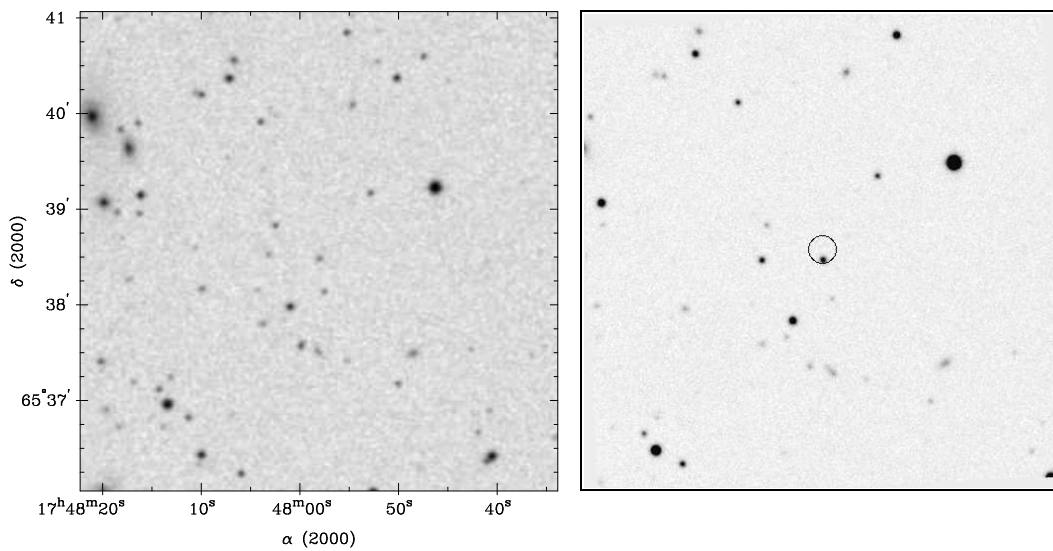
Galaxy $z = 0.1738$ 19.0 mag



$\alpha/\delta_{\text{opt}} 17\ 47\ 58.4\ +66\ 23\ 27$

1RXS J174758.0+653835

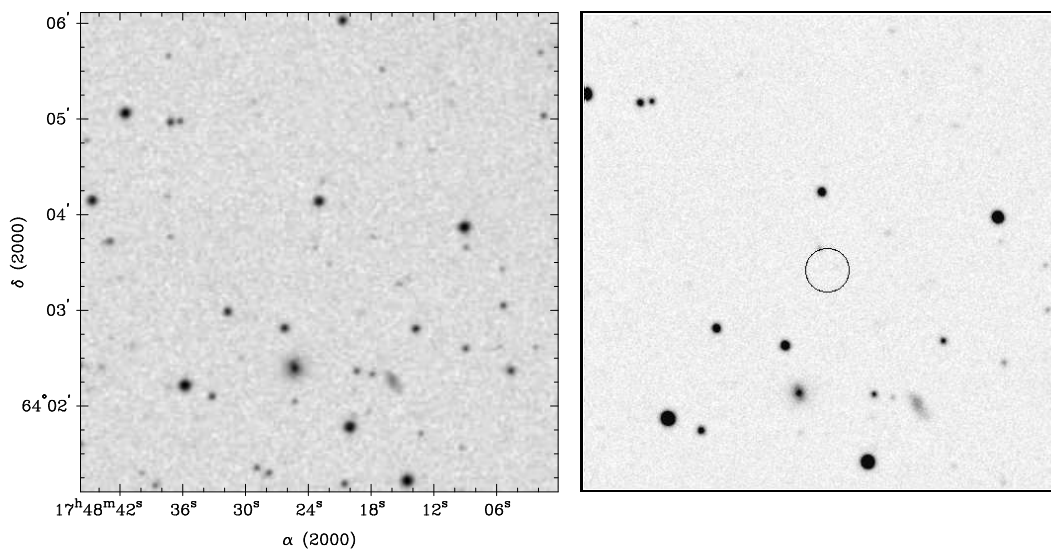
AGN $z = 0.3248$ 19.2 mag



$\alpha/\delta_{\text{opt}} 17\ 47\ 57.9\ +65\ 38\ 29$

1RXS J174822.7+640327

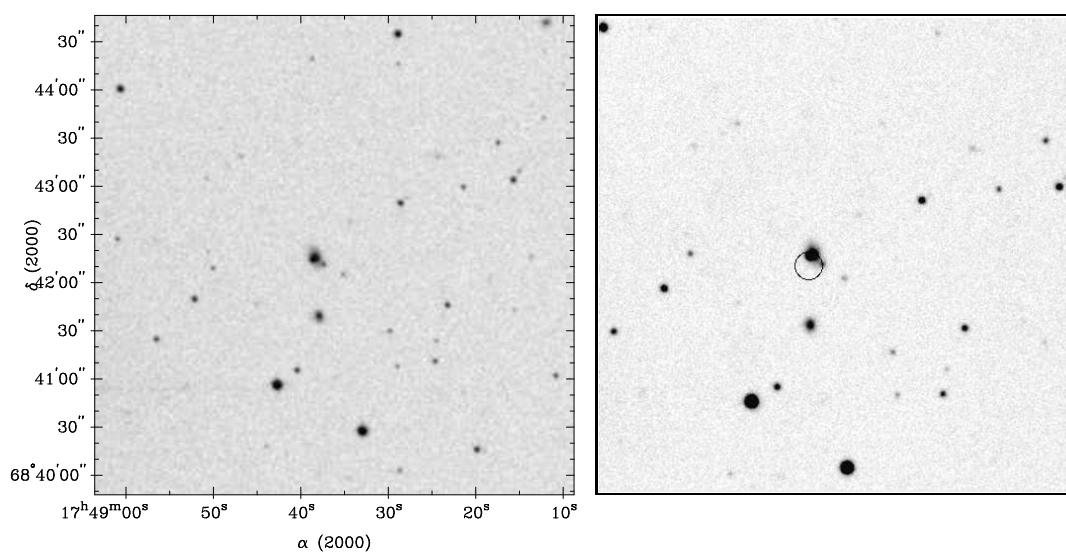
AGN $z = 0.9859$ 20.6 mag



$\alpha/\delta_{\text{opt}}$ 17 48 23.3 +64 3 38

1RXS J174838.8+684211

AGN $z = 0.0537$ 15.8 mag

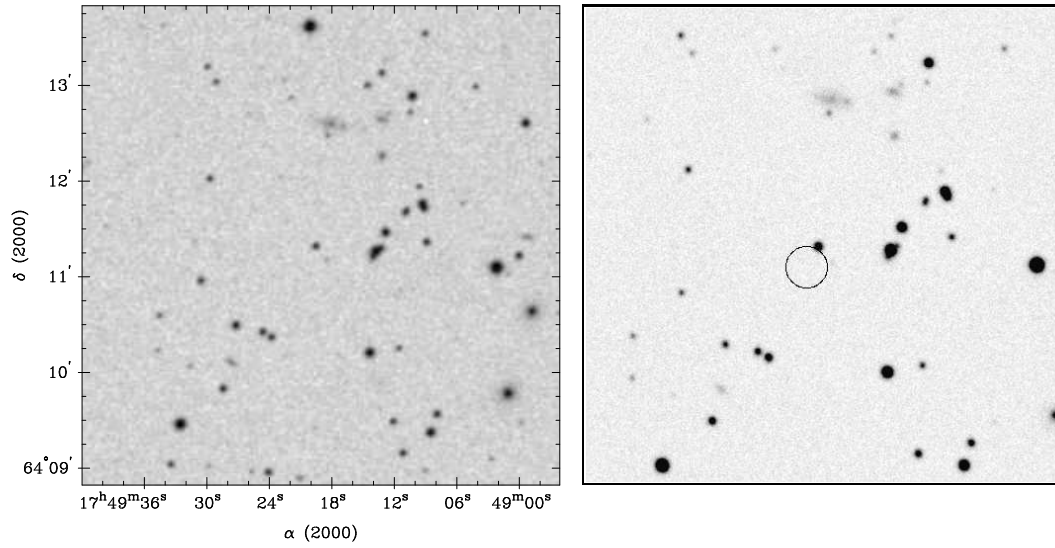


DSSII finding chart from POSSII-B

$\alpha/\delta_{\text{opt}}$ 17 48 38.5 +68 42 16

1RXS J174920.5+641108

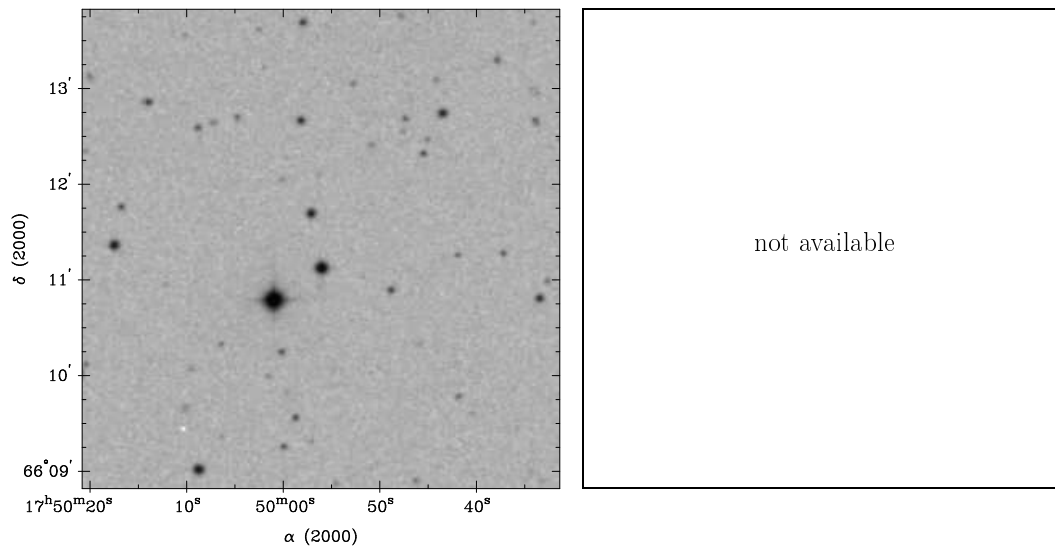
AGN $z = 0.9836$ 17.7 mag



$\alpha/\delta_{\text{opt}} 17\ 49\ 19.5\ +64\ 11\ 19$

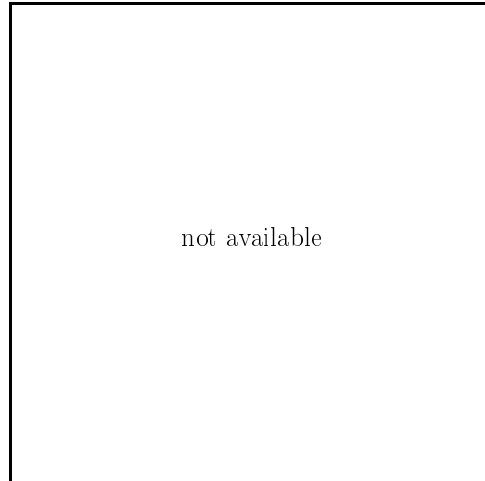
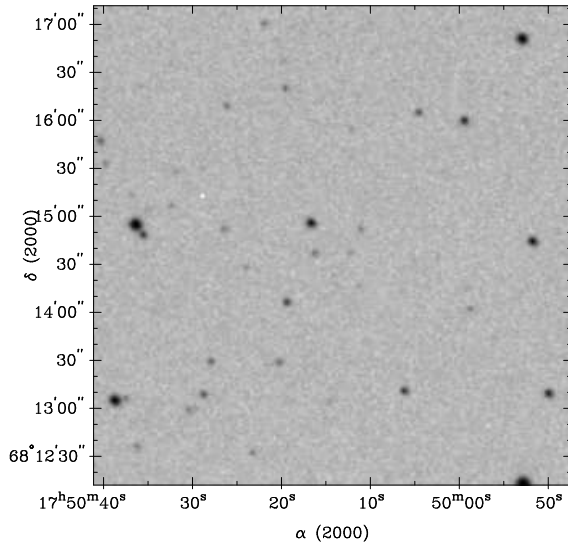
1RXS J174955.0+661116

Star



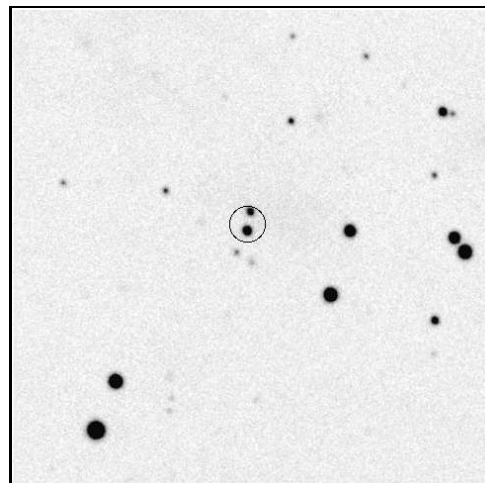
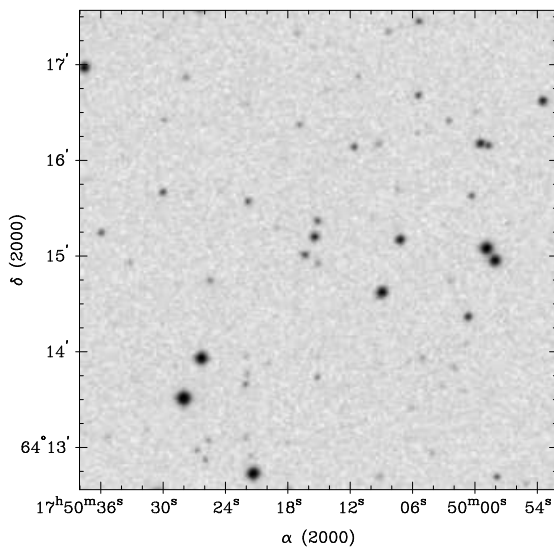
1RXS J175014.3+681433

AGN $z = 0.231$ 20.4: mag



1RXS J175015.5+641515

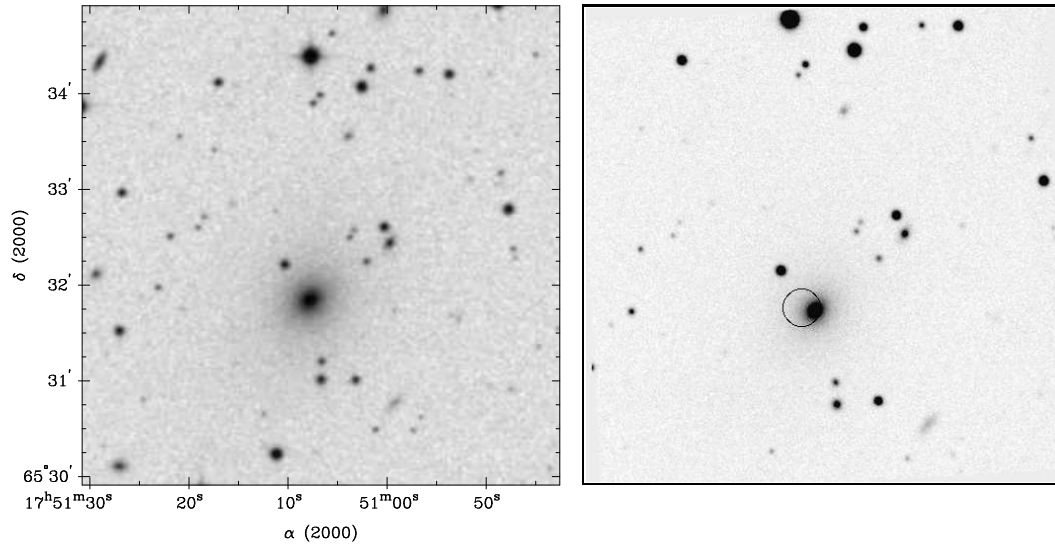
AGN $z = 0.2504$ 20.3 mag



$\alpha/\delta_{\text{opt}} 17\ 50\ 15.1 +64\ 14\ 57$

2RXP J175108.6+653153

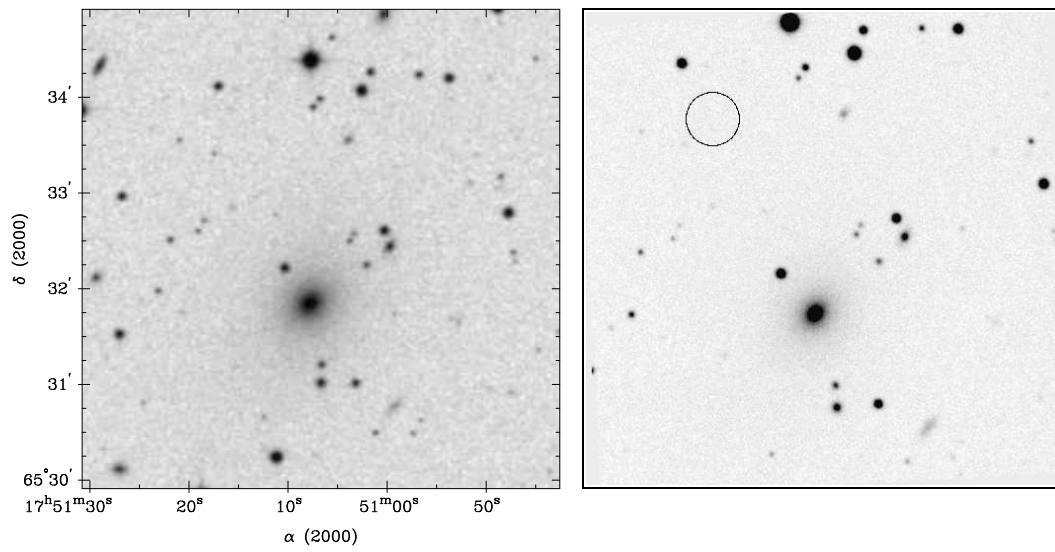
Galaxy $z = 0.0389$ 14.7 mag



$\alpha/\delta_{\text{opt}} 17\ 51\ 7.4 +65\ 31\ 51$

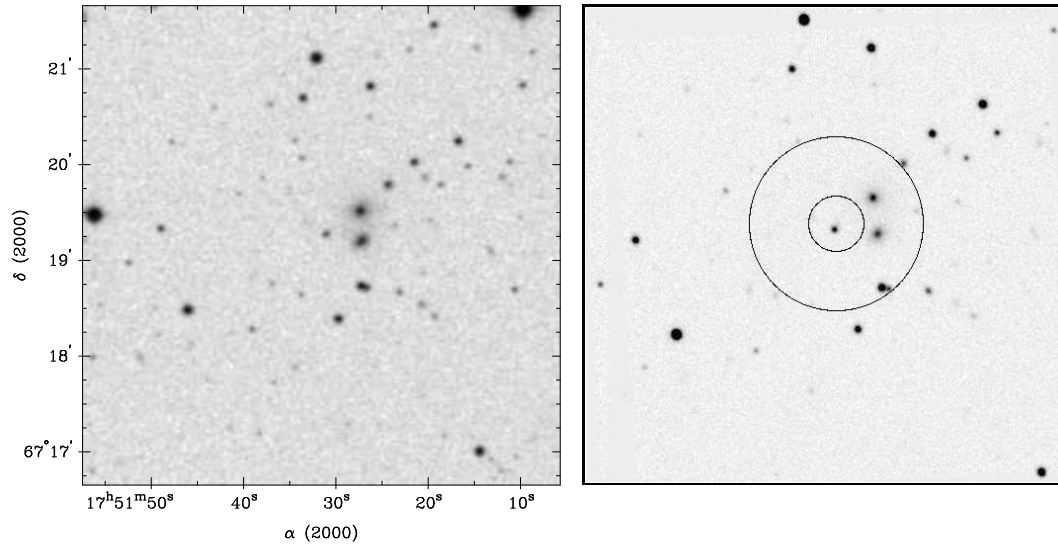
1RXS J175115.5+653334

Cluster $z = 0.0424$



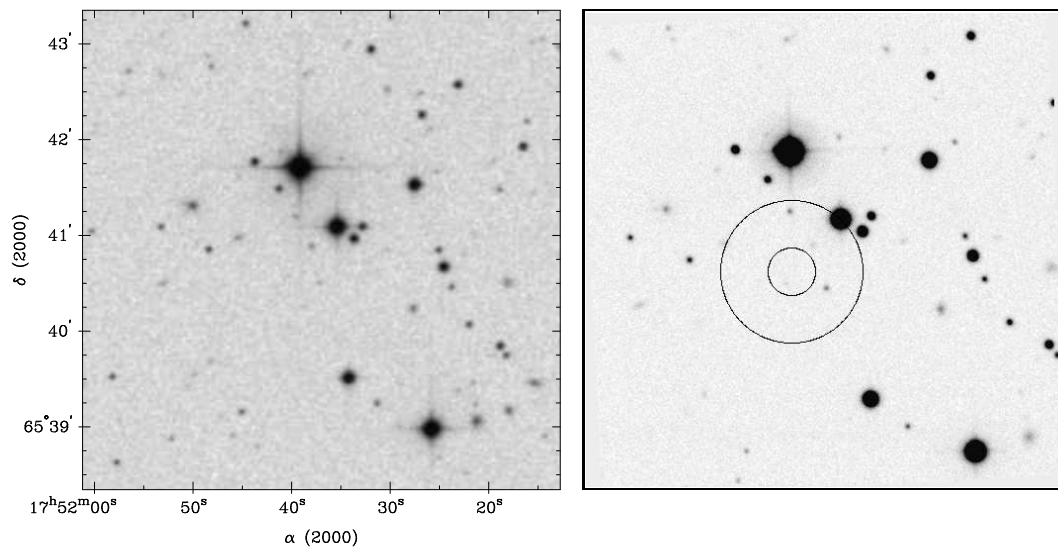
1RXS J175130.9+671920

Cluster $z = 0.0933$



1RXS J175139.8+654040

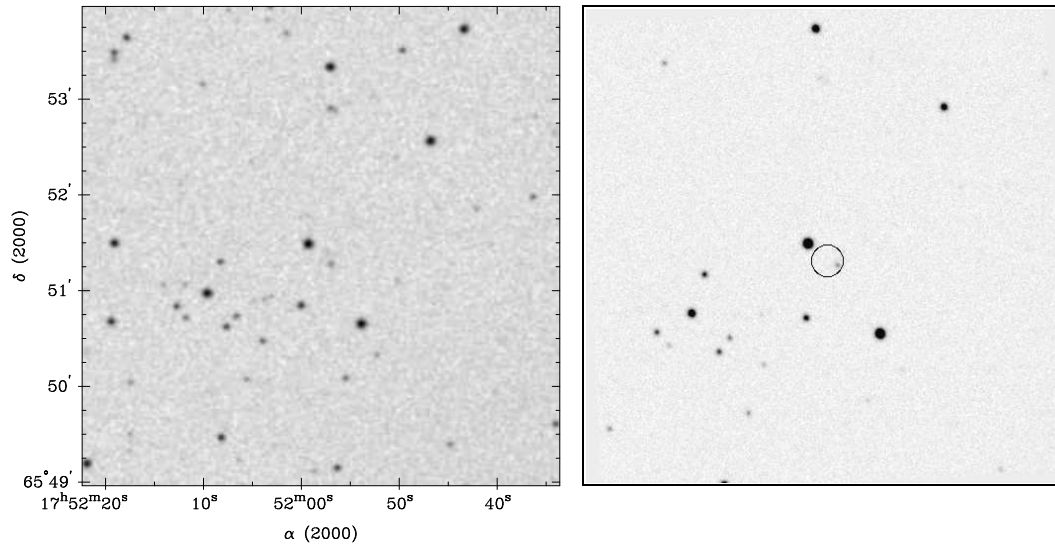
AGN $z = 0.8259$ 20.4 mag



$\alpha/\delta_{\text{opt}} 17\ 51\ 36.9\ +65\ 40\ 31$

1RXS J175157.7+655120

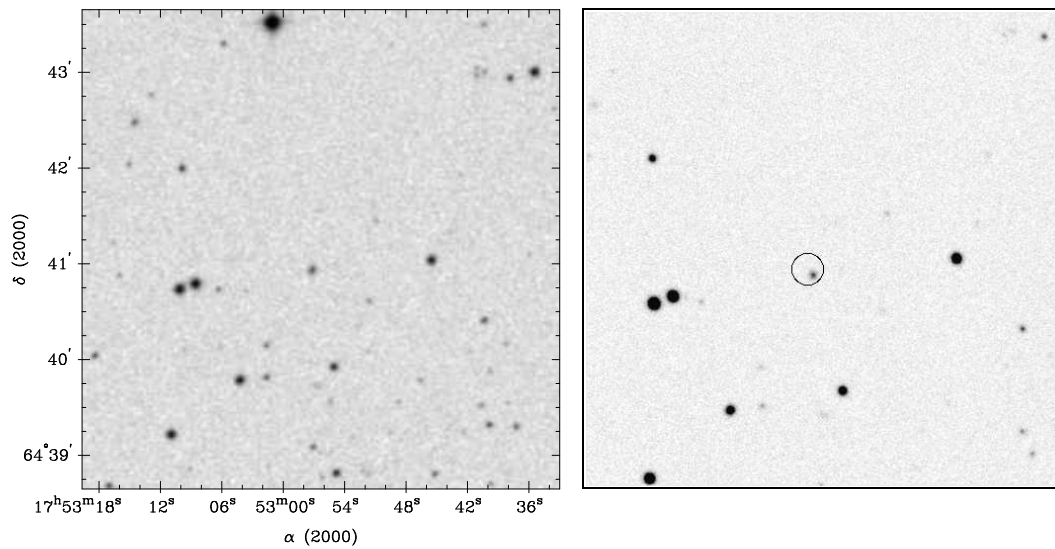
AGN $z = 0.3901$ 20.5 mag



$\alpha/\delta_{\text{opt}} 17\ 51\ 56.8 +65\ 51\ 18$

1RXS J175257.4+644058

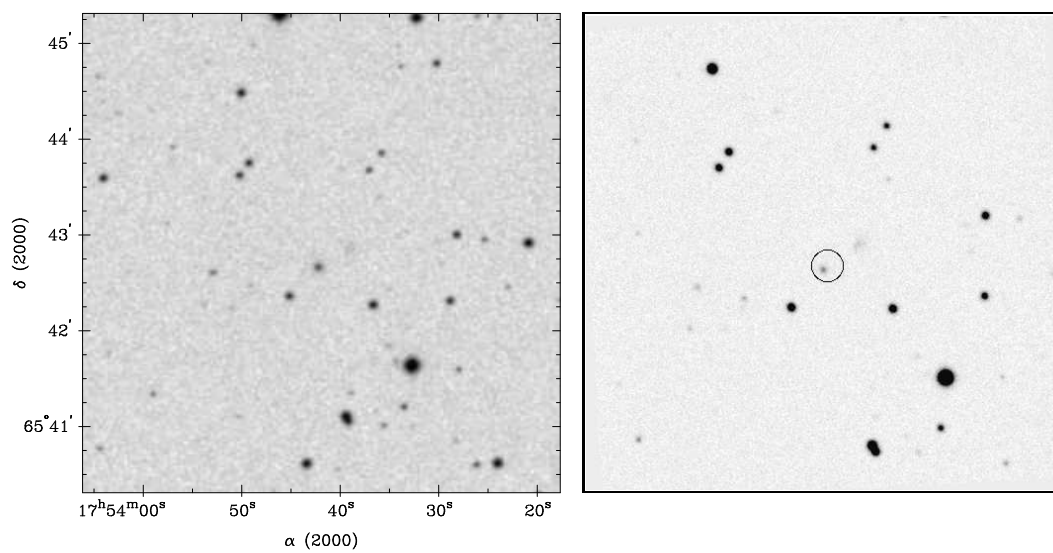
AGN $z = 0.123$ 19.4 mag



$\alpha/\delta_{\text{opt}} 17\ 52\ 56.9 +64\ 40\ 55$

1RXS J175341.7+654242

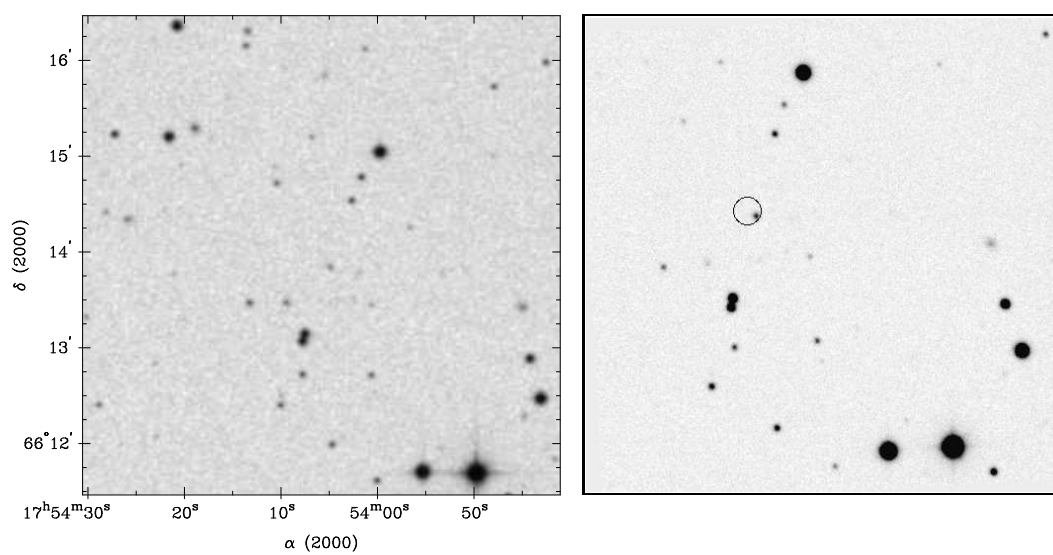
AGN $z = 0.140$ 20.0 mag



$\alpha/\delta_{\text{opt}}$ 17 53 42.1 +65 42 40

1RXS J175405.5+661354

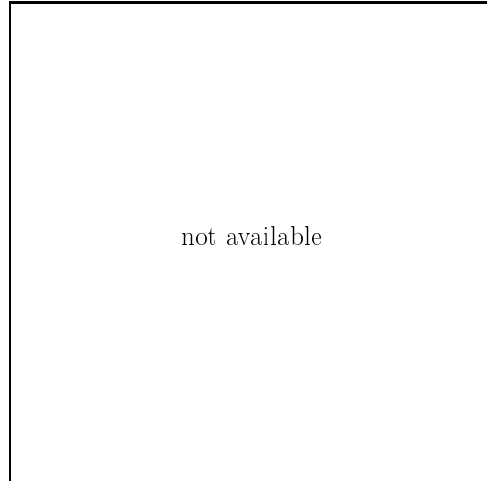
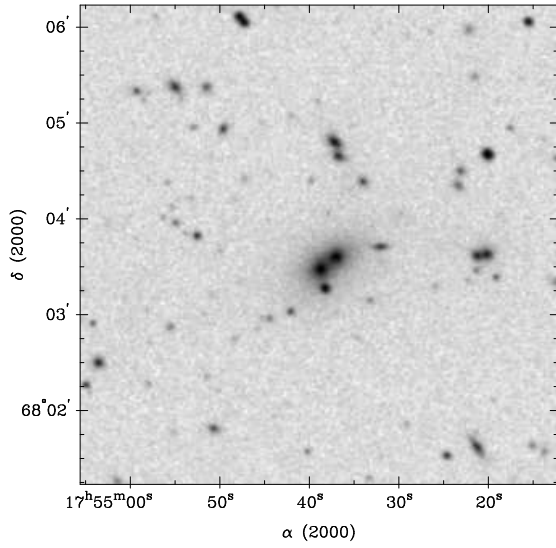
AGN $z = 0.4067$ 19.5 mag



$\alpha/\delta_{\text{opt}}$ 17 54 4.8 +66 13 51

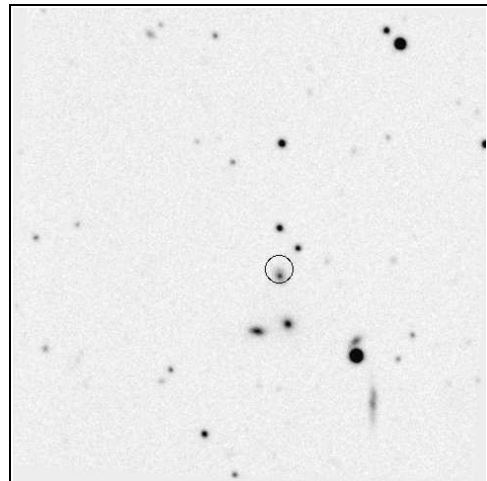
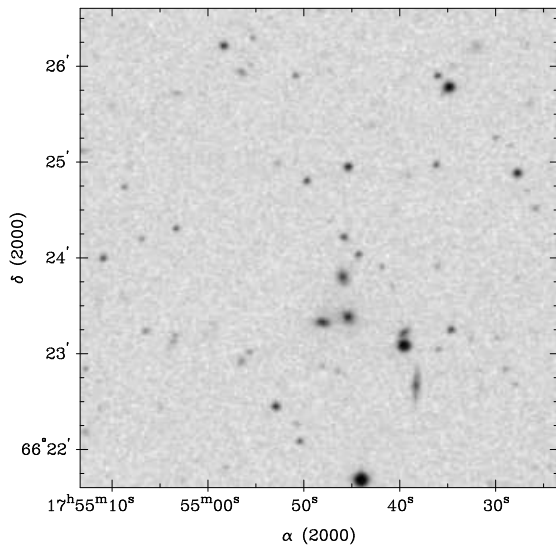
1RXS J175441.9+680334

Cluster $z = 0.077$



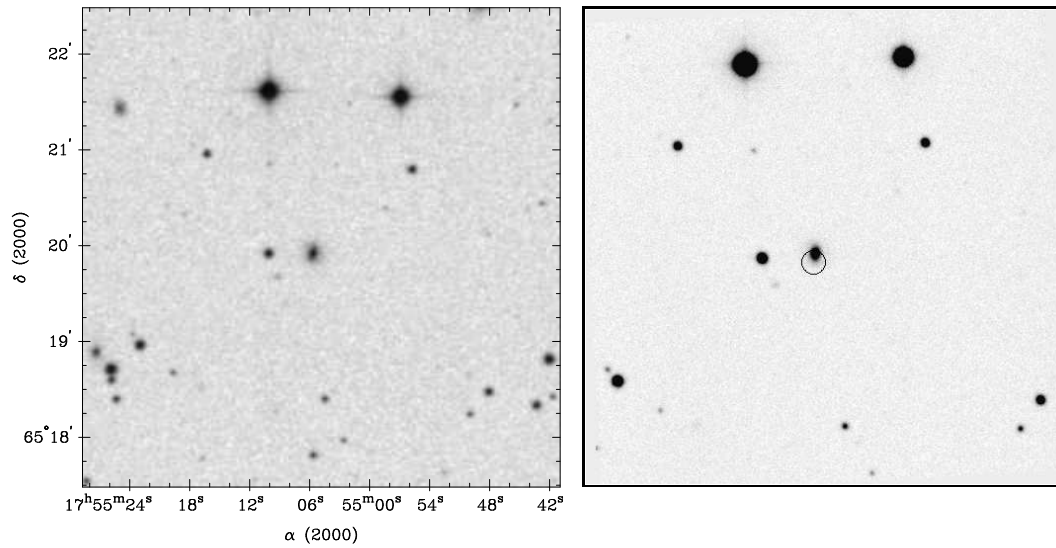
1RXS J175445.8+662353

Cluster $z = 0.0879$



1RXS J175505.8+651951

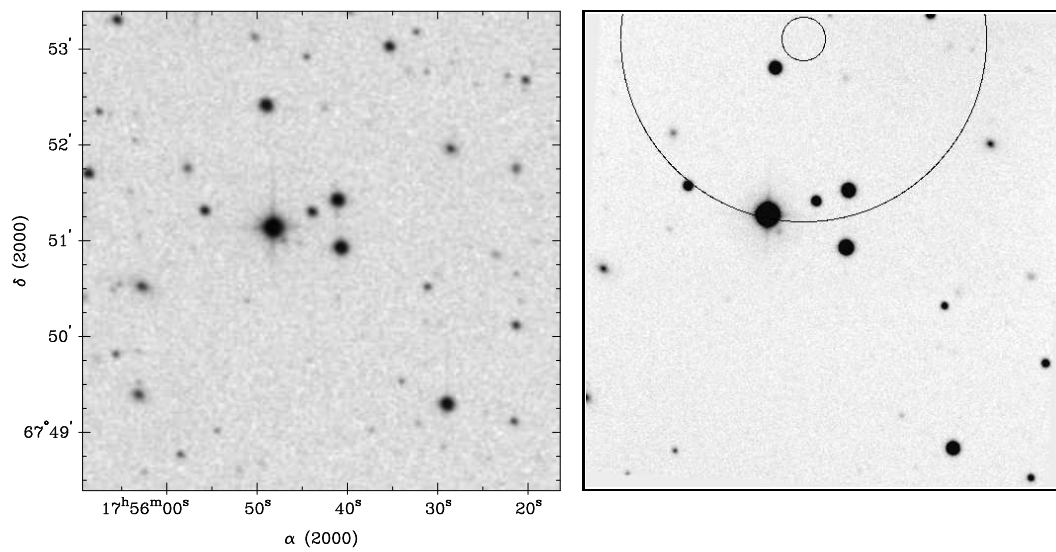
AGN $z = 0.0785$ 16.7 mag



$\alpha/\delta_{\text{opt}} 17\ 55\ 5.6\ +65\ 19\ 56$

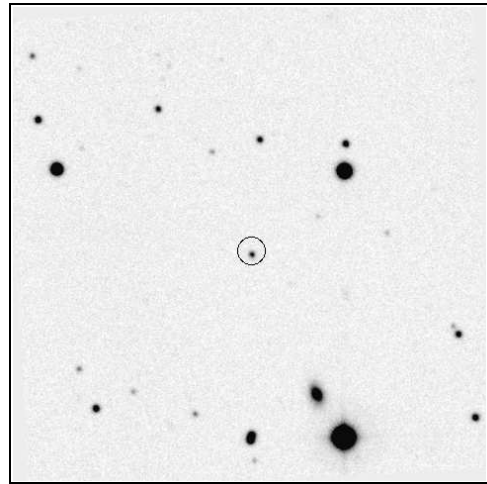
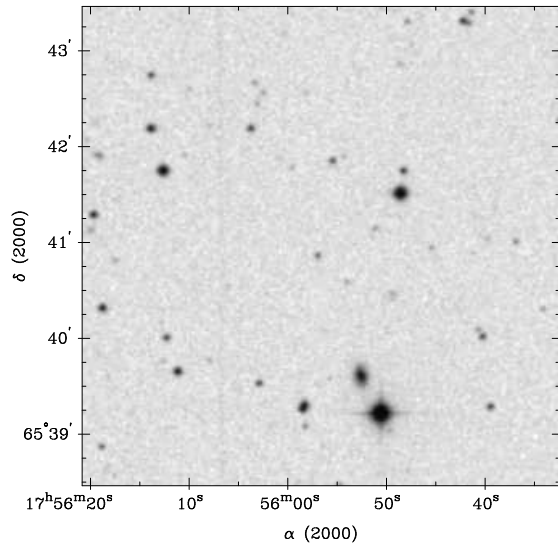
1RXS J175545.5+675242

Cluster $z = 0.0833$



1RXS J175556.9+654054

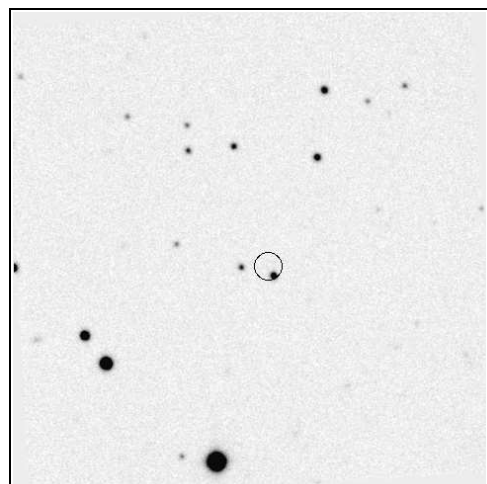
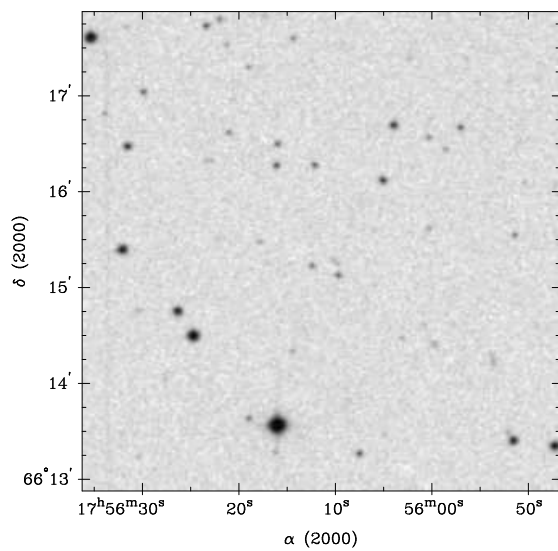
AGN $z = 0.3238$ 19.5 mag



$\alpha/\delta_{\text{opt}}$ 17 55 56.8 +65 40 52

1RXS J175610.0+661514

AGN $z = 0.6357$ 18.6 mag

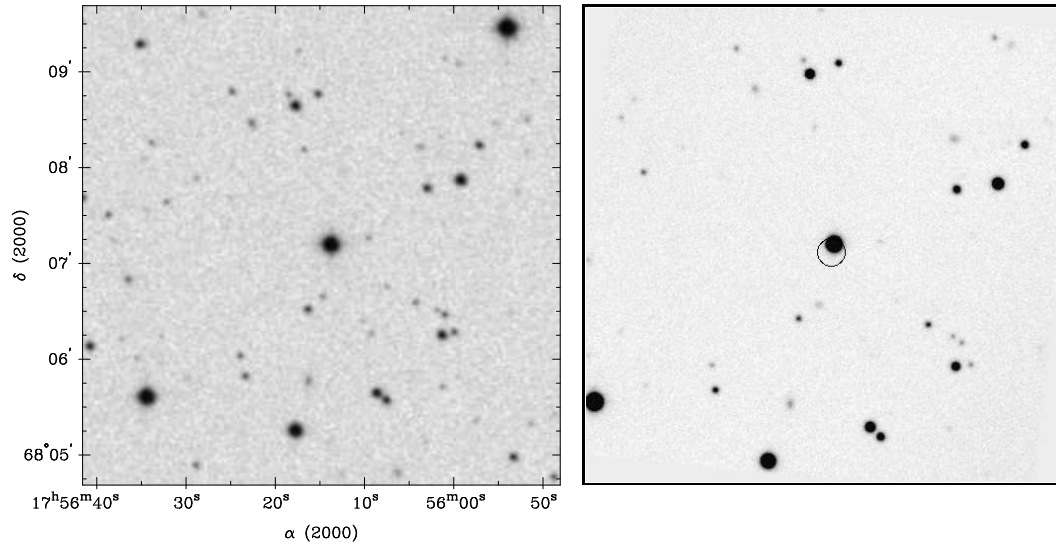


$\alpha/\delta_{\text{opt}}$ 17 56 9.5 +66 15 9

1RXS J175614.1+680707

Star

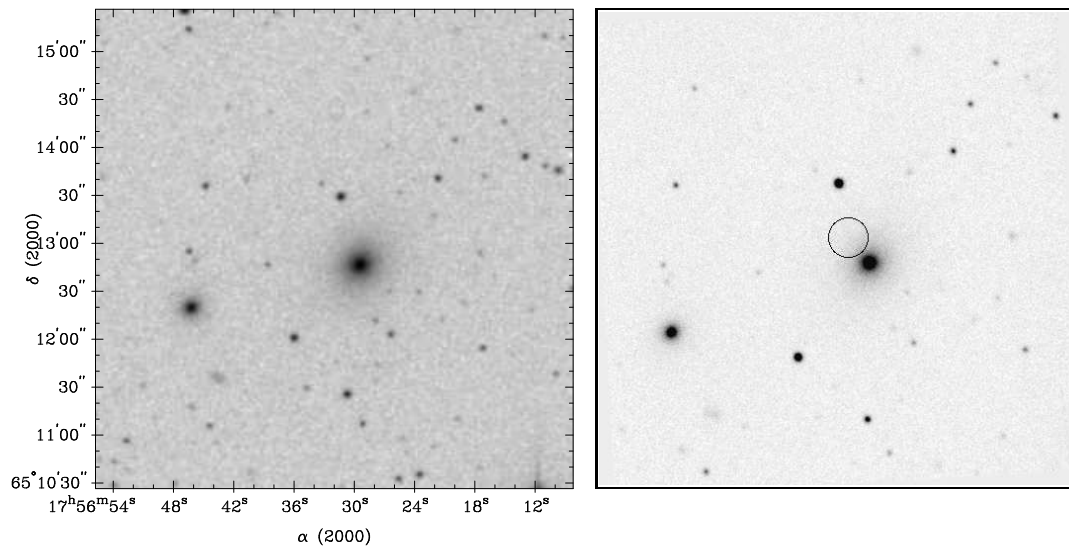
13.8 mag



$\alpha/\delta_{\text{opt}}$ 17 56 13.8 +68 7 11

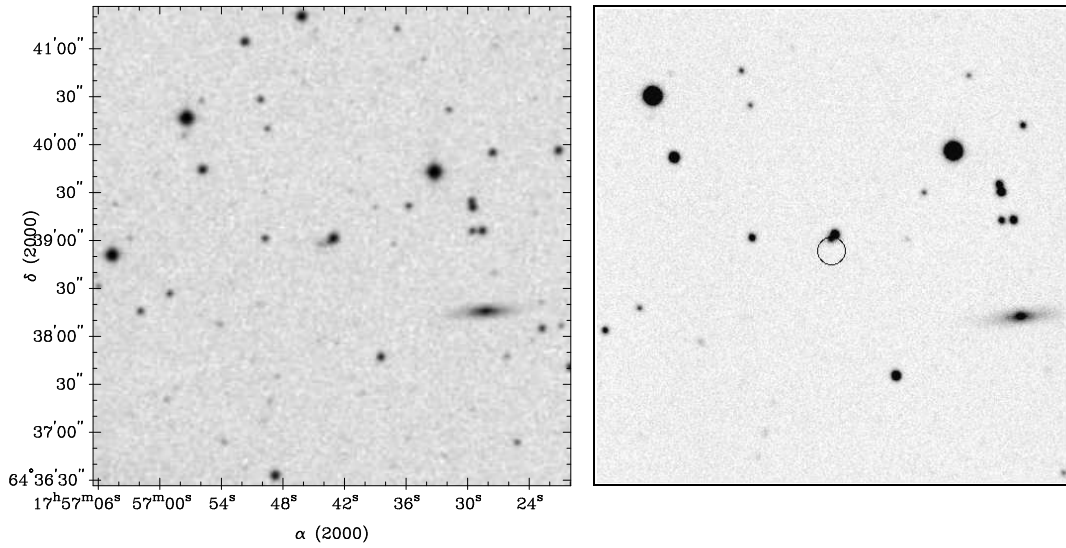
1RXS J175631.0+651302

Cluster $z = 0.0284$



1RXS J175643.3+643853

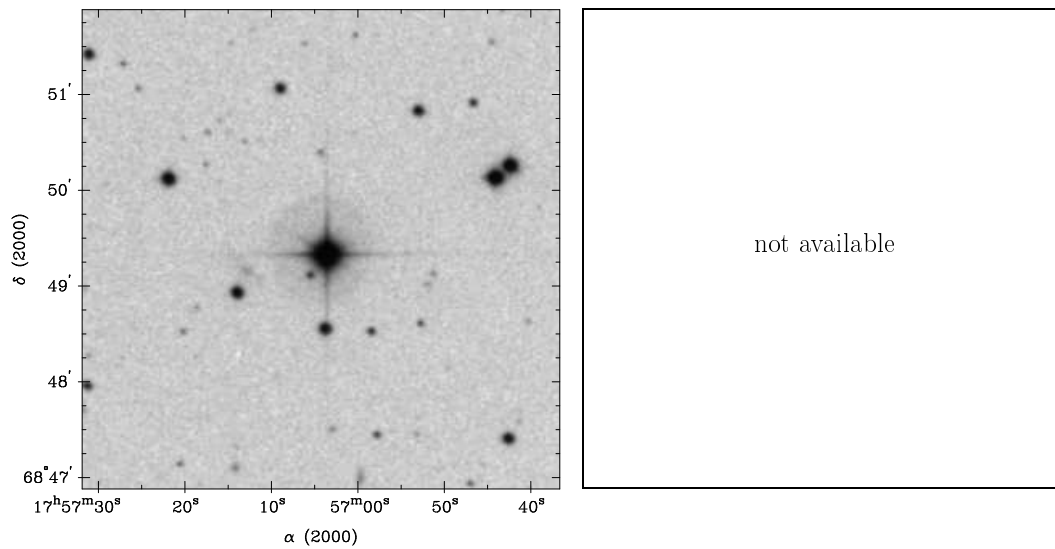
AGN $z = 0.2233$ 17.1 mag



$\alpha/\delta_{\text{opt}}$ 17 56 43.1 +64 39 1

1RXS J175703.7+684923

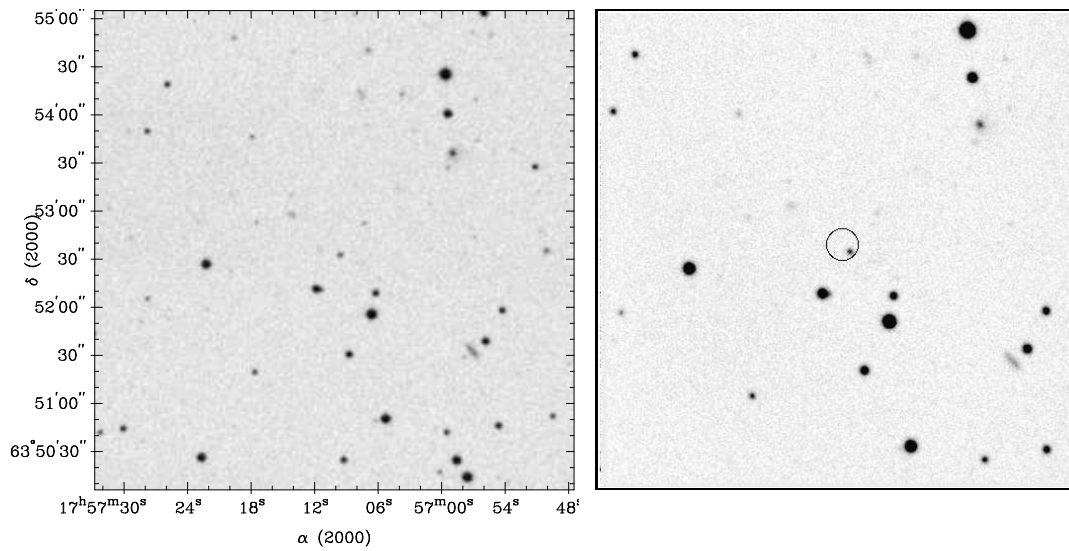
Star 9.69 mag



$\alpha/\delta_{\text{opt}}$ 17 57 3.6 +68 49 20

1RXS J175709.8+635238

AGN $z = 0.322$ 19.6 mag

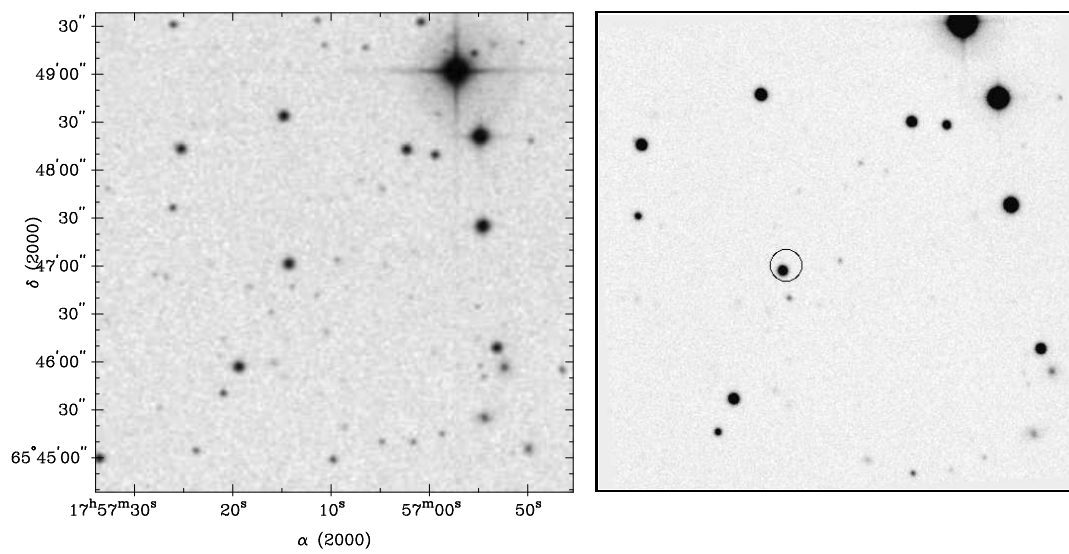


DSSII finding chart from POSSII-B

$\alpha/\delta_{\text{opt}} 17 57 9.2 +63 52 34$

1RXS J175713.9+654702

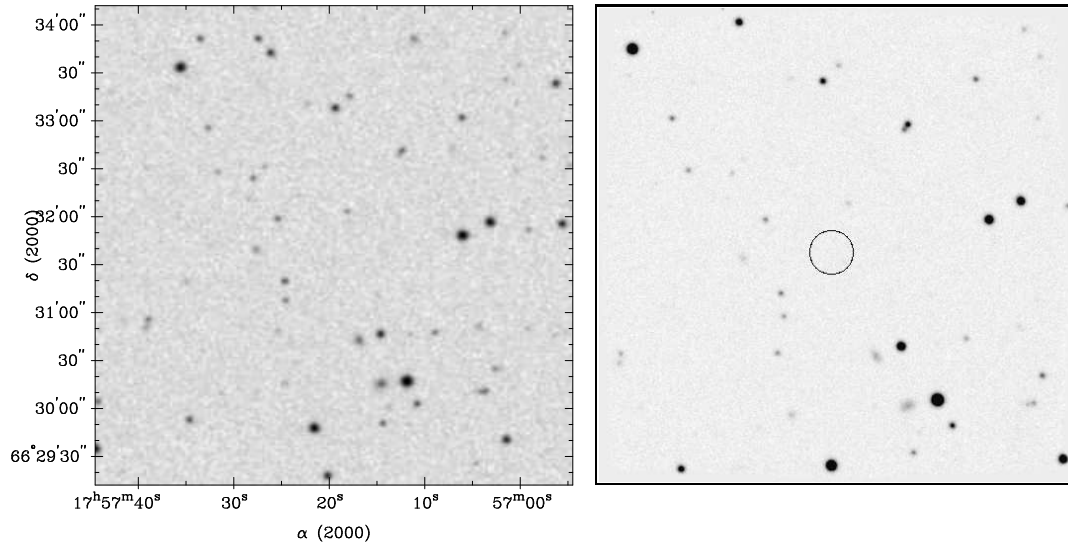
Star 16.8 mag



$\alpha/\delta_{\text{opt}} 17 57 14.2 +65 47 0$

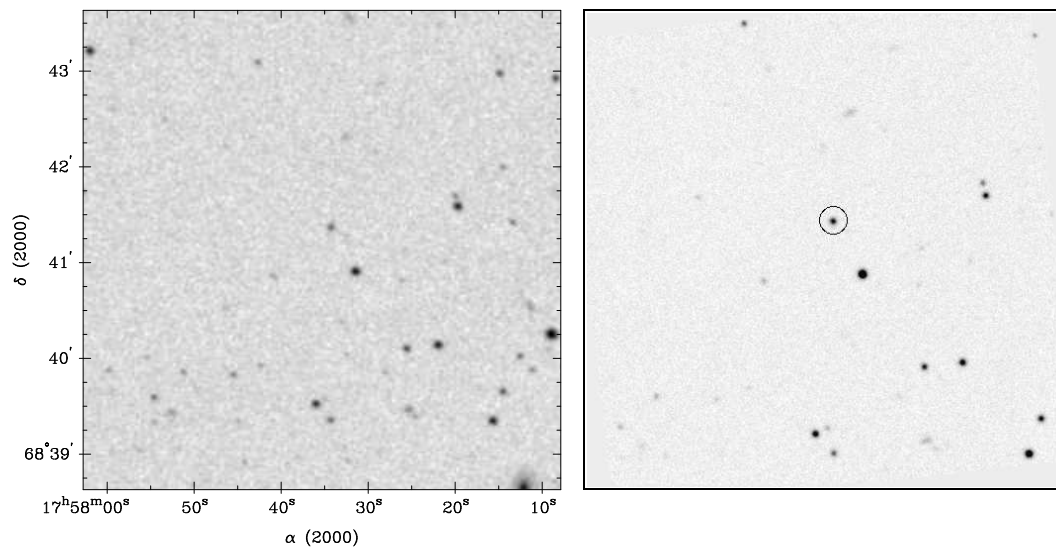
1RXS J175719.9+663139

Cluster $z = 0.6909$



1RXS J175734.1+684122

AGN $z = 0.1814$ 19.2 mag

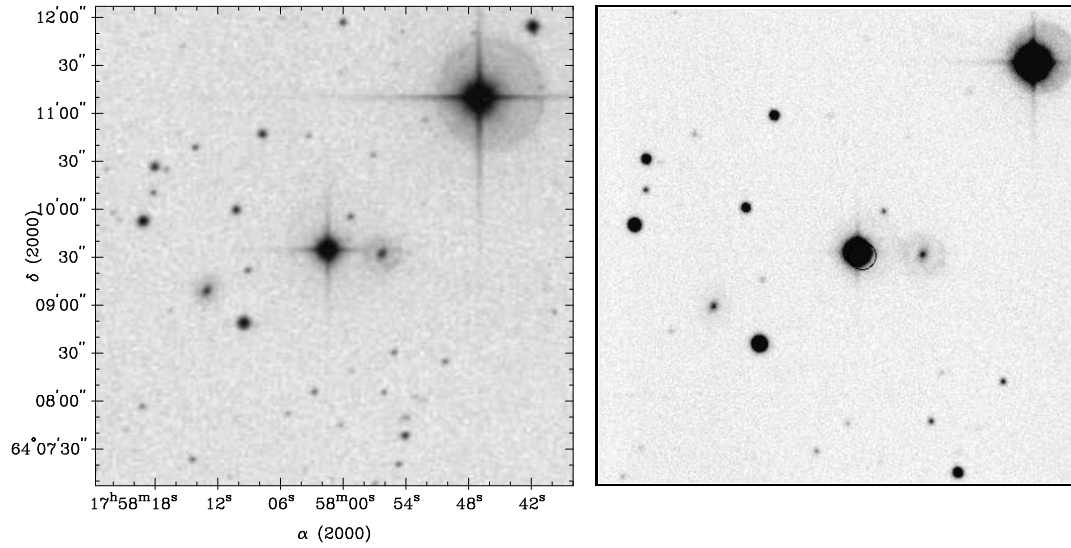


$\alpha/\delta_{\text{opt}} 17 57 34.1 +68 41 21$

1RXS J175801.0+640932

Star

11.2 mag

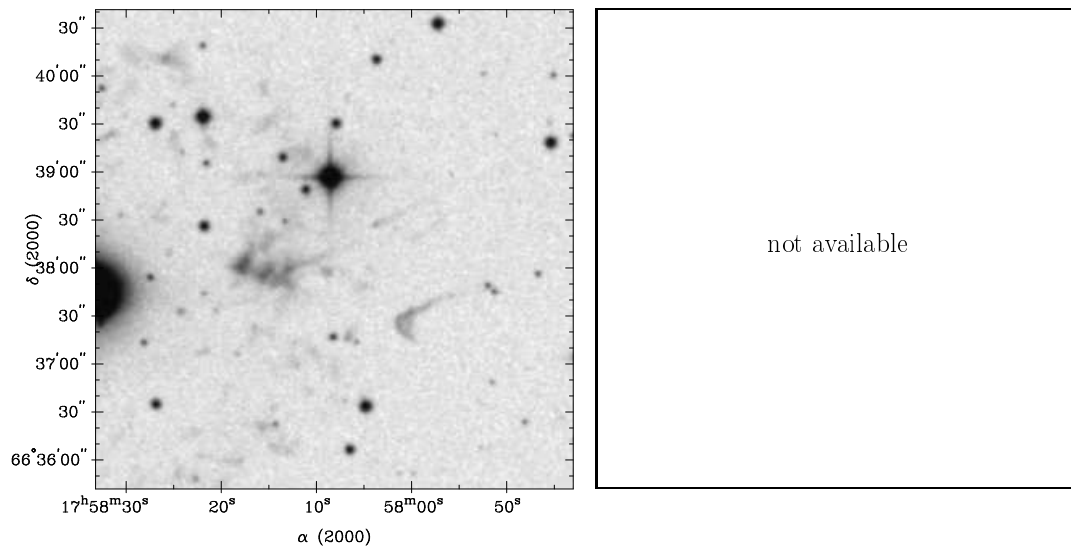


$\alpha/\delta_{\text{opt}}$ 17 58 1.4 +64 9 34

RX J1758.1+6639

Star

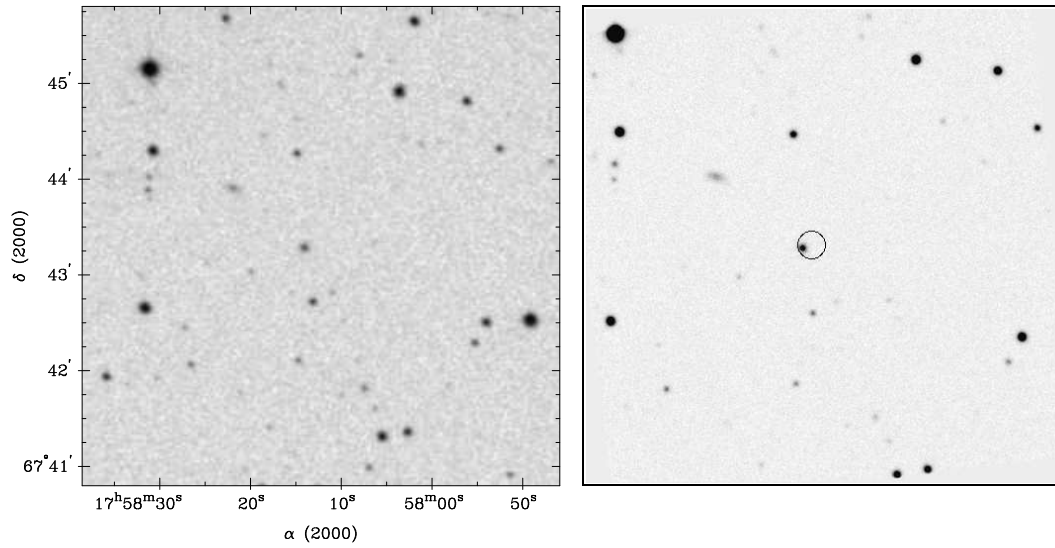
10.3 mag



$\alpha/\delta_{\text{opt}}$ 17 58 7.8 +66 38 57

1RXS J175813.2+674319

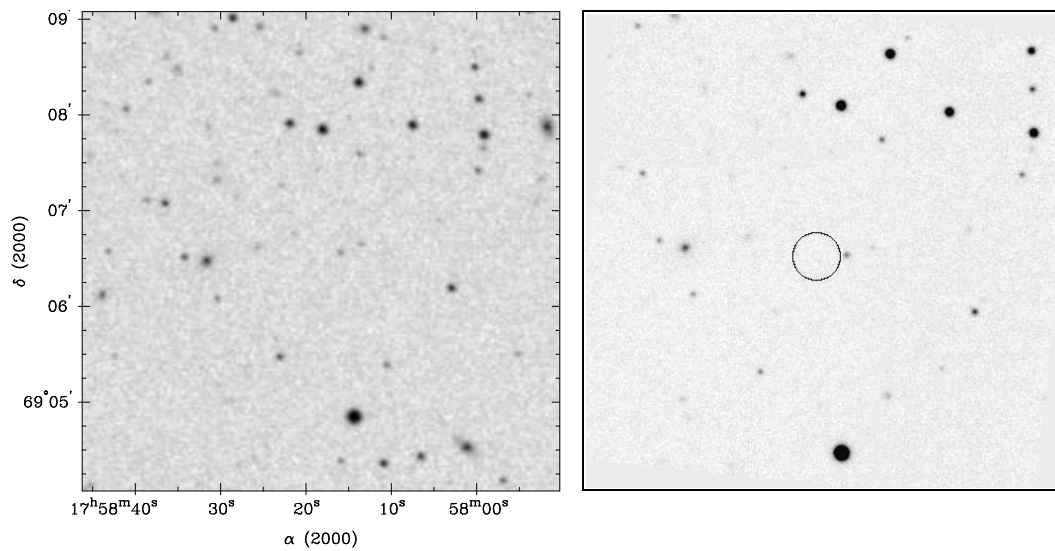
AGN $z = 0.2045$ 18.8 mag



$\alpha/\delta_{\text{opt}} 17\ 58\ 14.0\ +67\ 43\ 18$

1RXS J175818.8+690631

AGN $z = 2.1572$ 20.2 mag

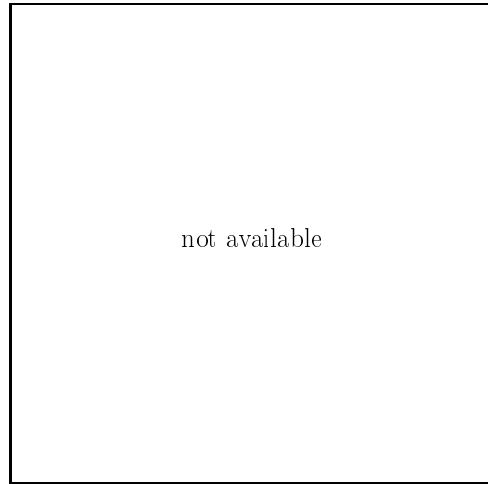
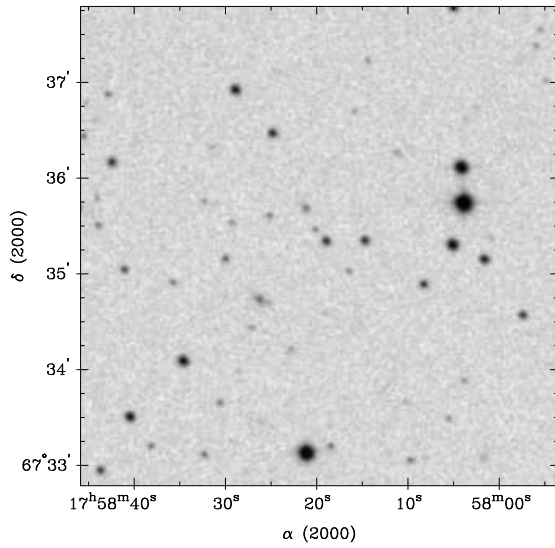


$\alpha/\delta_{\text{opt}} 17\ 58\ 15.9\ +69\ 6\ 32$

1RXS J175819.1+673515

Star

18.6 mag



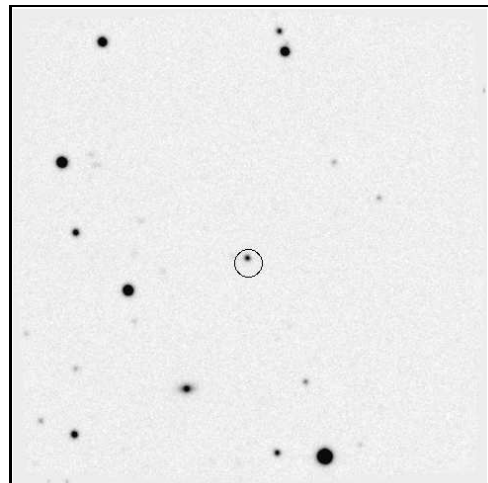
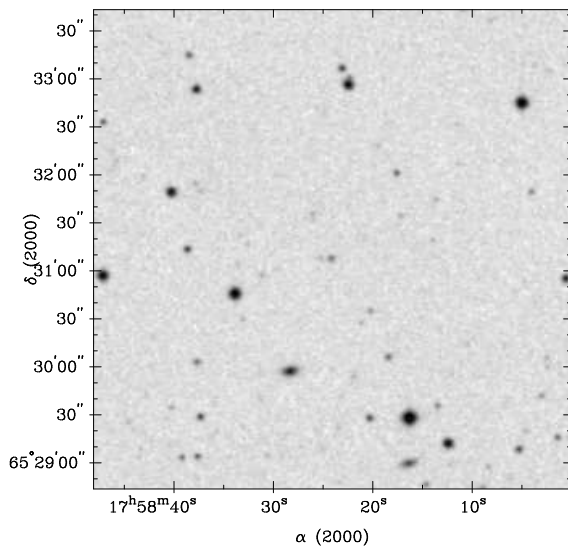
$\alpha/\delta_{\text{opt}}$ 17 58 18.7 +67 35 19

1RXS J175824.2+653105

AGN

$z = 0.325$

19.5 mag

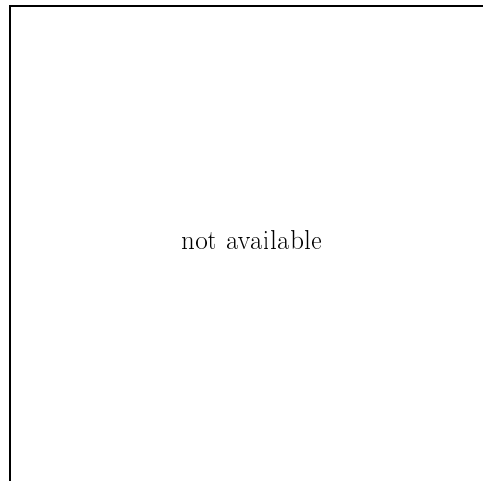
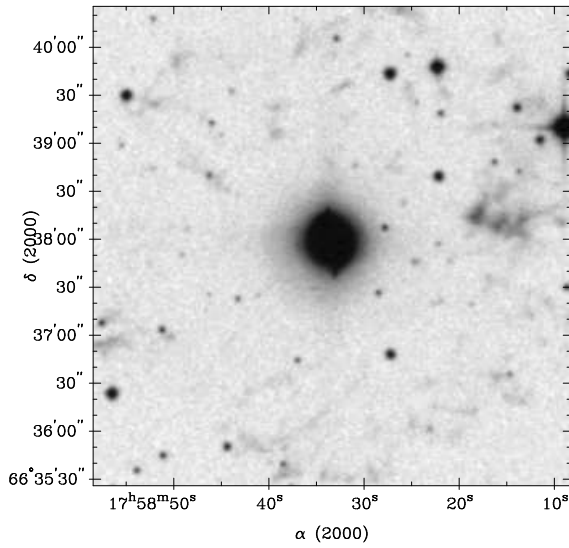


$\alpha/\delta_{\text{opt}}$ 17 58 24.3 +65 31 8

1RXS J175833.4+663759

PN

9.80 mag

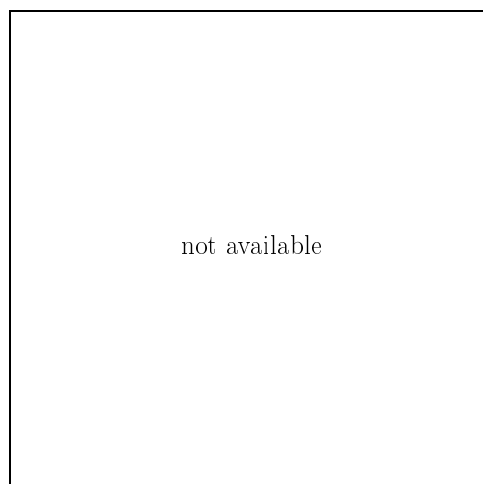
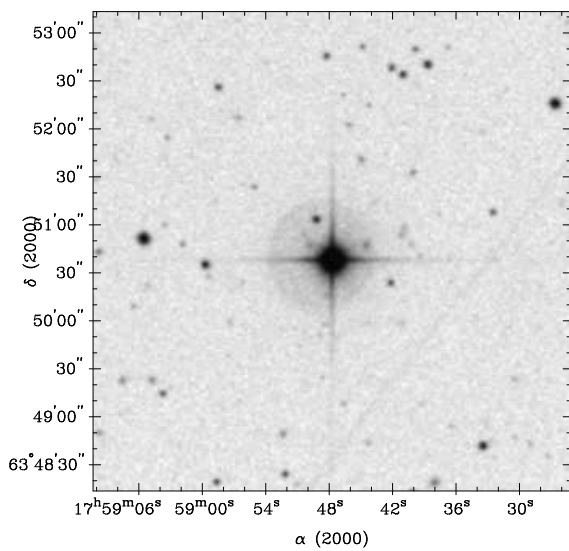


$\alpha/\delta_{\text{opt}}$ 17 58 34.2 +66 38 6

1RXS J175847.2+635039

Star

8.66 mag

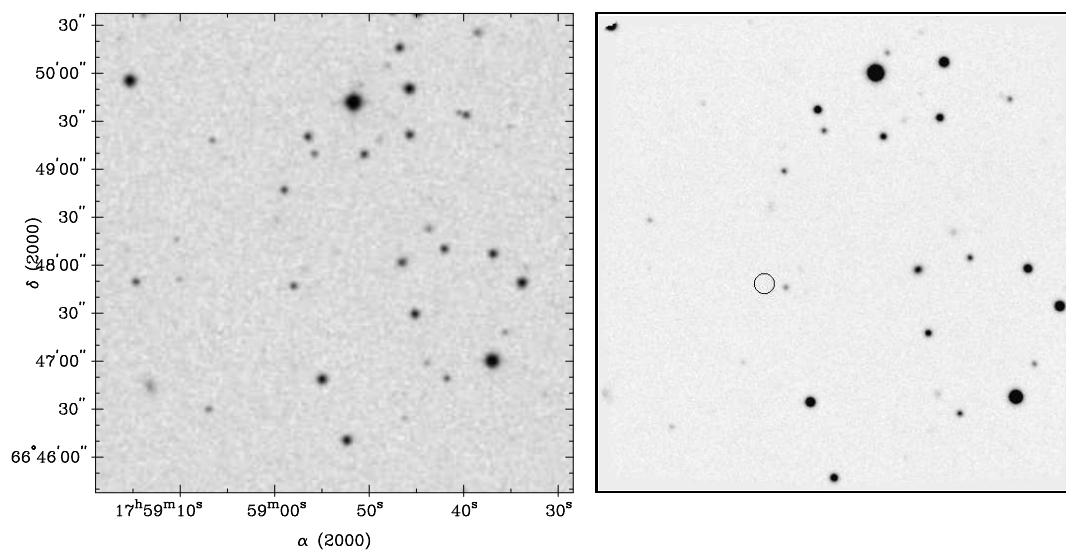


$\alpha/\delta_{\text{opt}}$ 17 58 47.7 +63 50 38

2RXP J175900.1+664752

?

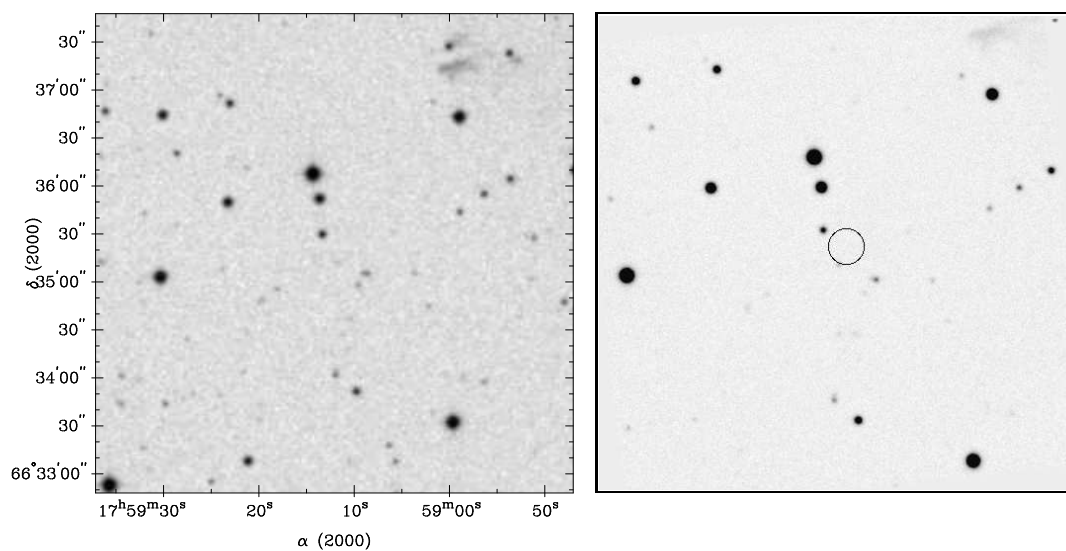
20.4 mag



$\alpha/\delta_{\text{opt}}$ 17 58 58.2 +66 47 50

1RXS J175911.3+663521

AGN $z = 0.630$ 20.9 mag

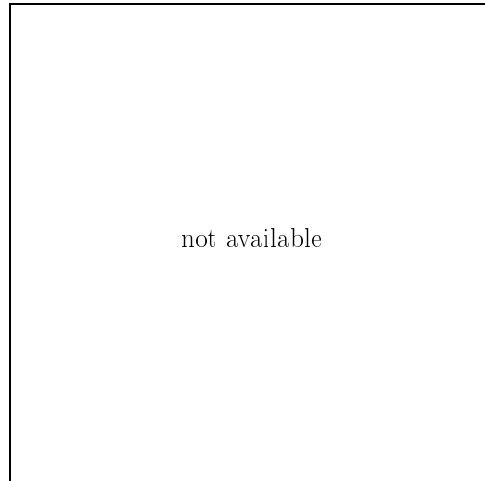
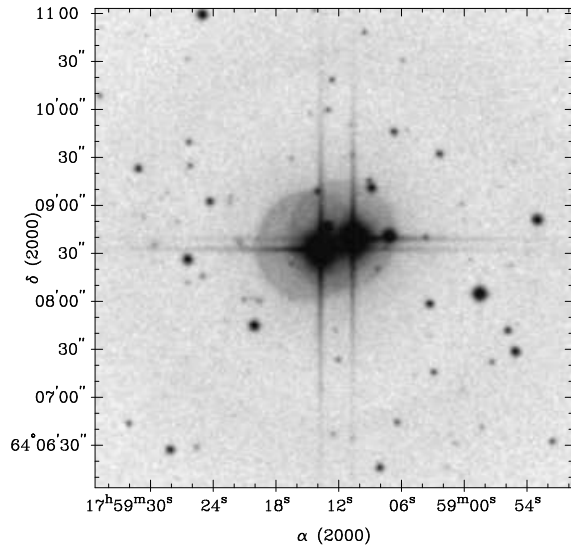


$\alpha/\delta_{\text{opt}}$ 17 59 12.1 +66 35 12

1RXS J175912.5+640833

Star

7.64 mag



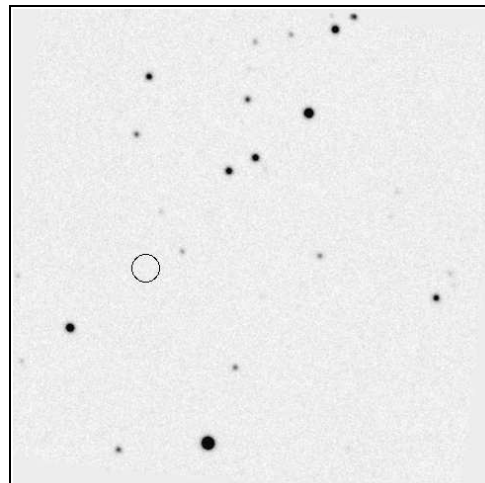
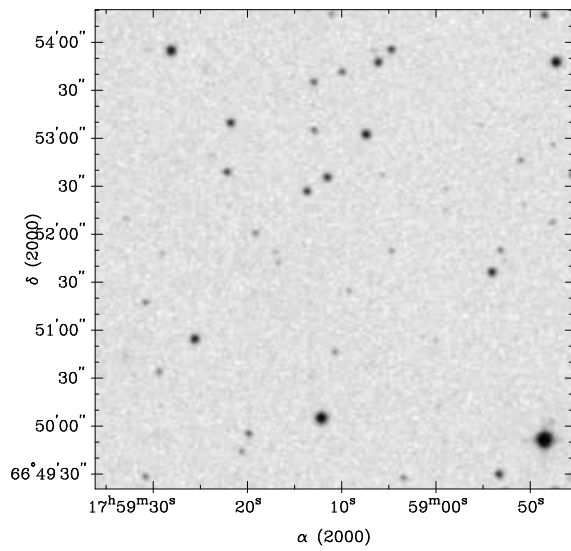
$\alpha/\delta_{\text{opt}}$ 17 59 13.6 +64 8 34

2RXP J175919.9+665135

AGN

$z = 0.944$

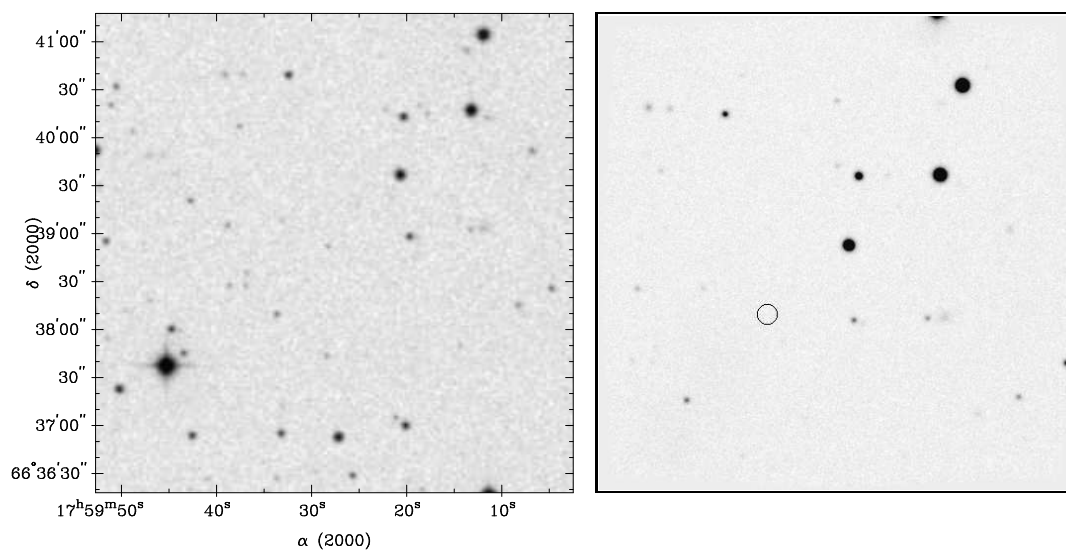
20.7 mag



$\alpha/\delta_{\text{opt}}$ 17 59 16.8 +66 51 44

2RXP J175930.1+663848

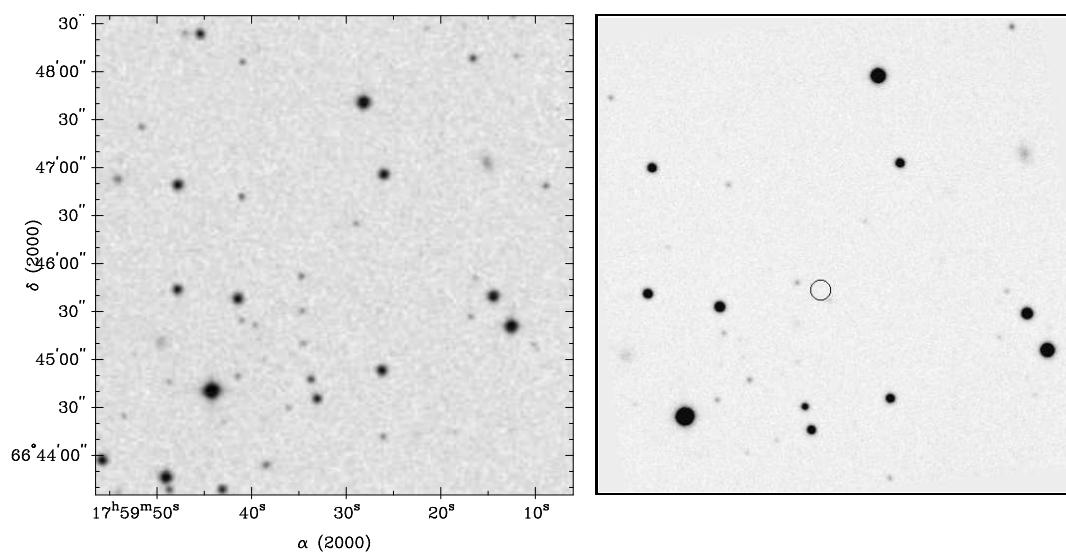
AGN $z = 4.32$ $> 21.9\text{mag}$



$\alpha/\delta_{\text{opt}} 17\ 59\ 27.9\ +66\ 38\ 53$

2RXP J175934.4+664533

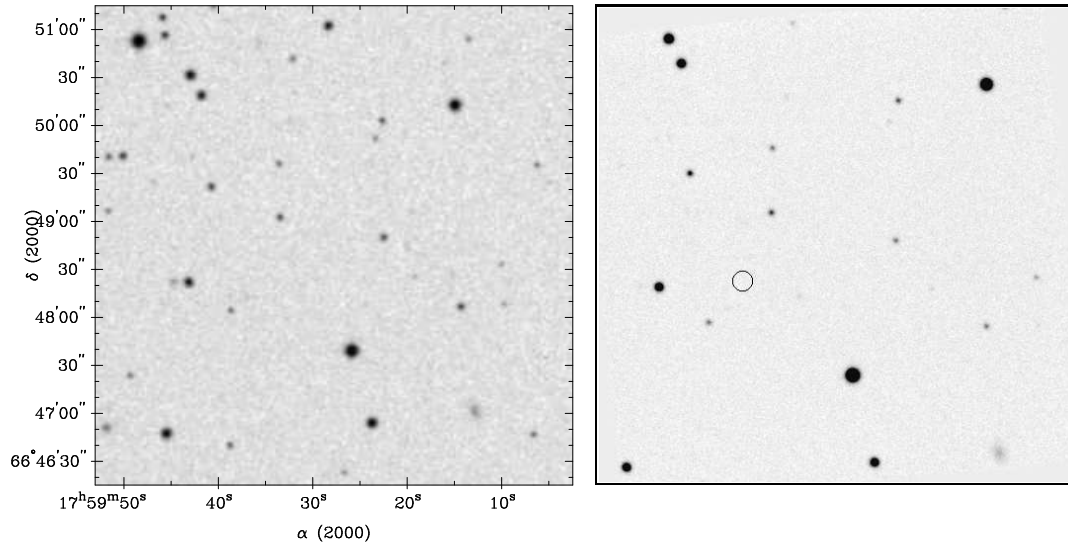
AGN $z = 1.17$ $21.0\ \text{mag}$



$\alpha/\delta_{\text{opt}} 17\ 59\ 32.2\ +66\ 45\ 42$

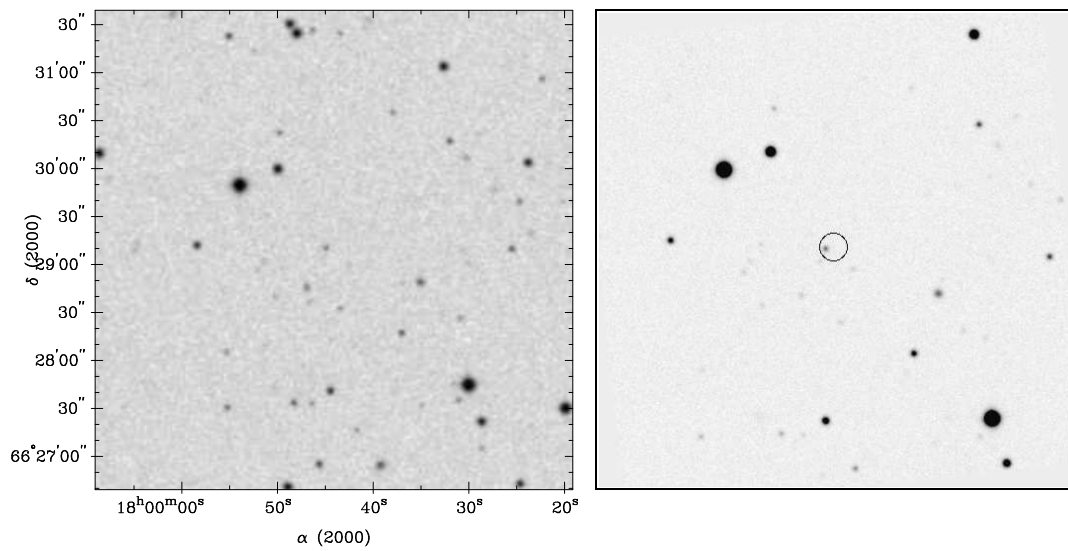
2RXP J175937.9+664818

?



1RXS J175944.3+662911

AGN $z = 0.399$ 20.2 mag

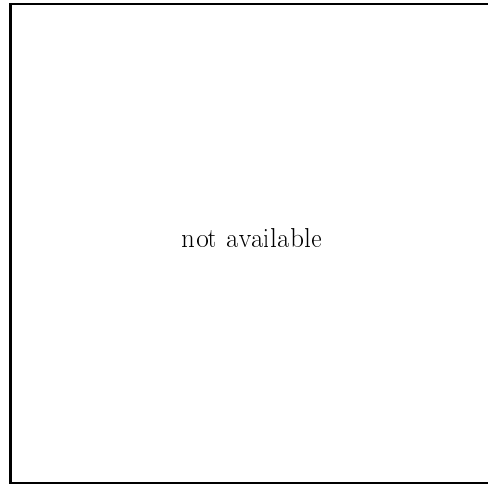
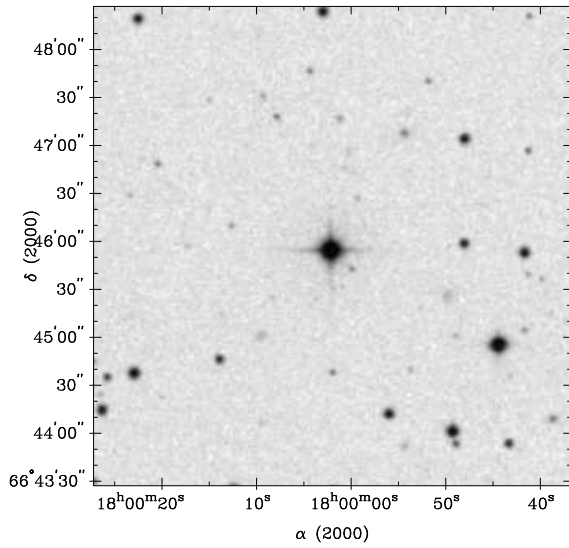


$\alpha/\delta_{\text{opt}} 17 59 45.0 +66 29 10$

1RXS J180001.9+664559

Star

11.3 mag

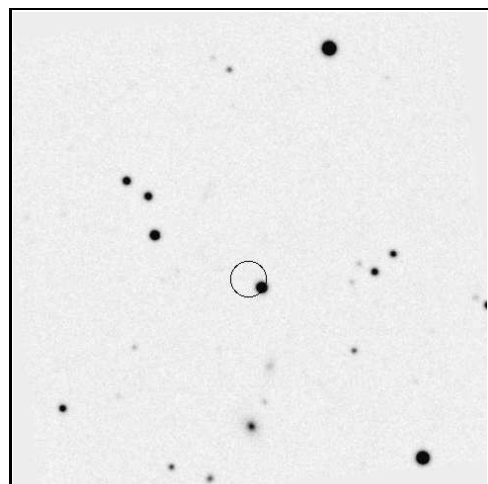
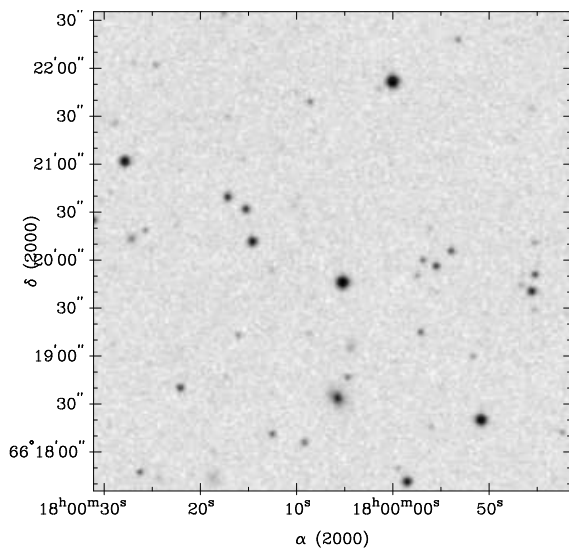


$\alpha/\delta_{\text{opt}}$ 18 0 2.1 +66 45 55

2RXP J180006.6+661950

Star ?

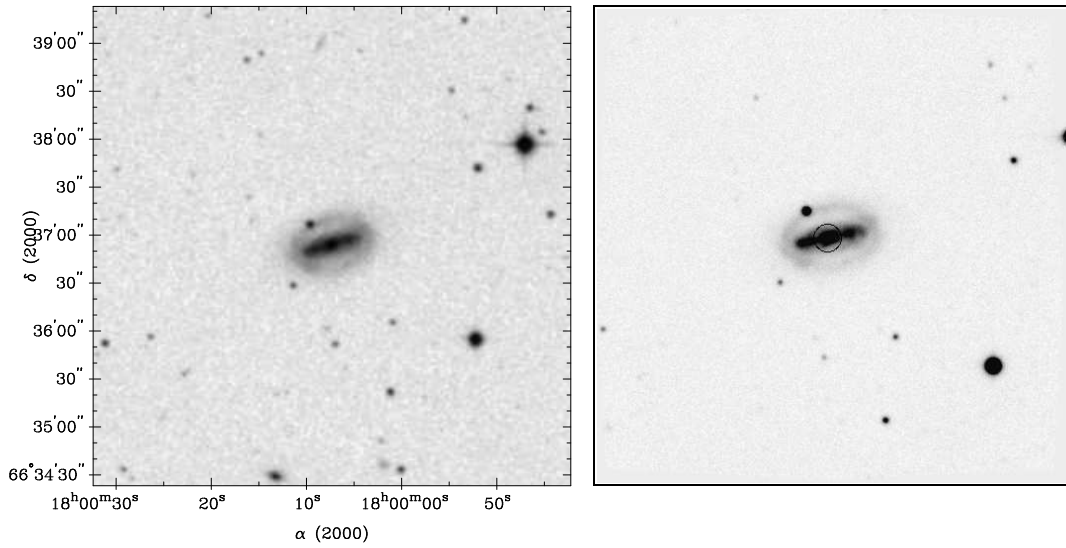
16.3 mag



$\alpha/\delta_{\text{opt}}$ 18 0 5.5 +66 19 45

1RXS J180007.5+663654

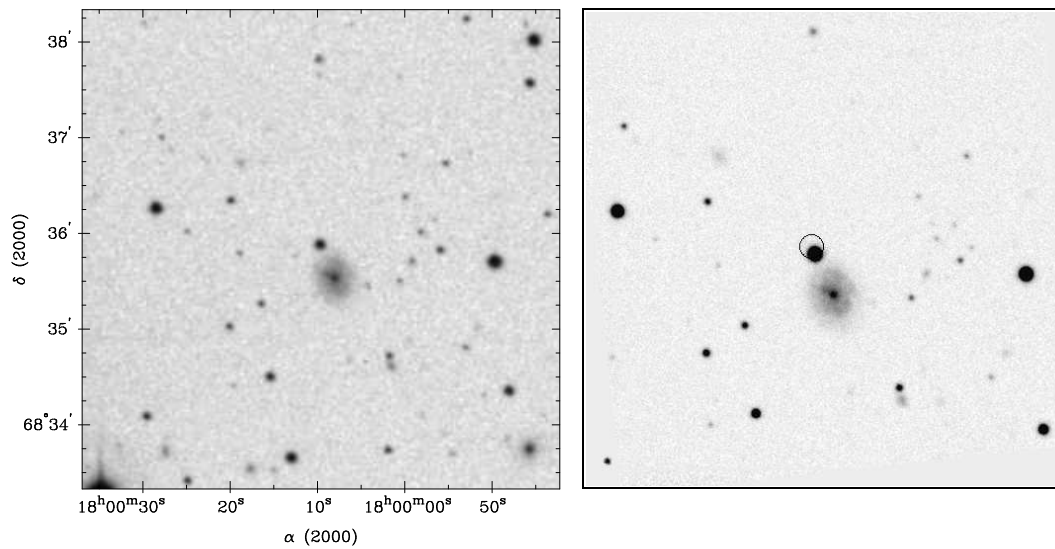
AGN $z = 0.026$ 13.6 mag



$\alpha/\delta_{\text{opt}}$ 18 0 7.3 +66 36 54

1RXS J180009.9+683557

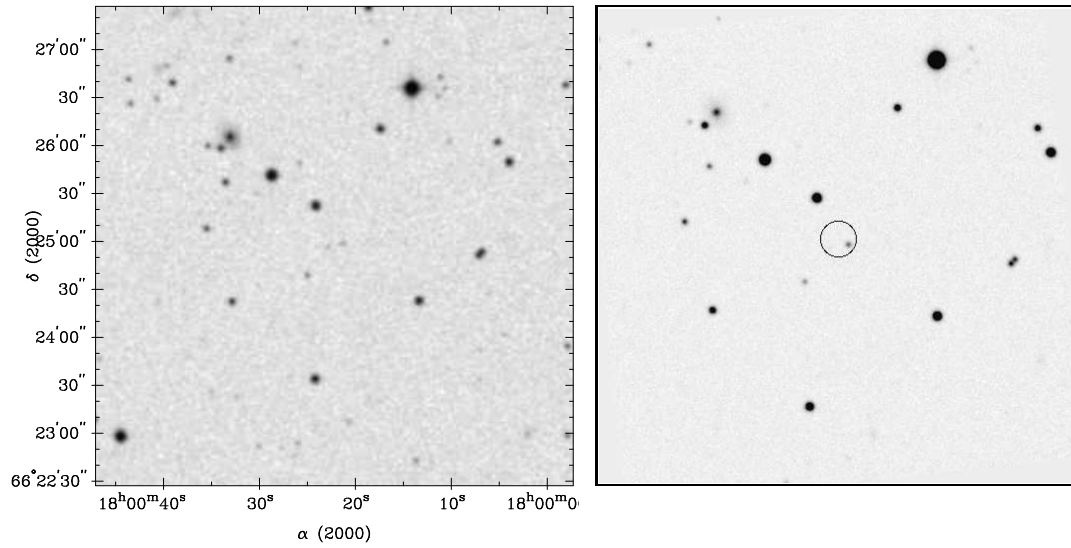
white dwarf 14.5 mag



$\alpha/\delta_{\text{opt}}$ 18 0 9.6 +68 35 53

1RXS J180022.1+662501

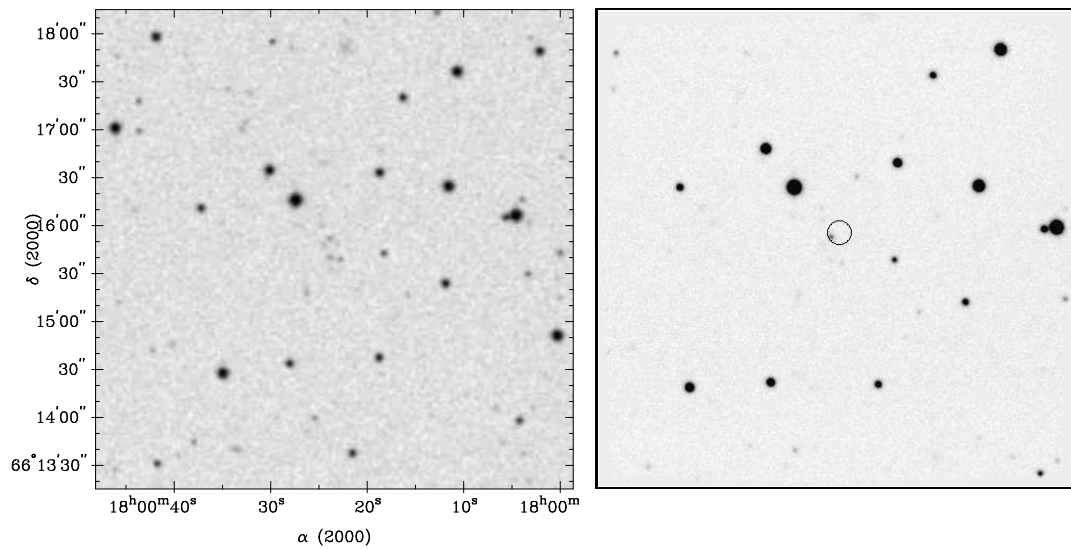
AGN $z = 1.62$ 20.2 mag



$\alpha/\delta_{\text{opt}}$ 18 0 21.3 +66 24 58

1RXS J180023.1+661554

AGN $z = 0.4475$ 20.2 mag

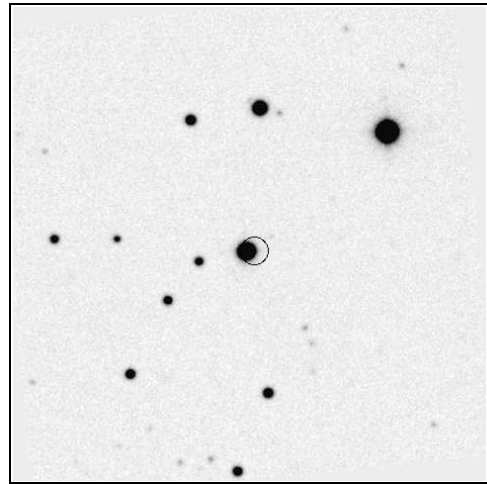
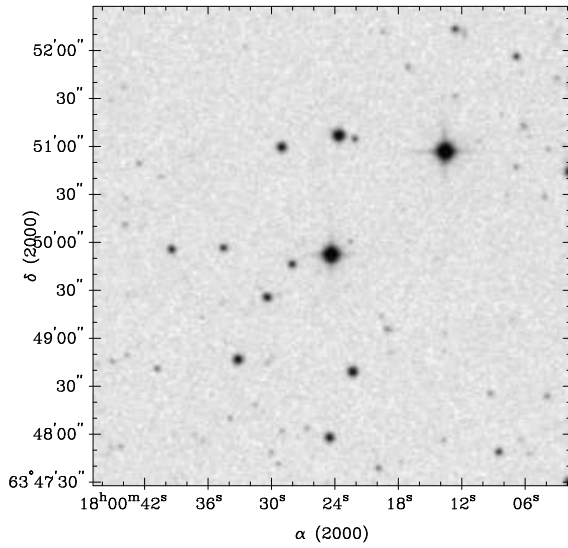


$\alpha/\delta_{\text{opt}}$ 18 0 23.8 +66 15 52

1RXS J180023.9+634953

Star

13.3 mag



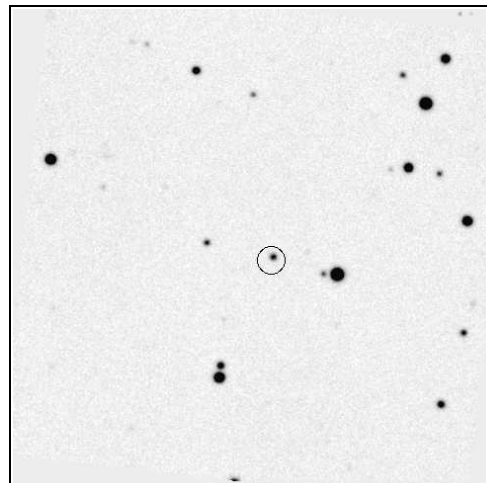
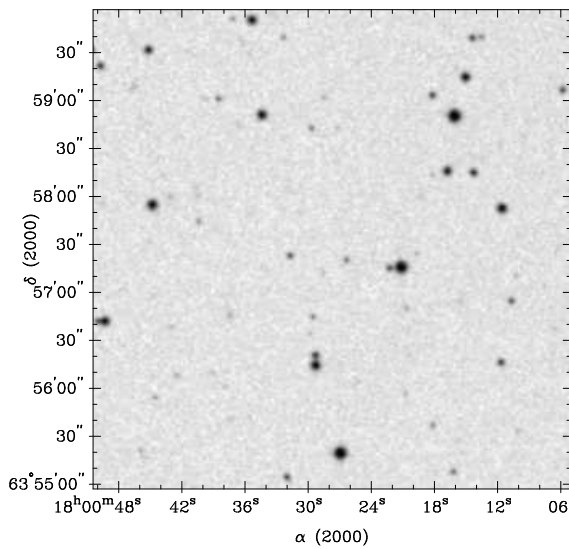
$\alpha/\delta_{\text{opt}}$ 18 0 24.5 +63 49 53

1RXS J180026.2+635719

AGN

$z = 0.6828$

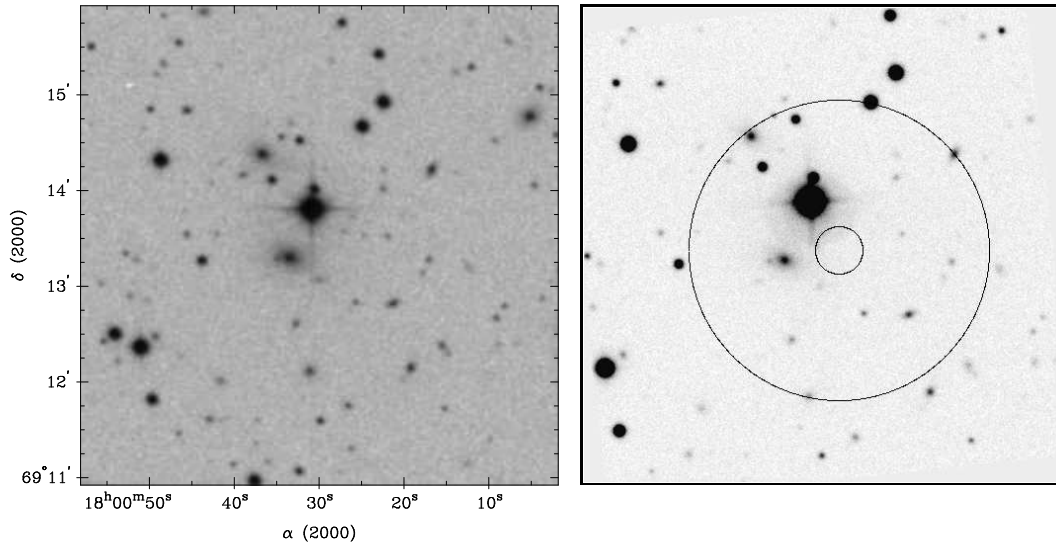
19.1 mag



$\alpha/\delta_{\text{opt}}$ 18 0 26.1 +63 57 21

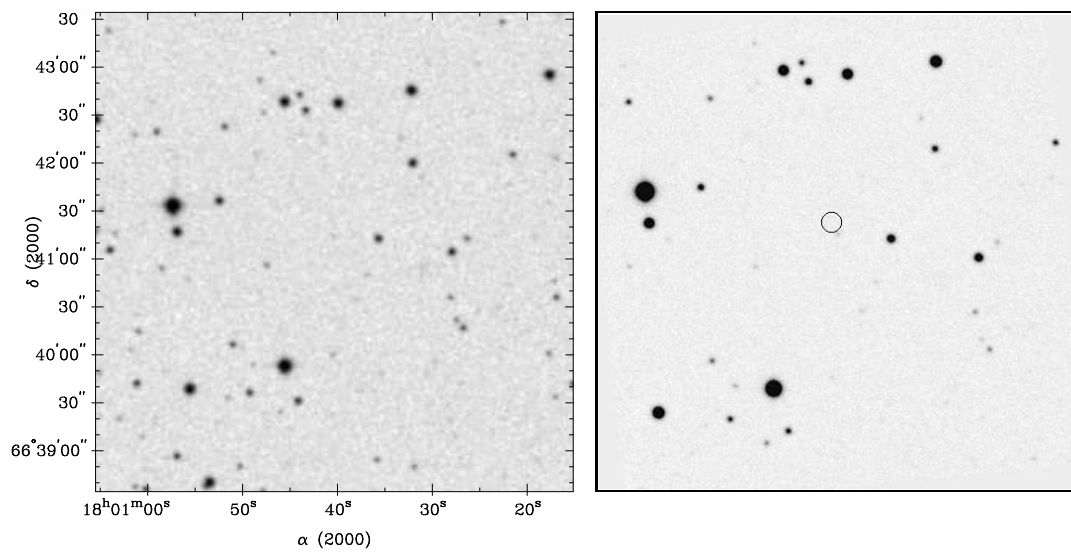
1RXS J180028.2+691322

Cluster $z = 0.0821$



2RXP J180041.5+664112

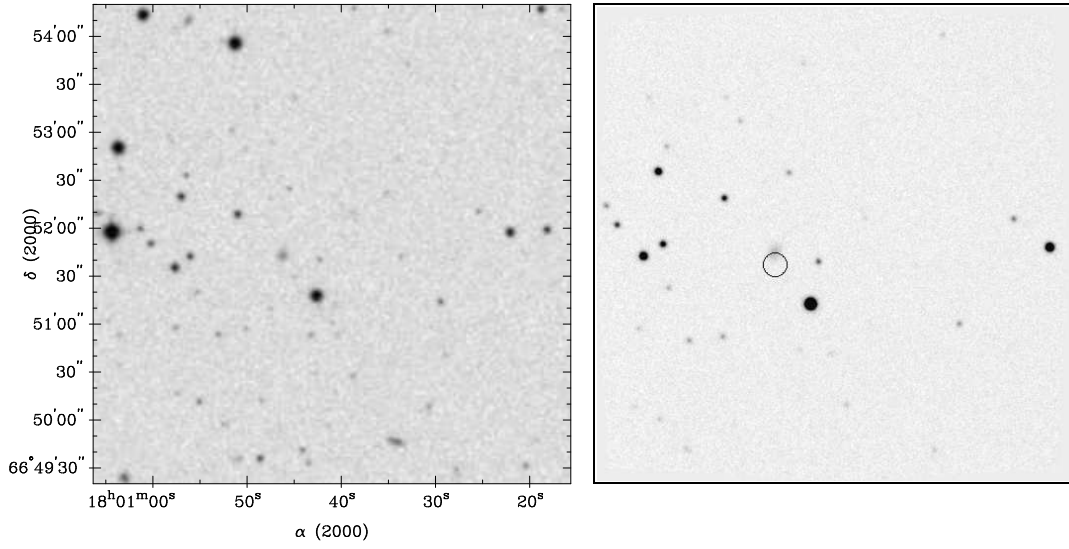
AGN $z = 0.940$ 21.1 mag



$\alpha/\delta_{\text{opt}} 18\ 0\ 40.2\ +66\ 41\ 14$

2RXP J180046.2+665140

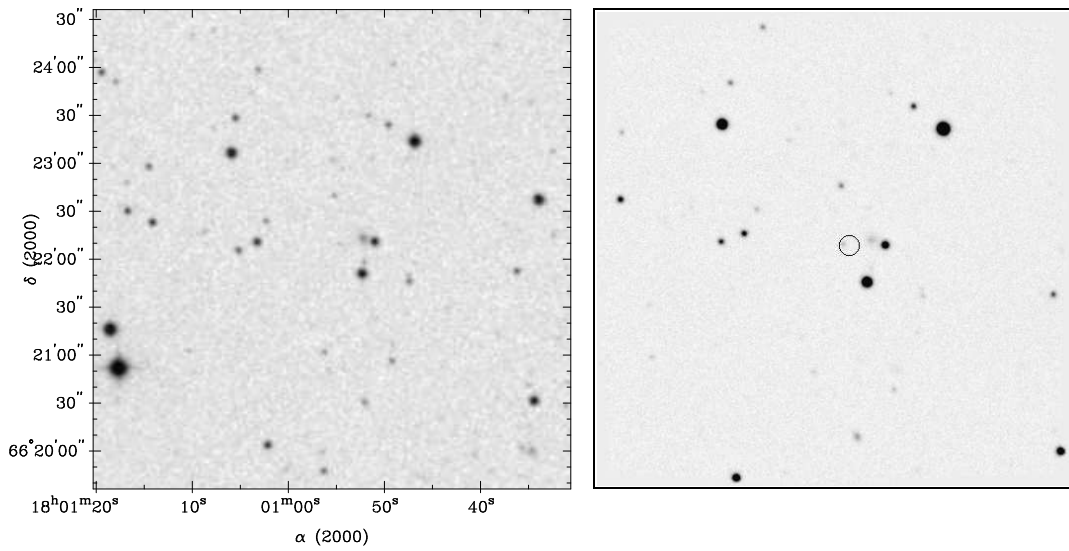
AGN $z = 1.971$ 20.1 mag



$\alpha/\delta_{\text{opt}}$ 18 0 42.3 +66 51 42

2RXP J180055.1+662207

AGN $z = 0.850$ 20.9 mag

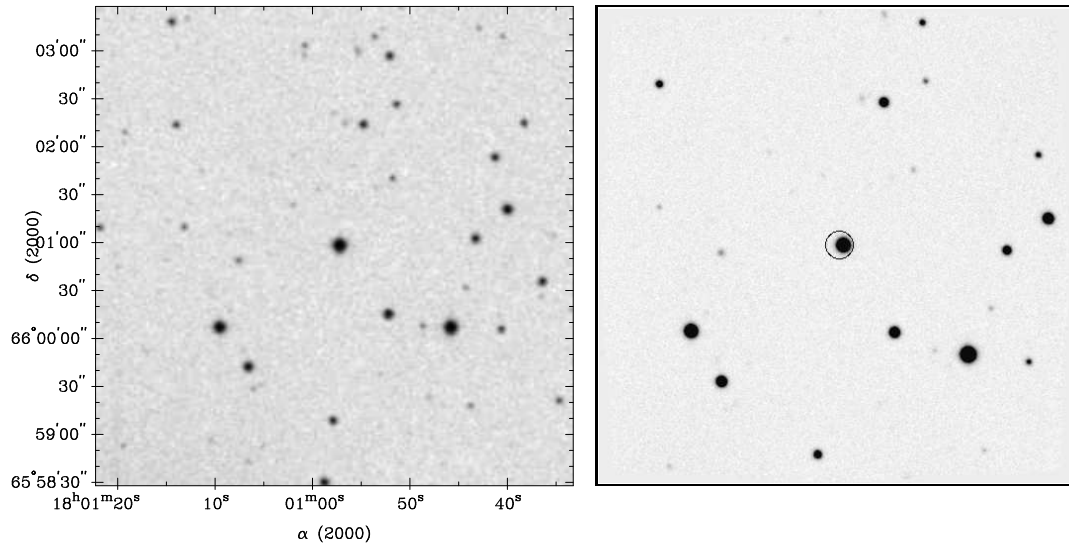


$\alpha/\delta_{\text{opt}}$ 18 0 54.6 +66 22 9

1RXS J180057.6+660058

Star

14.6 mag



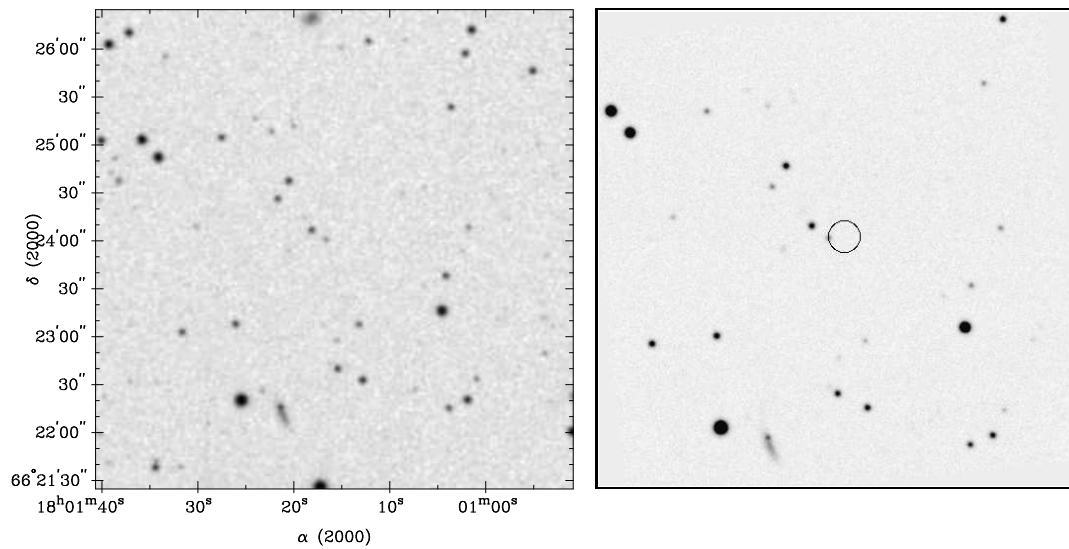
$\alpha/\delta_{\text{opt}}$ 18 0 57.2 +66 0 58

1RXS J180115.2+662401

AGN

$z = 1.2500$

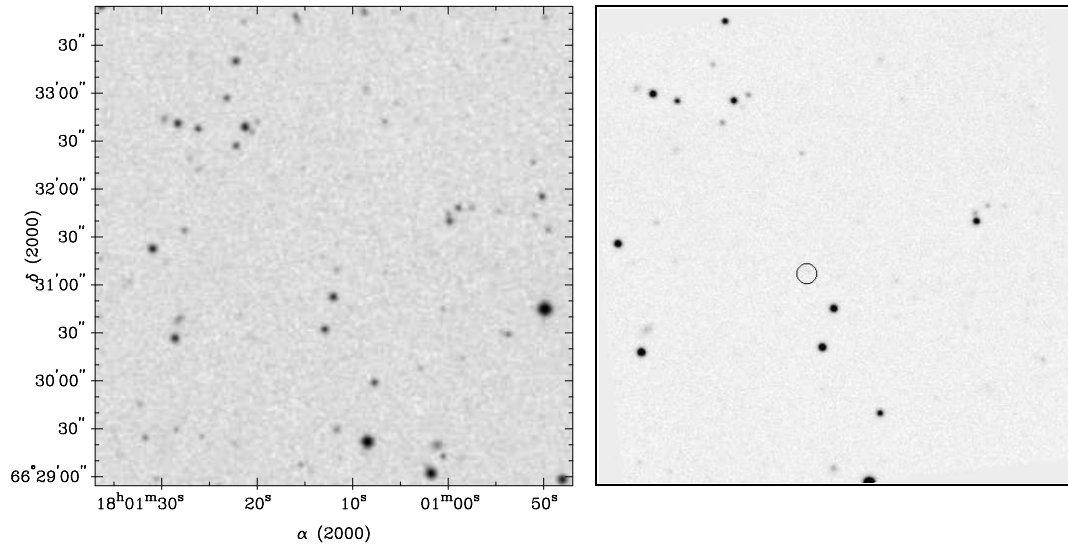
20.4 mag



$\alpha/\delta_{\text{opt}}$ 18 1 16.5 +66 24 1

2RXP J180116.7+663110

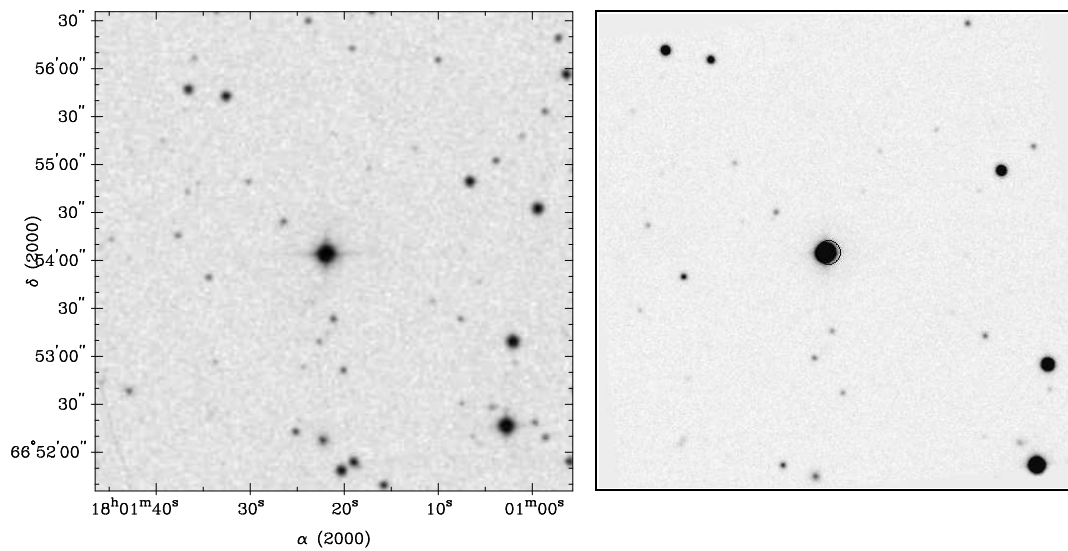
AGN $z = 0.570$ $> 21.5\text{mag}$



$\alpha/\delta_{\text{opt}}$ 18 1 14.3 +66 31 14

1RXS J180121.6+665405

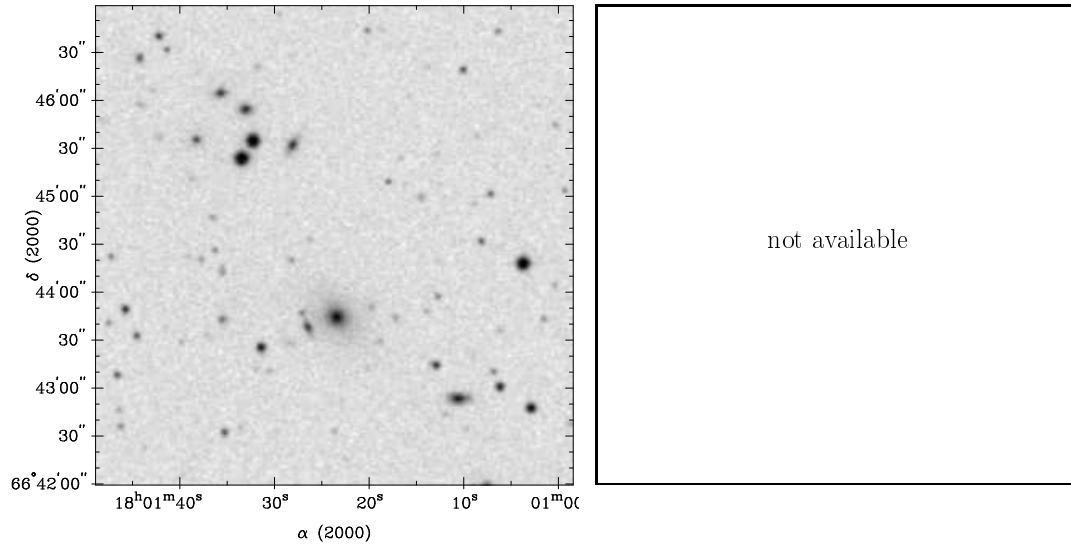
Star 12.5 mag



$\alpha/\delta_{\text{opt}}$ 18 1 21.8 +66 54 5

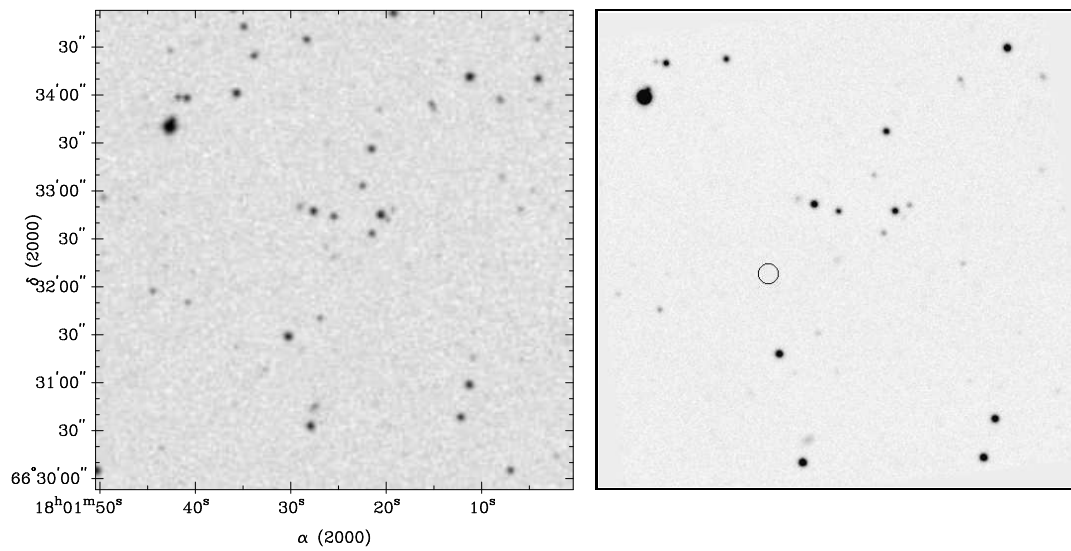
NEPX1 1801.5+6646.5

Cluster $z = 0.090$



2RXP J180133.1+663208

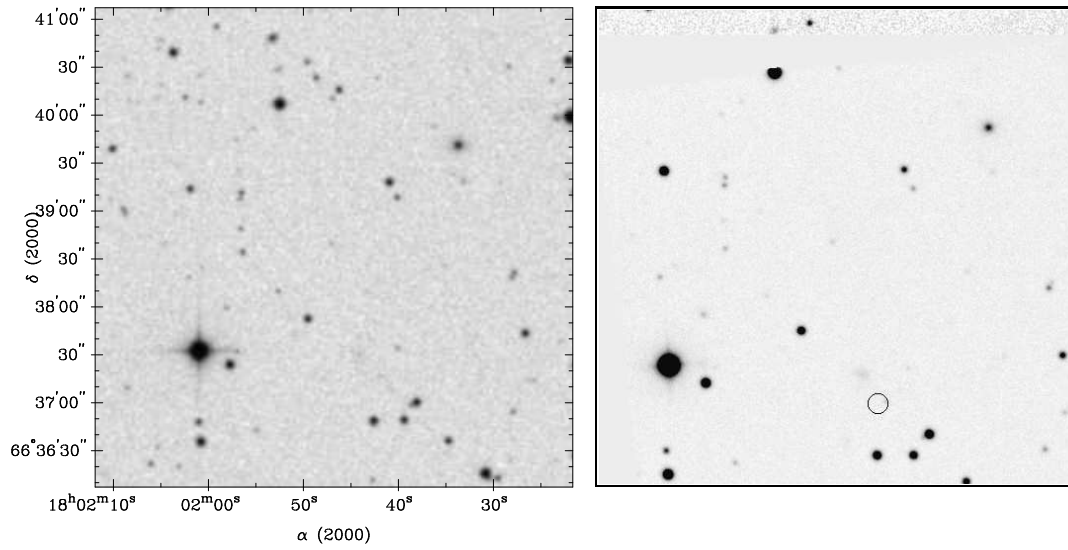
AGN $z = 1.30$ 21.7: mag



$\alpha/\delta_{\text{opt}} 18\ 1\ 30.8\ +66\ 32\ 9$

2RXP J180144.5+663708

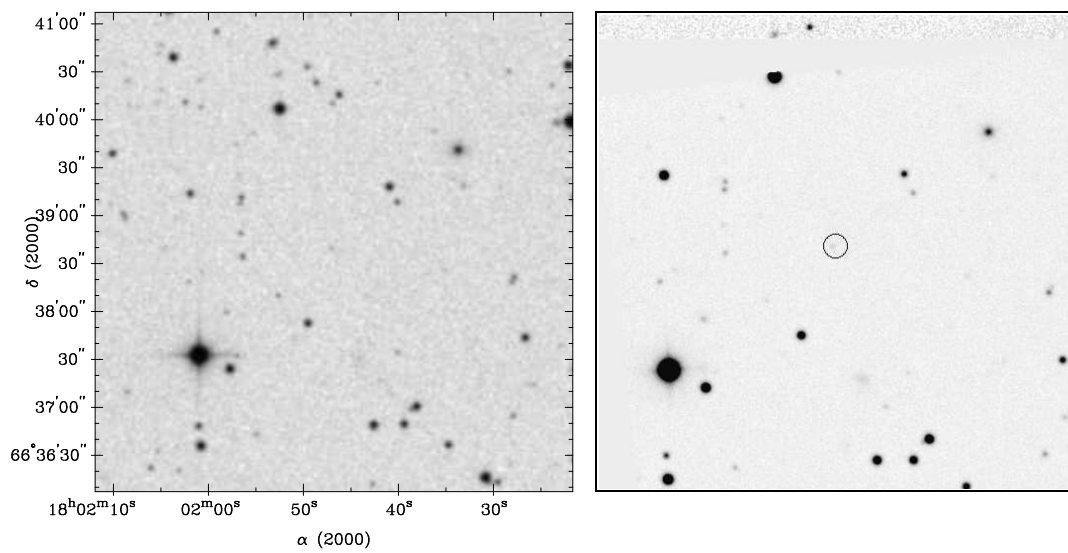
Cluster $z = 0.570$



1RXS J180146.7+663840

BL Lac

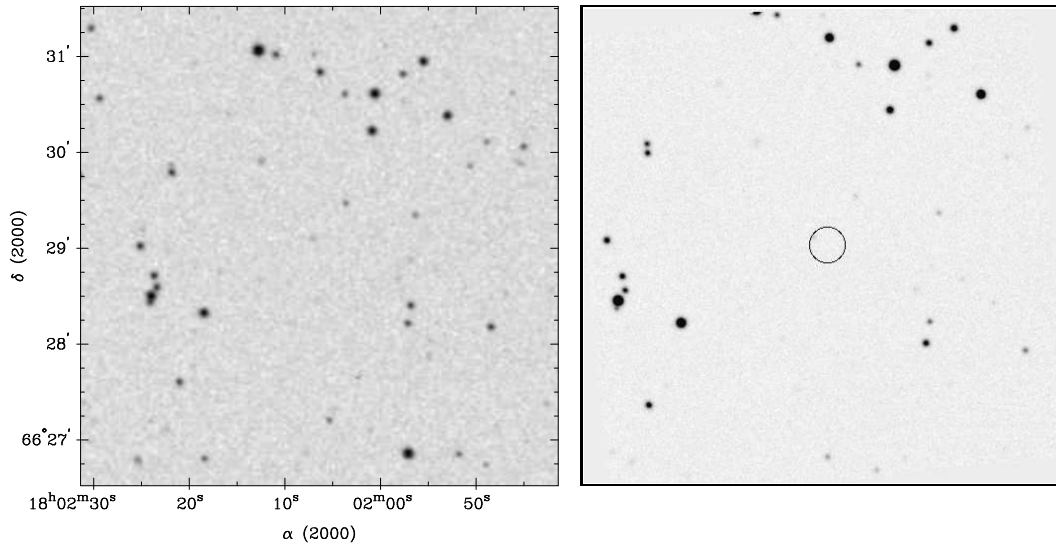
21.1 mag



$\alpha/\delta_{\text{opt}} 18 1 46.8 +66 38 40$

1RXS J180205.9+662902

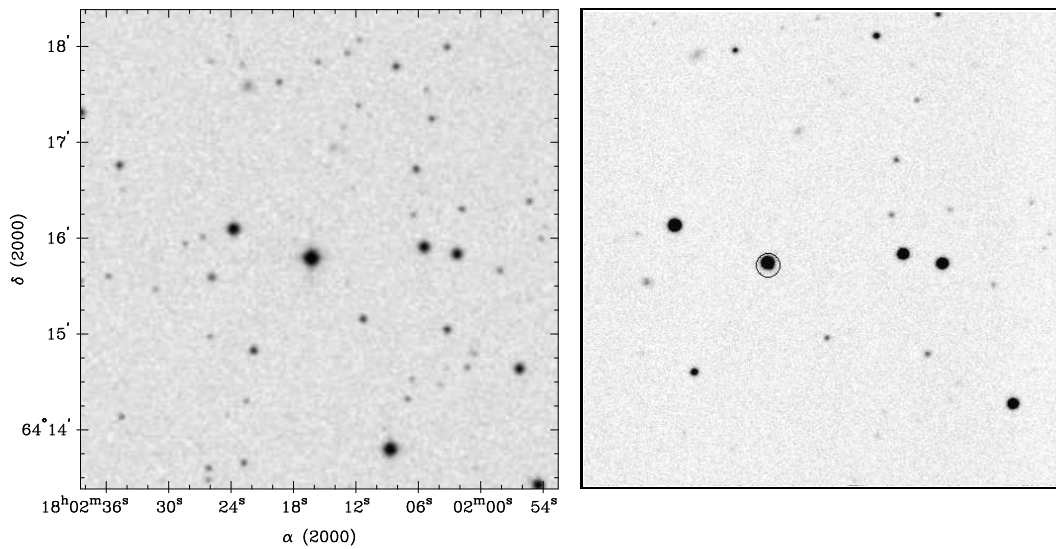
AGN $z = 0.265$ 21.0 mag



$\alpha/\delta_{\text{opt}}$ 18 2 7.3 +66 29 6

1RXS J180216.3+641546

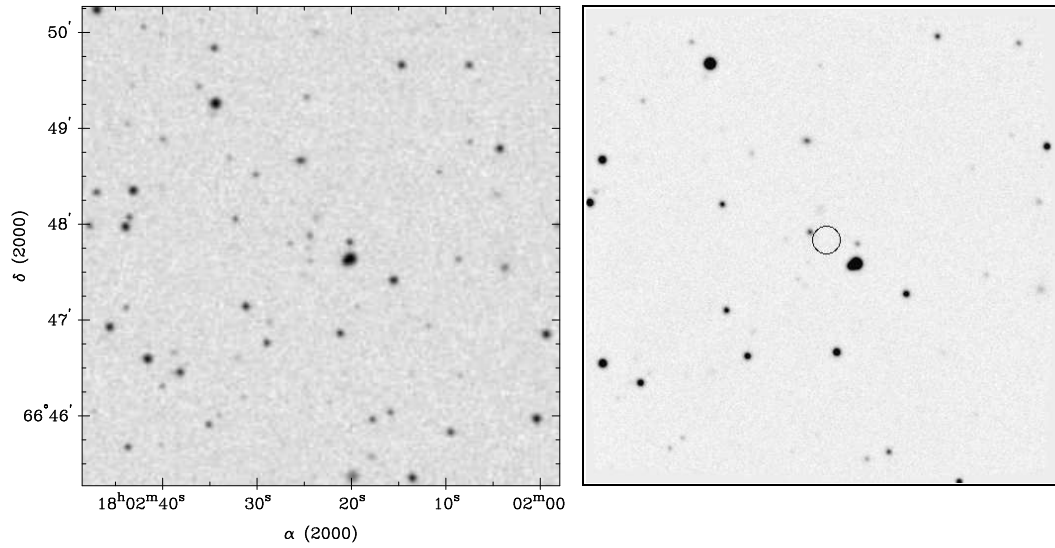
Star 15.0 mag



$\alpha/\delta_{\text{opt}}$ 18 2 16.4 +64 15 47

1RXS J180222.9+664750

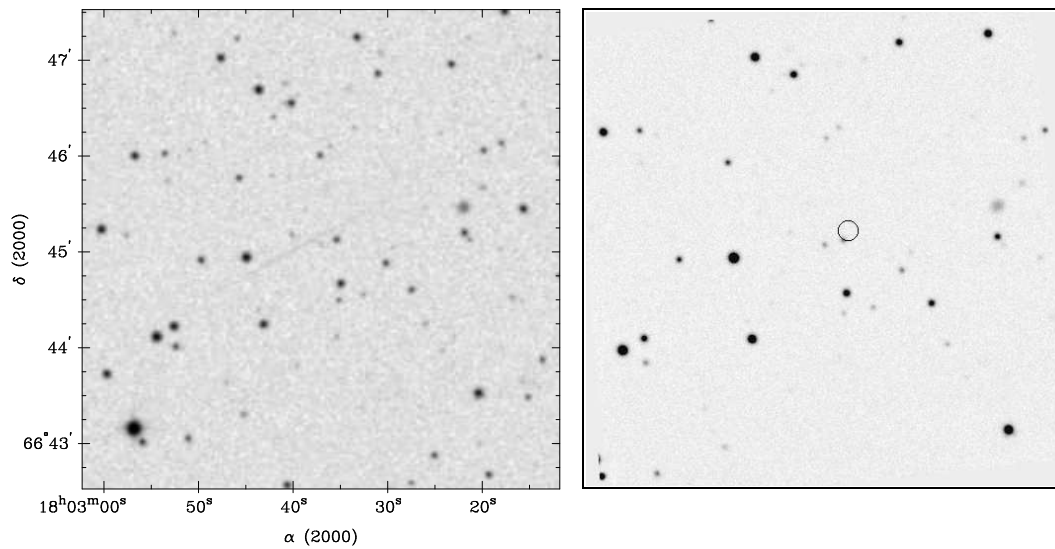
AGN $z = 0.3424$ 21.0: mag



$\alpha/\delta_{\text{opt}}$ 18 2 24.5 +66 47 35

2RXP J180236.6+664459

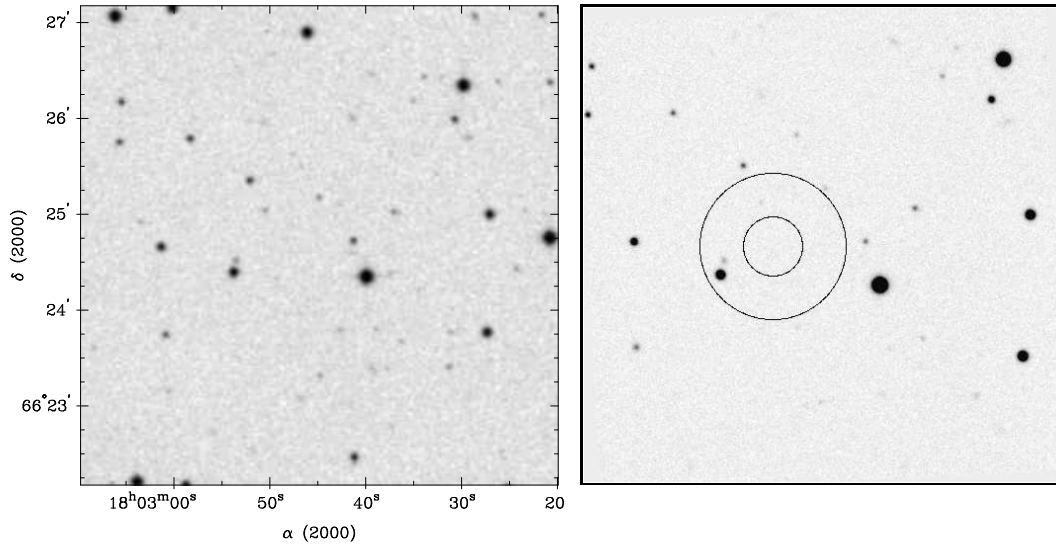
Star 20.4 mag



$\alpha/\delta_{\text{opt}}$ 18 2 35.3 +66 45 6

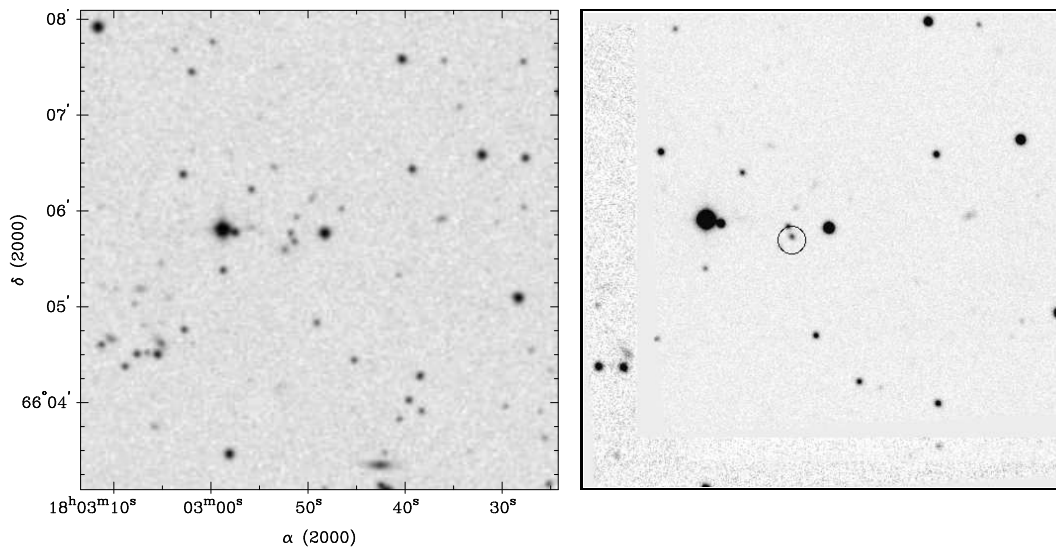
2RXP J180249.3+662441

Cluster ?



1RXS J180251.3+660540

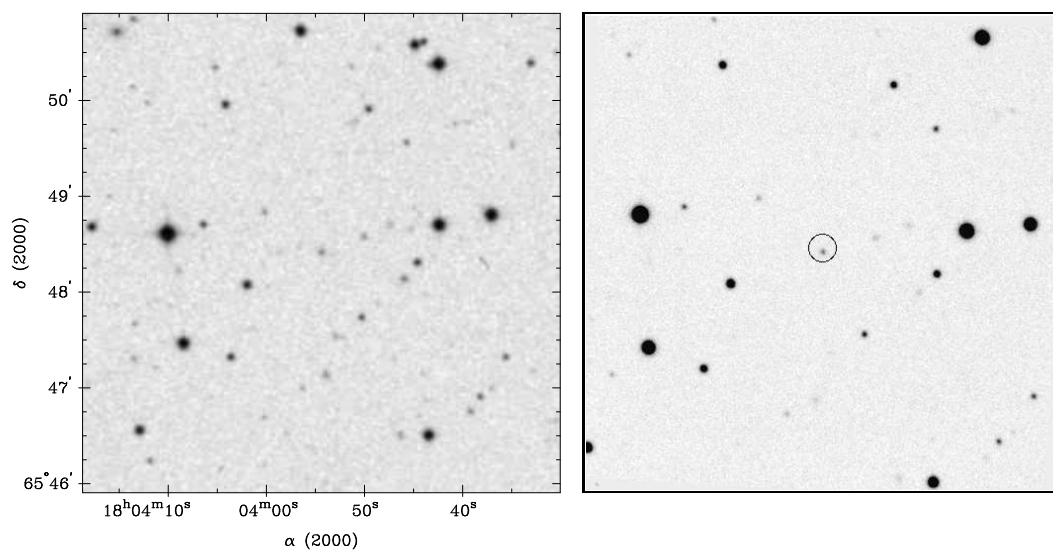
AGN $z = 0.2070$ 19.8 mag



$\alpha/\delta_{\text{opt}} 18\ 2\ 51.3\ +66\ 5\ 42$

1RXS J180354.5+654827

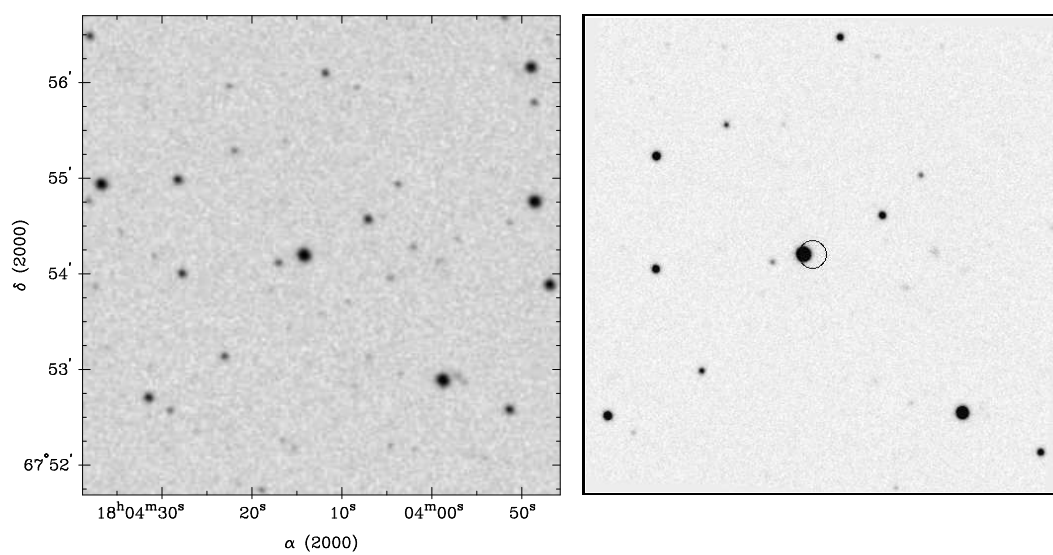
BL Lac $z = 0.085$: 20.3 mag



$\alpha/\delta_{\text{opt}}$ 18 3 54.4 +65 48 25

1RXS J180413.4+675412

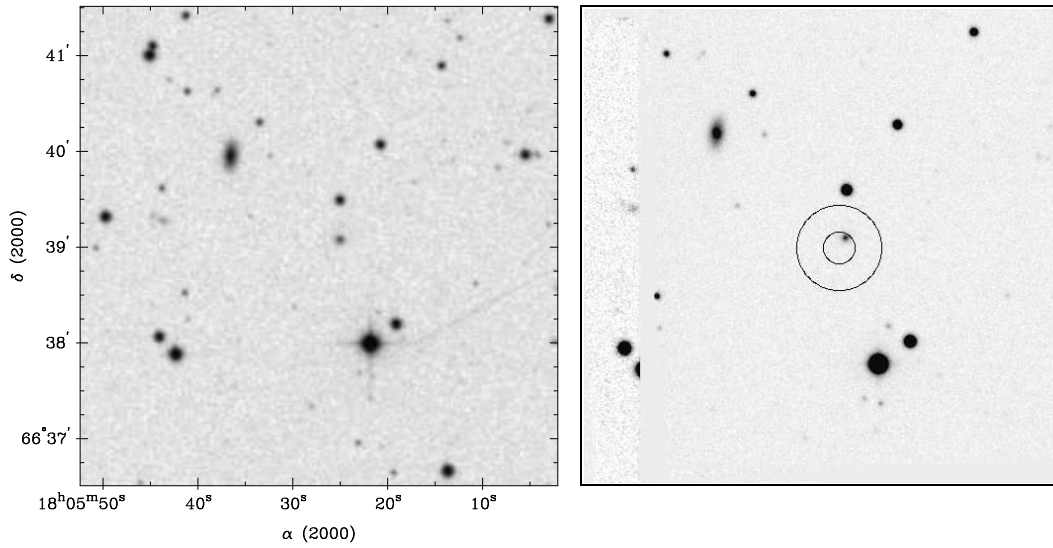
CV 14.7 mag



$\alpha/\delta_{\text{opt}}$ 18 4 14.3 +67 54 12

1RXS J180525.4+663859

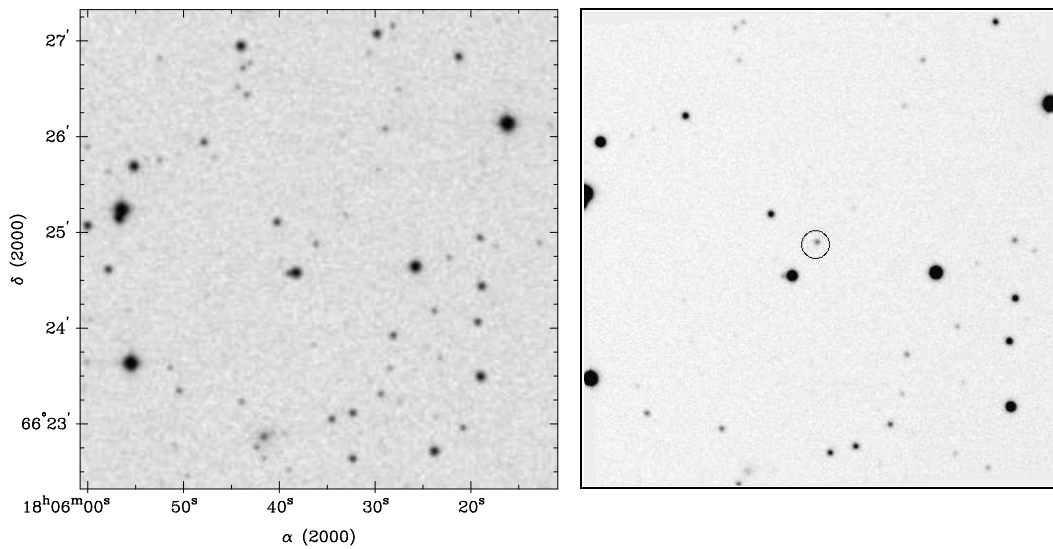
AGN $z = 0.1449$ 19.2 mag



$\alpha/\delta_{\text{opt}}$ 18 5 24.8 +66 39 4

1RXS J180536.2+662452

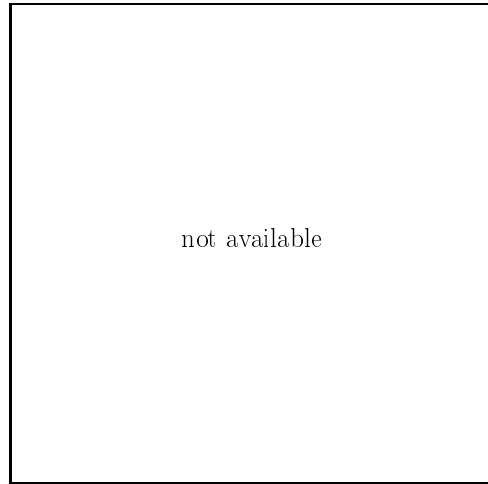
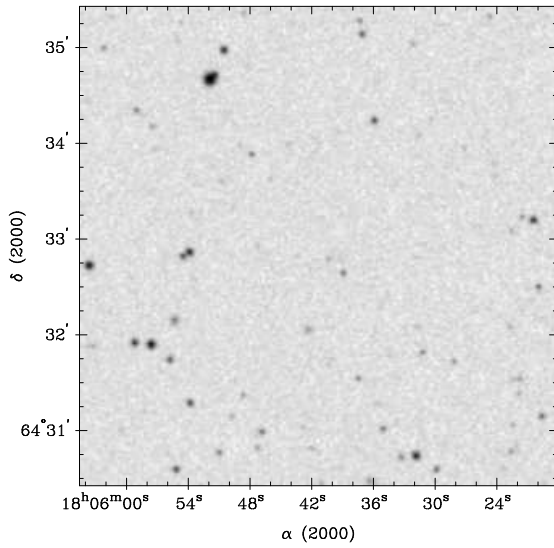
AGN $z = 0.721$ 20.2 mag



$\alpha/\delta_{\text{opt}}$ 18 5 36.0 +66 24 53

1RXS J180541.4+643251

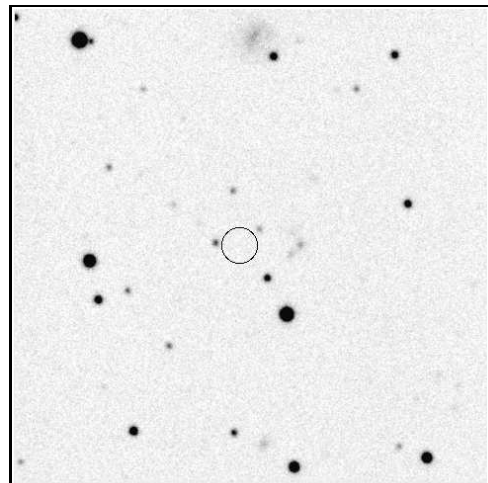
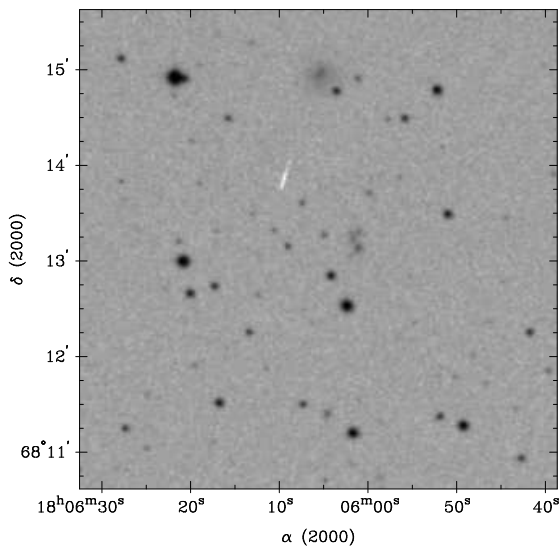
AGN $z = 0.7432$ $> 21.0\text{mag}$



$\alpha/\delta_{\text{opt}}$ 18 5 40.5 +64 32 47

1RXS J180606.7+681308

AGN/Cl. $z = 0.2953/0.303$ 20.4/19.6 mag

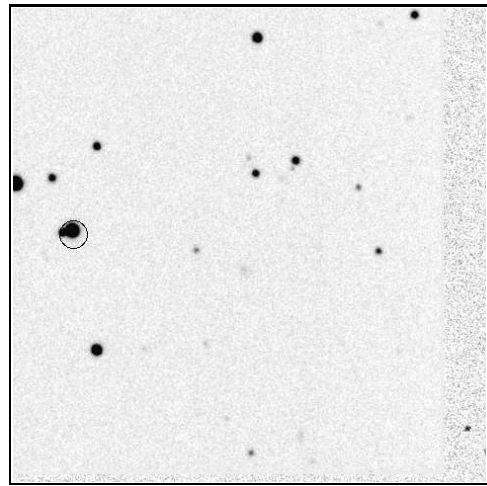
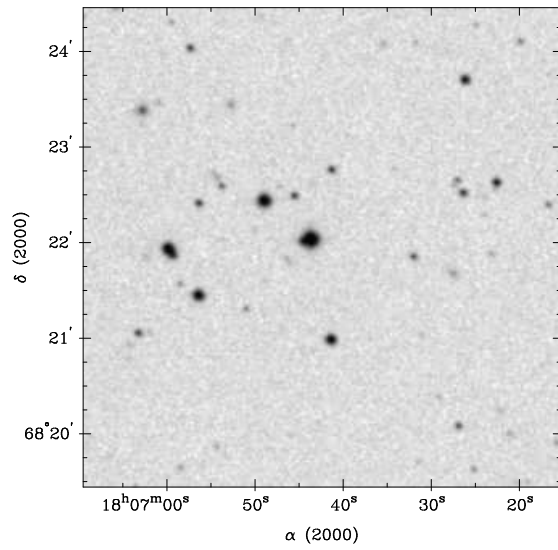


$\alpha/\delta_{\text{opt}}$ 18 6 4.8 +68 13 16 / 18 6 8.9 +68 13 10

1RXS J180643.4+682200

Star

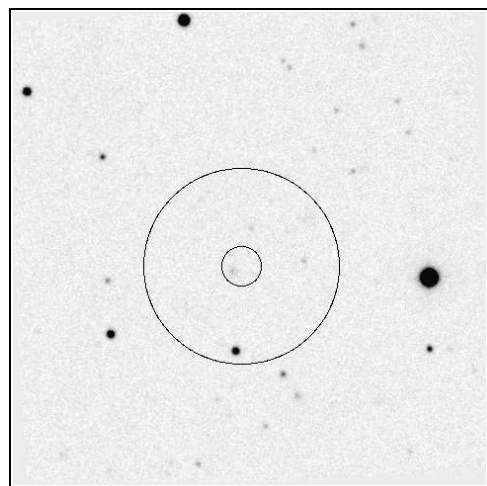
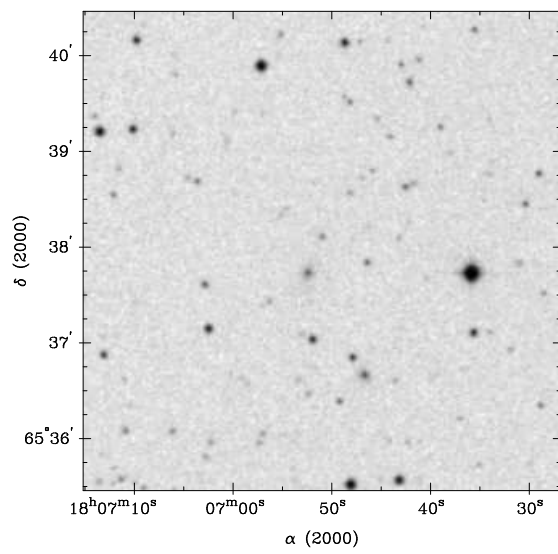
14.7 mag



$\alpha/\delta_{\text{opt}}$ 18 6 43.5 +68 22 2

1RXS J180651.7+653747

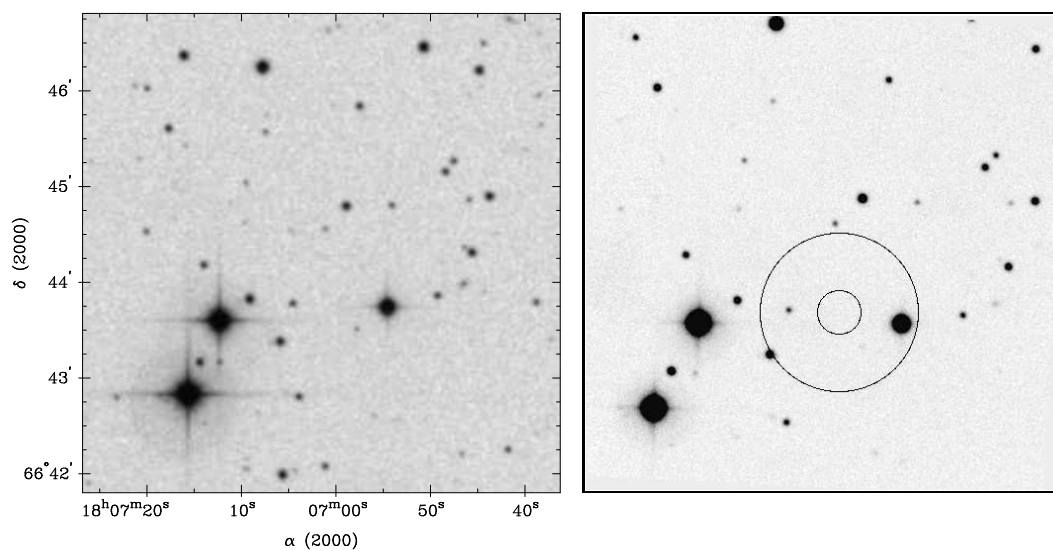
Cluster $z = 0.2626$



1RXS J180700.5+664348

Star

21.0: mag

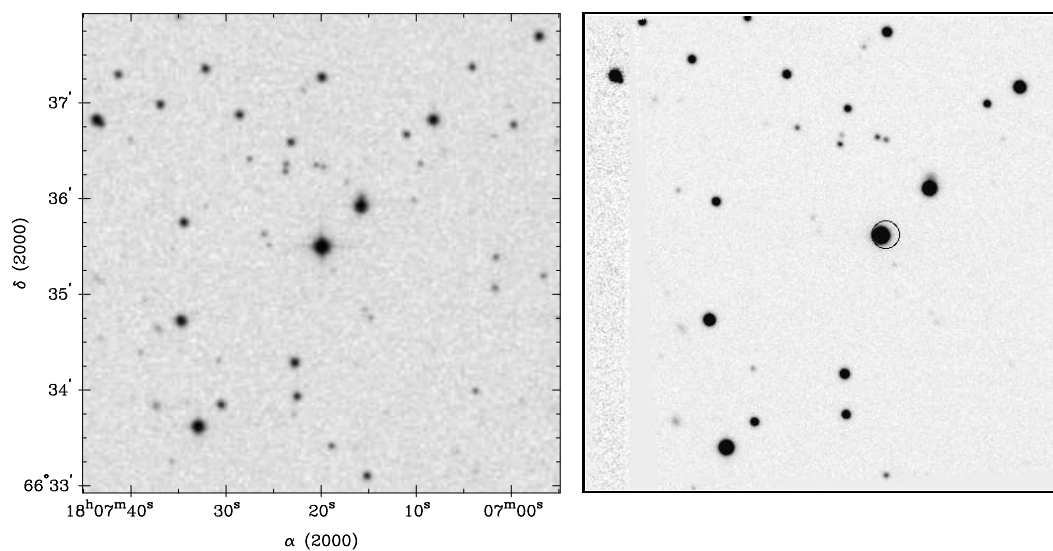


$\alpha/\delta_{\text{opt}}$ 18 6 58.2 +66 43 30

1RXS J180719.4+663530

Star

13.5 mag

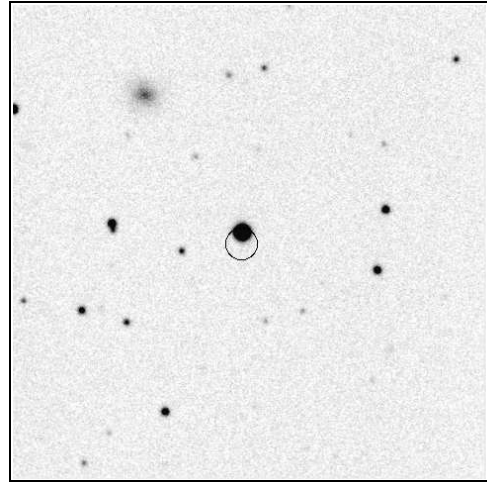
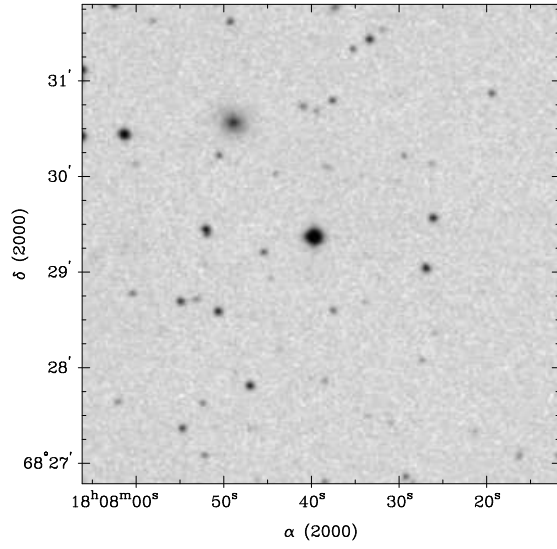


$\alpha/\delta_{\text{opt}}$ 18 7 19.8 +66 35 30

1RXS J180739.7+682917

Star

13.7 mag



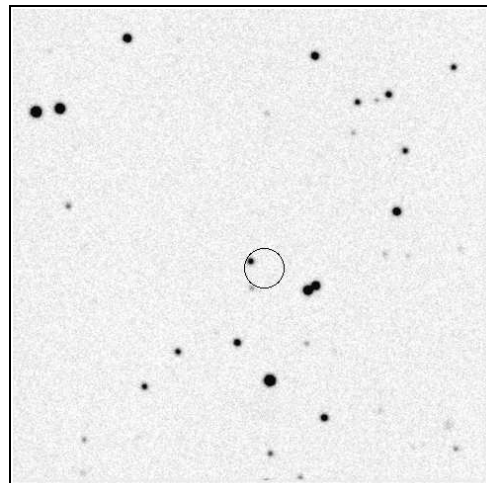
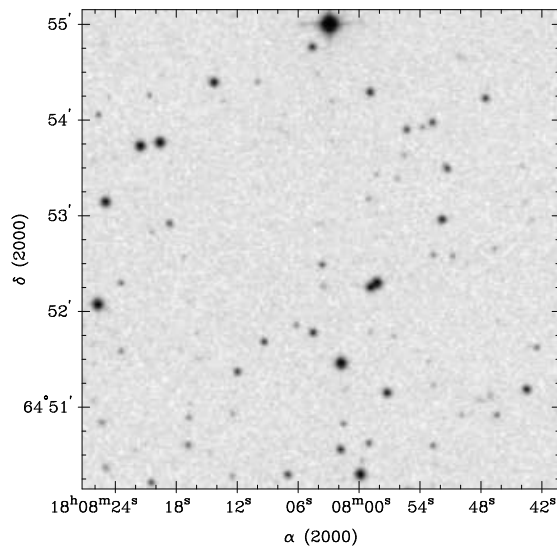
$\alpha/\delta_{\text{opt}}$ 18 7 39.6 +68 29 23

1RXS J180802.6+645225

AGN

$z = 1.0360$

18.9 mag

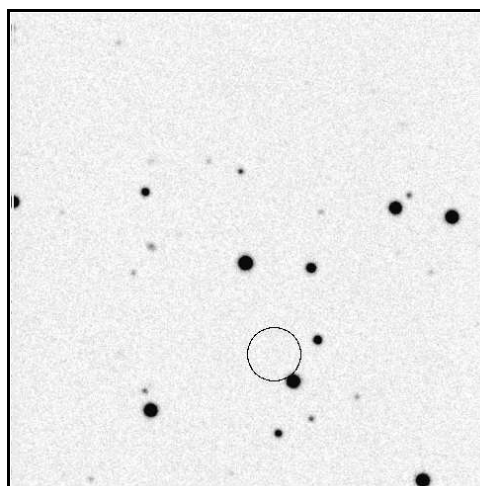
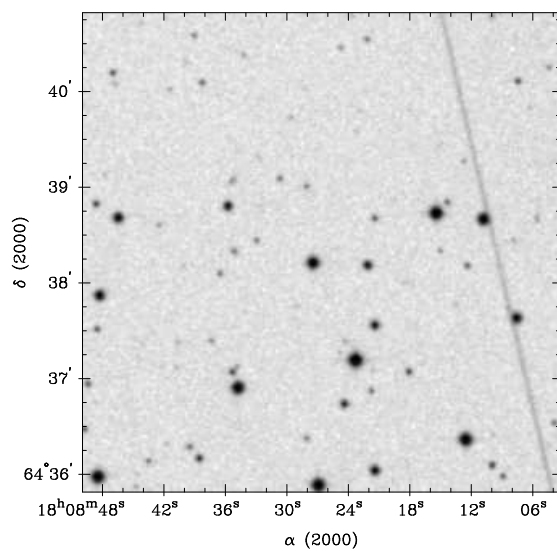


$\alpha/\delta_{\text{opt}}$ 18 8 3.6 +64 52 29

1RXS J180825.3+643725

Star

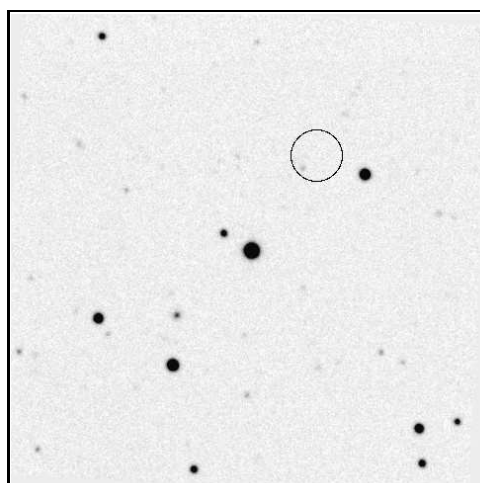
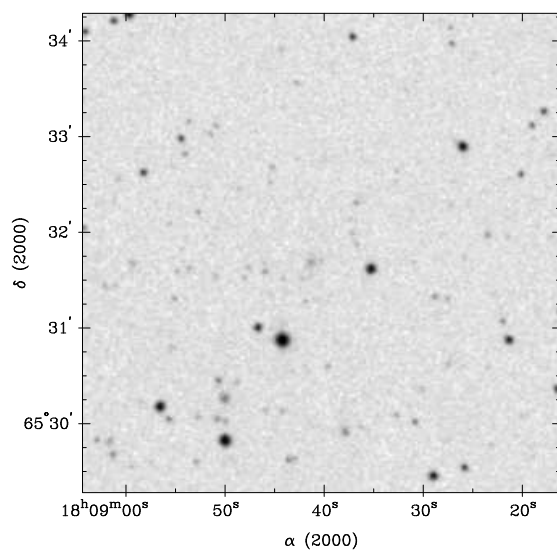
15.0 mag



$\alpha/\delta_{\text{opt}}$ 18 8 23.7 +64 37 11

2RXP J180839.6+653145

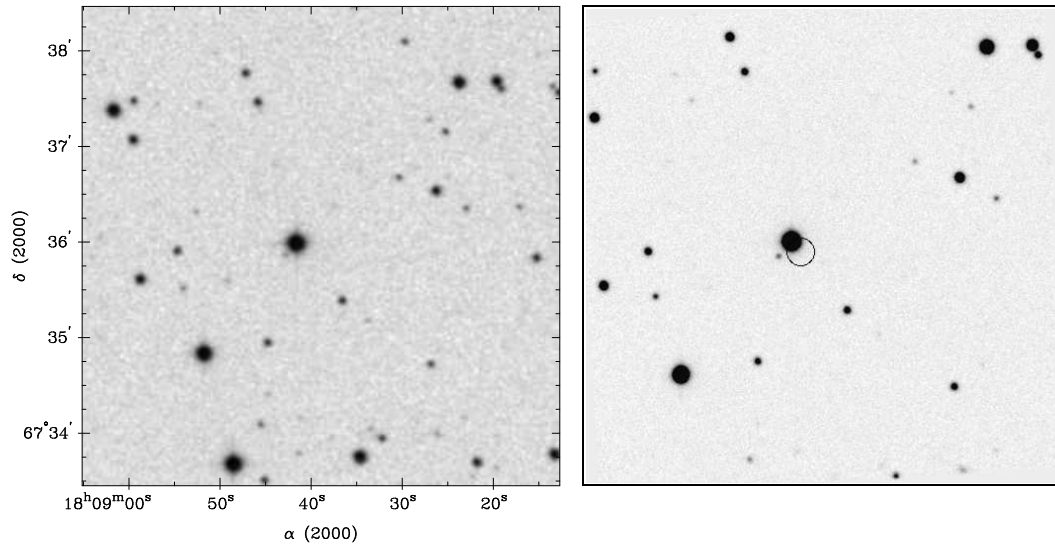
Cluster ?



1RXS J180840.7+673554

Star

12.9 mag



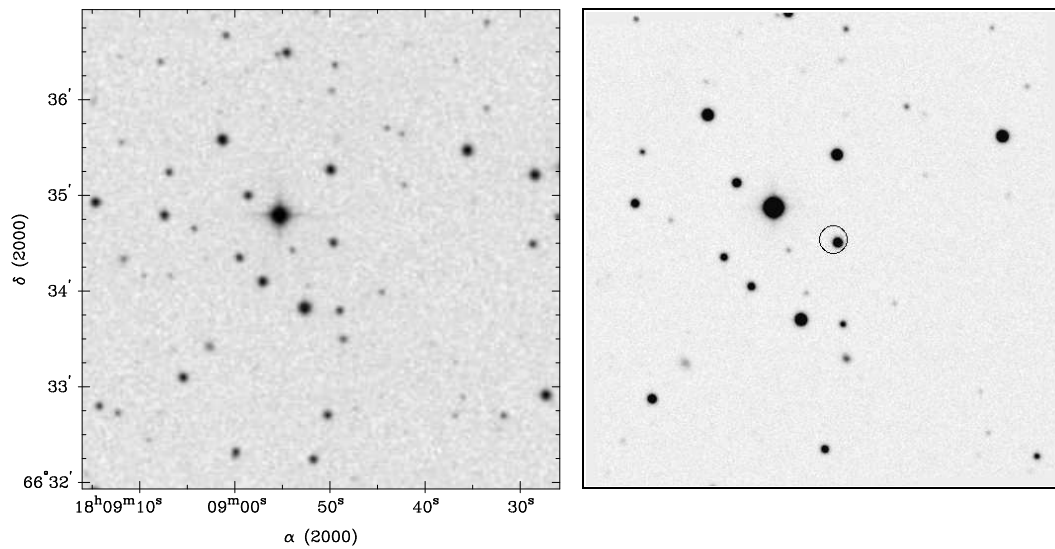
$\alpha/\delta_{\text{opt}}$ 18 8 41.5 +67 36 0

1RXS J180849.9+663431

AGN

$z = 0.6970$

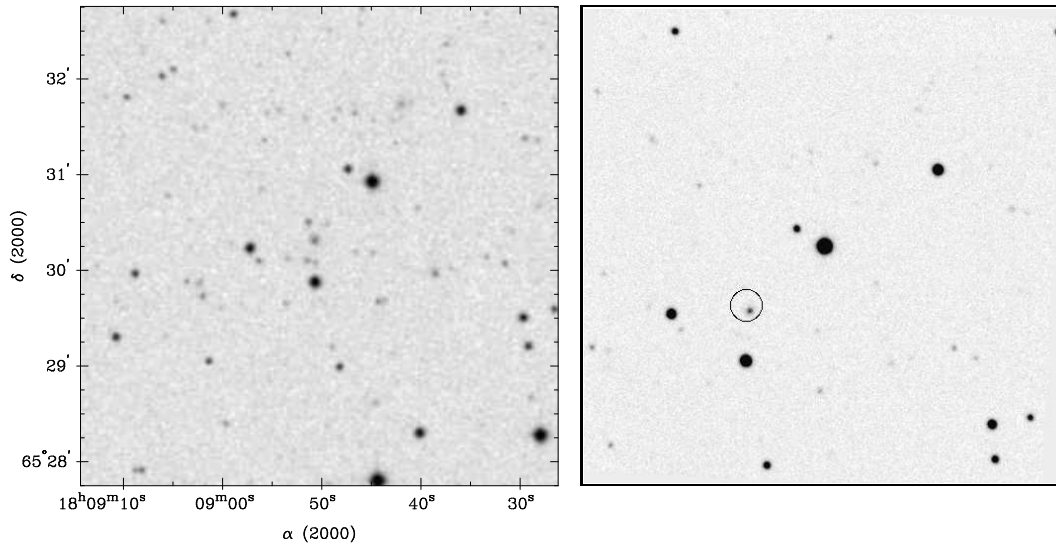
16.9 mag



$\alpha/\delta_{\text{opt}}$ 18 8 49.5 +66 34 30

1RXS J180851.1+653022

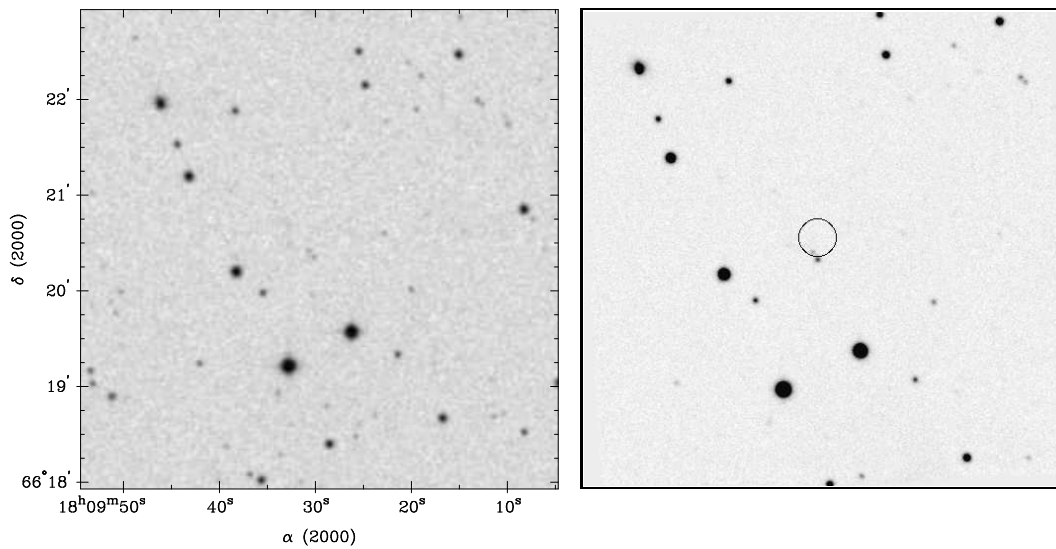
AGN $z = 0.2937$ 19.5 mag



$\alpha/\delta_{\text{opt}} 18\ 8\ 50.7\ +65\ 30\ 19$

1RXS J180930.2+662033

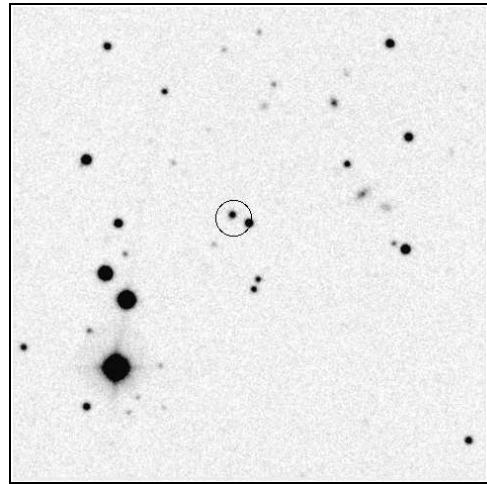
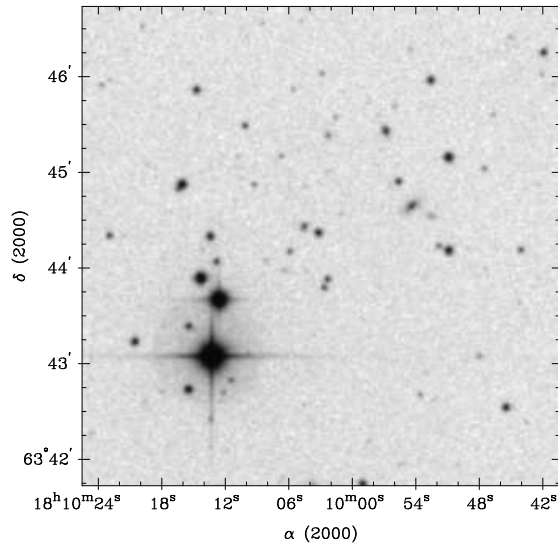
AGN $z = 0.6350$ 19.9 mag



$\alpha/\delta_{\text{opt}} 18\ 9\ 30.2\ +66\ 20\ 21$

1RXS J181004.3+634424

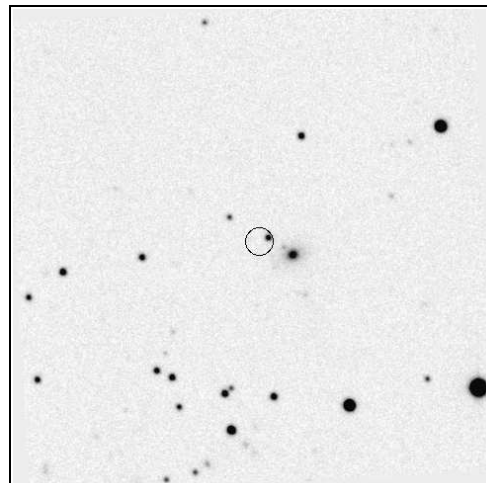
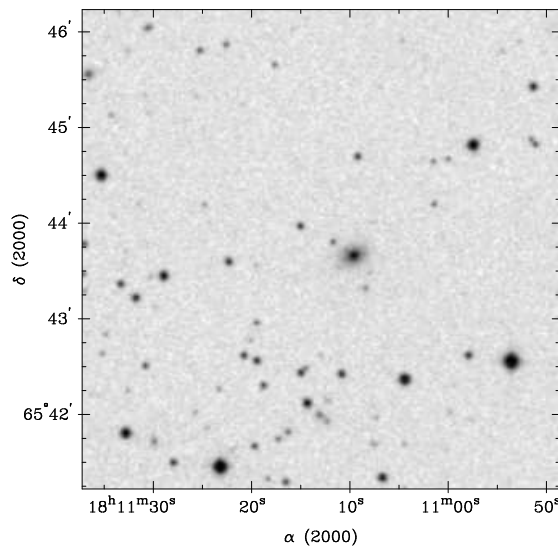
AGN $z = 0.3770$ 18.5 mag



$\alpha/\delta_{\text{opt}}$ 18 10 4.4 +63 44 26

1RXS J181112.4+654346

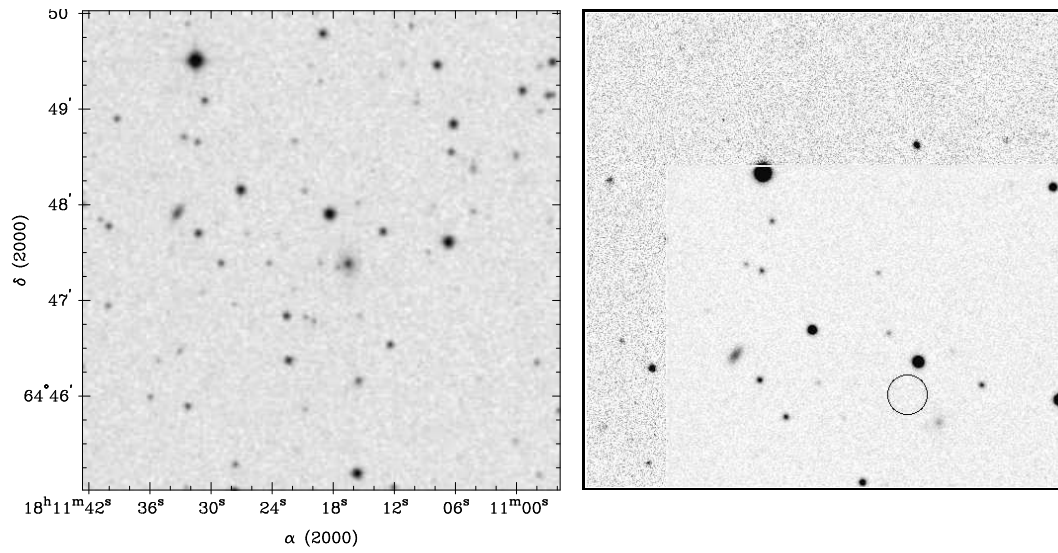
AGN $z = 0.4895$ 19.1 mag



$\alpha/\delta_{\text{opt}}$ 18 11 11.6 +65 43 48

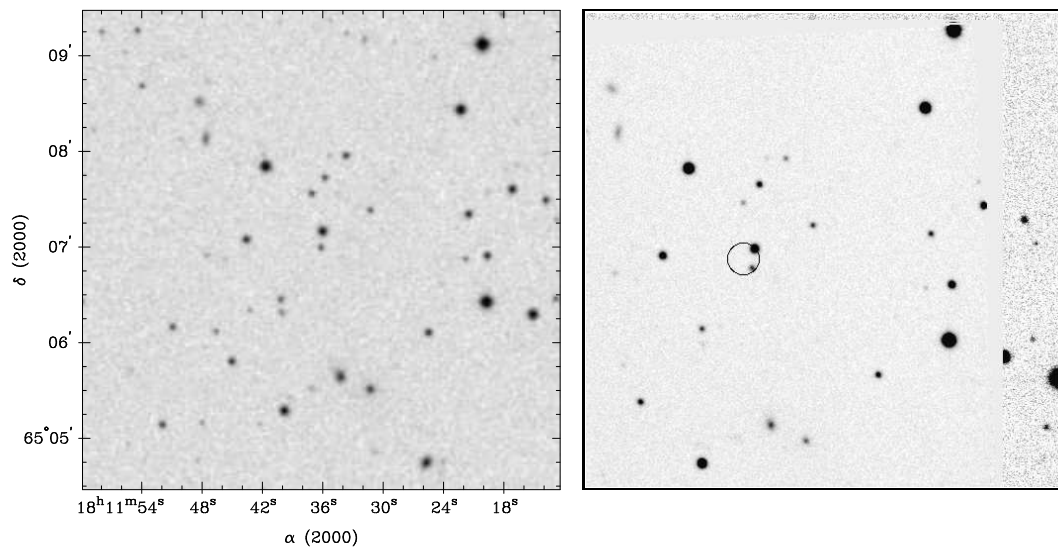
1RXS J181119.1+644736

Cluster $z = 0.4510$



1RXS J181136.9+650704

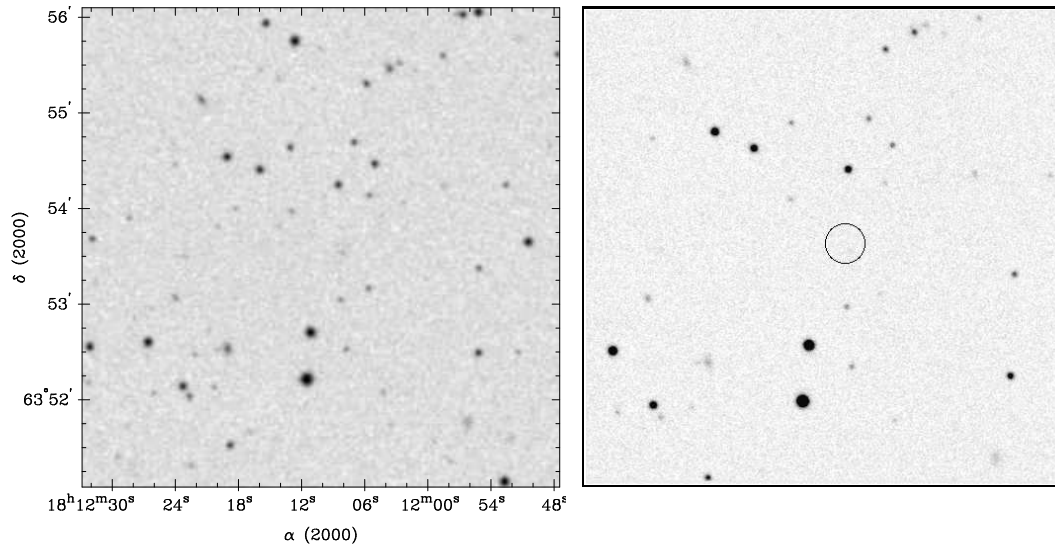
AGN $z = 0.8470$ 19.7 mag



$\alpha/\delta_{\text{opt}}$ 18 11 36.1 +65 6 59

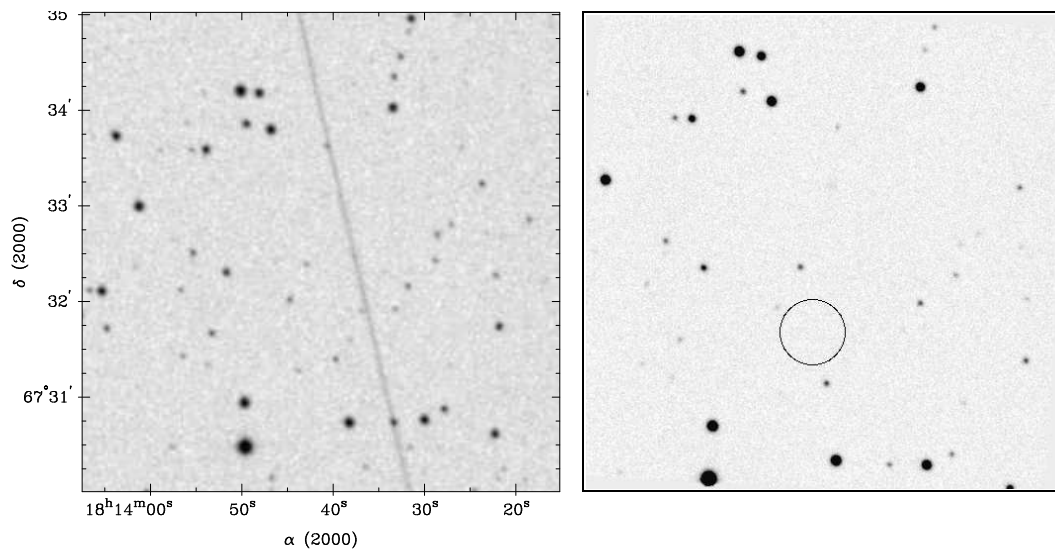
1RXS J181208.5+635335

Cluster $z = 0.5408$



1RXS J181341.6+673150

AGN $z = 0.6168$ 19.9 mag

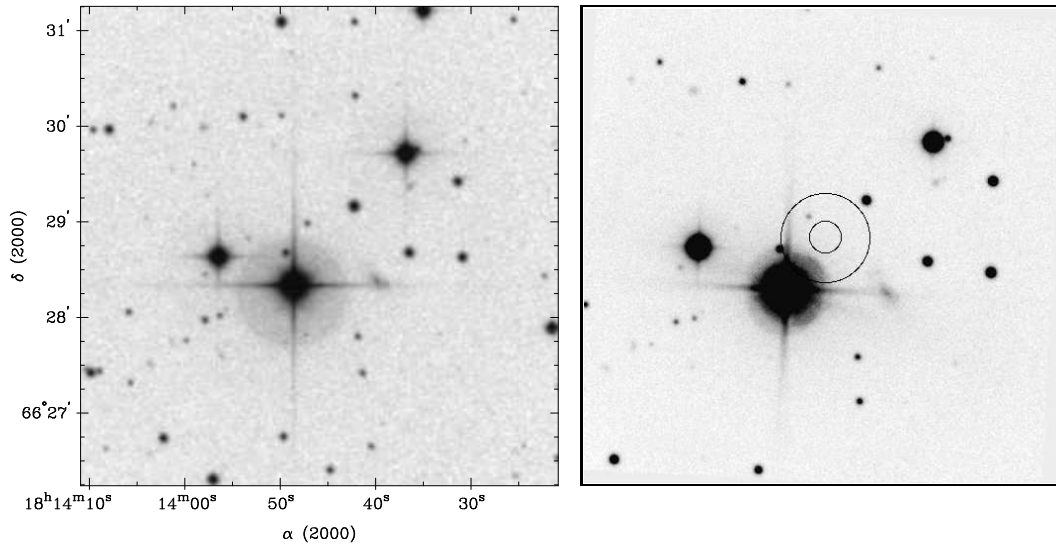


$\alpha/\delta_{\text{opt}} 18 13 43.0 +67 32 23$

1RXS J181345.6+662849

Star

20.6 mag



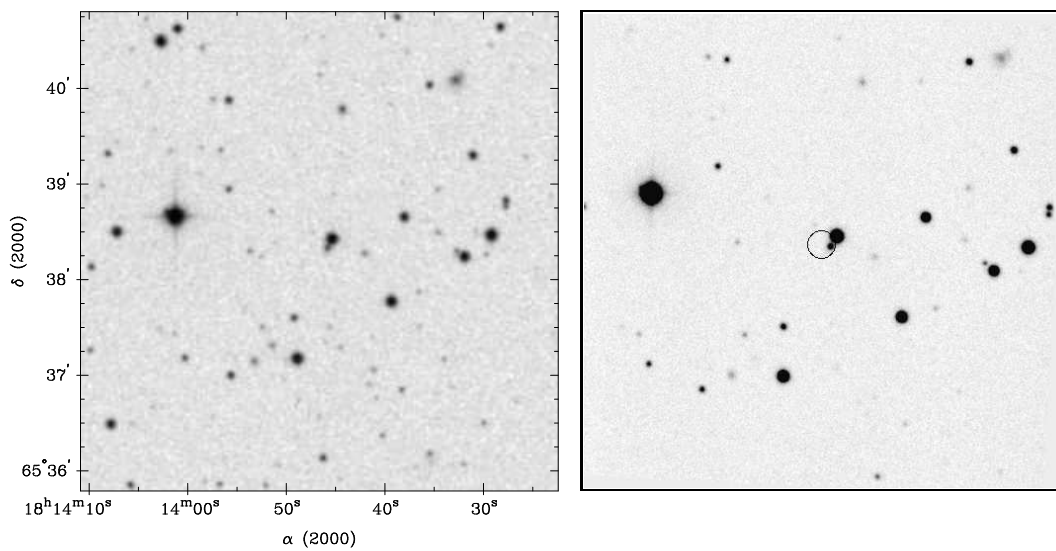
$\alpha/\delta_{\text{opt}}$ 18 13 47.2 +66 29 0

1RXS J181346.6+653821

AGN

$z = 0.1912$

18.5 mag

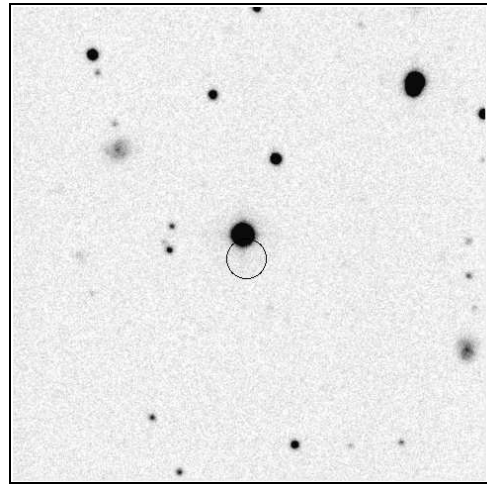
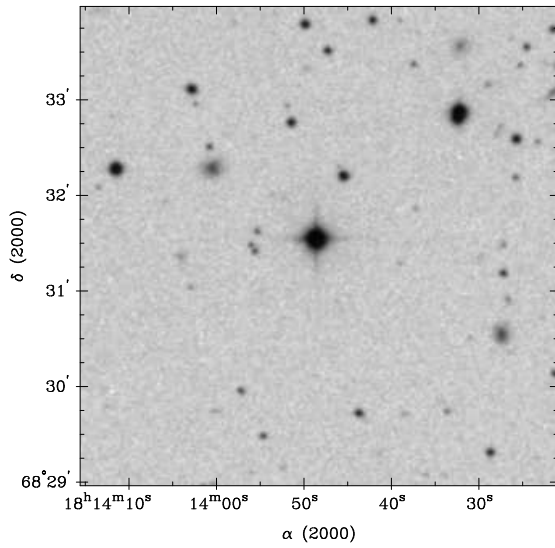


$\alpha/\delta_{\text{opt}}$ 18 13 45.8 +65 38 20

1RXS J181348.3+683121

Star ?

12.1 mag



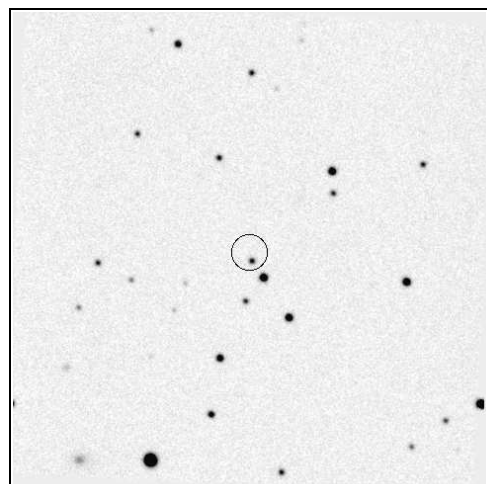
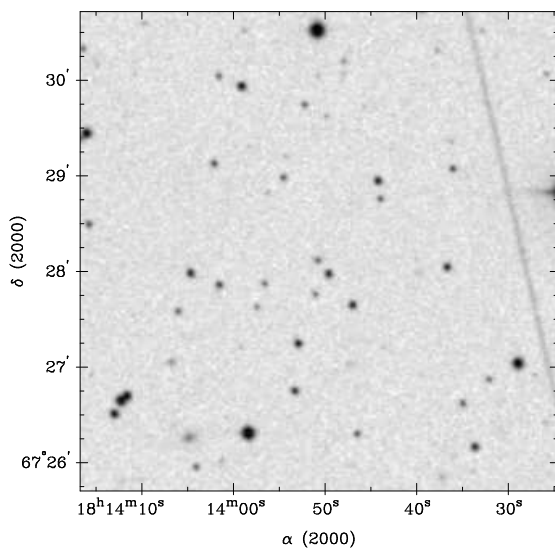
$\alpha/\delta_{\text{opt}}$ 18 13 48.6 +68 31 33

1RXS J181351.0+672811

AGN

$z = 0.3196$

19.3 mag

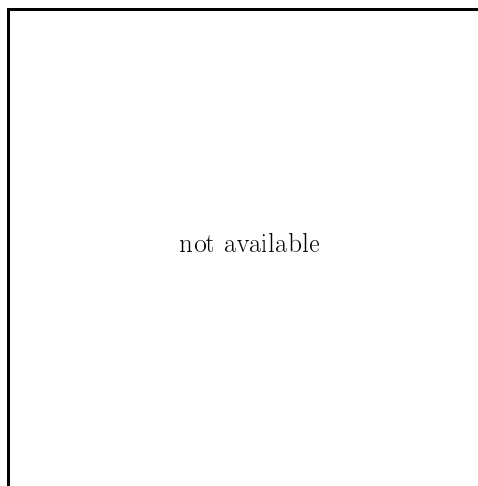
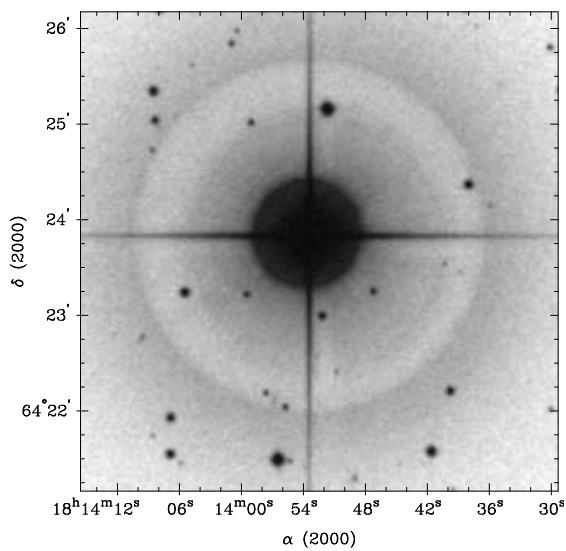


$\alpha/\delta_{\text{opt}}$ 18 13 50.7 +67 28 6

1RXS J181353.7+642348

Star

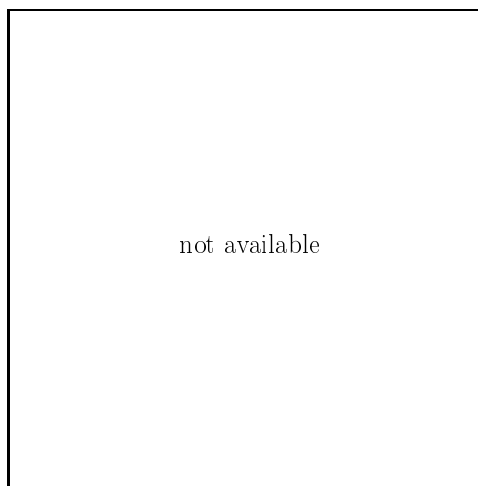
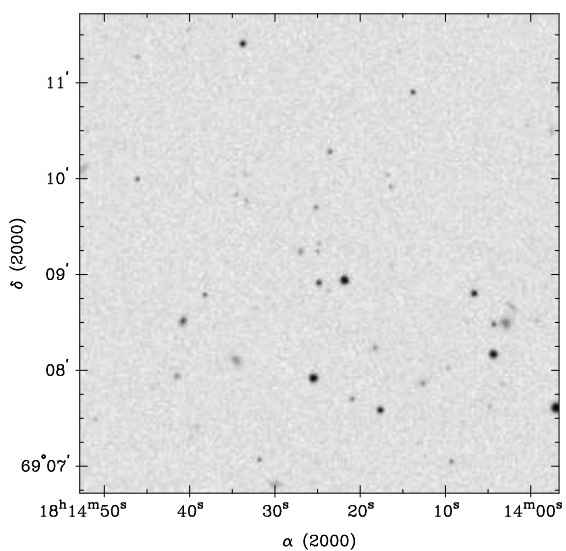
5.40 mag



$\alpha/\delta_{\text{opt}}$ 18 13 53.8 +64 23 50

1RXS J181422.4+690804

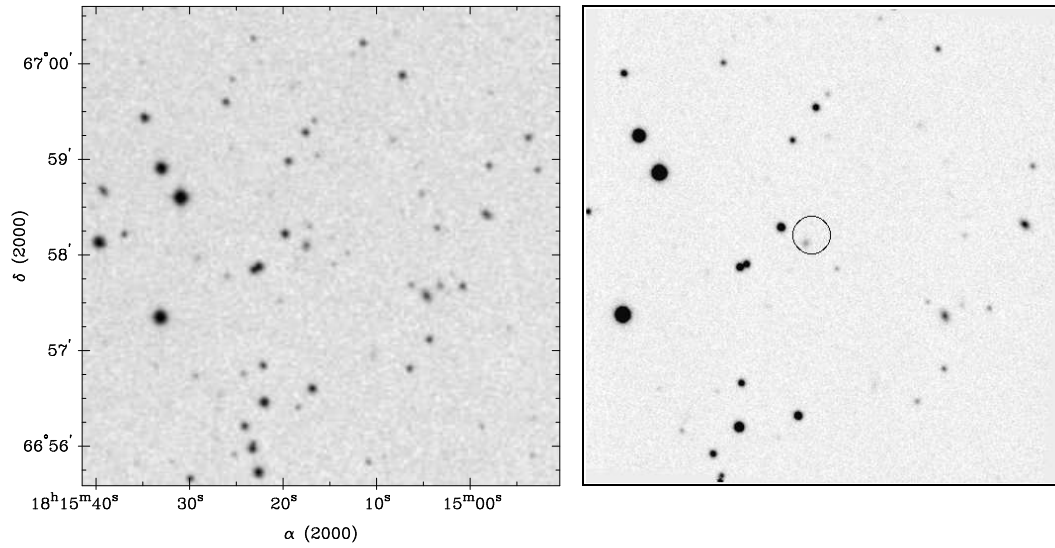
?



DSSII finding chart from POSSII-B

1RXS J181517.1+665811

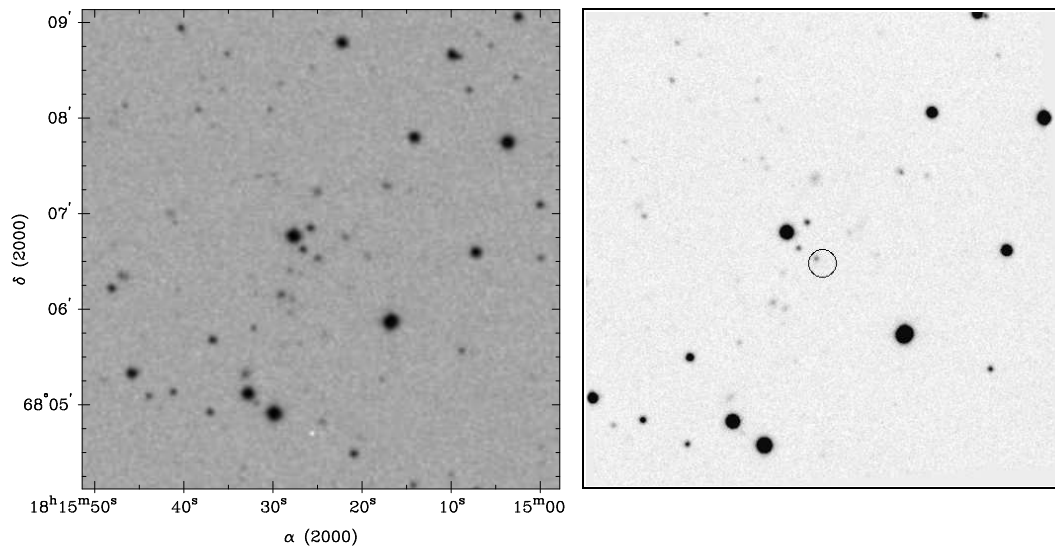
AGN $z = 0.2287$ 20.0 mag



$\alpha/\delta_{\text{opt}}$ 18 15 17.5 +66 58 6

1RXS J181524.4+680630

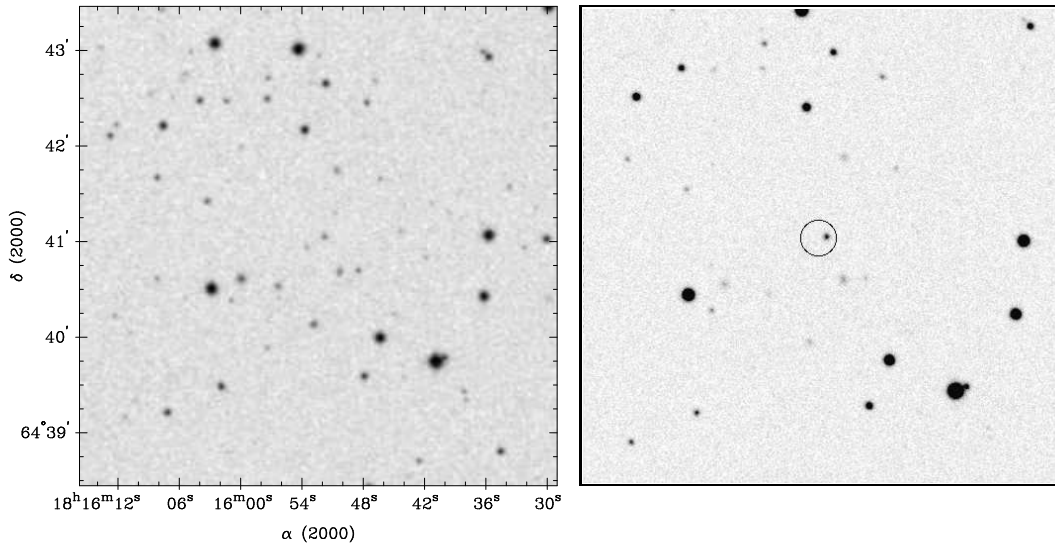
AGN $z = 0.2390$ 20.3 mag



$\alpha/\delta_{\text{opt}}$ 18 15 25.0 +68 6 32

1RXS J181552.4+644101

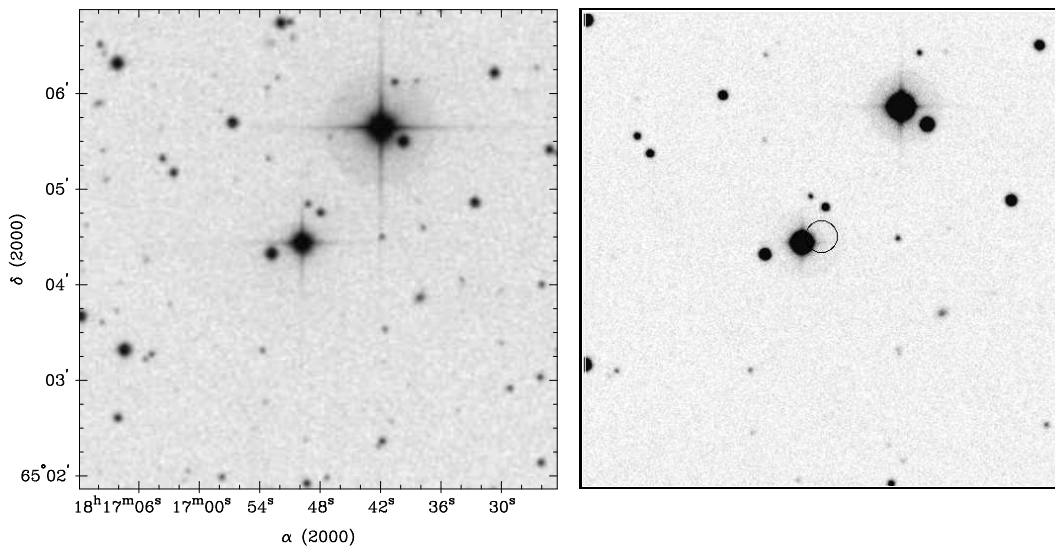
AGN $z = 0.4116$ 19.5 mag



$\alpha/\delta_{\text{opt}}$ 18 15 51.8 +64 41 2

1RXS J181648.2+650429

Star 11.6 mag

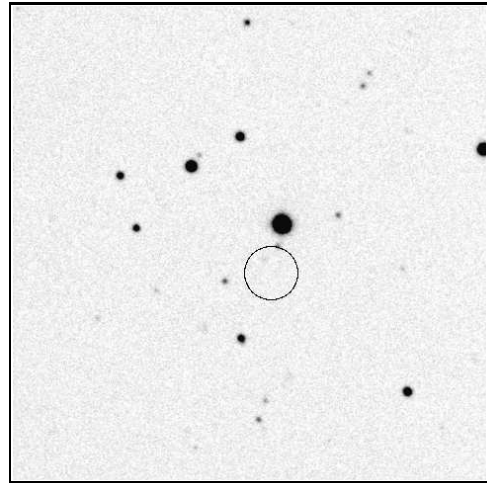
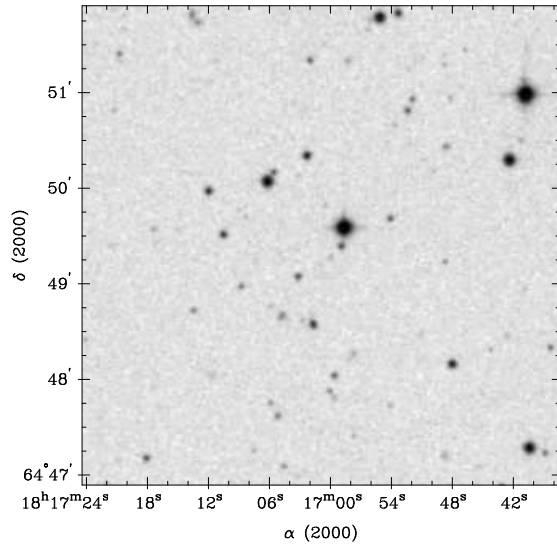


$\alpha/\delta_{\text{opt}}$ 18 16 49.8 +65 4 26

1RXS J181659.5+644909

Star / ?

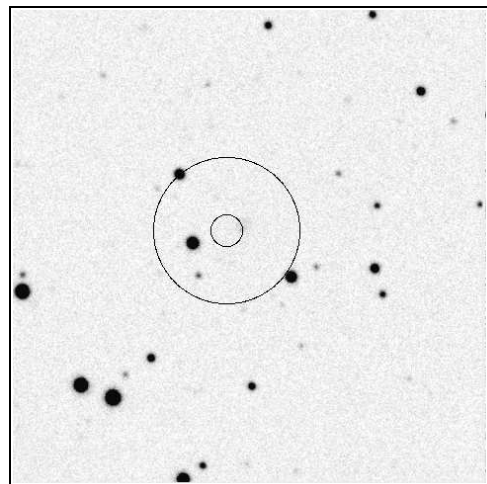
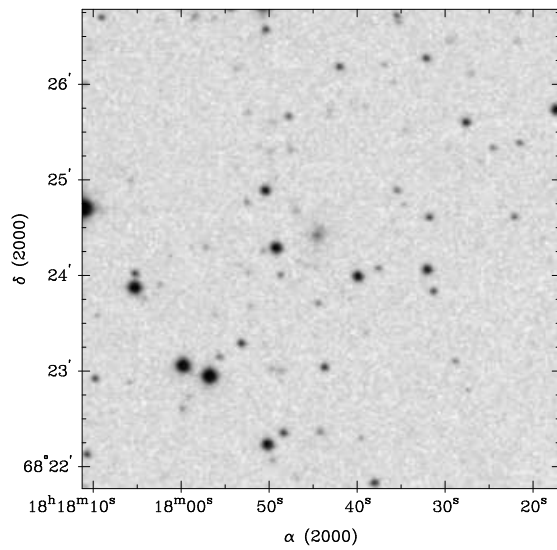
12.9 / 20.1 mag



$\alpha/\delta_{\text{opt}}$ 18 16 58.6 +64 49 35 / 18 16 58.9 +64 49 23

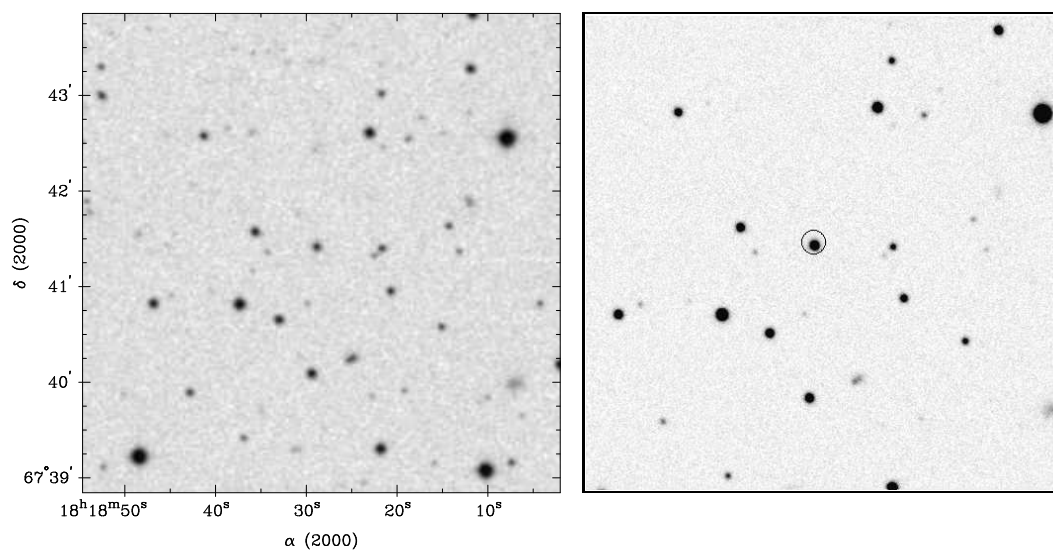
1RXS J181746.1+682424

Cluster $z = 0.2820$



1RXS J181829.0+674127

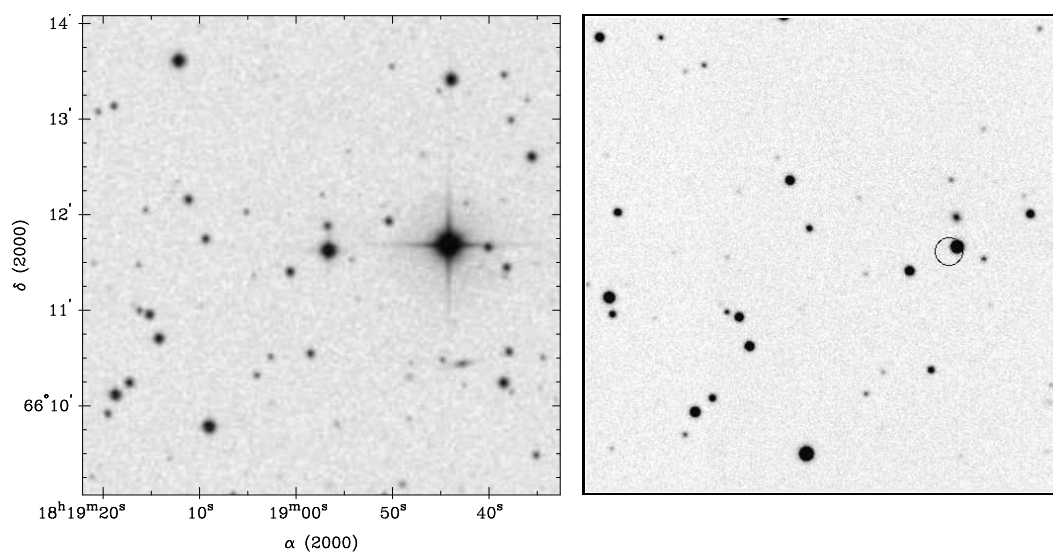
AGN $z = 0.3140$ 16.8 mag



$\alpha/\delta_{\text{opt}}$ 18 18 28.9 +67 41 25

1RXS J181857.3+661135

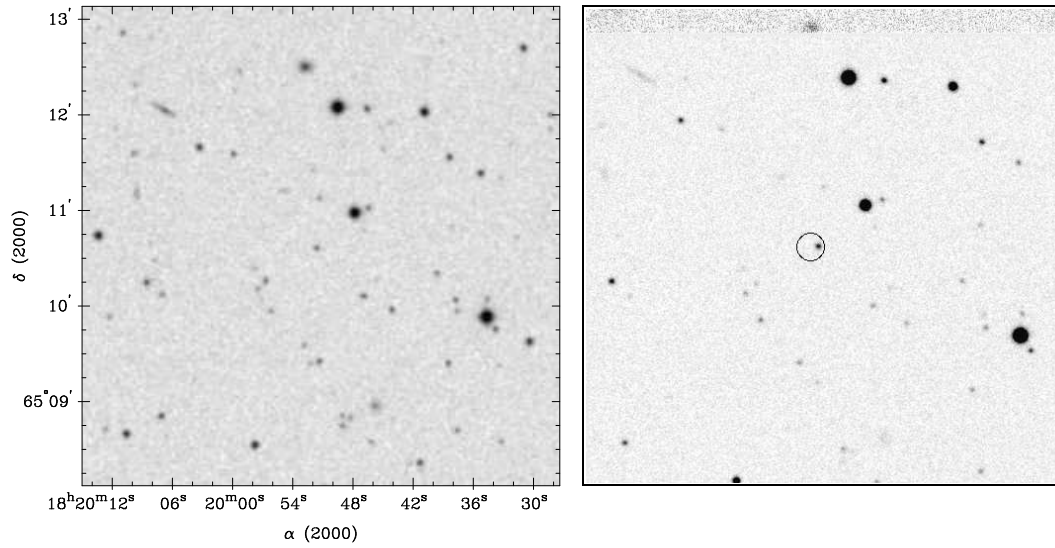
Star 15.3 mag



$\alpha/\delta_{\text{opt}}$ 18 18 56.5 +66 11 38

1RXS J181952.3+651035

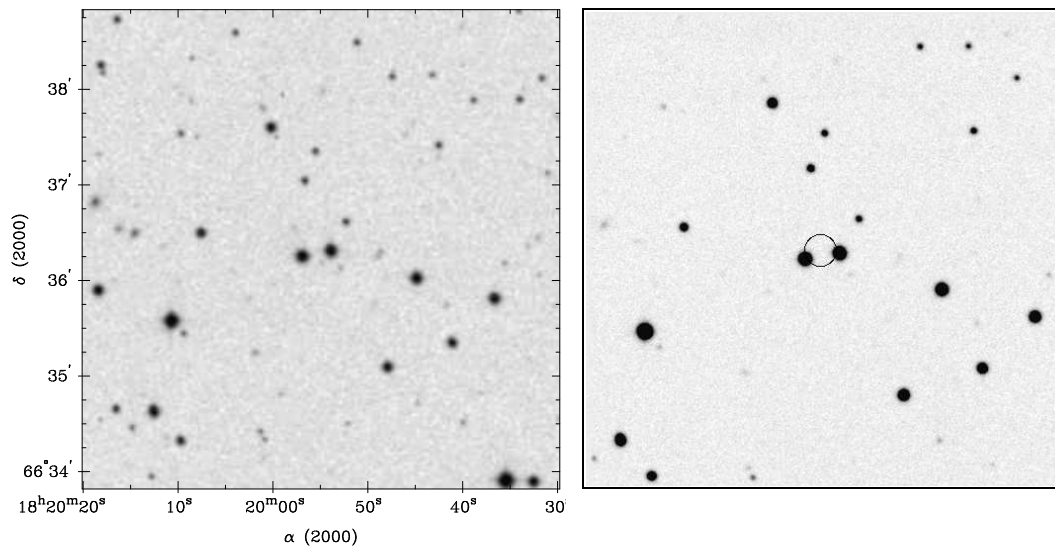
AGN $z = 0.1894$ 19.5 mag



$\alpha/\delta_{\text{opt}} 18 19 51.6 +65 10 36$

1RXS J181955.5+663619

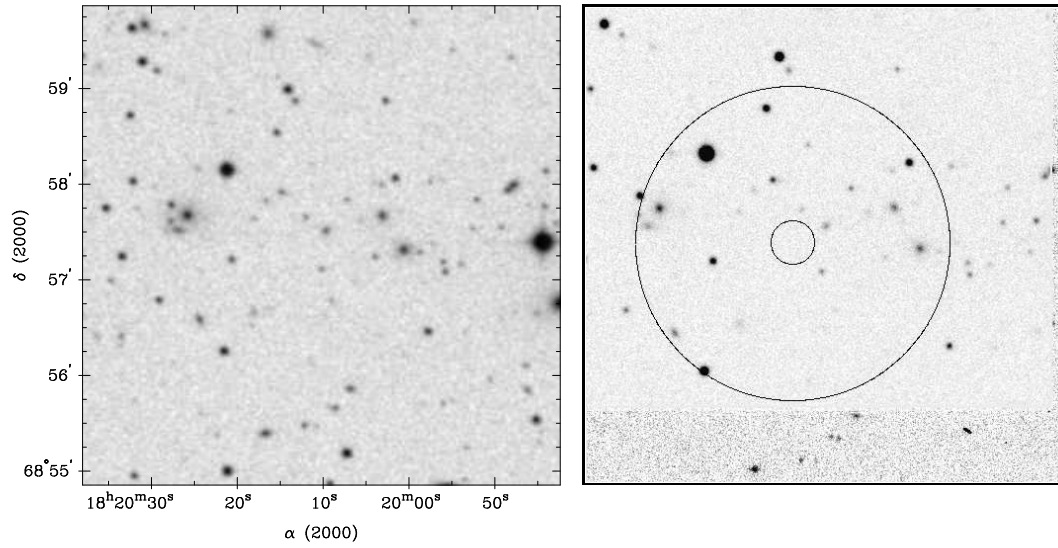
Star / Star ? 14.8 / 14.8 mag



$\alpha/\delta_{\text{opt}} 18 19 53.8 +66 36 18 / 18 19 56.8 +66 36 15$

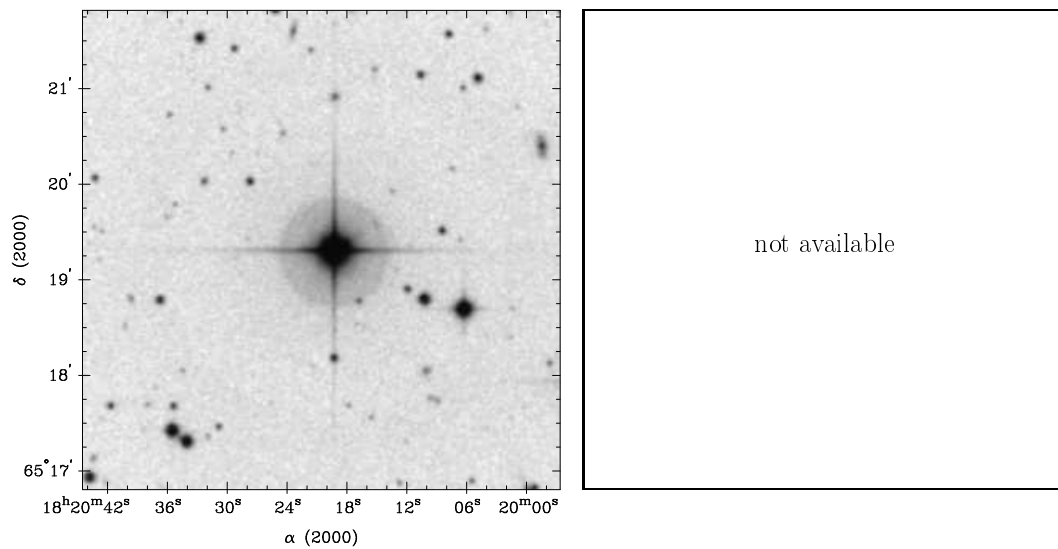
1RXS J182013.0+685722

Cluster $z = 0.0890$



1RXS J182019.7+651918

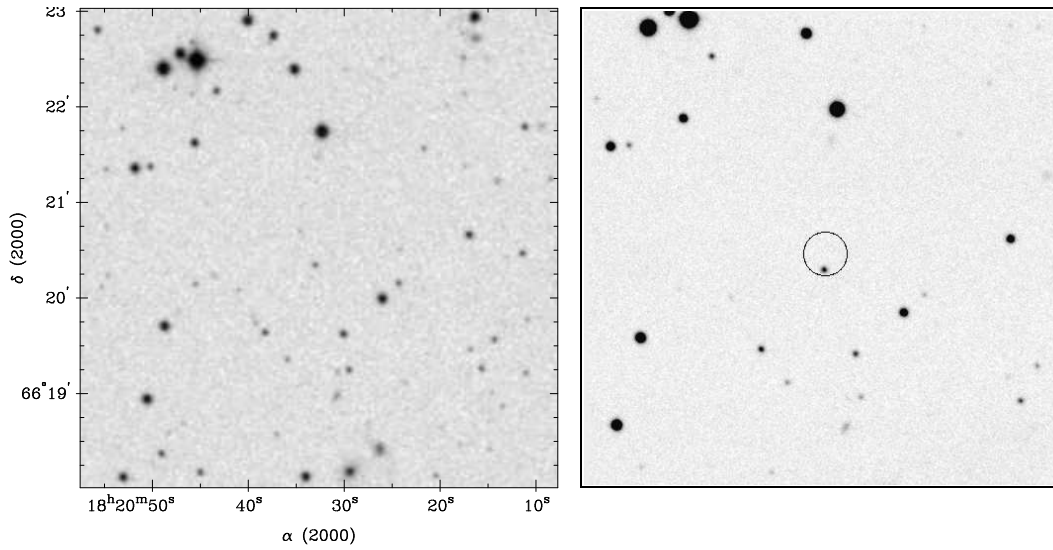
Star 8.42 mag



$\alpha/\delta_{\text{opt}} 18 20 19.3 +65 19 19$

1RXS J182032.9+662029

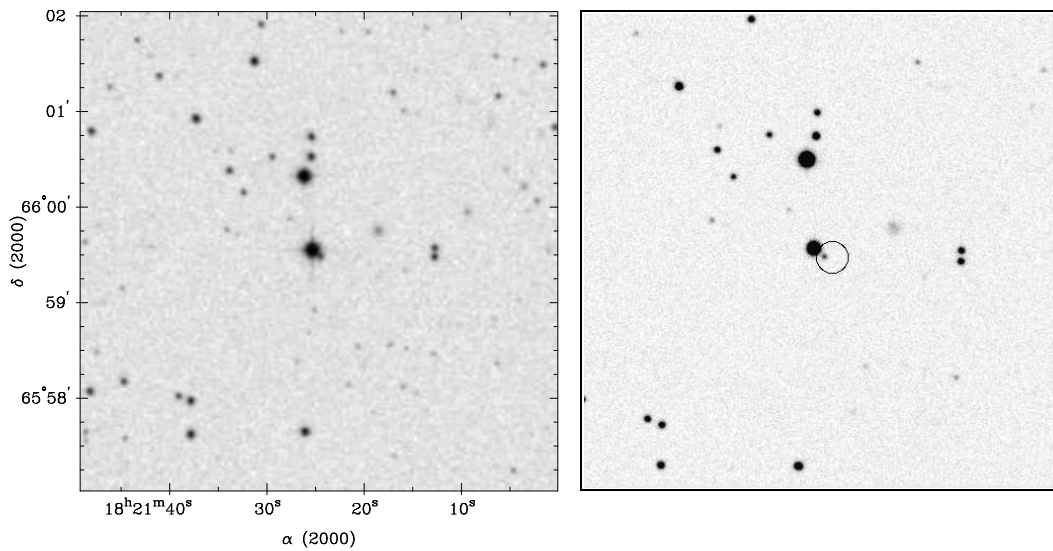
AGN $z = 0.5057$ 19.3 mag



$\alpha/\delta_{\text{opt}} 18\ 20\ 33.0\ +66\ 20\ 20$

1RXS J182123.8+655928

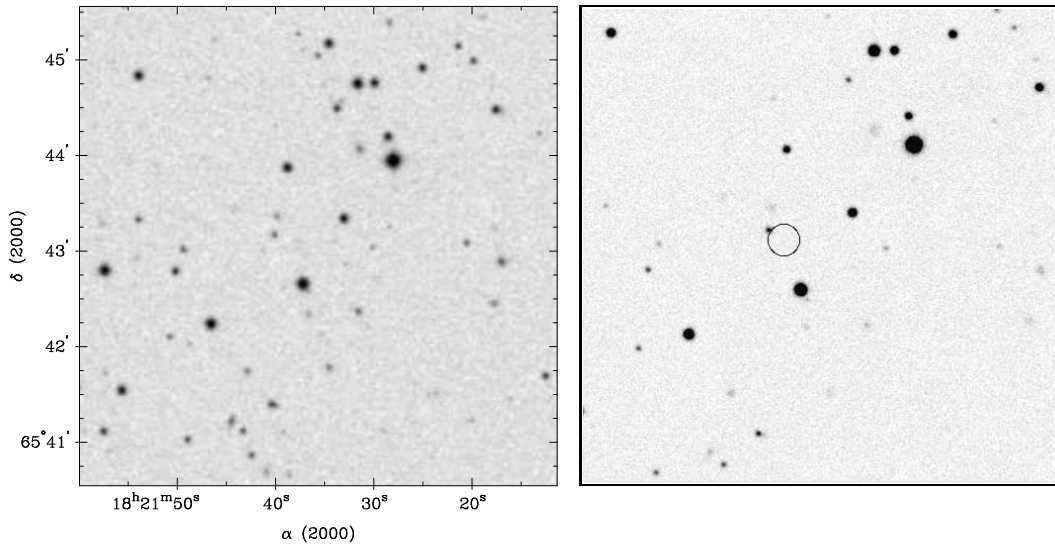
Star 19.5 mag



$\alpha/\delta_{\text{opt}} 18\ 21\ 24.4\ +65\ 59\ 29$

1RXS J182138.8+654304

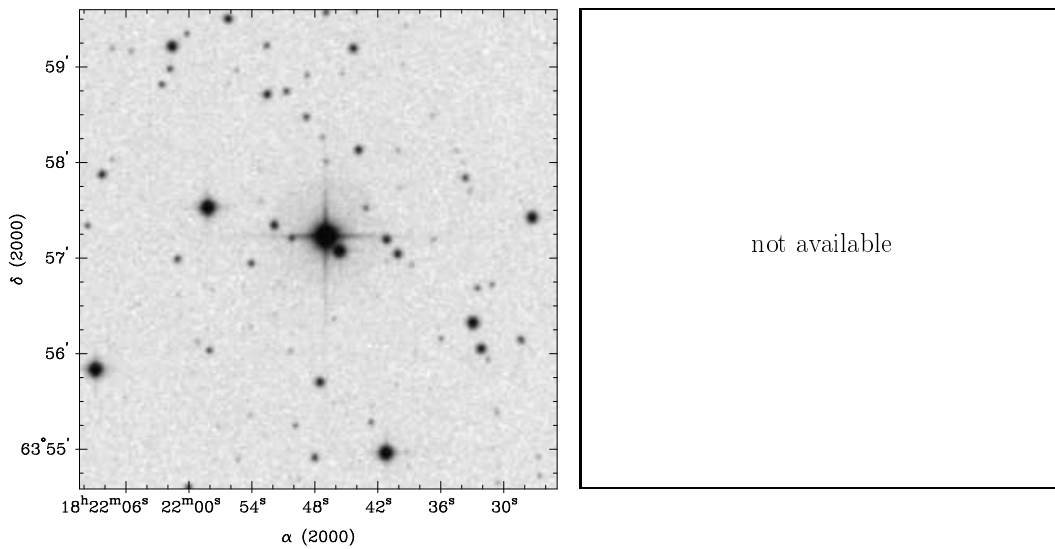
AGN $z = 0.2666$ 19.3 mag



$\alpha/\delta_{\text{opt}}$ 18 21 40.1 +65 43 10

1RXS J182146.6+635716

Star 10.5 mag

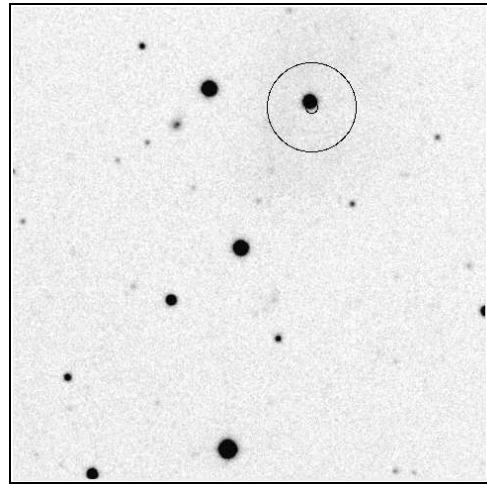
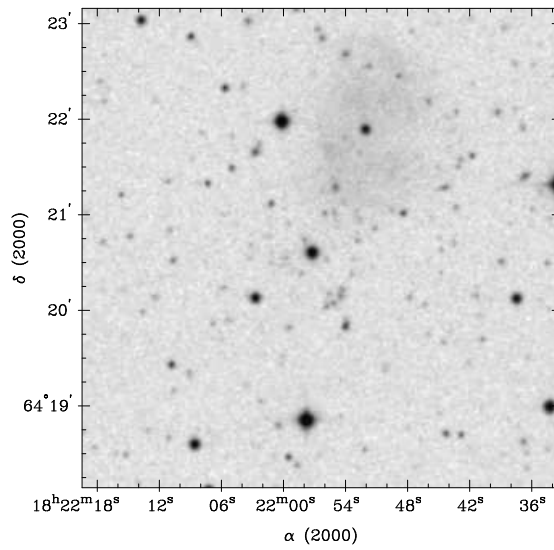


$\alpha/\delta_{\text{opt}}$ 18 21 47.0 +63 57 15

2RXP J182152.0+642147

PN

14.6 mag



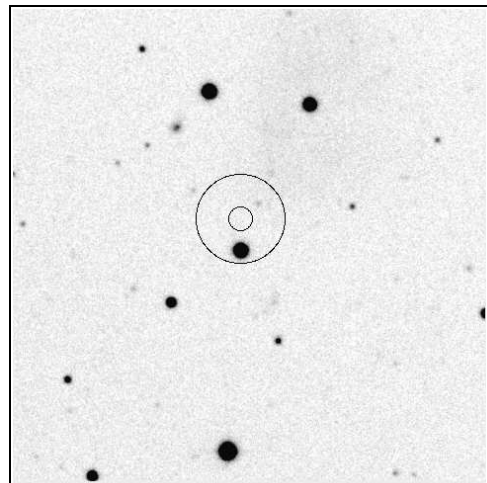
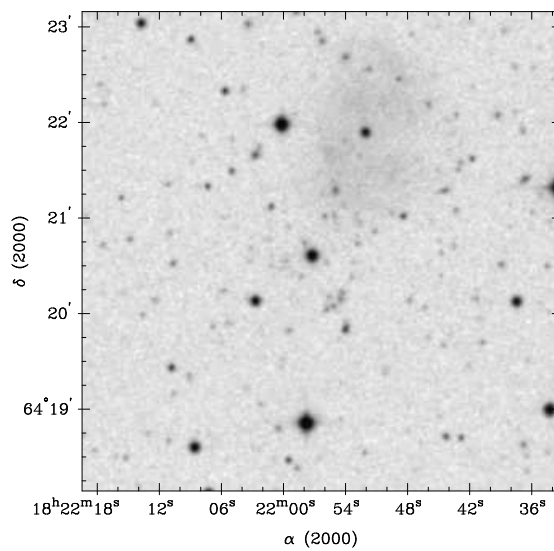
$\alpha/\delta_{\text{opt}}$ 18 21 52.1 +64 21 53

1RXS J182157.4+642051

AGN

$z = 0.2970$

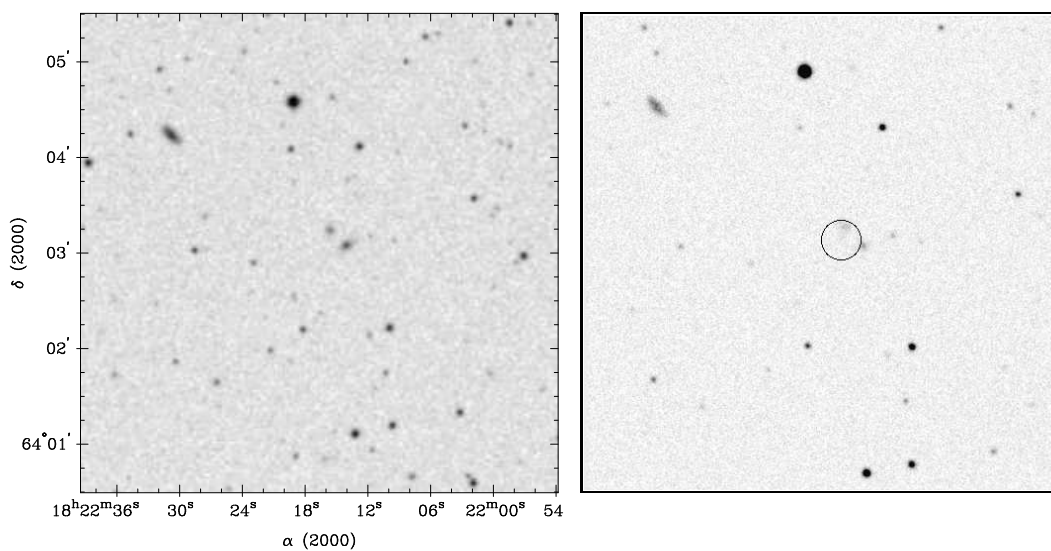
14.2 mag



$\alpha/\delta_{\text{opt}}$ 18 21 57.2 +64 20 35

1RXS J182215.8+640307

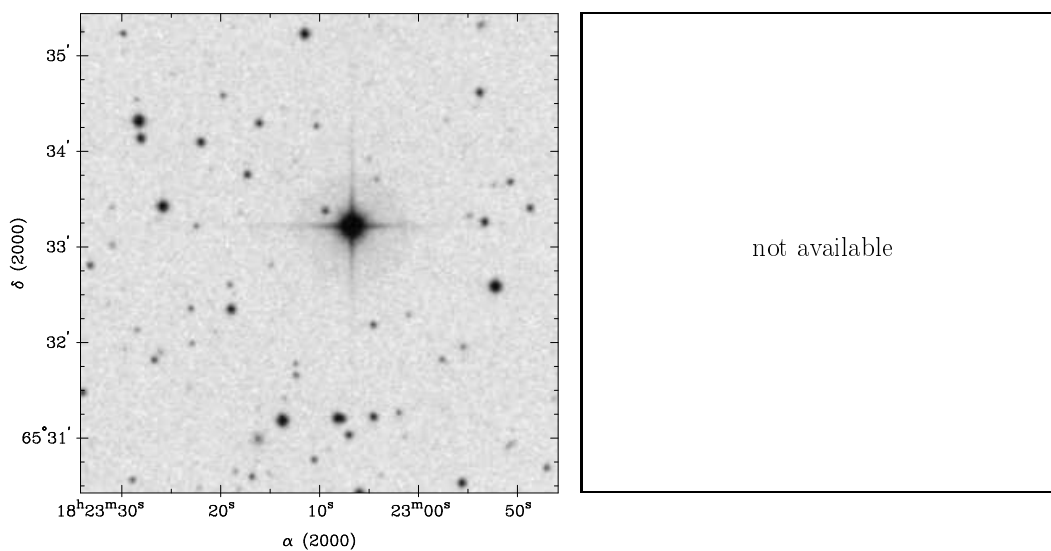
Cl. ? / Gal. ? $z = 0.200$: 19.9 mag



$\alpha/\delta_{\text{opt}}$ 18 22 14.0 +64 3 4

1RXS J182308.8+653320

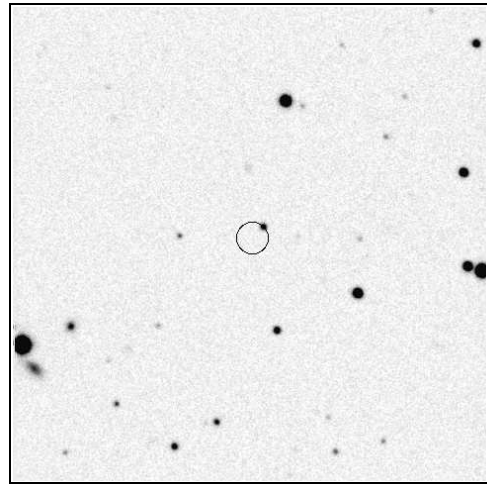
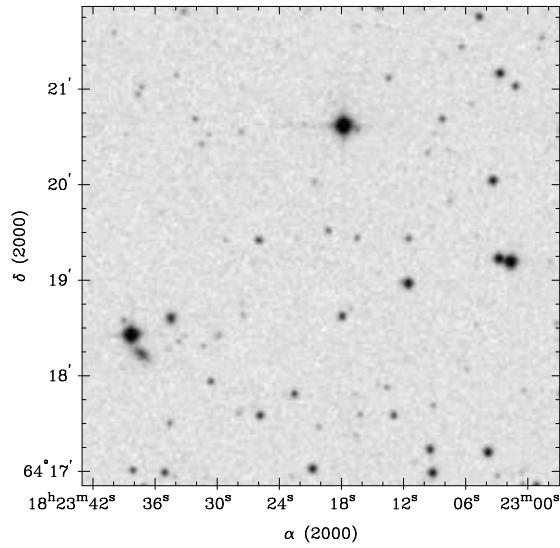
Star 9.21 mag



$\alpha/\delta_{\text{opt}}$ 18 23 6.8 +65 33 13

1RXS J182320.1+641924

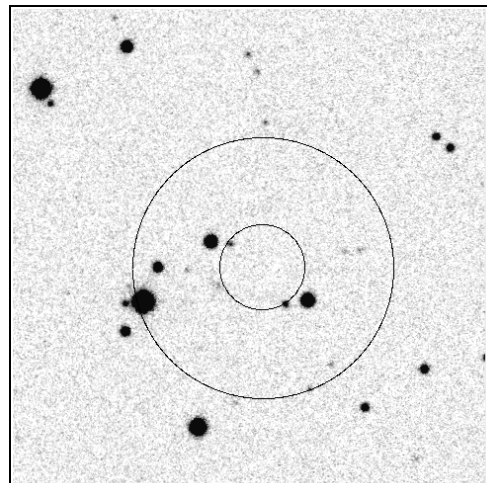
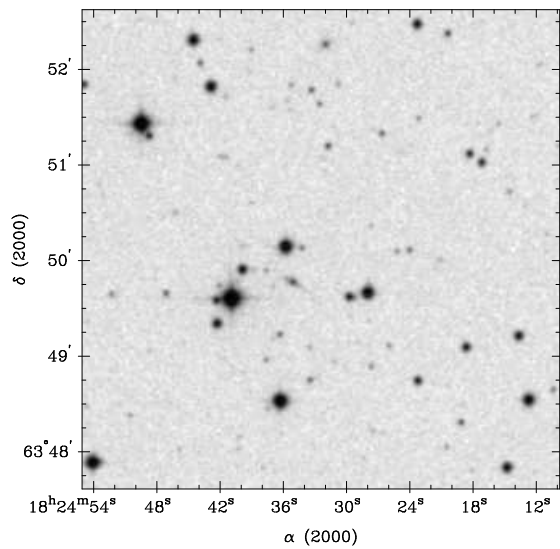
AGN $z = 0.5766$ 18.8 mag



$\alpha/\delta_{\text{opt}} 18\ 23\ 19.3\ +64\ 19\ 30$

1RXS J182431.5+634956

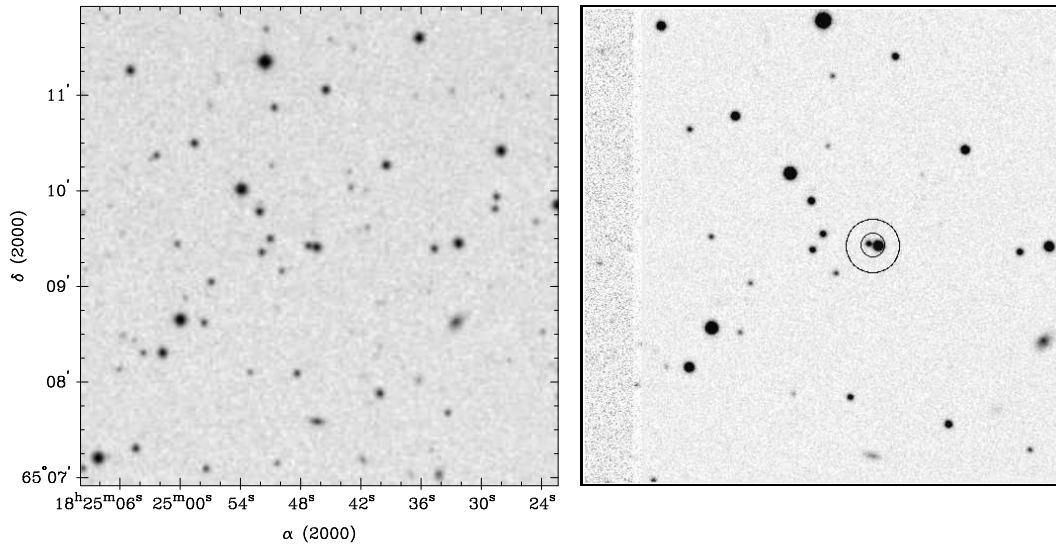
Star 18.5 mag



$\alpha/\delta_{\text{opt}} 18\ 24\ 29.6\ +63\ 49\ 38$

1RXS J182447.0+650924

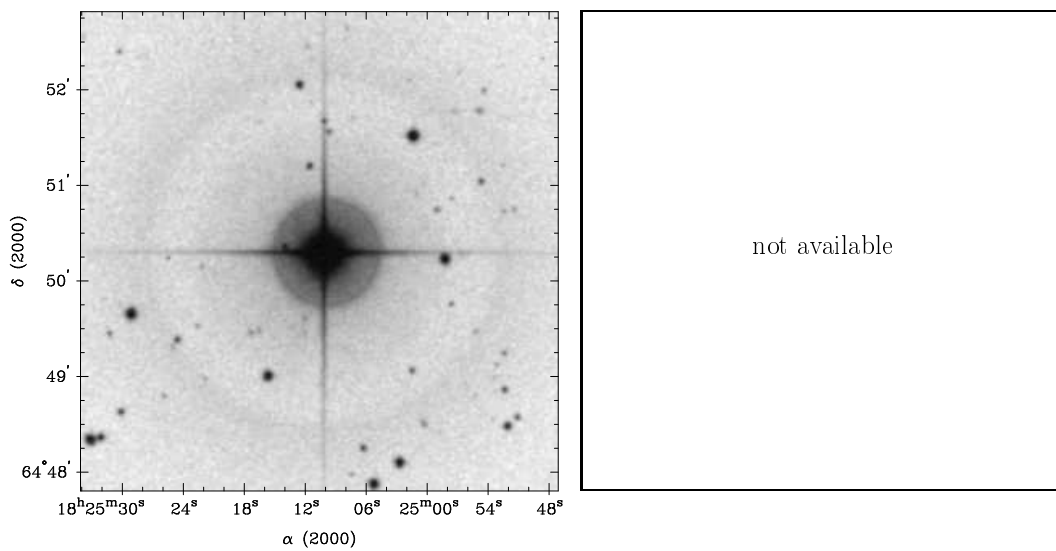
AGN $z = 0.3030$ 16.3 mag



$\alpha/\delta_{\text{opt}}$ 18 24 46.4 +65 9 24

1RXS J182510.6+645017

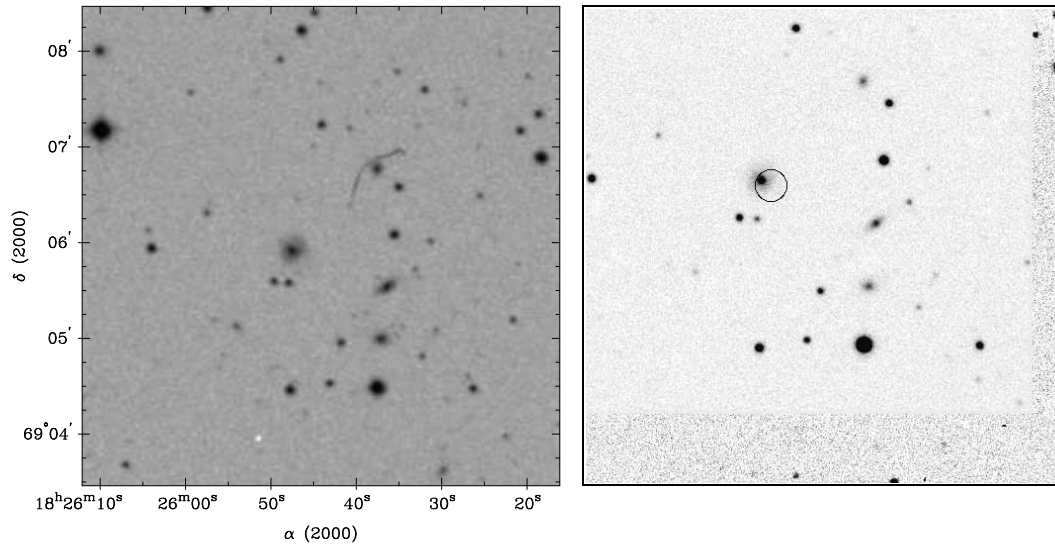
Star 7.85 mag



$\alpha/\delta_{\text{opt}}$ 18 25 10.1 +64 50 18

1RXS J182546.4+690551

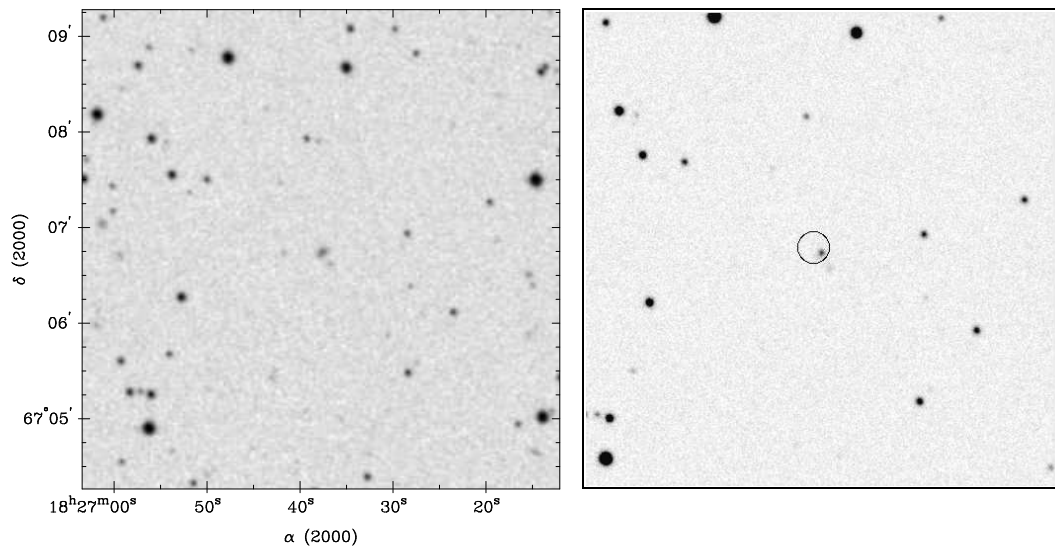
AGN $z = 0.0888$ 17.3 mag



$\alpha/\delta_{\text{opt}}$ 18 25 47.4 +69 5 54

1RXS J182638.3+670647

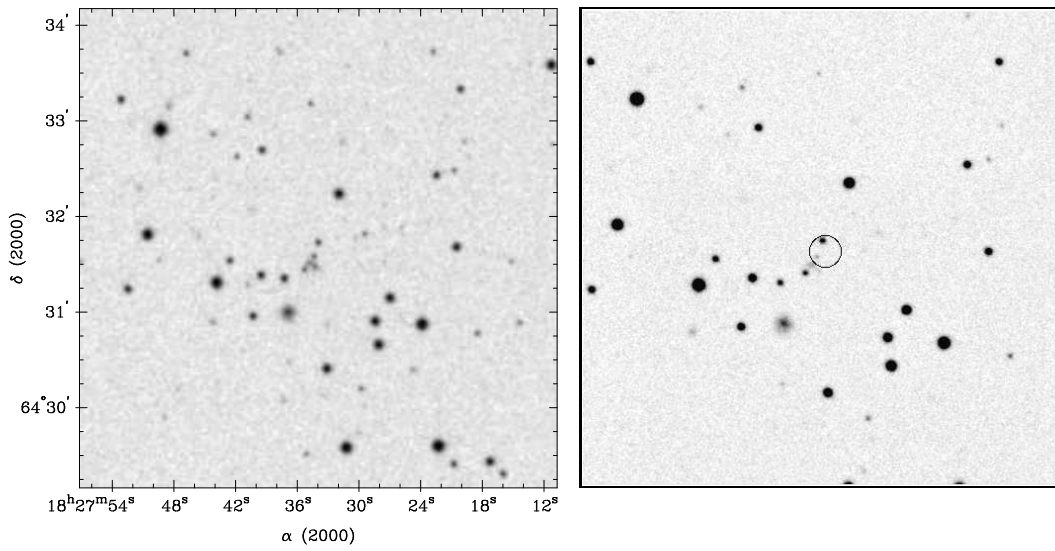
AGN $z = 0.2870$ 19.5 mag



$\alpha/\delta_{\text{opt}}$ 18 26 37.5 +67 6 44

1RXS J182733.6+643138

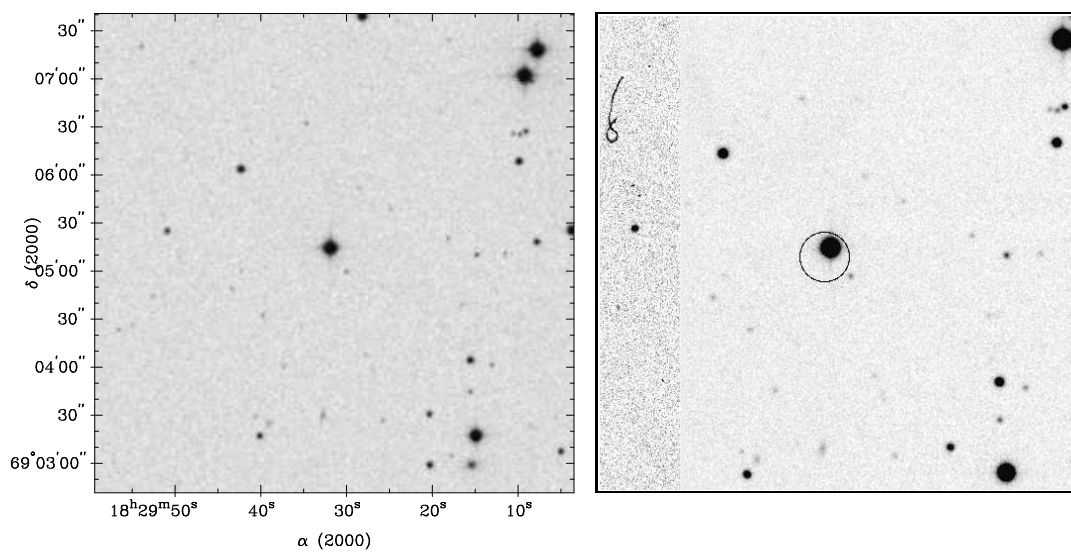
AGN $z = 0.0977$ 19.0 mag



$\alpha/\delta_{\text{opt}}$ 18 27 33.9 +64 31 43

1RXS J182932.3+690509

Star ? 12.9 mag

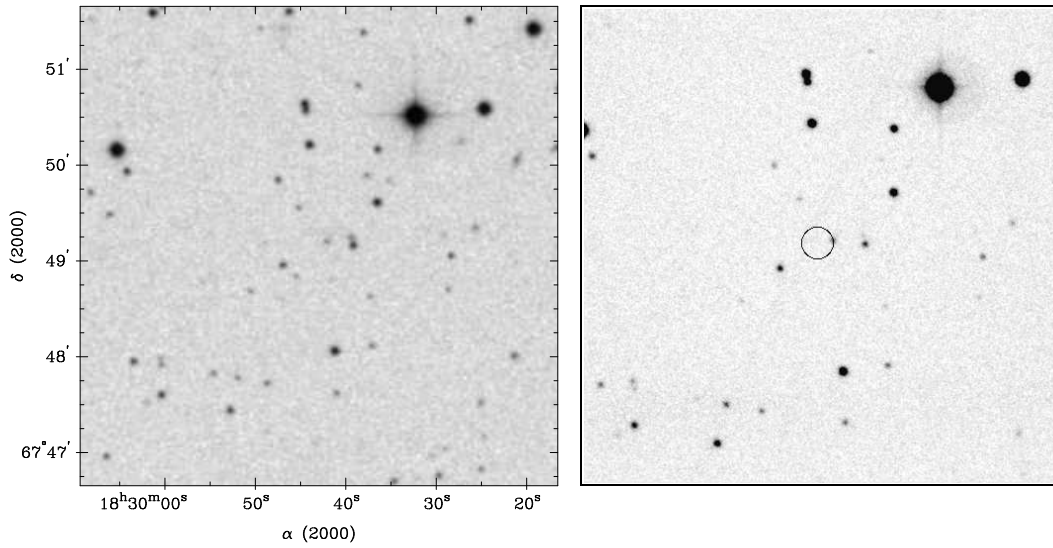


DSSII finding chart from POSSII-B

$\alpha/\delta_{\text{opt}}$ 18 29 31.8 +69 5 14

1RXS J182943.5+674910

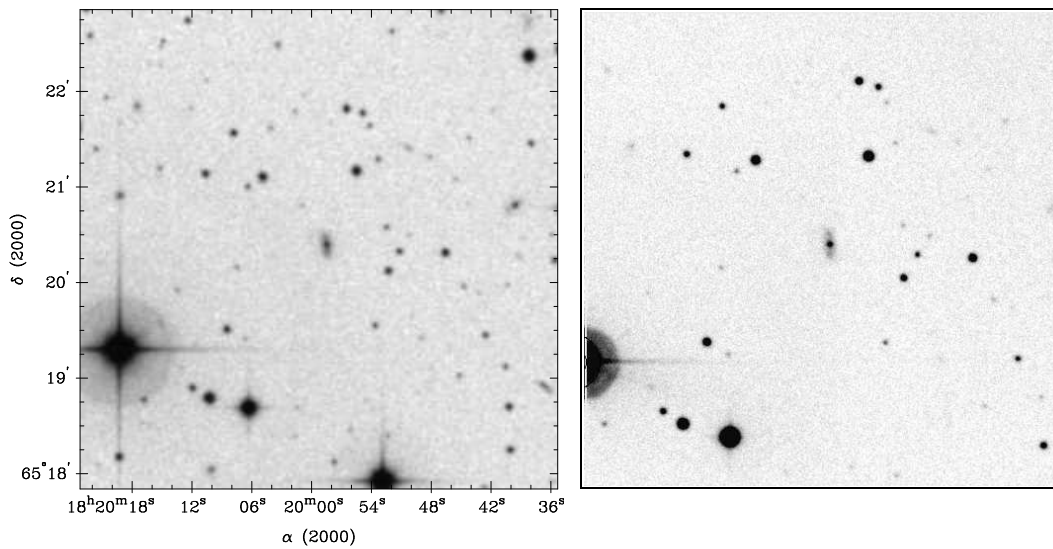
AGN $z = 0.4783$ 19.9 mag



$\alpha/\delta_{\text{opt}}$ 18 29 42.0 +67 49 12

V J181958.6+652023

Galaxy/AGN, no X-counterpart 17.9 mag



$\alpha/\delta_{\text{opt}}$ 18 19 58.6 +65 20 23

H Curriculum Vitae

Name Carsten Simon
born June 4th 1963, Berlin, Germany
Marital status married, two children

School Education

1969 – 1973 Münchhausen-Grundschule, Berlin
1973 – 1975 Hoffmann-von-Fallersleben Grundschule, Berlin
1975 – 1981 Rheingau-Gymnasium, Berlin
Dec. 1981 Abitur

University education

1982 – 1990 Study of physics at the Technical University Berlin
Sept. 1990 Diploma of physics
Diploma thesis "Objektivprismen- und Spaltspektroskopie von Kernen aktiver Galaxien"

Professional activities

1981 – 1984 Software programmer, Bernhard Koehne Industrieelektronik, Berlin
1985 Particle accelerator 2nd Operator, Hahn-Meitner Institute, Berlin
1985 – 1986 Teaching assistant, Institute of Mathematics, Technical University
Berlin
1986 – 1987 Student helper, project "TUBSAT", Space science faculty, Technical
University Berlin
1988 – 1989 Teaching assistant, Institute of Astronomy and Astrophysics, Technical
University Berlin
1990 – 1992 Research assistant, Institute of Astronomy and Astrophysics, Technical
University Berlin
1992 – 1994 Research assistant, Astronomical Institute, Georg-August-Universität
Göttingen
since 1997 Software design engineer, Siemens AG, Berlin